Inelastic mechanisms in mesocopic circuits realized in two dimensional electron gases

Carles Altimiras

Faculté des sciences d'Orsay

UNIVERSITÉ PARIS-SUD 11

THÈSE DE DOCTORAT

SPECIALITE : PHYSIQUE

Ecole Doctorale « Physique de la Région Parisienne »

Présentée par Carles-Oriol ALTIMIRAS MARTIN

Sujet :

Inelastic mechanisms in mesocopic circuits realized in two dimensional electron gases. (Mécanismes inélastiques dans des circuits mésoscopiques réalisés dans des gaz bidimensionnels d'électrons)

Thèse préparée au Laboratoire de Photonique et de Nanostructures, CNRS-UPR20, Route de Nozay, 91460 Marcoussis

Sous la direction de M Dominique MAILLY son directeur de recherches, et co-encadrée par M Frédéric PIERRE.

Soutenue le 29 Octobre 2010 devant les membres du jury :

M Christian GLATTLI, Directeur de Recherche

M Dominique MAILLY, Directeur de Recherche

M Thierry MARTIN, Rapporteur, Professeur

M Claude PASQUIER, Président du jury, Professeur

M Frédéric PIERRE, Chargé de Recherche

M Christoph STRUNK, Rapporteur, Professeur

LABORATOIRE DE PHOTONIQUE ET DE NANOSTRUCTURES

cnrs

Contents

Chapter 1

Résumé en français

Cette thèse est consacrée à l'étude expérimentale des processus d'interaction inélastiques à l'œuvre dans les circuits mésoscopiques. Les circuits mesurés sont réalisés dans des gaz bidimensionnels d'électrons crées à l'interface d'une hétérojonction semi-conductrice GaAs/Ga(Al)As. Nous avons exploré les régimes de l'effet Hall quantique entier et fractionnaire, ainsi que les interactions entre un conducteur cohérent et le circuit dans lequel il s'insère.

Transport d'énergie dans le régime de l'effet Hall quantique

Dans l'effet Hall quantique, les excitations électroniques de basse énergie se propagent le long des bords de l'échantillon dans des canaux unidimensionnels et chiraux. Nous avons étudié les mécanismes d'interaction, auxquels sont sensibles ces excitations, à travers les échanges d'énergie qui en découlent dans des situations hors d'équilibre. Une situation hors-équilibre est générée dans un canal en utilisant un contact ponctuel quantique partiellement transmis et, après propagation, la distribution en énergie est sondée en mesurant le courant tunnel traversant une boîte quantique. Nos expériences menées dans le régime entier, pour deux canaux co-propageants (ν_L=2), démontrent que la spectroscopie complète de la distribution en énergie d'un canal de bord peut être mesurée avec une boîte quantique. Nous observons une forte relaxation d'énergie le long d'un canal qui défie l'image usuelle d'électrons libres, et nous identifions les interactions inter-canal comme le mécanisme inélastique dominant. Nos résultats révèlent que les interactions au sein du même canal, ou avec des excitations thermalisées, sont irrelevantes, mais suggèrent la présence de modes co-propagatifs additionnels. Finalement, on démontre expérimentalement qu'il est possible de contrôler efficacement la relaxation en énergie. D'abord, on force la relaxation d'un canal hors-équilibre en le diluant vers un contact ohmique flottant. A l'opposé, sa dynamique de relaxation est gelée en fermant son canal co-propageant dans une petite boucle. Des expériences similaires, menées dans le régime fractionnaire au facteur de remplissage ν_L=4/3, nous ont permis d'étudier la

chiralité du flux d'énergie. Nos mesures révèlent que le flux d'énergie est non chiral alors que le courant électrique longe les bords avec une chiralité bien définie. Nous démontrons que le flux d'énergie antichiral est porté par des excitations de volume, montrant un couplage entre les excitations de bord et de volume.

Blocage de Coulomb dynamique dans un conducteur cohérent modèle

Du fait de la granularité de la charge et de l'interaction Coulombienne, un conducteur cohérent est couplé au circuit dans lequel il s'insère. En particulier, son impédance est modifiée par son environnement, modifiant les lois usuelles de composition d'impédances. C'est effet des interactions, connu comme blocage de Coulomb dynamique, est prédit d'être pondéré par le même facteur de Fano apparaissant dans le bruit de grenaille. Nous avons démontré ce fort lien en mesurant la conductance d'un contact ponctuel quantique inséré dans un circuit modifiable in-situ.

Mots-clé Physique mésoscopique, gaz bidimensionnel d'électrons, mécanismes inélastiques; effets Hall quantique entier et fractionnaire, canaux de bord, dynamique hors-équilibre, boîte quantique, contact ponctuel quantique; lois de composition d'impédances, blocage de Coulomb dynamique, conducteur cohérent.

1.1 Résultats principaux obtenus pendant la thèse

- **Démonstration d'une nouvelle technique de spectroscopie pour mesurer la fonction de distribution en énergie électronique, en utilisant une boîte quantique [1].** Cette quantité fondamentale est obtenue, pour la première fois, dans un circuit mésoscopique sémiconducteur.

- **L'observation d'une forte relaxation en énergie le long de deux canaux de bord co-propageants qui conteste l'image usuelle de canaux sans intéraction de l'effet Hall quantique à $\nu_L = 2$ [2].** Nos résultats montrent que l'interaction inter-canal, *sans échanges de particules*, est le mécanisme inélastique dominant, cependant, une fuite d'énergie du système suggère un couplage additionnel envers d'autres excitations co-propageantes pas encore identifiées.

- **Démonstration de deux techniques qui permettent de contrôler les échanges d'énergie le long de deux canaux co-propageants à $\nu_L = 2$ [3].** En modifiant les chemins parcourus par les canaux, il est possible d'augmenter, ou de geler, la relaxation en énergie d'un canal hors-équilibre.

- **L'observation d'un flux d'énergie antichiral dans l'effet Hall quantique fractionnaire à $\nu_L = 4/3$, alors que le courant électrique reste chiral.** Nous montrons que le flux d'énergie antichiral se propage dans le coeur de l'échantillon, alors que le courant électrique circule le long du bord de l'échantillon. Le flux antichiral est porté par des excitations de volume neutres.

- **Démonstration du fort lien entre le blocage de Coulomb dynamique et le bruit de grenaille chez les conducteurs cohérents [4].** Nos mesures montrent que les corrections à la conductance d'un contact ponctuel quantique, dues au blocage de Coulomb dynamique, sont renormalisées en amplitude par le facteur de Fano qui résulte de ses coefficients de transmission, en accord quantitatif avec les prédictions récentes [5, 6].

1.2 Transport d'énergie dans l'effet Hall quantique entier

1.2.1 Canaux de bords dans l'effet Hall quantique entier

Transport: description sans interactions

L'effet Hall quantique entier, découvert en 1982 par von Klitzing, Dorda et Pepper [7], est un phénomène quantique macroscopique qui apparaît lorsqu'un gaz bidimensionnel d'électrons

est soumis à un fort champ magnétique perpendiculaire. L'effet est caractérisé par une résistance longitudinale nulle, ainsi que par une résistance de Hall quantifiée en fractions entières du quantum de resistance: $R_{Hall} = \frac{1}{\nu_L}\frac{h}{e^2}$, où ν_L est un nombre entier. Dans ce régime, les seules excitations de basse énergie se propagent le long des bords de l'échantillon dans un sens bien défini par le champ megnétique, réalisant des canaux de bord co-propageants dont le nombre est égal a ν_L. En négligeant l'intéraction Coulombienne, les ν_L canaux de bords sont décrits comme des conducteurs unidimensionnels idéaux et chiraux. Une analogie entre les canaux de bord et les faisceaux lumineux, ainsi que la possibilité de les manipuler avec des constrictions ajustables comme l'injection et détection sélective, et l'usage comme diviseur de faisceau (lame semi-refléchissante), ont ouvert la voie à des expériences interférentielles sur les canaux de bords [8, 9, 10, 11, 12, 13, 14, 15]

L'impact de l'interaction coulombienne

La description usuelle des canaux de bords ignore l'interaction coulombienne car les mesures de transport standard n'y sont pas sensibles [16]: à cause de la la chiralité, les électrons injectés dans una canal de bord ne peuvent pas être rétrodiffusés dans les échantillons macroscopiques, de sorte que le courant électrique circule le long des bords en ignorant les détails microscopiques des échantillons. Cependant, il est attendu que l'intéraction coulombienne puisse modifier de façon dramatique la nature même des excitations de bord:

1. Dans des potentiels de confinement doux obtenus dans la plupart de réalisations expérimentales, il est prédit que l'intéraction coulombienne reconstruit le profil de densité proche du bord [17, 18, 19]. A cause de cette reconstruction, des branches additionnelles d'excitations de bord on été est prédites [19, 20].

2. Pour une intéraction suffisamment forte entre canaux de bords co-propageants, ils est prédit que le dynamique en résultant est décrite par des excitations bosoniques delocalisées parmis les canaux [21]. Dans le cas de deux canaux à $\nu_L = 2$ qui portent des spins opposés, la dynamique de spin et de charge sont séparées dans un mode de charge rapide et un mode de spin lent [22].

En étant sensibles a la cohérence de phase d'un seul canal de bord, les expériences récentes d'interférométrie Mach-Zehnder [11, 12, 13, 14, 15, 23] ont démontré toute une zoologie de phenomènes incompatibles avec la description sans intéraction. Il en a suivi un débat théorique considérable, mais il n'y a toujours pas de modèle permettant d'englober tous les résultats expérimentaux. Les expériences d'interférométrie Mach-Zehnder sont difficiles à interpreter directement car elles sont sensibles à deux processus distincts de déphasage: D'un côté, les méchanismes inélastiques qui vont limiter de façon fondamentale le temps de

vie des excitations électroniques sondées. D'un autre côté, le bruit de basse fréquence[1] qui peut se coupler aux excitations sondées, et brouiller artificiellement la phase mesurée. Nous proposons de s'affranchir de la deuxième contribution en mesurant directement des effets dus uniquement aux mécanismes inélastiques. Pour cela, il suffit de mesurer les échanges d'énergie qui en découlent, lorsqu'un canal de bord est excité dans un état hors d'équilibre.

Dans ce but, nous avons mis en place une nouvelle technique de spectroscopie nous permettant de sonder le fonction de distribution électronique, $f(E)$, dans des situations hors-équilibre. La mesure de $f(E)$ nous a permis de mesurer les courants d'énergie portés par les excitations électron-trou du canal de bord mesuré, sans paramètres ajustables, et d'identifier les mécanismes inélastiques auxquels elles sont sensibles.

1.2.2 Approche experimentale

Dans un système électronique unidimensionnel et chiral, les excitations électron-trou de la mer de Fermi, sans intéractions, portent un flux d'énergie (chaleur), J_H, directement charactérisé par la fonction de distribution électronique, $f(E)$. Dans ce cas, J_H ne dépend point des détails microscopiques [24]:

$$J_H = \frac{1}{h}\int \big(E - E_F\big)\Big(f(E) - \Theta(E_F - E)\Big)\mathrm{d}E, \tag{1.1}$$

où E_F est l'énergie de Fermi et $\Theta(E)$ la fonction marche unité de Heaviside.

Indépendamment du flux d'énergie total, des changements dans la forme de $f(E)$ sont une signature directe d'échanges d'énergie, et ils peuvent être utilisés pour traquer les mécanismes inélastiques en jeu. Ce principe a été implémenté avec succès dans des fils métalliques mésoscopiques [25] et dans des nanotubes de carbone [26].

Dans le régime de l'effet Hall quantique entier, la distribution en énergie d'un canal de bord peut être extraite du courant passant à travers un état localisé, réalisé dans une boîte quantique, couplé dans le régime tunnel. De plus, une situation hors-équilibre, contrôlée et ajustable, peut être génerée dans une petite constriction, réalisée par un contact ponctuel quantique, lorsqu'elle est opérée comme diviseur de faisceaux et polarisée en tension.

Une boîte quantique comme filtre à énergie

Une boîte quantique est une flaque d'électrons suffisamment petite pour que le spectre résultant du confinement soit discret. Quand elle est couplée à des électrodes par des barrières tunnel opaques, seuls les électrons ayant la même énergie qu'un niveau discret de la boîte peuvent la traverser. Dans la limite où un seul niveau discret est dans le fenêtre de tranport (Figure 1.1.a), le courant traversant la boîte, I_{QD}, est directement proportionnel à la

[1] Mais a des fréquences suppérieures à l'inverse du temps de mesure.

différence entre les distributions en énergie électronique dans les deux électrodes drain (D) et source (S), à l'énergie du niveau discret, E_{lev}:

$$I_{QD} = I_{Max}(f_D(E_{lev}) - f_S(E_{lev})), \tag{1.2}$$

où I_{Max} encapsule les détails microscopiques du couplage tunnel, et est constante pour des densité d'états tunnel dont la variation en énergie est négligeable. Une grille métallique couplée capacitivement à la boîte permet de changer l'énergie du niveau discret et donc de l'énergie sondée, en changeant la tension de grille V_G. De plus, l'application d'une différence de potentiel entre les deux électrodes, permet de séparer leur contribution à (2.2) et donc de sonder distinctement leur distribution en énergie, $f_{D/S}(E)$, en balayant l'énergie du niveau discret. En pratique, on a mesuré la transconductance de la boîte quantique, $\partial I_{QD}/\partial V_G$, qui est donc proportionnelle à $[\partial(f_D(E) - f_S(E))/\partial E]_{E=E_{lev}}$ (Figure 1.1.a, droite).

Un contact ponctuel quantique comme source de situations hors-équilibre

Un contact ponctuel quantique (CPQ) est une petite constriction du gaz bidimensionnel d'électrons dont la largeur est ajustable [27]. Dans le regime de l'effet Hall quantique entier, ils peuvent être utilisés comme des diviseurs de faisceux de sorte qu'ils transmettent/réfléchissent partiellement une paire de canaux de bords incidents. Quand la transmission est réglée dans la gamme $0 < \tau < 1$, et le CPQ est polarisé en tension, il mélange les populations des canaux incidents qui portent des potentiels électrochimiques différents. Lorsque la diffusion par le CPQ est élastique et τ indépendante de l'énergie, la distribution en énergie des canaux sortants est simplement la somme de deux fonctions de Fermi $f_F(E)$ translatées en énergie, pondérées par le coefficient de transmission/réflection correspondants, $\tau/1-\tau$. En conséquence, la distribution en énergie des canaux sortants a une forme en double-marche [28] (encart gauche dans Figure 1.1.b):

$$f(E) = \tau f_F(E - eV_{D1}) + (1-\tau) f_F(E - eV_{D2}), \tag{1.3}$$

où $V_{D1/2}$ sont les potentiels appliqués aux canaux incidents (avec les notations de la Figure 1.1.b). Au delà de la diffusion élastique, the flux de chaleur, J_H^{QPC}, injecté par le CPQ dans chacun des deux canaux sortants partiellement couplés, peut être déduit de considérations très générales de bilan de puissances. Il vaut:

$$J_H^{QPC} = \frac{\tau(1-\tau)e^2(V_{D1} - V_{D2})^2}{2h} + \frac{\pi^2}{6h}(k_B T)^2, \tag{1.4}$$

où le premier terme est la contribution des excitations hors-équilibre injectées par le CPQ, alors que le deuxième est le flux de chaleur[2] porté par les excitations chirales purement thermiques à la température finie T.

[2] Ce flux de chaleur est directement obtenu en injectant une fonction de Fermi de tempeérature T dans (1.1) [29].

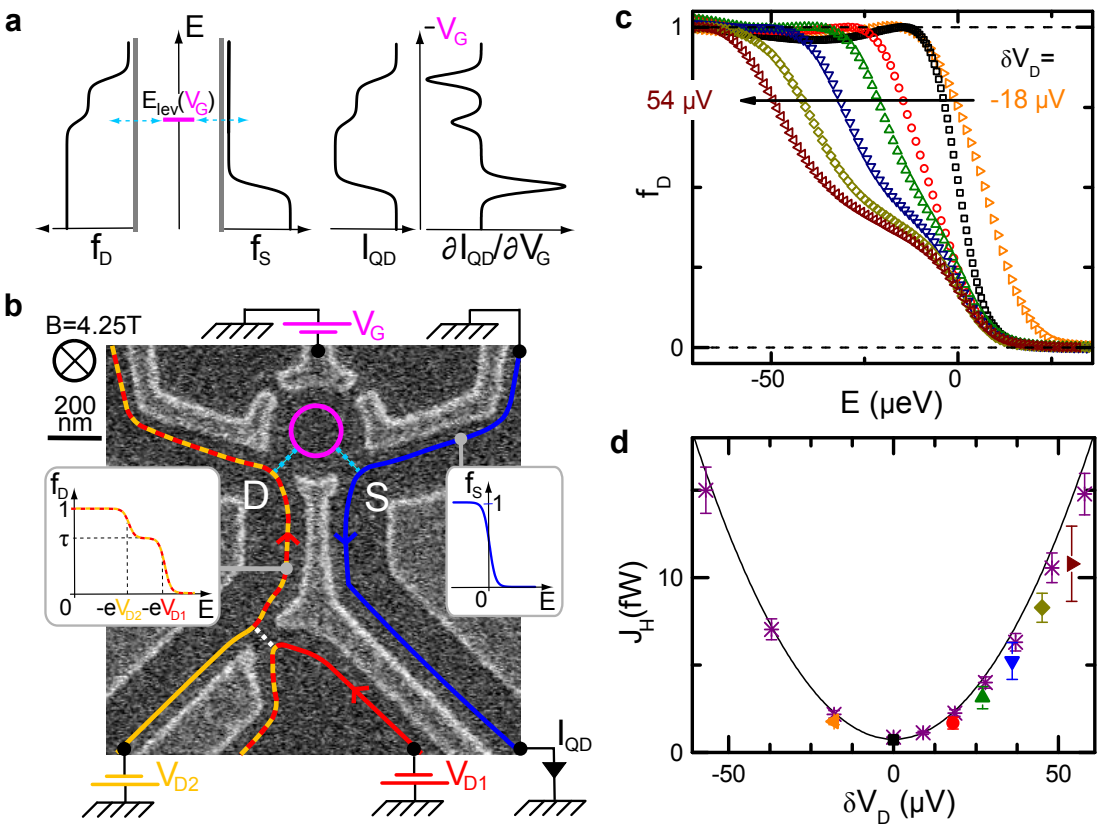

Figure 1.1: **Spectroscopie hors-équilibre avec une boîte quantique.** **a** Schéma du principe: (Gauche) Transitions tunnel possibles avec un seul niveau discret. (Droite) Le courant traversant la boîte $I_{QD}(V_G)$ est proportionnel à la différence de distributions $f_{D/S}(E)$ de chaque côté de la boîte (D/S: drain/source). En pratique, nous mesurons la transconductance $\partial I_{QD}/\partial V_G$, proportionnelle à $[\partial(f_D(E) - f_S(E))/\partial E]_{E=E_{lev}}$. **b** Micrographie de l'échantillon mesuré: les grilles y apparaîsssent en clair. Un CPQ (grilles du bas), polarisé en tension, injecte une situation hors-équilibre dans un canal de bord côté drain (encart gauche). Une boîte quantique (grilles du haut) mesure la $f_D(E)$ après une propagation de 0.8 μm. Côté source, $f_S(E)$ est à un équilibre froid (encart droite). **c** $f_D(E)$ extraites en intégrant les mesures brutes $\partial I_{QD}/\partial V_G$, pour une transmission de CPQ $\tau \simeq 0.5$ et des polarisations de CPQ differentes $\delta V_D = V_{D1} - V_{D2}$. Les $f_D(E)$ mesurées ont une forme en double marche, comme prédit par l'equation (1.3). **d** Symboles: Flux de chaleur, J_H, extrait des données dans les mêmes conditions experimentalles qu'en c. Mêmes symboles que c: mêmes données, $*$: données issues d'un deuxième refroidissement. Courbe: prediction (1.4) du flux de chaleur injecté par le CPQ. On n'observe pas de fuite d'énergie significative, à notre résolution près, après une propagation de 0.8 μm.

1.2.3 Résultats experimentaux pour deux canaux co-propageants, $\nu_L = 2$

D'abord, nous démontrons expérimentalement le principe de spectroscopie hors-équilibre avec une boîte quantique comme filtre à énergie [1]. Les mêmes mesures montrent que

l'analogie optique entre les contacts ponctuels quantiques et les lames semi-réfléchissantes tient aussi pour le transport d'énergie.

Deuxièmement, nous démontrons une forte relaxation en énergie tout au long du chemin de propagation [2]. Ces mesures contestent l'image usuelle de canaux indépendants et nous discutons les possibles mécanismes inélastiques responsables.

Finalement, nous démontrons qu'il est possible de contrôler la relaxation en énergie de canaux de bords hors-équilibre [3]. Une première technique permet de forcer la relaxation vers un équilibre froid. Alors qu'une deuxième technique permet de geler la relaxation et d'atteindre des longueurs de relaxation au moins quatre fois suppérieures.

Spectroscopie de la distribution en énergie d'un canal de bord hors-équilibre

Pour démontrer la validité de notre approche experimentale, nous mesurons la distribution en énergie après une courte distance de propagation depuis l'injection de la situation hors-équilibre. Nous utilisons un contact ponctuel quantique (CPQ), avec une transmission et polarisation en tension ajustables, pour injecter diverses situations hors-équilibre dans un canal bord. Une boîte quantique, placée après une propagation de L =0.8 μm, sonde la distribution en énergie correspondante (Figure 1.1.b).

Les distributions en énergie mesurées (Figure 1.1.c) sont proches des prédictions pour une diffusion élastique données par (1.1). De plus, le flux de chaleur extrait grâce à (1.3), est égal au flux injecté par le CPQ (1.4), à notre résolution près (Figure 1.1.d).

Ces mesures démontrent qu'un CPQ est un diviseur de canaux élastique et donc l'analogie optique entre CPQ et lames semi-réfléchissantes reste valide pour le transport d'énergie. De plus, elles montrent que la fonction de distribution en énergie électronique peut être extraite quantitativement a partir du courant traversant un boîte quantique. Finalement, la relaxation en énergie pour deux canaux co-propageants est petite à l'échelle sous-micronique.

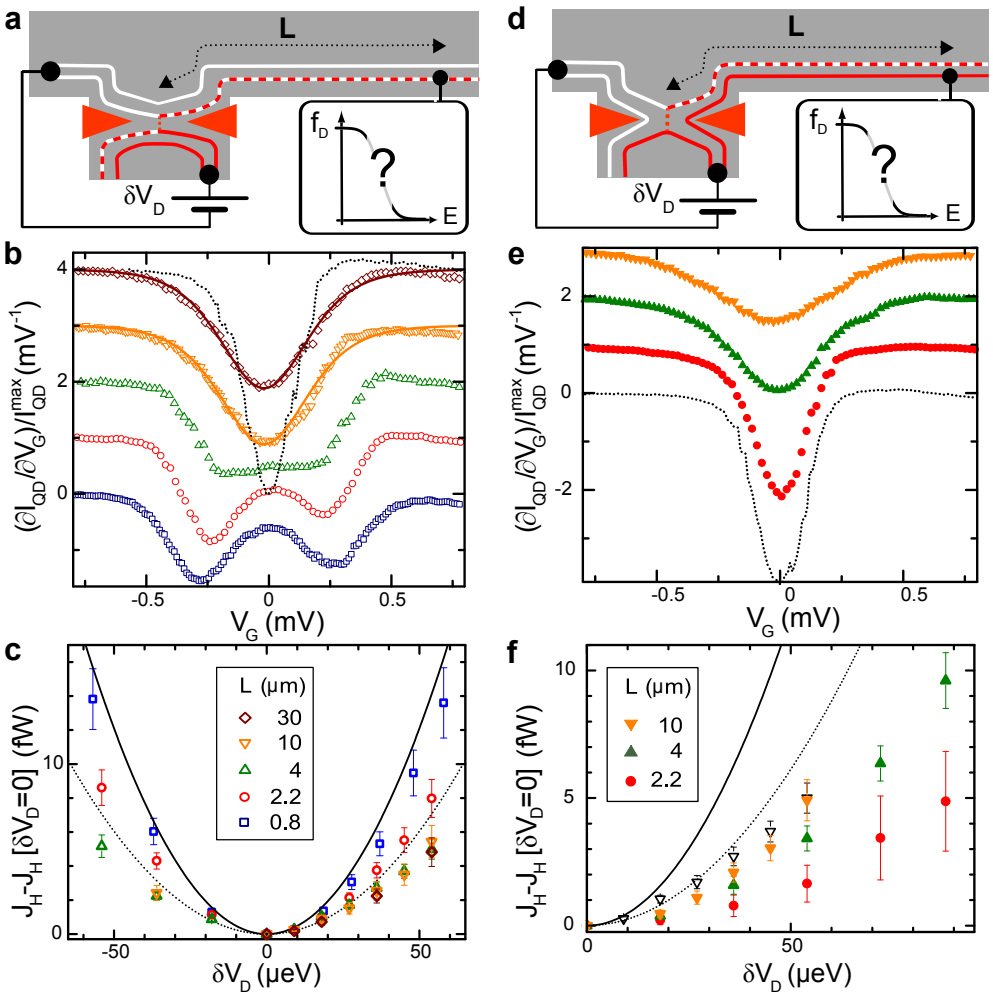

Figure 1.2: **Échanges d'énergie à $\nu_L = 2$** **a** Schéma du dispositif utilisé pour mesurer la relaxation d'un canal de bord. **b** Données brutes de relaxation ($\propto \partial f(E)/\partial E$) pour δV_D =36 µV (symboles) translatées verticalement pour différents L. Le signal évolue avec la distance de propagation et sature dans un régime d'électrons chauds. Lignes continues: fit de Fermi avec $T = 85$ mK, plus chaud (large) que le signal d'équilibre (ligne discontinue) **c** Flux de chaleur mesuré soustrait du flux d'équilibre (symboles) et prediction du flux injecté par le CPQ (ligne continue). Le flux diminue avec L et sature plus bas que la limite permise pour un système à 2 canaux fermé (line discontinue). **d** Schéma du dispositif utilisé pour mesurer les échanges d'énergie entre canaux. **e** Données brutes à l'équilibre (ligne discontinue) et δV_D =54 µV (symboles), translatées verticalement. Le pic d'équilibre s'élargit (chauffe) avec L. **f** Flux de chaleur mesuré soustrait du flux d'équilibre (symboles pleins), prediction du flux injecté par le CPQ (ligne continue) et limite d'équipartition pour un système à 2 canaux fermé (line discontinue). Le canal chauffe avec L, et sature à un flux proche de la saturation mesurée en c [L =10 µm du c montré en symbole ouvert (▽)].

Échanges d'énergie dans l'effet Hall quantique à $\nu_L = 2$

Nous avons sondé la dynamique de relaxation des canaux de bords en mesurant la distribution en énergie $f(E)$, après différentes longueurs de propagation L depuis le point d'injection de la situation hors-équilibre. La situation hors-équilibre est obtenue avec une transmission fixe de $\tau = 0.5$ pour le canal partiellement transmis par le CPQ.

Relaxation en énergie: Dans un premier temps, nous injectons la situation hors équilibre dans le même canal qui est sondé après propagation (Figure 1.2.a). Nos mesures $\partial I_{QD}/\partial V_G \propto \partial f(E)/\partial E$ presentées en Figure 1.2.b, démontrent la présence de mécanismes inélastiques car la forme de $f(E)$ évolue le long de la propagation. Le canal atteint un régime d'électrons chauds, car il sature, dans les longues distances, à une fonction de Fermi de température $T = 85$ mK (lignes continues pour $L = 10$ et 30 µm) alors que la température de base est de ~ 30 mK. Pour une analyse plus quantitative, nous extrayons le flux de chaleur atteignant la boîte quantique avec (1.1) et on soustrait le flux d'équilibre pour charactériser les excitations hors-équilibre uniquement (Figure 1.2.c). La dépendance avec L du flux de chaleur hors-équilibre, nous permet de définir une longueur de relaxation L_{inel}. En utilisant les vitesses de propagation mesurées par d'autres groupes dans des échantillons similaires, nous obtenons une fourchette pour le temps de vie des excitations injectées. Ce temps de vie fini, nous donne une incertitude en énergie grâce a la relation d'Heisenberg, qui au final est comparable voir supérieure à l'énergie moyenne des excitations injectées. Ceci suggère que l'énergie des excitations électron-trou d'un seul canal est mal définie, ce qui *conteste l'image usuelle de canaux sans intéractions.*

Échanges d'énergie entre canaux co-propageants: A fin de tester directement les échanges d'énergie entre canaux, nous générons la situation hors équilibre dans le canal interne, alors qu'on sonde $f(E)$ dans le canal externe (Figure 1.2.d). Le canal sondé devient de plus en plus chaud, comme suggéré par les données brutes Figures 1.2.e. Ceci est confirmé par la Figure 1.2.e, où l'on voit que le courant de chaleur porté par des excitations du canal non-excité augmente avec la propagation le long du canal mis hors d'équilibre. Nous trouvons que le flux de chaleur mesuré aux grandes distances est *indépendant* du canal excité, montrant que les échanges d'énergie inter-canal sont trés efficaces. Cependant, ce mécanisme n'est pas le seul en jeu car les flux de chaleur de saturation tombent en dehors de la fourchette prédite pour des intéractions inter-canal uniquement [30, 31] (ligne continue dans les Figures 1.2.c et f).

Couplage vers d'autres excitations co-propageantes: Néanmoins, la dépendance en énergie, et en distance de propagation, des flux de chaleur mesurés montrent que les excita-

tions thermalisées n'interviennent pas dans la relaxation mesurée. Cette conclusion englobe par exemple les phonons du substrat, les spins nucléaires, ou les excitations électroniques des grilles utilisées pour définir les différents parcours. Cependant, nos mesures sont compatibles avec des échanges d'énergie avec des branches d'excitations co-propageantes. Mais par contre, aucun transfer de charge inter-canal n'est observé.

Deux techniques pour contrôler la relaxation en énergie

Dans le but de réaliser des expériences d'optique quantique sur les canaux de bords, ou de les utiliser pour le traitement quantique de l'information, il est souhaitable d'augmenter leur longueur de relaxation et donc de décohérence. D'un autre côté, il est utile de disposer d'une technique permettant de forcer la relaxation vers l'équilibre, par exemple pour réinitialser l'état d'un canal. Nous avons démontré deux techniques nous permettant de réaliser ces deux situations opposées, en modifiant la géométrie des chemins de propagation.

Forcer la relaxation vers l'équilibre avec une sonde de tension: Les contacts ohmiques flottants (sondes de tension) ont été utilisés par les théoritiens [32] pour imiter les effets de relaxation en énergie et de décohérence dans le cadre de la théorie de la diffusion élastique (*sans-intéractions*).

Suivant cette idée, nous utilisons une sonde de tension pour forcer la relaxation vers l'équilibre: un canal de bord est mis hors d'équilibre comme dans l'expérience de relaxation précédente, mais dans son chemin de propagation il est couplé, à travers un CPQ intermédiaire, vers une sonde de tension (Figure 1.3.a). La distribution en énergie de ce même canal est mesurée par une boîte quantique située a 0.8 µm du CPQ intermédiare, de sorte que les effets de relaxation sont négligeables le long de cette petite distance (comme démontré en Figure 1.1).

La Figure 1.3.b montre nos données brutes $\propto \partial f(E)/\partial E$ (symboles) pour différentes transmissions du CPQ intermédiaire, $\tau_{im} = G_{im} \times h/e^2$. Lorsque le canal n'est pas couplé à la sonde de tension $\tau_{im} = 0$, on observe un signal hors-équilibre. Ce signal évolue avec la transmission du CPQ intermédiaire vers un pic d'équilibre (froid) à $\tau_{im} = 1$, montrant que la sonde de tension force la relaxation des excitions hors-équilibre qui lui sont incidentes et les thermalise à la température de base. Les lignes continues sont la prédiction de la théorie de la diffusion élastique:la somme des signaux $\tau_{im} = 0$ et $\tau_{im} = 1$ pondérés respectivement par la transmission et reflection du CPQ intermédiaire. Le bon accord obtenu avec la theéorie de la diffusion élastique nous assure: i) un bon contrôle sur cette technique pour forcer la relaxation ii) nous informe que les échanges d'énergie entre un canal froid et un canal hors-équilibre anti-propageant à ~ 0.5 µm sont négligeables et iii) confirme que la relaxation le long de chemin sous-micronique reliant le CPQ intermédiare à la boîte quantique est

négligeable.

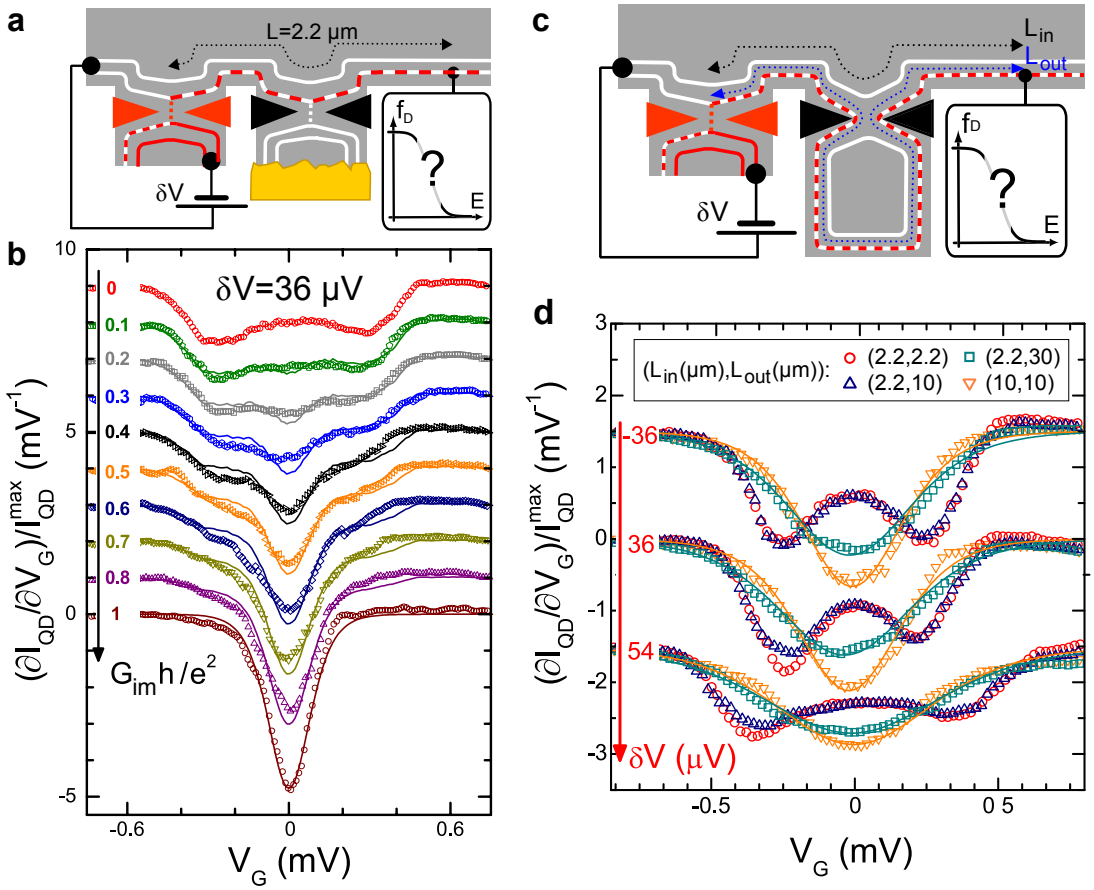

Figure 1.3: **Contrôle de la relaxation en énergie.** **a** Schéma du dispositif utilisé pour forcer la relaxation vers l'équilibre avec une sonde de tension. **b** Données brutes de relaxation $\propto \partial f(E)/\partial E$ du canal externe (symboles) translatées verticalement pour différentes transmissions du CPQ intermédiaire $\tau_{im} = G_{im} \times h/e^2$. Lignes continues: prédictions de la théorie de la diffusion élastique. Le signal hors-équilibre à $\tau_{im} = 0$ évolue avec τ_{im} vers un pic d'équilibre froid à $\tau_{im} = 1$. **c** Schéma du dispositif utilisé pour geler la relaxation le long d'un canal avec une boucle fermée. **d** Données brutes de relaxation $\propto \partial f(E)/\partial E$ (symboles) translatées verticalement pour différentes polarisations du CPQ d'injection, pour différentes géométries caractérisées par (L_{in},L_{out}) en microns. Le signal est identique à notre résolution dans les configurations (2.2,2.2) et (2.2,10) montrant le gèl de la relaxation (la relaxation est complète pour (10,10), ligne continue est un fit de Fermi). Le signal de (2.2,30) montre une relaxation en énergie, mais le flux de chaleur correspondant est identique à (2.2,2.2) et (2.2,10) à notre incertitude expérimentale près (données non montrées ici).

Geler la relaxation le long d'un canal avec une boucle fermée: De façon plus surprenante, nous avons démontré qu'il est possible de geler la dynamique de relaxation d'un canal de bord hors-équilibre. Pour cela, il suffit de fermer son canal co-propageant (ici le canal interne) dans une boucle suffisamment petite.

Le principe de l'expérience est présenté dans la Figure 1.3.c: Le canal externe est mis hors-équilibre avec un CPQ, comme dans les expériences précentes de relaxation, et propage pendant une distance L_{out} avant d'être mesuré. Le canal interne est propagatif pour une distance L_{in} qui peut être égale ou inférieure à L_{out}. Ce deuxième cas est obtenu grâce à un CPQ intermédiaire qui transmet parfaitement le canal externe et réfléchit complètement le canal interne. Le long du parcours supplémentaire du canal externe $L_{out} - L_{in}$, le canal interne est enfermé dans une boucle de même périmètre $L_{out} - L_{in}$. Comme la boucle forme un état localisé, elle ne peut absorber de l'énergie, dans le régime stationnaire, à moins d'être couplée a d'autres excitations. De plus, une boucle suffisamment petite donne lieu à une densité d'états discrète qui peut diminuer les échanges d'énergie entre canaux.

Nos mesures brutes $\propto \partial f(E)/\partial E$ du canal externe sont présentées dans la Figure 1.3 pour différentes géometries caractériseées par (L_{in}, L_{out}) en microns, et pour différentes polarisations en tension du CPQ d'injection (translatées verticalement) de transmission $\tau = 0.5$ pour le canal externe. Le signal mesuré est le même, à notre résolution près, pour $(2.2, 2.2)$ et $(2.2, 10)$ ce qui montre que la relaxation du canal externe est gelée le long d'une boucle de $\sim$8 µm. Ce résultat est d'autant plus saisissant car pour une propagation commune de 10 µm (10,10) le canal a déja complètement relaxé à son équilibre local d'électrons chauds (ligne continue fits de Fermi). La boucle de 8 µm gèle de façon efficace la relaxation du canal externe. Ce qui démontre en plus qu'il n'y pas mécanismes inélastiques au sein du canal externe pour les énergies et distances < 10 µm considérées.

Pour mieux comprendre cet effet, nous avons mesuré la relaxation le long d'une boucle de 28 µm (2.2,30). Nos mesures montrent que le signal change par rapport à (2.2,10) et (2.2,30), et donc que la canal externe relaxe. Par contre, le flux de chaleur du canal externe après propagation est identique dans les trois géometries (2.2,2.2-10-30). En conséquence, une boucle fermée de 28 µm n'empèche pas la relaxation, mais conserve l'énergie du canal externe.

On peut comprendre ces effets à cause de la discrétisation de la densité d'états dans la boucle dues aux conditions aux limites périodiques. Utilisant la valeur standard de vitesse de propagation 10^5 m/s, on obtient un spectre espacé de ~ 52 µeV pour la petite boucle de (2.2,10), et espacé de ~ 15 µeV pour la grande boucle (2.2,30). Dans la petite boucle, l'écart d'énergie du canal interne est comparable ou suppérieur à le fenêtre dénergie injectée dans le canal externe (36 et 54 µeV), et supprime les échanges d'énergie entre les deux canaux. Ce qui n'est pas le cas pour la grande boucle. De plus, le fait que l'énergie en sortie de la

grande boucle est identique aux autres configurations (2.2,2.2) et (2.2,10), montre que les possibles degrés additionnels predits pour les canal externe [20] n'absorbent pas d'énergie pour les énergies considérée et des distances < 30 µm et que le canal interne fermé en boucle n'est point couplé à d'autres excitations que celles mesurées sur le canal externe. Les degrés de liberté responsables de la fuite d'énergie manifeste en Figure 1.2.c ne sont donc toujours pas identifiés.

1.3 Transport d'énergie dans le régime de l'effet Hall quantique fractionnaire

1.3.1 L'effet Hall quantique fractionnaire

L'effet Hall quantique fractionnaire fut découvert en 1982 par Tsui, Störmer et Gossard [33] et est un des phénomès les plus intriguants de la matière condensée. Contrairement à l'effet Hall quantique entier, il est intrinsèquement du à l'intéraction coulombienne, et en resultent des effets surprenants: par exemple, dans ce régime les excitations chargées portent une charge fractionnaire [34], comme démontré en [35, 36], et elles sont prédites [37] d'exhiber une statistique d'échange fractionnaire (interpolant entre les statistiques usuelles de Fermi-Dirac et de Bose-Einstein).

Comme dans l'effet Hall quantique entier, le corps du système a un gap dans son spectre d'excitations, et les seules excitations de basse énergie ne peuvent se propager que le long des bords de l'échantillon dans des canaux chiraux. Ceci résulte en une résistance longitudinale nulle et une résistance de Hall quantifiée. Par contre, dans l'effet Hall quantique fractionnaire, les canaux de bord ne peuvent pas être décrits par des branches d'excitations chirales de fermions sans-intéractions. La théorie effective développée par Wen [38], les décrit par des liquides de Luttinger chiraux. Cette théorie prédit des caractéristiques I-V non lineéaires dans des contacts tunnel [39], avec des lois de puissances dont les exposants sont universels et ne dépendent que du facteur de remplissage, ν_L, caractérisant la résistance de Hall fractionnaire. Même si les expériences observent couramment ces lois de puissances, les exposants sont systématiquemnt inférieurs [40] à ceux prédits par le théorie. Ces déviations systématiques pourraient résulter des détails microscopiques du bord, comme la reconstruction du profil de densité attendue pour les potentiels de confinement doux [17, 19]. Mais de nos jours, les détails microscopiques des canaux de bords sont mal connus expérimentalement. Même des informations aussi importantes comme le nombre de branches d'excitations de bords et leur chiralité, qui peuvent être non triviaux pour certains régimes de l'effet hall fractionnaire [41, 42], ne sont toujours pas connus.

1.3.2 Vers la mesure des détails microscopiques des bords avec du transport d'énergie

Le transport d'énergie, notamment de chaleur, peut donner des informations précieuses sur la structures des canaux de bord. Par exemple, des branches d'excitations neutres sont attendues pour certains régimes (comme $\nu_L = 2/3$ ou $5/3$) [42]. Ces modes neutres n'ont toujours pas été observés car ils sont transparents au transport de charge, mais par contre ils devraient transporter un flux de chaleur antichiral [43]. Nous avons développé un système expérimental qui permet de mesurer des flux de chaleur dans le rgime de l'effet Hall quantique fractionnaire. Les premières mesures préliminaires, dans le régime de $\nu_L = 4/3$, montrent le potentiel de cette technique en dévoilant une dynamique hors équilibre riche.

Exploiter le blocage de Coulomb d'un îlot de charge comme filtre à énergie

Dans le but de tester la chiralité des flux de chaleur, il suffit d'utiliser une sonde d'énergie qualitative. Nous avons employé un îlot sensible au blocage de Coulomb comme un filtre passe haut d'énergie:

Le transport de charge à travers l'îlot, dans le régime tunnel séquentiel, est bloqué tant que l'énergie des excitations électroniques incidentes est inférieure à l'énergie de charge de l'îlot [44, 45]. Le courant qui le traverse, intègre donc les excitations incidentes de plus haute énergie que l'énergie de charge, et permet de l'utiliser comme un filtre passe-haut d'énergie.

Dans nos expériences, nous avons avons utilisé un contact ponctuel quantique (CPQ) dans la limite de faible transmission. Dans notre échantillon, le CPQ présente des diamants de Coulomb dans cette limite (Figure 1.4.a), montrant que le transport électrique est sensible à une physique d'énergie de charge[3].

1.3.3 Mesures de tranport d'énergie à $\nu_L = 4/3$

Le principe de l'expérience est schématisé dans la Figure 1.4.b: deux CPQs "d'injection" (en rouge) sont utilisés pour générer un situation hors d'équilibre dans deux endroits le long d'un canal de bord. L'énergie portée par le même canal est sondée par un troisième CPQ (noir), opéré dans un régime de blocage de Coulomb, et situé entre les deux points d'injection. Cette géométrie permet la comparaison *directe* entre les flux chiral et antichiral de chaleur générés par les CPQ d'injection situés respectivement en amont et en aval de la *même* sonde.

[3] C'est effet est possiblement dû au désordre résiduel de l'échantillon, qui peut créer un petit état localisé a proximité du CPQ.

Chiralité du flux de chaleur et du courant électrique

Le courant électrique mesuré, dans les situations d'équilibre et hors-équilibre, suit le bord de l'échantillon avec la chiralitée imposée par le champ magnétique. Par contre, nous observons que le signal du CPQ sonde dépend non seulement de l'énergie injectée en amont, mais aussi en aval (Figure 1.4.c). Ce qui démontre que *le flux de chaleur n'est pas chiral, alors que le courant électrique l'est.* La géométrie elliptique du signal de sonde, en fonction de la polarisation en tension des CPQs en amont et en aval, montre que le flux de chaleur antichiral est insensible à l'énergie injectée en amont. En conséquence, il ne peut pas être du à un simple chauffage local au dessus du gap d'activation thermique du régime fractionnaire testé[4].

Couplage avec des excitations de volume neutres

En effectuant les même mesures dans des géométries différentes, nous observons que le signal ne dépend que de la distance "à vol d'oiseau" entre l'injection et la sonde, et non pas du parcours précis des canaux de bord. Le test le plus strict, est de connecter un contact ohmique flottant au canaux de bord entre le CPQ sonde et le CPQ d'injection en aval, sans modifier la distance à vol d'oiseau entre sonde et injection. Ces observations démontrent que le flux de chaleur anti-chiral est porté par des excitations de volume neutres. Et donc, que le canal de bord hors équilibre est couplé à ces excitations.

[4] Qui de surplus s'accompagnerait d'une rétrodiffusion finie du courant électrique.

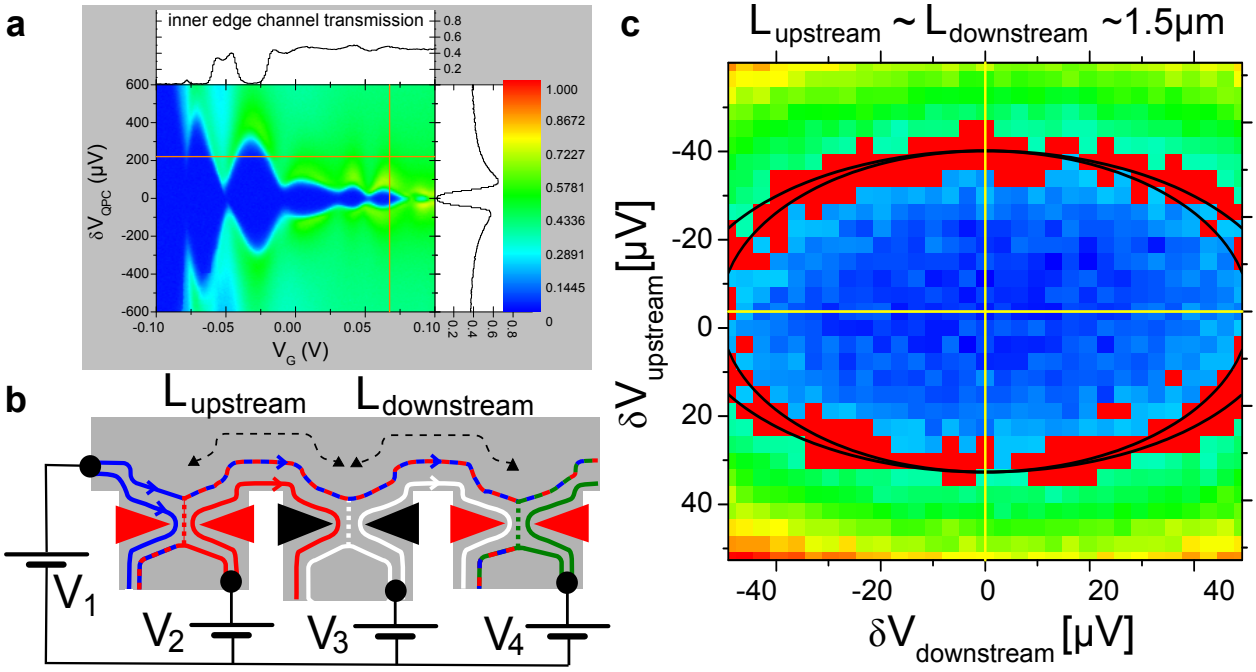

Figure 1.4: **Flux de chaleur antichiral dans le régime de l'effet Hall quantique fractionnaire à $\nu_L = 4/3$.** **a** Graphe 3D en couleur de la transmission du CPQ sonde, en fonction de ses tensions de grille et de polarisation. Les projections en tension de grille et en polarisation (encarts haut et droit respectivement) correspondent aux droites jaunes du graphe. Des diamants de Coulomb sont visibles aux petites transmissions (tension de grille). **b** Schéma du dispositif utilisé pour tester la chiralité du tranposrt de chaleur. Un CPQ sonde (noir) compare le flux de chaleur chiral et antichiral généré par deux CPQ d'injection (rouges) situés en amont et en aval respectivement. **c** Graphe 3D en couleur de la transmission du CPQ sonde en fonction de la polarisation des CPQ d'injection en aval ($\delta V_{downstream}$) et en amont ($\delta V_{upstream}$). Le CPQ sonde est opéré avec une énergie de charge ~ 30 μeV (encart de droite en a). Le signal à travers la sonde dépend de la polarisation du CPQ en aval, démontrant un flux d'énergie antichiral. La géometrie elliptique du signal montre que le flux antichiral ne dépend pas de l'énergie totale locale, mais seulement de l'énergie injectée en aval.

1.4 Blocage de Coulomb dynamique dans un conducteur cohérent

La dernière partie de cette thèse s'intéresse à comment les lois classiques de composition d'impédance sont modifiées par l'intéraction coulombienne dans les circuits quantiques. La théorie du blocage de Coulomb dynamique [46] explique comment la conductance d'un conducteur cohérent est modifiée par le circuit dans lequel il s'insère. Des prédictions récentes [5, 6] prédisent un fort lien entre cet effet et le bruit de grenaille du conducteur cohérent. Nous avons testé cette prédiction forte en mesurant le blocage de Coulomb dynamique d'un conducteur cohérent modèle, un contact ponctuel quantique (CPQ), dont les coefficients de transmission (et donc son bruit de grenaille) peuvent être modifiés *in-situ*.

1.4.1 Composition d'impédances dans les circuits quantiques

Dans les circuit classiques, les conducteurs sont décrits par leurs relations constitutives encapsulées dans leur impédance, ou admittance. La dynamique d'un circuit complexe est complètement déterminée par ces impédances et par les règles de composition d'impédances données par les lois de Kirschoff. Dans les circuits quantiques, un conducteur (élastique) est caracterisé par ses coefficients de transmission pour les ondes électroniques qui lui sont incidentes [47, 48, 49]. Si les électrons maintiennent une cohérence de phase entre les différents conducteurs du circuit, des phénomènes d'interférences peuvent modifier les lois classiques de composition [32, 50]. Mais, même quand les conducteurs sont espacés de plus de la longueur de cohérence de phase, des effets associés à la granuralité de la charge et à l'intéraction coulombienne peuvent modifier les lois de composition classiques. Le blocage de Coulomb dynamique décrit ces effets [46], et en pratique, il en résulte que la conductance d'un conducteur cohérent diminue aux basses tensions et tempéraures lorsqu'il est inséré dans un circuit résistif.

1.4.2 Blocage de Coulomb dynamique

Quand un électron est transmis, ou réfléchit, par une barrière de potentiel, le pulse de courant associé peut exciter les modes électromagnétiques du circuit dans lequel il s'insère. Comme un partie de l'énergie portée par l'électron est transférée au circuit, le processus de transmission devient inélastique et dépendant en énergie. De plus, la transmission, et donc la conductance, de la barrière vont donc dépendre de l'impédance qui caractérise le circuit dans lequel elle s'insère [46]. C'est effet à été balisé pour les jonctions tunnel opaques depuis le début des années 90, pour lesquelles la théorie du blocage de Coulomb dynamique [46] donne une description complète. Cependant, ce phénomène n'est pas restreint aux jonctions

tunnels, mais à tout conducteur cohérent ayant des coefficients transmission, τ_i, quelconques. Seulement récemment, deux théories [5, 6] ont été capables de traiter ce cas plus général, mais dans la limite d'environnements de faible impédance. Les deux théories trouvent que les corrections à la conductance d'un conducteur cohérent quelconque ont la même dépendeance fonctionnelle en énergie (tension et température) et en impédance de l'environnement que pour les jonctions tunnel opaques. Mais l'amplitude de cette correction par rapport au cas des jonctions tunnel est renormalisée par le facteur de Fano, $F = \sum \tau_i(1-\tau_i)/\sum \tau_i$, comme pour le bruit de grenaille [48, 49]. Par exemple, les barrières de transmission parfaite ($\tau_i \in \{0,1\}$) ne génèrent pas de bruit de grenaille, et comme il n'y a plus de pulses de courant, les électrons transmis ne peuvent plus exciter les modes électromagnétiques. Même si une expérience pionnière dans des contacts atomiques [51] a testé qualitativement cette forte prediction en 2001, il manquait toujours une expérience explorant la dépendance du bloacage de Coulomb dynamique pour un rang large de facteurs Fano.

1.4.3 Test expérimental de la théorie du blocage de Coulomb dynamique dans un conducteur cohérent modèle

Dans le but de tester les prédictions du blocage de Coulomb dynamique pour différents facteurs de Fano, nous avons mesuré cet effet dans un CPQ dont les coefficients de transmissions (et donc son facteur de Fano) peuvent être modifiés continûment *in-situ*. Grâce à cette modularité, ils constituent un banc d'essai privilégié pour le transport quantique. Et ils ont déjà été utilisés avec succès, comme tels, pour tester les prédictions de la théorie de la diffusion élastique, pour la conductance [27] ou le bruit de grenaille [52, 53] d'un conducteur cohérent quelconque.

Nous avons inséré un CPQ dans un circuit ajustable (Figure 1.5.a): L'impédance en série au CPQ peut être selectionnée parmis différentes valeurs, dont un court circuit à haute fréquence pour lequel le blocage de Coulomb est pratiquement nul. Avec cette limite de basse impédance, nous pouvons caractériser le CPQ pour extraire et sélectionner ses coefficients de transmission τ_i (Figure 1.5.b). Pour un jeu de τ_i donné, nous basculons à une impédance série plus élevée qui donne cause au blocage de Coulomb dynamique, et mesurons comment la conductance du CPQ est modifiée. La dépendance en température et l'amplitude des corrections à la conductance mesurées sont sont bien reproduites par le théorie du blocage de Coulomb dynamique. Finalement, en refaisant ces mesures pour un ensemble large de coefficients de transmission, nous démontrons que les corrections à la conductance d'un conducteur cohérent, due au blocage de Coulomb dynamique, sont renormalisées par rapport à celles d'un jonction tunnel, par le même facteur de Fano qui caractérise le bruit de grenaille du conducteur (Figure 1.5.c).

Ces résultats fournissent des bases solides à la compréhension des lois de composition d'impédance dans les circuit quantiques.

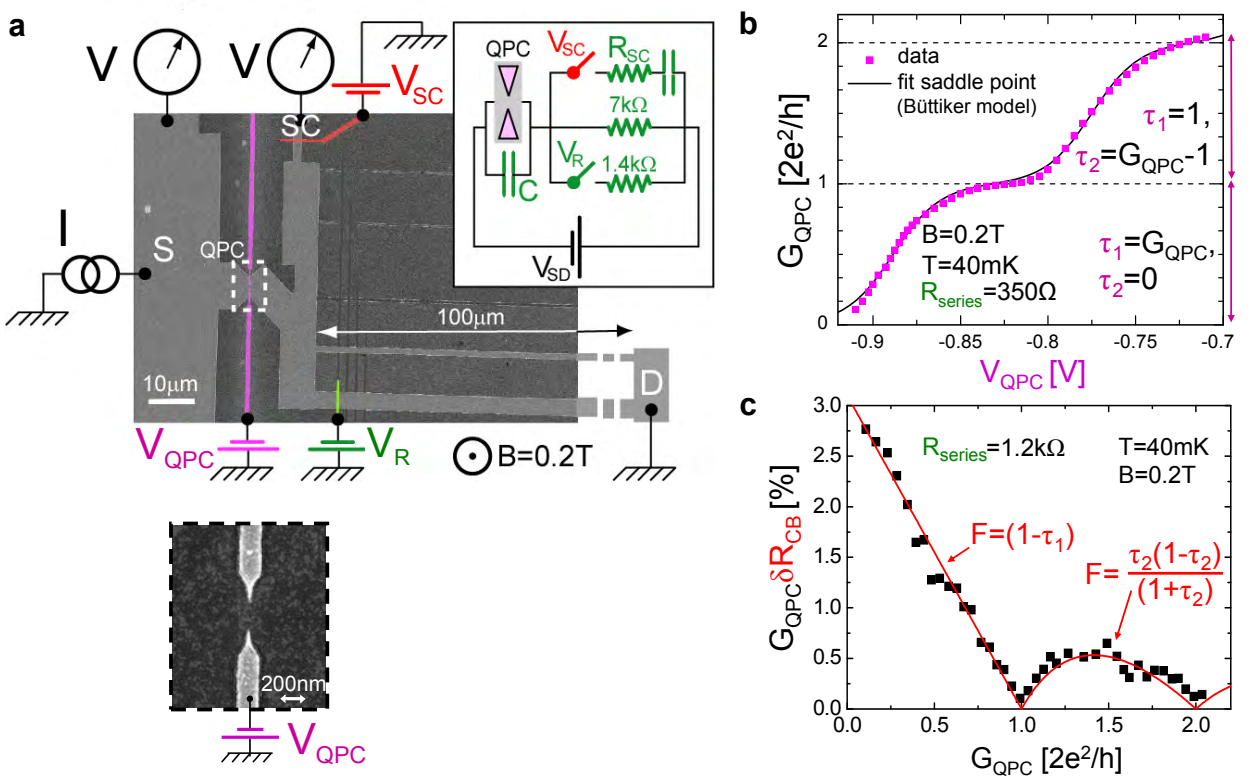

Figure 1.5: **Test expérimental de la théorie du blocage de Coulomb dynamique avec un contact ponctuel quantique**. **a** Image au microscope électronique de l'échantillon et schéma électrique correspondant (insert droit). Un contact ponctuel quantique est placé en série avec une résistance. La résistance série peut être sélectionnée parmi trois valeurs in-situ, en polarisant sélectivement les grilles métalliques rouge et verte utilisées comme des interrupteurs électriques. Insert bas: image au microscope électronique du contact ponctuel quantique situé au centre de la zone encadrée sur l'image globale de l'échantillon. **b** Le contact ponctuel quantique est caractérisé par la mesure de sa conductance lorsque la résistance série court-circuitée. **c** Correction relative à la conductance du contact ponctuel quantique en présence d'une résistance série de 1.2 kΩ, tracée en fonction de sa conductance. Ligne continue: prédiction théorique pour une jonction tunnel renormalisée par le facteur de Fano obtenu à partir de la conductance du contact ponctuel quantique.

Chapter 2

Introduction

2.1 Mesoscopic physics in solid state circuits

We live in a "big" world ruled by classical laws build upon "small" objects ruled by quantum mechanics. This dichotomy may be used to distinguish the macroscopic from the microscopic world, but the frontier between them is fuzzy since it is system and energy scale dependent. Mesoscopic physics [54] focuses on systems which are large in comparison to usual microscopic (atomic) scales but which nevertheless exhibit quantum coherent phenomena.

Solid state electronic circuits are pioneering systems where mesoscopic effects have been observed. Since the 80's, the microfabrication techniques inherited from the computer industry, coupled with the cryogenics techniques developed in the 50's, have permitted to investigate submicron scale circuits. Even if constituted by large amounts of atoms, quantum effects are found to be important in these circuits at low temperatures, usually in the sub-Kelvin range. Investigating quantum effects in small circuits gives access to a new axis of complexity to test and develop our basic understanding of nature, and is also particularly relevant for the computer industry. Indeed, quantum effects, such as tunnel leakages or interference phenomena, become important as the size decreases and could affect the devices functionalities even at room temperature. On the other hand, quantum mechanics offers new potentially powerful perspectives for information processing and transmission. In this respect, quantum circuits are most promising since they can be engineered to realize quantum bits, to perform logic operations and are, in principle, easily integrable.

2.2 Coulomb interactions in quantum circuits

Non-interacting approaches have provided fairly accurate descriptions of solid state conducting systems since the very early theoretical models, like Drude's or Sommerfeld's. This may appear surprising since they ignore the long range Coulomb interaction that tends to couple

the charged carriers. The main reason is that, as electrons tend to repel each other, they are surrounded by a neutralizing positive background charge furnished by the lattice ions so that Coulomb interaction becomes screened and short ranged. In most systems, the Landau theory of Fermi liquids [29] predicts that a Fermi sea develops and that the low energy physics remains described by long lived single-particle excitations (quasiparticles). These quasiparticles obey a fermionic statistics and carry the same charge as electrons. However, quasiparticles are not really free but still subjected to the residual screened Coulomb interactions by which they couple to each other and loose their quantum coherence. These residual interactions increase with the confinement and are expected to have dramatic consequences in one dimensional conductors [55]. Moreover, quasiparticles also couple to their electromagnetic environment. Understanding such electrodynamic effects is not only interesting in fundamental science, but is necessary to engineer the functionalities of quantum circuits.

This thesis is devoted to investigating Coulomb interaction effects in three distinct regimes accessible in 2D electron gas (2DEGs) circuits. In the first part of the manuscript, I will present a series of experiments investigating the quantum Hall effect in the the integer and fractional regimes. Our approach relies on the measurement of the energy transfers (energy exchanges and energy currents) arising in low dimensional circuits driven out-of-equilibrium. In the second part, I present an experiment investigating the non-trivial impedance composition laws arising, in quantum circuits, from the interplay of Coulomb interaction and the discreteness of charge.

2.3 Main experimental results obtained during my PhD

- **The demonstration of a novel spectroscopic technique to extract the electronic energy distribution function using a quantum dot [1].** This fundamental quantity is obtained for the first time in a mesoscopic semiconductor circuit.

- **The observation of strong energy relaxation along $\nu_L = 2$ quantum Hall edge-channels, challenging the wide-spread non-interacting picture [2].** While the dominant inelastic mechanism is found to follow from inter-channel interactions *without particle exchanges*, a small energy leak suggests the coupling to additional co-propagating excitations.

- **The demonstration that energy exchanges can be efficiently tuned in $\nu_L = 2$ quantum Hall edge-channels [3].** By manipulating the edge-channel paths it was possible to tune up or down the energy relaxation of a non-equilibrium edge-channel.

- **The observation of a non chiral energy current at $\nu_L = 4/3$, while charge current remains chiral.** We show that this antichiral energy current flows through

the bulk, whereas the electrical current flows chirally along the edge.

- **The demonstration of the strong link between the dynamical Coulomb blockade and shot-noise for short coherent conductors [4].** Dynamical Coulomb blockade corrections to the conductance of a quantum point contact are found to be renormalized by the Fano factor resulting from its finite transmission coefficients, in quantitative agreement with recent predictions [5, 6]

2.4 Energy transfers in the integer quantum Hall regime

The non-interacting picture of the integer quantum Hall effect has a strong analogy with optics [8, 9, 10], where edge-channels play the role of light beams. While several experiments have demonstrated the potential of this analogy to perform electron quantum optics experiments, they have also revealed the first signatures of interaction effects in the integer quantum Hall effect, which are not yet fully understood [11, 12, 13, 14, 15]. In order to shed new light on this issue, we have developed a scheme to perform the energy distribution spectroscopy of single-particle excitations in an edge-channel driven out of equilibrium. With this scheme, we could investigate experimentally the energy exchanges and currents along two co-propagating edge-channels ($\nu_L = 2$) of the integer quantum Hall effect.

2.4.1 The integer quantum Hall effect and edge-channels

Non-interacting description

The integer quantum Hall effect, discovered in 1982 by von Klitzing, Dorda and Pepper [7], is a macroscopic quantum effect that arises when a 2D electron gas is submitted to a strong perpendicular magnetic field. It is characterized by a vanishing longitudinal resistance and a Hall resistance quantized in units of the resistance quantum $R_{Hall} = \frac{1}{\nu_L}\frac{h}{e^2}$, where ν_L is an integer. In this regime, the only low energy excitations propagate along the edge, in the so-called edge-channels whose number match the filling factor ν_L. In the non-interacting picture, the ν_L edge-channels are described as ν_L 1D co-propagating chiral conductors. The analogy between edge-channels and light beams and the possibility to manipulate them with tunable small constrictions (quantum point contacts), such as selective populating, detecting and beam-splitting them, permits to implement electron analogues of interferential devices [9].

The role of Coulomb interactions

The usual description of edge-channels neglects Coulomb interactions since standard transport measurements are not sensitive to them [16]: the edge-channels' chirality forbids electron

backscattering and the electric current flows along the edge, irrespective of the microscopic details. However, we know that interactions can have dramatic consequences on the very nature of the edge excitations: Coulomb interactions are expected to reconstruct the edge density profile [17, 19] for the smooth confinement potentials realized in most experiments. This gives rise to additional branches of acoustic edge excitations of the reconstructed edge [19, 20]. Moreover, strong enough interactions between co-propagating edge-channels are expected to yield to collective bosonic excitations delocalized amongst the edge-channels [21]. For instance, at $\nu_L = 2$ the dynamics may split in a fast symmetric charge mode and a slow antisymmetric spin mode [22].

Being sensitive to the phase coherence of a single edge-channel, the Mach-Zehnder experiments have recently demonstrated a zoology of phenomena incompatible with the single-electron picture [11, 12, 14, 23]. These phenomena provide the first pieces of evidence for interaction effects in the integer quantum Hall effect. Up to now, there is an active debate in order to describe all the experimental findings within a single theoretical model. A drawback of Mach-Zehnder experiments is that they are sensitive to different contributions to dephasing: On the one hand, the inelastic mechanisms at work fundamentally limit the quantum lifetime of the interfering excitations. On the other hand, low frequency noise, at frequencies higher than the inverse measurement time, can blur the electronic phase measured in these experiments. This limitation can be overcome by directly investigating the inelastic mechanisms through the energy exchanges they induce in non-equilibrium situations.

2.4.2 Energy distribution spectroscopy and energy currents along quantum Hall edge-channels

In 1D chiral systems the heat flow carried by single particle, electron-hole, excitations of the 1D Fermi sea can be directly related to the electronic energy distribution function, $f(E)$, without sample dependent parameters [24]:

$$J_H = \frac{1}{h}\int \big(E - E_F\big)\Big(f(E) - \Theta(E_F - E)\Big)dE, \tag{2.1}$$

where E_F is the Fermi energy and $\Theta(E)$ the Heaviside step function. Moreover, in out-of-equilibrium situations changes in $f(E)$ are a direct signature of energy exchanges and can be used to track the inelastic mechanisms at work, as demonstrated in mesoscopic metallic wires [25] and carbon nanotubes [26]. In the integer quantum Hall effect, the edge-channels' energy distribution can be extracted from the tunneling current flowing through a localized state (in a quantum dot), while a voltage biased constriction (a quantum point contact) can be used to drive an edge-channel out-of-equilibrium in a controlled way.

A quantum dot as an energy filter

A quantum dot is a small electron box whose density of states is discrete due to confinement quantization. When it is coupled to two electrodes by opaque tunneling barriers, only the electrons matching the discrete energy levels inside the box can flow through it. Assuming a single level lies inside the transport window, the current flowing through the quantum dot, I_{QD}, is directly proportional to the difference of electron populations on both drain (D) and source (S) electrodes at the energy of the resonant level, E_{lev}, as depicted in Figure 2.1.a:

$$I_{QD} = I_{Max}(f_D(E_{lev}) - f_S(E_{lev})). \tag{2.2}$$

The distributions in both electrodes are obtained separately by applying a global electrochemical potential difference between them, such that an electrode population is zero, or one, when the other is not, as shown in Figure 2.1.a. A capacitively coupled metallic gate, is used to sweep the energy of the resonant level, which gives access to the full drain and source electrodes' energy distributions, $f_{D/S}(E)$. In practice, we measured the quantum dot transconductance with the gate voltage which is proportional to the derivative of the energy distributions $\partial_E f_{D/S}(E)$ (Figure 2.1.a, right).

A quantum point contact as a tunable heat source

A quantum point contact is realized with a small 2DEG constriction of tunable width [27]. In the integer regime of the quantum Hall effect, they can be used as beamsplitters that partially transmit/reflect the incoming edge-channels. When a quantum point contact of intermediate transmission probability $0 < \tau < 1$ is voltage biased, it mixes the populations of incoming edge-channels having different electrochemical potentials. Assuming the scattering is elastic, the outgoing non-equilibrium edge-channel energy distribution is the sum of two energy translated Fermi functions, $f_F(E)$, weighted by the respective transmission/reflection, probabilities $\tau/1-\tau$. Consequently, the outgoing energy distribution displays a double-step shape [28] (left inset in Figure 2.1.b):

$$f(E) = \tau f_F(E - eV_{D1}) + (1-\tau) f_F(E - eV_{D2}), \tag{2.3}$$

where $V_{D1/2}$ are the potential biases applied to the incoming edge-channels (see Figure 2.1.b). Beyond the non-interacting picture, the heat flow, J_H^{QPC}, in both outgoing edge-channels at the quantum point contact can be deduced from general power balance considerations:

$$J_H^{QPC} = \frac{\tau(1-\tau)e^2(V_{D1} - V_{D2})^2}{2h} + \frac{\pi^2}{6h}(k_B T)^2, \tag{2.4}$$

where the first term is the non-equilibrium contribution that adds to the equilibrium heat flow carried by thermal chiral electron-hole excitations at temperature T (second term).

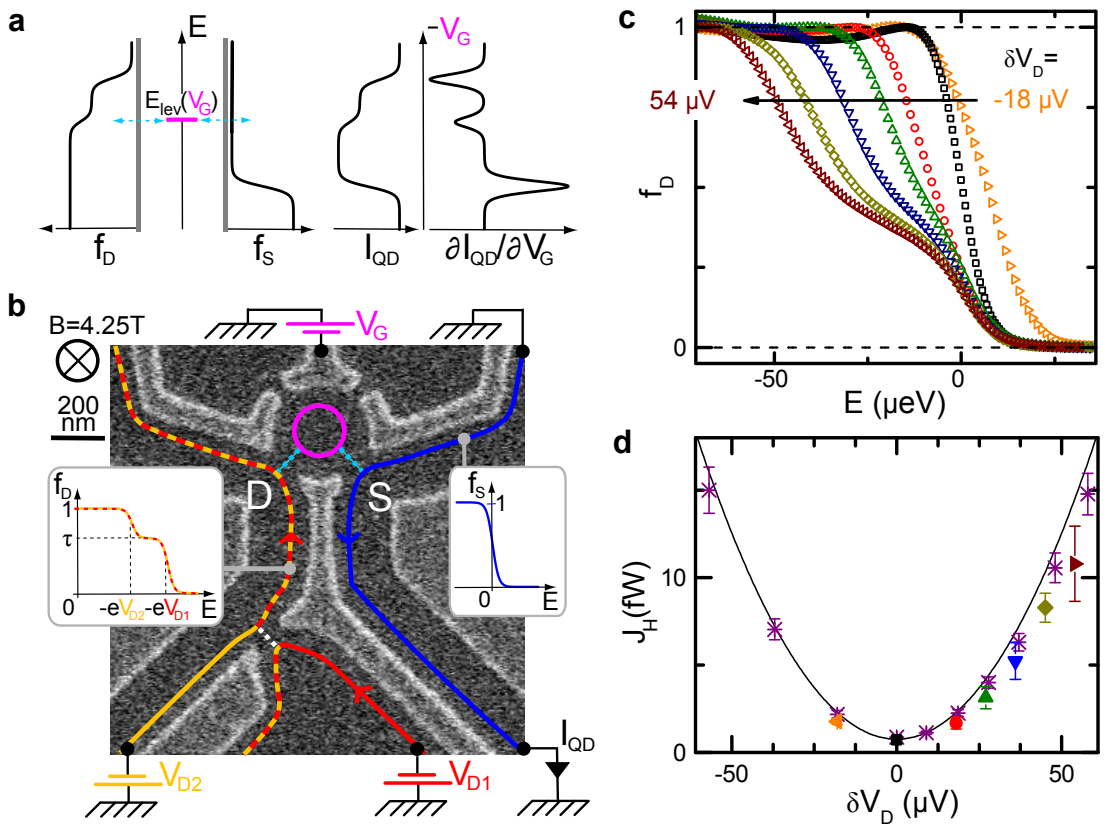

Figure 2.1: **Non-equilibrium edge-channel spectroscopy using a quantum dot. a** Schematical description of the energy spectroscopy principle: (Left) Possible tunneling events when a single active level lies in the transport window. (Right) The current flowing through the quantum dot, I_{QD}, is proportional to the difference of energy distributions, $f_{D/S}(E)$, on both drain/source (D/S) sides to the quantum dot. In practice, we measure the transconductance $\partial I_{QD}/\partial V_G$, proportional to the energy derivative of the difference between $f_D(E)$ and $f_S(E)$. A global potential difference is applied between D and S in order to separate their contributions to the quantum dot signal. **b** Sample micrograph: Surface gates appear bright. A voltage biased quantum point contact (defined by the bottom gates) injects a non-equilibrium energy distribution in an edge-channel on the drain side. The quantum dot (defined by gates on top) is used to probe the resulting $f_D(E)$ after a short propagation length of 0.8 μm. The source $f_S(E)$ is at cold equilibrium (right inset). **c** Energy distributions in the drain edge-channel extracted by integrating the quantum dot signal for a fixed quantum point contact transmission probability $\tau \simeq 0.5$ and different biases $\delta V_D = V_{D1} - V_{D2}$. The resulting energy distributions show a double-step structure, as predicted by the scattering approach. **d** Symbols: Heat current, J_H, extracted from the data shown in c and from a second run with the same quantum point contact transmission (∗). Continuous line: prediction (2.4) for the heat current injected by the voltage biased quantum point contact. No significant energy loss is found at our experimental accuracy after a 0.8 μm propagation length.

2.4.3 Experimental results, $\nu_L = 2$

First we demonstrate the experiment principle and the optical analogy between quantum point contacts and beam-splitters regarding energy transport [1]. Second, we demonstrate a strong energy relaxation along the edge-channels' path, challenging the single-particle picture, and we discuss the responsible inelastic mechanism [2]. Third, we demonstrate how to tune the energy exchanges in non-equilibrium edge-channels [3].

Non-equilibrium edge-channel energy distribution spectroscopy

We generate a non-equilibrium situation in an edge-channel using a voltage biased quantum point contact for different biases and transmissions. We use a quantum dot to measure the resulting energy distribution a short distance downhill L =0.8 μm (Figure 2.1.b). The measured energy distributions (Figure 2.1.c) are found close to the non-interacting prediction (2.3). The heat flow extracted using (2.1) (Figure 2.1.d) matches the heat flow injected at the quantum point contact (2.4), at our experimental accuracy. This demonstrates that quantum point contacts are well described as tunable beam-splitters regarding energy resolved transport. It also shows that a quantum dot is a reliable tool for performing the energy distribution spectroscopy. Regarding the low energy dynamics of the integer quantum Hall effect edge-channels at $\nu_L = 2$, these measurements demonstrate that relaxation effects are small in the short propagation path between the quantum point contact and the quantum dot at the probed energies.

Energy relaxation of non-equilibrium edge-channels

It is possible to address the relaxation dynamics of single-particle excitations by probing $f(E)$ after different propagation lengths from the heat injection point [25]. Changes in $f(E)$ are a direct signature of the inelastic mechanisms at work.

In our second experiment, we have varied the propagation distance between the heat injection point and the $f(E)$ probe (Figure 2.2.a). This experiment revealed an energy relaxation towards a hot electron regime. This can be seen in Figure 2.2.b, where the measured quantum dot transconductances, $\partial_{V_G} I_{QD}$ proportional to $\partial_E f(E)$ (symbols), are fitted using Fermi functions (continuous lines) at long propagation lengths. Performing an exponential fit of the local heat current (Figure 2.2.c) relaxation with the propagation length we obtained an inelastic length of about 2.5 μm at mean excitation energies of about 125 mK. With the knowledge of the drift velocity, this quantity gives an upper limit to the quantum lifetime of the probed excitations. Using the drift velocities measured in similar samples in other groups, we find that the energy uncertainty associated with the quantum lifetime is larger than, or comparable to, the mean excitation energy. Consequently, the single particle

states' energy appears ill defined. This result challenges the usual non-interacting picture of edge-channels at $\nu_L = 2$.

By probing $f(E)$ in an edge-channel, while driving out of equilibrium its co-propagating edge-channel (Figure 2.2.d), we provide direct proof (Figures 2.2.e and f) of energy exchanges between edge-channels, *without particle exchanges*. This interaction mechanism is found to be dominant. However, it is not the only mechanism, since some heat is found to leak out of the two edge-channel system as shown in Figures 2.2.c and f. The energy and propagation length dependence of the relaxation rules out interactions with thermalized excitations such as bulk phonons, as expected from the predictions of [56] or electronic states in the metallic gates used to define the edge-channel paths. Instead, the data suggests the presence of additional co-propagating excitations.

Up and down control of the energy relaxation in an edge-channel

In order to perform quantum optics experiments and for quantum information applications with edge-channels, it is beneficial to increase the relaxation and coherence length. It is also useful to dispose of techniques permitting to drive the system back to equilibrium, for instance to perform fast resets. We have demonstrated experimentally the up/down control of energy relaxation of a single integer quantum Hall effect edge-channel.

Driving the energy relaxation with a voltage probe:

Floating ohmic contacts (voltage probes) have been used by theoreticians to mimic energy relaxation and decoherence effects within the non-interacting scattering approach. We have performed a relaxation experiment where the non-equilibrium edge-channel is diverted to a floating ohmic contact through an intermediate quantum point contact (Figure 2.3.a). The resulting energy distribution is probed at the quantum dot after a short subsequent propagation length. Our measurements (Figure 2.3.b) are found to follow accurately, without fitting parameters, the scattering approach predictions.

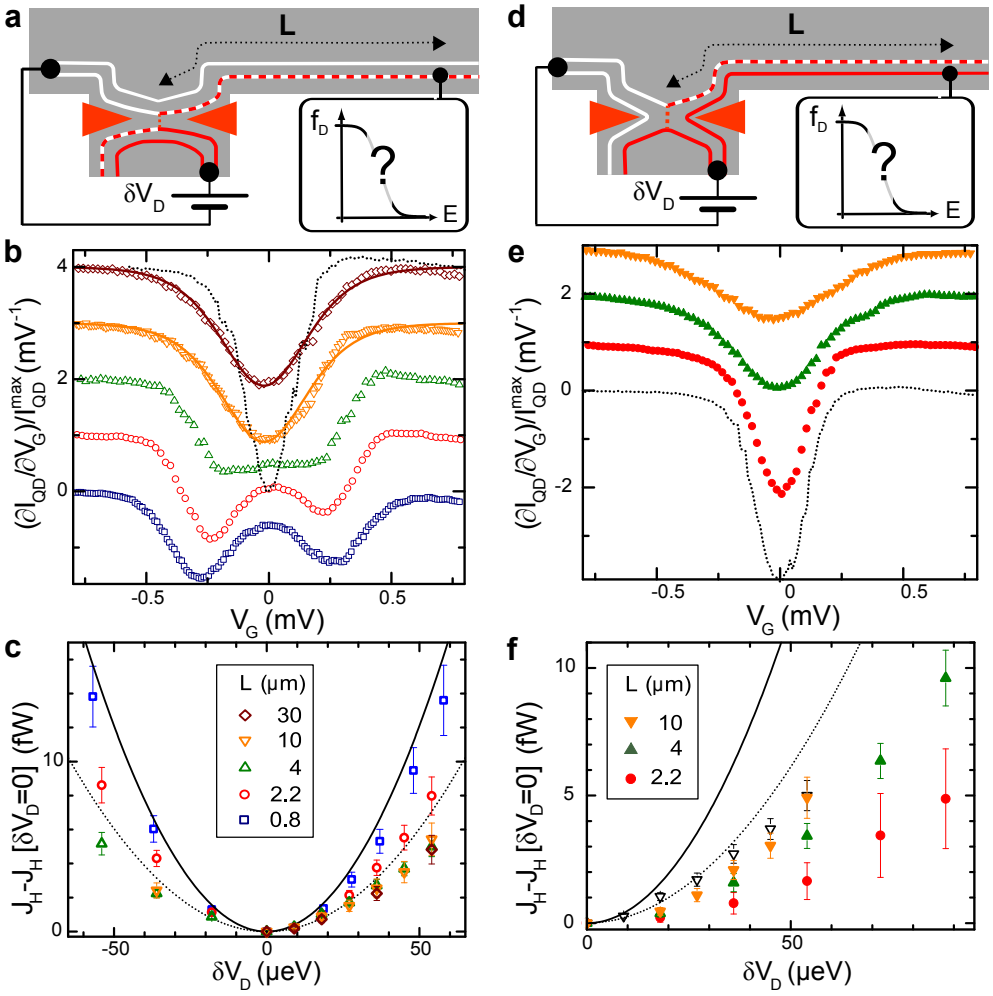

Figure 2.2: **Energy exchanges along $\nu_L = 2$ edge channels.** **a,** Energy relaxation: A voltage biased quantum point contact of conductance $0.5e^2/h$ heats the outer outgoing edge-channel whose energy distribution, $f_D(E)$, is probed with a quantum dot after a propagation distance L. **b,** Raw data for setup a at δV_D =36 μV(symbols) shifted vertically for several L. The nonequilibrium double dip relaxes over $L_{inel} \simeq 3$ μm towards a dip broader than the equilibrium dip at $\delta V_D = 0$ (dotted line). Solid lines are calculations with a Fermi distribution at 85 mK. **c** Excess heat current extracted from data (symbols) and prediction at quantum point contact output (continuous line). The outer edge-channel cools down as L is increased and saturates at a value below expectations for two interacting edge-channels (dotted line). **d** Energy exchanges between edge-channels: A voltage biased quantum point contact of conductance $1.5e^2/h$ heats the *inner* outgoing edge-channel, while the *outer* edge-channel's $f_D(E)$ is probed at distance L. **e** Raw data for setup d at $\delta V_D = 0$ (dotted line) and δV_D =54 μV (symbols), shifted vertically for several L. The dip broadens as L is increased. **f** Excess heat current extracted from data (full symbols), prediction at the quantum point contact output (continuous line) and expected for two interacting edge-channels (dotted line). The outer edge-channel heats as L increases, up to an excess temperature close to that of setup a [L =10 μm in c is shown here as open symbols (▽)].

Freezing energy exchanges with a closed loop:

More importantly, we have demonstrated a technique permitting us to freeze the relaxation dynamics. We have performed an energy relaxation experiment on the outer edge-channel while the inner edge-channel is closed in a looped geometry for most of the outer edge-channel propagation (Figure 2.3.c). This scheme may be informative since an edge-channel localized in a loop cannot absorb energy in the stationary regime and its density of states is discrete due to the periodic boundary conditions.

We find that when the inner edge-channel is sufficiently small, the non-equilibrium outer edge-channel $f(E)$ remains constant. Indeed, the measured quantum dot transconductance signal is identical, at our accuracy, in both ($L_{in} = L_{out}$ =2.2 μm) and (L_{in} =2.2 μm, L_{out} =10 μm) configurations, whereas the probed outer edge channel path is 8 μm longer in the second configuration (see Figure 2.3.d). In contrast, the fully co-propagative geometry, ($L_{in} = L_{out}$ =10 μm), yielded to a full energy redistribution for the same propagation length ($\triangledown$). The length characterizing the energy exchanges is therefore increased by at least a factor of four. We attribute this behavior to the discrete energy spacing of the inner edge-channel, which is larger than the energy injected in the outer edge-channel for the (L_{in} =2.2 μm, L_{out} =10 μm) loop.

This finding also provides very strong constraints regarding the pertinent energy exchange mechanisms. It implies that interactions within the non-equilibrium edge-channel excitations are incontrovertibly negligible to the relaxation dynamics on an 8 μm length scale at the probed energies. Moreover, we find that the electronic energy at the quantum dot in the probed outer edge-channel is identical at our experimental accuracy in the configurations ($L_{in} = L_{out}$ =2.2 μm) and (L_{in} =2.2 μm, L_{out} =30 μm), despite the important changes observed in the shape of $f(E)$. This shows that energy redistribution with the predicted additional modes of the excited outer edge-channel [19, 20] remain small for a 28 μm propagation length.

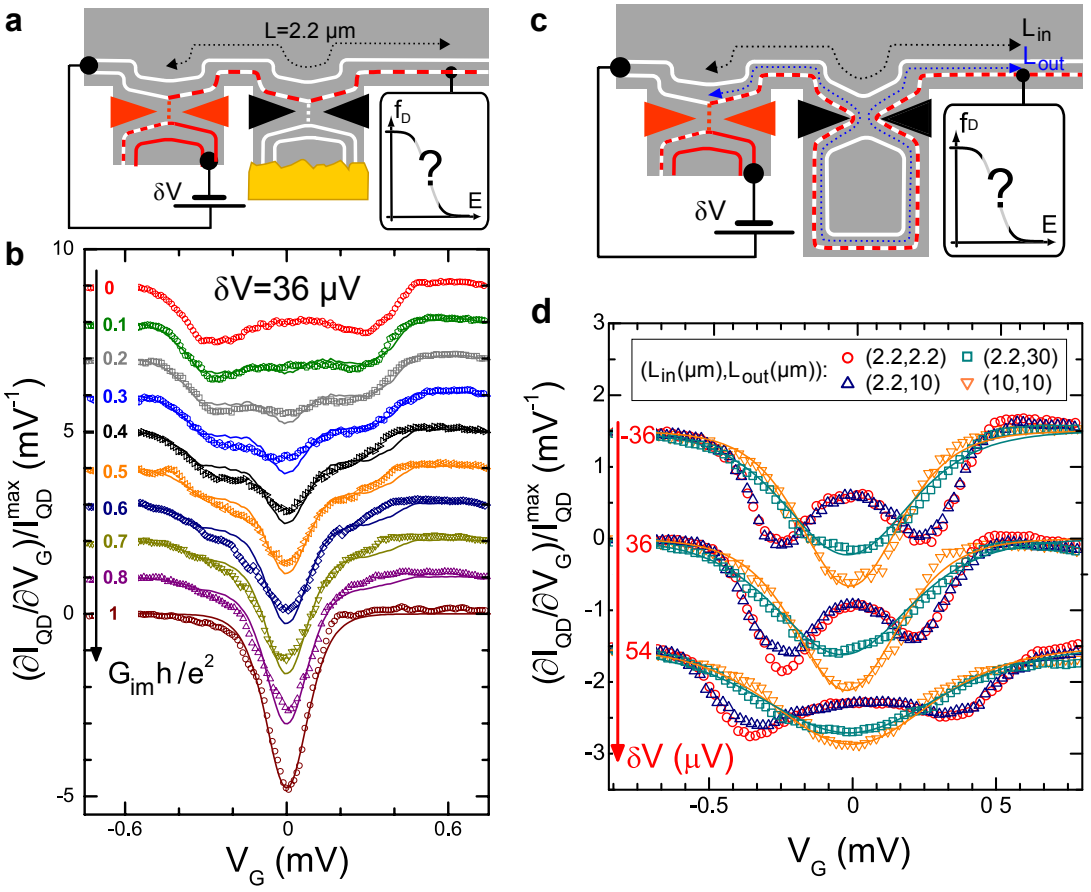

Figure 2.3: **Tunning the edge-channel relaxation.** **a** Increased relaxation setup: A non-equilibrium edge-channel is diverted towards a floating ohmic contact (voltage probe) through an intermediate quantum point contact. The resulting $f_D(E)$ is probed with a quantum dot 0.8 µm downstream the intermediate quantum point contact. **b** Raw data for setup a for different transmissions, $G_{im}h/e^2$, of the intermediate quantum point contact. The non-equilibrium double dip at 0 transmission evolves towards an equilibrium single dip as the intermediate transmission is increased to 1 (continuous line: predictions from the scattering approach). **c** Freezed relaxation setup: The outer edge-channel is driven out of equilibrium and probed after a tunable propagation length, L_{out}. The inner edge-channel is fully reflected by an intermediate quantum point contact of conductance e^2/h and reaches the quantum dot after a L_{in} =2.2 µm propagation path. Below the intermediate quantum point contact, the inner edge-channel forms a closed loop of tunable length $L_{loop} = L_{out} - L_{in}$. **d** Raw data in different configurations (L_{in}, L_{out}) for different heating quantum point contact biases (symbols). The same signal is obtained when $L_{in} = L_{out}$ =2.2 µm and (L_{in} =2.2 µm, L_{out} =10 µm), so that a 8 µm loop freezes the relaxation dynamics that take place when both edge-channels follow the same propagation path ($L_{in} = L_{out}$ =10 µm). A larger loop of 28 µm does not suppress the energy relaxation (L_{in} =2.2 µm, L_{out} =30 µm). The resulting $f(E)$ can be fitted with a Fermi function (continuous lines) that corresponds to the same heat current as for $L_{in} = L_{out}$ =2.2 µm.

2.5 Energy transport in the fractional quantum Hall regime

2.5.1 The fractional quantum Hall effect

The fractional quantum Hall effect discovered in 1982 by Tsui, Störmer and Gossard [33] has proven to be one of the most intriguing phenomena in condensed matter physics. Contrary to the integer quantum Hall effect, it was soon realized it is an effect arising from Coulomb interactions. Its single particle excitations have been demonstrated to carry fractional charges [35, 36], and are predicted to display fractional exchange statistics, interpolating between Bose-Einstein and Fermi-Dirac statistics.

As in the integer quantum Hall effect, the bulk is gapped and the only low energy excitations can propagate at the edge of the sample in chiral edge-channels. This results in a vanishing longitudinal resistances and a quantized Hall resistance. However, in the fractional quantum Hall effect, edge-channels cannot be described as non-interacting 1D chiral fermions. The effective theory developed by Wen [38], describes edge-channels as chiral Luttinger liquids. It predicts a non linear I-V curve of tunneling point contacts [39], with a universal power law behavior whose exponent is directly linked to the filling factor ν_L. Several experiments have demonstrated such power law behavior, however the found exponents are systematically lower than the predicted ones [40]. Such deviations could possibly result from sample dependent effects, like the reconstructed edge profile for a smooth confinement. Up to now, many crucial information regarding the fractional edge-channels is still missing. For example, the number of edge modes, their chirality and their coupling, which are expected to be non trivial for some FQHE regimes, are still not known.

2.5.2 Towards testing the edge structure with heat transport

Heat transport is expected to provide new information on the edge structure. For instance neutral modes are predicted in hole conjugated regimes to the $1/m$ fractions (like the $1-1/3$ or $2-1/3$ regimes) [42]. These neutral modes remain up to now elusive to experiments because they are transparent to charge transport. However, they are expected to carry antichiral heat currents [43]. We have developed a setup to perform heat transport experiments in the fractional quantum Hall effect. The first heat transport measurements performed in the $\nu_L = 4/3$ regime have already revealed a rich behavior.

A Coulomb blockaded island as heat probe

In order to test the heat current chirality, qualitative heat transport measurements are sufficient. We have used a Coulomb blockaded island as high-pass energy filter:

The current flowing through the island, when tunnel coupled to two electrodes, is blocked

as long as the incident electronic excitations do not carry an energy comparable or superior to the charging energy. Such Coulomb blockaded islands [44] act as high pass energy filters that can be used to probe the excitations hotter than the addition energy.

In the following experiments, the Coulomb blockaded island is realized with the help of a quantum point contact near its pinch off region. In this situation, our quantum point contacts displays Coulomb diamonds (Figure 2.4.a) when sweeping both gate voltage and bias demonstrating that charging energy physics influence the electrical transport[1].

2.5.3 Energy transport measurements, $\nu_L = 4/3$

The experiments we have performed are described schematically in Figure 2.4.b. Two "injection" quantum point contacts (red) both tuned to half transmission, are used to drive an edge-channel out of equilibrium in two distinct points along the edge. The local heat is probed with a "probe" quantum point contact (black) operated in the Coulomb blockaded regime, and located between the two injection quantum point contacts. This geometry allows us to make a one to one comparison between the forward and the backward heat current, with the *same* heat probe.

Charge vs. heat transport chirality

The electrical current is found to follow the edge with the chirality imposed by the magnetic field, even in the probed non-equilibrium situations. In contrast, we find (Figure 2.4.c) that the edge-channel is locally heated when injecting the non-equilibrium situation in both upstream and downstream quantum point contacts. This demonstrates that *the heat flow is not chiral, while the charge flow remains chiral.* The elliptical geometry of the heat signal measured as a function of the upstream and downstream quantum point contact biases demonstrates the antichiral heat flow is unsensitive to the energy injected by the upstream quantum point contact. Therefore it cannot be explained by a plain local "killing" of the fractional quantum Hall effect due to heating.

Coupling to neutral bulk excitations

Performing the same measurements in different geometries, we find that the antichiral heat signal depends only on the direct distance between the injection quantum point contact and the probe quantum point contact irrespective of the edge propagation path linking both quantum point contacts. The most stringent test is to connect a floating ohmic contact to the edge, which forces the edge-channels' relaxation, without changing the direct, "as

[1] The residual static disorder close to the quantum point contacts may be responsible for the single particle charging effects.

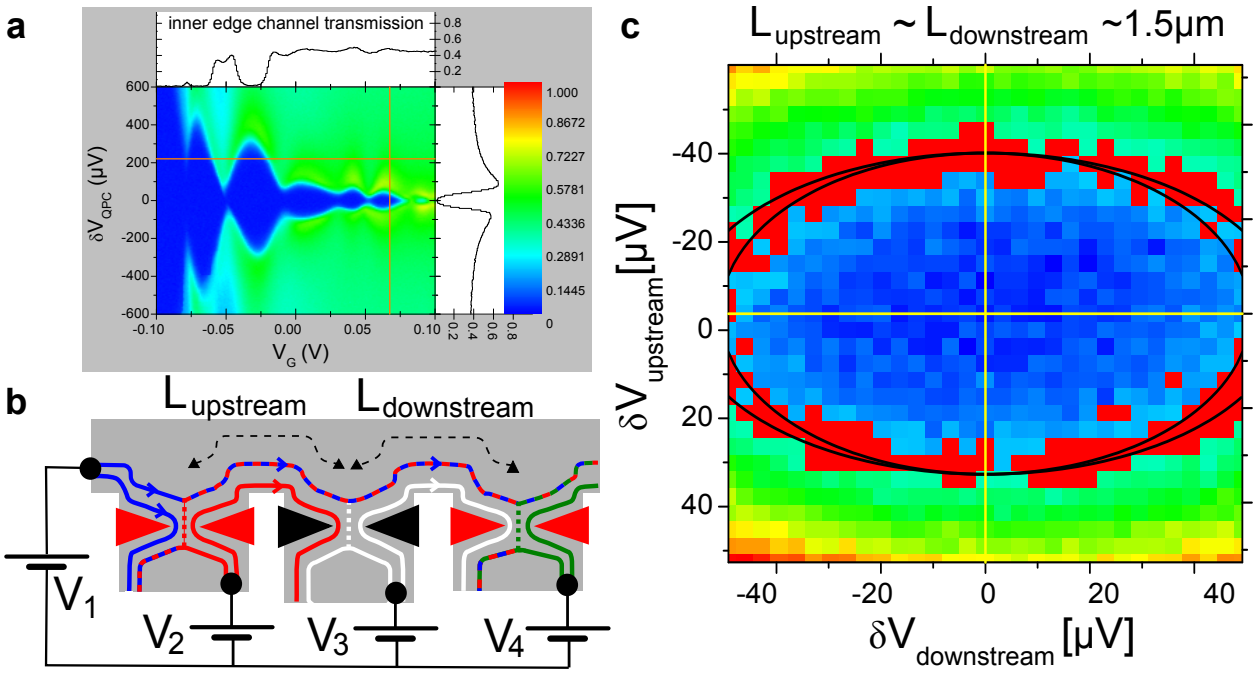

Figure 2.4: **Antichiral heat flow in the $\nu_L = 4/3$ fractional quantum Hall effect. a** Color plot of the transmission of the probe quantum point contact as a function of its gate and bias voltage (gate voltage and bias projections correspond to the yellow line). Coulomb diamonds develop at small transmissions (gate voltage). **b** Scheme used to test the heat flow chirality: Two quantum point contacts (red), tuned to half transmission, are voltage biased in order to create a non-equilibrium situation both upstream and downstream of a probe quantum point contact (black), used in the Coulomb blockaded regime. Voltage sources are used to bias the heat injection quantum point contacts, while the probe quantum point contact is kept unbiased. **c** Color plot of the transmission through the probe quantum point contact tuned to display an addition gap of 30 μeV (right projection in a), as a function of the injection quantum point contact biases placed ∼1.5 μm up and downstream. The energy injected in the downstream quantum point contact affects the probe quantum point contact signal, revealing an antichiral heat flow. The ellipsoidal geometry of the probe signal shows that the antichiral heat flow does not depend on the total local energy, but only on the energy injected downstream.

the crow flies" distance between injection and probe. These observations establish that the anti-chiral heat flow is fully carried by bulk excitations. Consequently, the non-equilibrium fractional edge-channels appear to be efficiently coupled to neutral bulk excitations.

2.6 Dynamical Coulomb blockade in short coherent conductors

The last part of this thesis is devoted to an experiment that investigates how the Coulomb interaction modifies the transport properties of a quantum conductor when it is embedded in a macroscopic circuit. By inserting a quantum point contact in a tunable circuit, we have measured the dynamical Coulomb blockade corrections to the quantum point contact's conductance as a function of its transmission coefficients. Our measurements demonstrate the strong predicted link [5, 6] between the dynamical Coulomb blockade and shot-noise.

2.6.1 Impedance composition laws in quantum circuits

In classical circuits, the circuit dynamics is fully characterized by the constitutive relations of the circuit elements. These are usually described as frequency dependent impedances. Combined with the relations given by Kirschoff's laws, the whole circuit dynamics results from the classical impedance composition laws. In quantum circuits, such simple composition laws do not hold anymore even in the presence of well defined coherent conductors separated by a distance longer than the phase coherence length. In practice, the conductance of a quantum conductor is reduced at low bias and temperature when inserted in a resistive circuit. This phenomenon is called dynamical Coulomb blockade (see [46] for a review).

2.6.2 Dynamical Coulomb blockade

When an electron tunnels through a barrier, the corresponding current pulse excites the electromagnetic modes of the circuit in which it is embedded. As a result, some energy is transferred from the electron to the circuit. Electron tunneling becomes inelastic and the barrier's conductance depends on the impedance of the environment [46]. This effect has been thoroughly investigated in small and opaque tunnel junctions since the beginning of the 90's and has proven to be well described by the dynamical Coulomb blockade theory. However, this phenomenon is not restricted to tunnel junctions. Only recently, two theoretical works [5, 6] have been able to handle the general case of a short coherent conductor with arbitrary transmission coefficients, τ_i, for the limit of low impedance environments. Both theories find that the dynamical Coulomb corrections to a quantum conductor's conductance exhibit the same energy dependence as for tunnel junctions, but is renormalized in amplitude by the same Fano factor, $F = \sum \tau_i(1-\tau_i)/\sum \tau_i$, that also renormalizes the current shot-noise (see [48, 49] for a review on noise in quantum transport). For instance, a perfectly transmitting "barrier" ($\tau_i \in \{0, 1\}$) does not give rise to current fluctuations and the electron flow cannot couple to its electromagnetic environment. Although a pioneering work on atomic contacts

[51] tested qualitatively these predictions in 2001, an experiment exploring the full parameter dependence of the theory was still missing.

2.6.3 Experimental test of the dynamical Coulomb blockade theory for short coherent conductors

In order to test the dynamical Coulomb blockade predictions for arbitrary transmissions, we have measured the dynamical Coulomb blockade corrections to a quantum point contact conductance. Quantum point contacts are local scatterers whose transmission coefficients can be tuned in-situ. Thanks to this modularity, they realize test beds for coherent conductors. As such, they have already been used [27, 52, 53] to demonstrate the scattering approach predictions linking the transport properties of a quantum resistor to its transmission coefficients, like the multichannel Landauer formula [47, 57] of conductance, or the shot-noise theory [58, 59].

We have embedded the quantum point contact in a tunable circuit (Figure 2.5.a) where the series impedance can take several values, including a shorting low impedance path. In the low impedance limit, dynamical Coulomb blockade correction are relatively small. Therefore, we can characterize and select the quantum point contact's transmission coefficients (Figure 2.5.b). For a given transmission coefficients set, we selected a higher series impedance and measured the resulting correction to the quantum point contact conductance. The conductance corrections are found to be quantitatively described by the dynamical Coulomb blockade theory in both amplitude and temperature dependence. By repeating these steps for a wide range of transmission coefficient sets defining different Fano factors, we demonstrate that dynamical Coulomb blockade corrections to conductance are renormalized, with respect to those arising in tunnel junctions, by the same Fano factor renormalizing the shot-noise (Figure 2.5.c).

Our result gives solid grounds to the understanding of impedance composition laws in quantum circuits. Moreover, we have demonstrate a reliable method to measure dynamical Coulomb blockade corrections in 2DEGs.

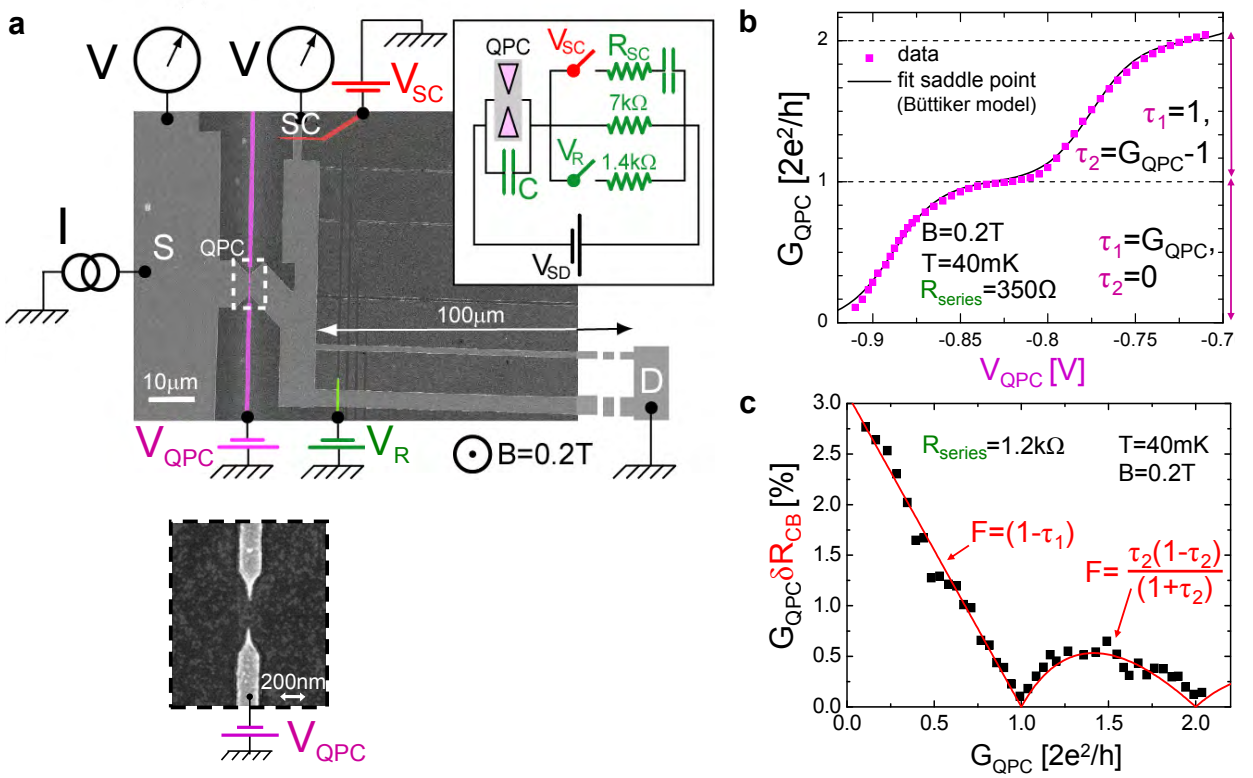

Figure 2.5: **Experimental test of the dynamical Coulomb blockade theory with a quantum point contact.a** Sample micrograph and electrical scheme (right inset). A quantum point contact is set in series with different resistance paths. The series resistance can be selected by voltage biasing the red and green gates used as electrical switches. Bottom inset: quantum point contact micrograph corresponding to the highlighted area above. **b** Conductance characterization of the quantum point contact transmission coefficients, when the series resistance is shunted. **c** Dynamical Coulomb blockade correction to the quantum point contact conductance arising from a series resistance of $1.2k\Omega$ for different quantum point contact's conductances. Solid line: Fano factor dependence resulting from the quantum point contact's transmission sets, the dynamical Coulomb blockade corrections are renormalized by the Fano factor.

Part I

Energy transport in the quantum Hall regime

This Part describes an experimental investigation of the low energy physics in the regime of the quantum Hall effect, under the point of view of energy transport measurements. Chapter 2 introduces the basis of the quantum Hall effect, putting special emphasis on its edge properties and highlighting some open questions on Coulomb interactions effects on the edge structure. Chapter 3 presents the principle of our experimental approach: We will use well known nanostructures to generate tunable non-equilibrium situations, using voltage biased quantum point contacts, and to probe the resulting non-equilibrium electronic distribution function, using a quantum dot as an energy filter. Chapter 4 demonstrates the experimental implementation of the proposed non-equilibrium spectroscopy technique in the regime of the integer quantum Hall effect at filling factor two. Using the same tools, Chapter 5 presents an investigation of the energy exchanges taking place at filling factor two, while Chapter 6 demonstrates two different setups permitting us to tune the energy relaxation, both increasing and freezing it. Chapter 7 recapitulates our findings regarding the low energy physics at filling factor two. Last, Chapter 8 presents a preliminary investigation of the fractional quantum Hall effect at filling factor 4/3, using a similar approach.

Chapter 3

The quantum Hall effect

3.1 Introduction

The integer quantum Hall effect (IQHE) was discovered by Von Klitzing, Dorda and Pepper in 1980 [7]. They discovered that a two dimensional electron gas (2DEG), realized in the inversion layer of a silicon MOSFET, displayed universal transport properties when a strong perpendicular magnetic field was applied to it. It is the first universal result obtained in Semiconductor Science and was awarded by a Nobel Prize. Irrespective of the microscopic details, the Hall resistance of the 2DEG was found to exhibit plateaus, as a function of the magnetic field, at integer quotients of the resistance quantum[1] $R_Q = \frac{h}{e^2}$,

$$R_{Hall} = \frac{1}{\nu_L}\frac{h}{e^2}, \qquad \nu_L \in \mathbf{N}^*. \tag{3.1}$$

The plateaus are accompanied by a vanishing longitudinal resistance, as can be seen in Figure 3.1. In the original article, it was already realized that the universality of the Hall plateaus could be used for metrological applications. The $\nu_L = 2$ plateau on Ga(Al)As 2DEGs is used since 1990 to maintain the Ohm standard of the International Unit System. State of the art measurements yield to a relative uncertainty on the resistance quantum R_Q of one part per billion[2]:

$$R_Q = \frac{h}{e^2} = 25812.807557(18)\ \Omega \tag{3.2}$$

Two years later, Tsui, Störmer and Gossard [60] discovered the fractional quantum Hall effect (FQHE) on high mobility 2DEGs realized in GaAS/Ga(Al)As heterojunctions. The FQHE manifests as fractional plateaus in the Hall resistance, $\nu_L \in \mathbf{Z}^*$. The 4/3 and 5/3 fractions are visible in Figure 3.1 giving rise to plateaus at the Hall resistances $R_{4/3} = \frac{3}{4}\frac{h}{e^2}$ and $R_{5/3} = \frac{3}{5}\frac{h}{e^2}$. In the FQHE regime, the 2D electrons are driven into an exotic state of matter. For instance, the low energy excitations of this new phase have been demonstrated to carry

[1] Also called Von Klizing's constant, R_K.

[2] Value taken from CODATA.

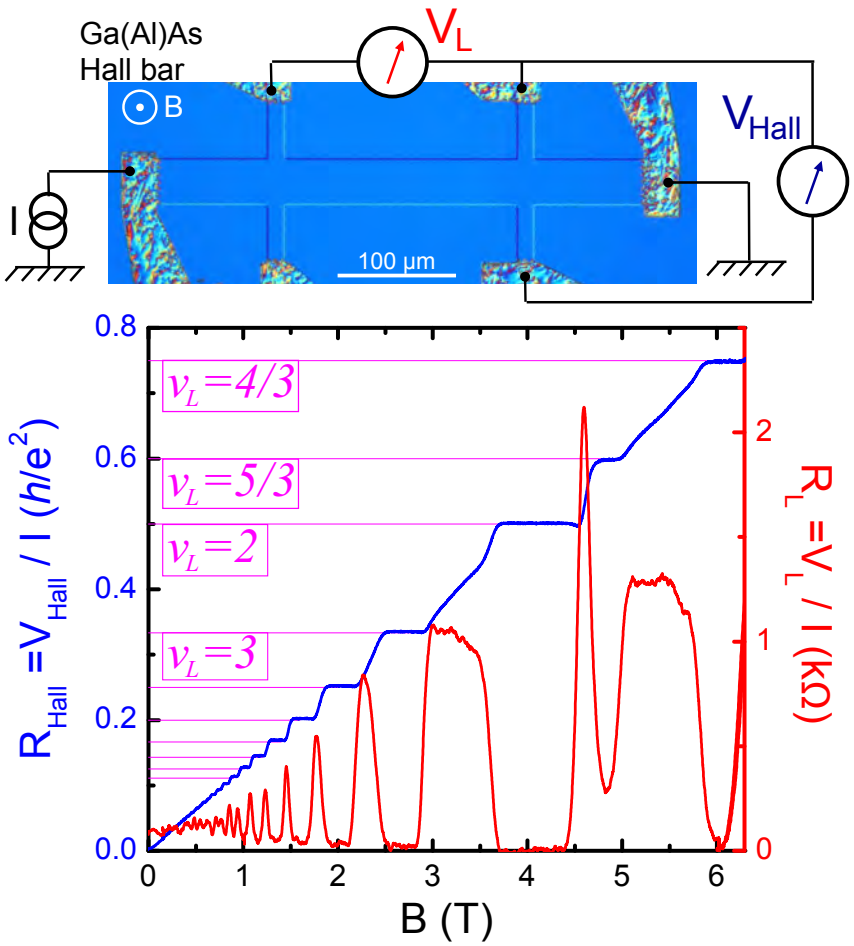

Figure 3.1: **Hall and longitudinal resistances of a 2DEG at low temperatures and strong magnetic fields.** Top: Optical micrograph of a Ga(Al)As 2DEG hall bar. Ohmic contacts (non homogenous) are used to bias and probe the 2DEG (blue, inside the clear cuts). Bottom: Wide plateaus develop at quotients of the resistance quantum h/e^2, while the longitudinal resistance vanishes. The classical limit of linear resistance is observed at low fields. Experimental conditions: 2DEG density $n_e = 2\ 10^{15}$ m^{-2} and temperature $T = 100$ mK.

fractional charges $\frac{e}{3}$ [35, 36], and are predicted to display anyonic statistics [37] interpolating between Bose-Einstein's and Fermi-Dirac's. The Nobel prize was awarded in 1998 to their discoverers, and to Laughlin for giving the basis [34] of our theoretical understanding of the FQHE.

Both IQHE and FQHE are similar[3] in that they display an excitation gap[4]. In consequence the low energy excitations, determining their transport properties, propagate along

[3]Excepting the half integer fractions that we are not going to deal with.

[4]For completely filled and empty energy levels, an infinitesimal variation of the chemical potential cannot change the electron number and the electronic fluid is incompressible.

the the edges of the sample. However IQHE and FQHE have starkly different origins: In the IQHE the excitation gap results from the quantization of the cyclotron motion driven by the magnetic field, and the incompressibility results from the Pauli principle. At the opposite, the incompressibility of the FQHE arises from the Coulombic repulsion between electrons in a partially filled cyclotron band.

In the following we are going to introduce the non-interacting quantum mechanics of a 2D electron gas submitted to strong perpendicular magnetic fields. With these tools, we will be able to introduce the notion of edge channels and see how the IQHE can be described within a powerful non-interacting picture. As an opening to the research carried during this Thesis, we will further discuss how Coulomb interactions may modify this simple picture. We will later introduce the FQHE, a truly many body phenomena driven by Coulomb interactions, where the edge channel picture holds as well. We will finish by highlighting some open questions regarding the edge physics of the FQHE.

3.2 From classical to quantum cyclotron motion

3.2.1 Classical dynamics

The classical dynamics of 2D non-interacting electrons in the presence of a uniform perpendicular magnetic field, B, are described by cyclotron orbits. The trajectories are circular, and their angular frequency is given by the cyclotron pulsation

$$\omega_C = \frac{eB}{m}$$

irrespectively of the orbit's radius[5]. The influence of the periodic lattice is obtained by replacing the free electron mass m_e by the effective mass of the 2DEG conduction band. In GaAS/Ga(Al)As 2DEGs, the band mass is $m = 0.067 m_e$.

3.2.2 Semi-classic dynamics

Since a 2DEG is a degenerate Fermi liquid ($E_F >> k_B T$, the electrons participating to its transport properties have a well defined (Fermi) kinetic energy, v_F. Therefore, their cyclotron radius, r_C, decreases with the applied magnetic field.

$$r_C = \frac{v_F}{\omega_C} = \frac{m v_F}{eB}$$

At low temperatures[6], the quantum coherence is maintained along the cyclotron loop and the density of states is affected by the periodic boundary conditions for the quantum phase.

[5] The dynamics are isochronous like in an harmonic oscillator.

[6] Electrons are decoupled from the phonons in the subKelvin range.

In consequence, the physical properties are periodic with the cyclotron radius and therefore with the inverse of the magnetic field. For instance, $1/B$ Shubnikov-de Haas oscillations [61] develop in the longitudinal resistance. Nevertheless, a 2DEG presents some elastic scattering due to residual disorder. Therefore, the picture holds only if the cyclotron radius is inferior to the elastic mean free path, $r_C < l_e$, in order to observe such modulations. The onset of Shubnikov-de Haas oscillations provides a straightforward method to determine l_e with simple transport measurements.

For higher fields, one reaches the quantum limit of $r_C k_F \sim 1$, where the very notion of trajectory fails.

3.2.3 Landau quantization

The quantum version of the cyclotron motion was solved by Landau in the 20's and is a textbook problem [62, 63]. Because of the applied magnetic field, one has to express the mechanical momentum, $\hat{p}_{mech}$, in terms of the canonical momentum, $\hat{p}$, so that $\vec{\hat{p}}_{mech} = \vec{\hat{p}} + e\vec{A}(\hat{r})$. The kinetic energy hamiltonian reads:

$$\hat{H} = \frac{1}{2m}(\vec{\hat{p}} + e\vec{A}(\hat{r}))^2 \tag{3.3}$$

Energy spectrum

Within the Landau gauge $\vec{A}(\hat{r}) = (0, \hat{x}B, 0)$, the ansatz $\psi_k(x, y) = e^{iky} f_k(x)$ leads to the reduced problem:

$$\hat{H}_k = \frac{1}{2m}\hat{p}_x^2 + \frac{1}{2}m\omega_C(\hat{x} + kl_B^2)^2, \tag{3.4}$$

where $l_B = \sqrt{h/eB}$. Eq. (3.4) describes a 1D transverse harmonic oscillator in the x direction, centered in $X_k = -kl_B^2$. The resulting energy spectrum is:

$$\epsilon_{k,n} = (n + \frac{1}{2})\hbar\omega_C. \tag{3.5}$$

The energy levels defined by (3.5) are called Landau levels and are independent of the gauge choice.

Degeneracy

Spinless electrons The absence of energy dependency on the momentum $\hbar k$ gives rise [62, 63] to a huge (macroscopic) degeneracy W which is the same for each Landau level:

$$W = BS/\Phi_0, \tag{3.6}$$

where $\Phi_0 = e/h$ is the flux quantum and S the sample surface. This means that every Landau level can afford as many electrons as the number of flux quanta threading through the sample.

Spin 1/2 In the case of 1/2 spin particles, the Zeeman coupling $E_{\rm Z} = g\mu_{\rm B}\vec{S}\cdot\vec{B}$ can resolve the spin degeneracy. There are two limiting regimes with respect the the Zeeman gap[7] $\Delta_{\rm Z} = E_{\rm Z}(S=-1/2) - E_{\rm Z}(S=+1/2)$:

1. $\Delta_{\rm Z} > k_{\rm B}T$: Every Landau level splits in two spin polarized branches, separated by the Zeeman energy. Each spin branch has the "spinless" degeneracy W given by (3.6).

2. $\Delta_{\rm Z} < k_{\rm B}T < \hbar\omega_C$: Thermal fluctuations mix the opposite spin branches and the resulting spin degeneracy multiplies W(3.6) by 2.

In Ga(Al)As/GaAs 2DEGs, the spin-orbit scattering renormalizes the gyromagnetic factor which reads $g = -0.4$. The Zeeman gap at 4T is about

$$\Delta_{\rm Z}(B=4T)/k_{\rm B} \simeq 1 \text{ K} \tag{3.7}$$

while the cyclotron energy is about

$$\hbar\omega_C(B=4T)/k_{\rm B} \simeq 80 \text{ K}. \tag{3.8}$$

Both energies scale linearly with B, so the ratio $\hbar\omega_C/2E_Z \sim 80$ is independent of the field. With the typical sheet densities $n_{\rm e} = 2\ 10^{15}$ m^{-2} in the sub Kelvin range, both spin split branches of the lowest Landau level are fully filled at $B \sim 4$ T.

Eigenfunctions

The Landau gauge is useful for dealing with translation invariant geometries on the y direction. It is therefore well suited for extracting transport properties. The corresponding eigenfunctions are expressed in terms of the $n^{\rm th}$ Hermite polynomials H_n:

$$\psi_{n,k}(\vec{r}) = \frac{1}{\sqrt{L}} e^{iky} H_n(x + kl_B^2) e^{-\frac{1}{2l_B^2}(x+kl_B^2)^2} \tag{3.9}$$

The magnetic length l_B therefore characterizes the space dispersion around the central position X_k. In the lowest Landau level, l_B gives the variance of the zero point fluctuations in the transverse motion. The magnetic length is roughly ∼10 nm at 4 T, and scales as $1/\sqrt{B}$.

The symmetric gauge $\vec{A}(\vec{r}) = (-\frac{B}{2}\hat{y}, \frac{B}{2}\hat{x}, 0)$ has a continuous central symmetry and is therefore well suited for dealing with Coulomb interactions. The eigenfunction have therefore a definite angular momentum m. If we restrict to the lowest Landau level, the eigenfunctions read:

$$\psi_m(z) = \frac{1}{\sqrt{2\pi l_B^2 2^m m!}} z^m e^{-\frac{1}{4}|z|^2}, \quad m \in \mathbf{N}^{*+} \tag{3.10}$$

where $z = \frac{x+iy}{l_B}$ parameterizes the 2D plane. The chirality build by the magnetic field imposes only positive angular momenta, $m \in \mathbf{N}^{+*}$.

[7] The gyromagnetic factor is negative.

3.2.4 Conductivity

Mean current of eigenstates

We consider samples which are invariant in the y direction and use the Landau gauge. We restrict to the lowest Landau level for simplicity. Despite the e^{iky} dependence on (3.9), a state having a momentum $\hbar k$ does not carry any current. It is the *mechanical* momentum $\vec{\hat{p}} + e\vec{A}(\vec{\hat{r}})$ that is related to the particle current $\vec{\hat{J}} = \frac{e}{m}(\vec{\hat{p}} + e\vec{A}(\vec{\hat{r}}))$, and not the gauge dependent $\vec{\hat{p}}$. The x component of $< k|\vec{\hat{J}}|k >$ is obviously null since the transverse dynamics of (3.9) are those of a harmonic oscillator. It is easy to see that the y component vanishes too:

$$\begin{aligned} < k|J_y|k > &= -\frac{e}{m} < \psi_k|\hat{p}_y + eA_y(\hat{r})|\psi_k > \\ &= -\frac{e\omega_C}{\sqrt{\pi l_B^2}} \int \mathrm{d}x e^{-\frac{1}{l_B^2}(x+kl_B^2)^2} (x + kl_B^2) = 0. \end{aligned} \tag{3.11}$$

Transverse electric field

In the presence of an electric field $\vec{E} = (E, 0, 0)$, the potential term $V = eEx$ simply adds to the hamiltonian $\hat{H}_k$ (3.4). The potential translates the oscillator to the new position $X_k = -kl_B^2 - \frac{mE}{eB}$, and adds an electrostatic and a kinetic term with respect to X_k:

$$\epsilon_{n=0,k} = \frac{1}{2}\hbar\omega_C + eEX_k + \frac{1}{2}m|v_D|^2, \tag{3.12}$$

where $\vec{v}_D = \frac{\vec{E}\times\vec{B}}{B^2}$ is the classical drift velocity of the crossed field configuration $\vec{E} \perp \vec{B}$. The wave function has now a group velocity, $\vec{v}$, in the y direction equal to $\vec{v}_D$:

$$\vec{v} = (0, \frac{1}{h}\frac{\partial E_k}{\partial k}) = \frac{\vec{E} \times \vec{B}}{B^2}. \tag{3.13}$$

Therefore, X_k follows the equipotential lines $\vec{\nabla} V = 0$ and can be seen as the guiding center of a quantum drifting motion. The drifting motion is fully delocalized in the y direction and presents transverse zero point fluctuations on the l_B scale.

Since all states have the same drift velocity, the response of a Landau level to an electric field reads:

$$\vec{j} = \frac{n_e e}{B} \begin{pmatrix} 0 & -1 \\ +1 & 0 \end{pmatrix} \vec{E} \tag{3.14}$$

where n_e is the 2D electronic density. Therefore, a Landau level behaves as a good conductor in a perpendicular magnetic field, and has the same (local) response as in the classical Hall effect [61].

3.2.5 Metal/band insulator transition

Taking into account the Pauli principle, the relevant parameter describing the non-interacting physics is the filling factor of the Landau levels ν_L:

$$\nu_L = \frac{n_e S}{W} = \frac{n_e \Phi_0}{B} \tag{3.15}$$

Non-integer ν_L: For non-integer filling fractions, the chemical potential μ lies within the last Landau level $\lfloor \nu_L \rfloor + 1$, which is incompletely filled. Since electrons can be added without affecting μ, the system is perfectly metallic and displays the conductivity tensor (3.14).

Integer ν_L: For integer filling fractions $\nu_L \in \mathbf{N}^{*+}$, all bands are either full or empty. In consequence, a cyclotron gap $E_{\nu_L+1} - E_{\nu_L} = \hbar\omega_C$ separates the valence $n = \nu_L$ from the conduction band $n = \nu_L + 1$. The incompressible Fermi gas is a band insulator.

By sweeping the magnetic field at a constant density, a quantum phase transition is triggered between both phases with an $1/B$ periodicity. However, the insulating phase only appears for the discrete values of B defined by

$$\nu_L(B) = n, \quad n \in \mathbf{N}^{*+}. \tag{3.16}$$

3.3 Integer quantum Hall effect

It may seem surprising at first sight, but the universality and robustness of the IQHE are a consequence of finite size effects and a (small) disorder.

3.3.1 Edge channels

According to (3.13), the confinement that stucks the electrons in the sample gives a finite drift velocity v_D to the electrons located near the edges. Therefore, when the chemical potential lies between two Landau levels in the bulk of the sample, the only available low energy excitations are the drifting edge states crossing the Fermi energy at the edges of the sample [64], which is depicted in Figure 3.2. Since the drifting states follow the equipotential lines, they define 1D conducting channels. The quantized value of the Hall resistance will follow from the multichannel Landauer formula [47, 57] for perfectly transmitted channels. Finally, the edge channels are chiral: the drift velocity imposes a definite propagation sense which is opposite on opposite edges. Therefore, backscattering is forbidden along an edge, which yields to a vanishing longitudinal resistance [64, 65].

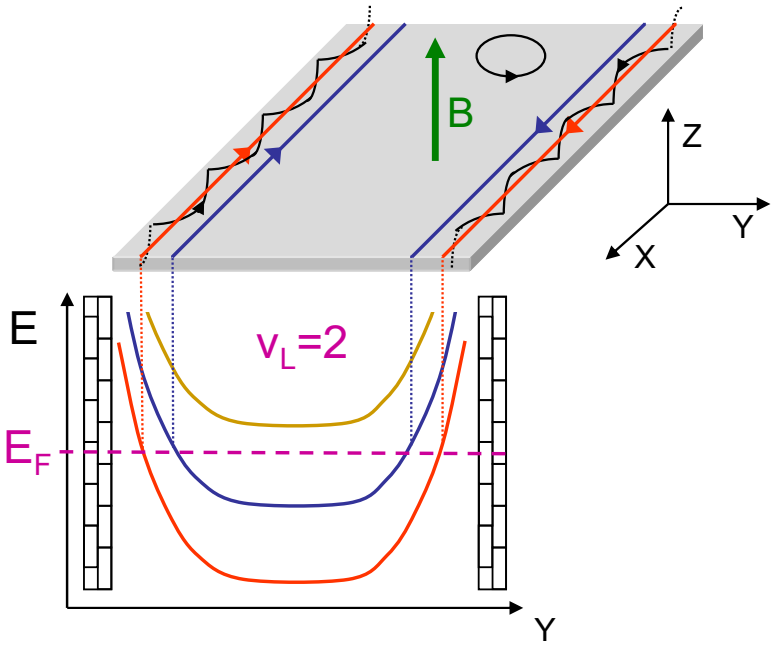

Figure 3.2: **Edge-channels in finite size clean samples** Localized states populate the Landau levels in the bulk of the sample. At the edge of the sample, the bending of the Landau levels gives rise to chiral propagative states (*Black:* semi-classical picture yields to skipping orbits). When the chemical potential lies between 2 Landau levels in the bulk, the only low energy excitations are the 1D chiral edge states crossing the Fermi energy E_F.

However, in translation invariant samples, edge channels arise only in a very small range of B, following the relation[8] (3.16). In order to explain the wide magnetic field range for which the Hall plateaus are observed, one needs to consider the effect of disorder. Before deriving the transport properties of edge channels, we first show how disorder leads to robust edge channels.

3.3.2 Effect of disorder

We consider the effect of small and smooth disorder: Its amplitude is smaller than the cyclotron gap (Zeeman), and its gradient is smaller than $\hbar\omega_C/l_B$ (Δ_Z/l_B). Within these conditions, disorder cannot mix different Landau levels (spin branches), and can be adiabatically added to their energy (3.12). This results in a potential landscape exhibiting additional

[8] This constraint is relaxed in the presence of edge channels, since the Fermi energy can evolve continuously between two Landau levels in the bulk. However in macroscopic samples, the surface where the Landau levels are bent is negligible in front of the total surface. Therefore, the magnetic field range giving rise to edge channels is extremely small.

valleys and hills.

Localized states

When the Fermi energy crosses a valley (or a hill) in the bulk of the sample, it gives rise to additional drifting states within the bulk, which are analogous to the edge channels. However, since the drifting motion follows the equipotential lines, these additional drifting states simply encircle the valleys (or hills), and are localized (see Figure 3.3 left). In consequence, they cannot contribute to the current flowing through the sample.

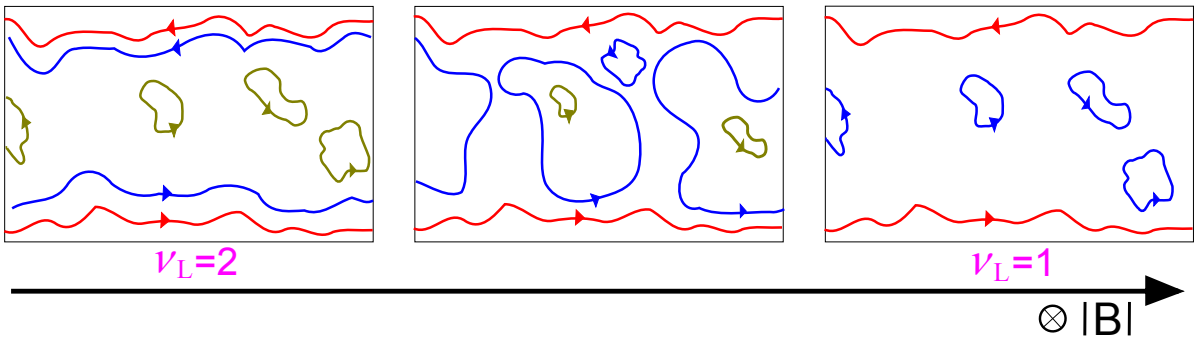

Figure 3.3: **Localized and extended states in a dirty sample.** Drifting states crossing the Fermi energy in a dirty sample originating from the lowest (red), 1st (blue) and 2nd (yellow) Landau levels. Edge channels are perfectly transmitted along the sample. Drifting states arising from disorder are localized within the bulk. The transition between two situations having a well defined number of edge channels is driven by the percolation of the innermost (here, the blue) edge-channel.

Percolation

For macroscopic samples, the drifting bulk states furnish a reservoir of localized states. At a fixed density, sweeping the magnetic field will change the size of the localized orbits. Therefore, even if they do not contribute to transport, they pin the Fermi energy between two Landau levels for wider ranges of magnetic field. Following this picture, the transition between two situations having a distinct number of well defined edge channels is driven by the percolation of the innermost edge channel as depicted in Figure 3.3.

This thesis focuses on the transport properties of edge channels. From now on, we will follow the literature and define ν_L as the number of well defined edge channels, unless explicitly specifying *filling factor*.

3.3.3 Transport properties of edge-channels

The scattering approach to quantum transport provides a powerful and intuitive framework to compute the transport properties of a quantum Hall system. Within this approach [47, 57, 59], it is not only possible to derive the quantized Hall resistances and vanishing longitudinal resistances, but also to describe [65] more refined experiments in which edge channels are distinctly biased and probed [66, 67]. The resulting properties of edge channels permit to develop an analogy between the IQHE and optics.

Two wire resistance

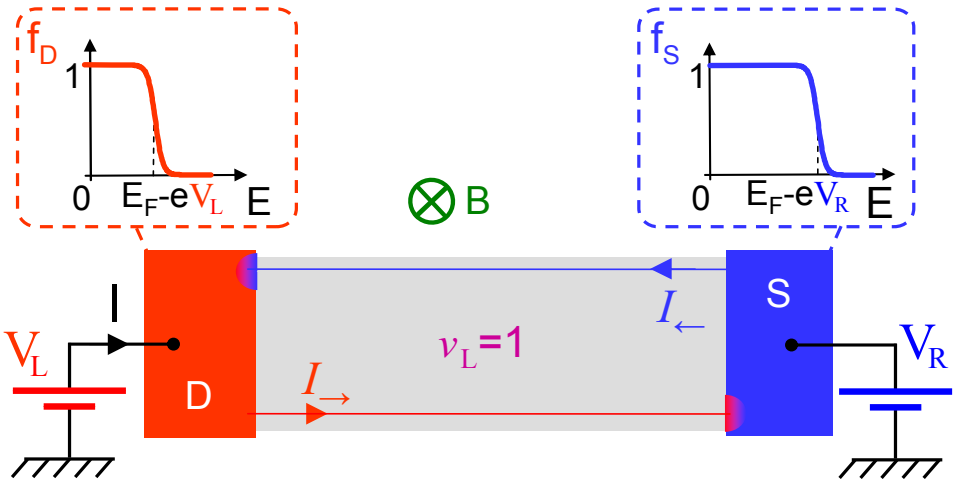

Figure 3.4: **Two wire probing of the IQHE, ν_L=1.** The sample is contacted by two reservoirs biased at electrochemical potentials V_R and V_L. The chiral edge-channels are only fed by the contact linked by causality, the up (down) edge-channel is fed by a Fermi distribution with a potential V_R (V_L) (top right and top left insets respectively).

The two wire resistance problem at $\nu_L = 1$ is depicted in Figure 3.4. Because of the chirality, the electrons flowing at one edge are only populated by the reservoir which is causally linked to them. The chiral currents therefore read,

$$I_{\rightarrow} = e \int v_D(E)\nu(E)n_{\rightarrow}(E)\mathrm{d}E \tag{3.17}$$

$$I_{\leftarrow} = e \int v_D(E)\nu(E)n_{\leftarrow}(E)\mathrm{d}E \tag{3.18}$$

where $v_D(E)$ is the drift velocity of the EC, $\nu(E)$ is the 1D energy density of states per unit length, and $n_{\rightarrow}$ ($n_{\leftarrow}$) are the populations imposed by the right (left) reservoirs. Since

the reservoirs are at equilibrium with their respective voltage sources $V_R(V_L)$, the electron populations are Fermi functions translated in energy one from the other:

$$n_{\rightarrow} = f_F(E - eV_L)$$
$$n_{\leftarrow} = f_F(E - eV_R)$$

Moreover, the velocity is given by $v_D(E) = 1/h(\partial E/\partial k)$, while the energy density of states in 1D is simply $\nu(E) = (\partial E/\partial k)^{-1}$. Thus, the product $v(E)\nu(E)$=1/h is universal. By applying the nodal law in each reservoir and performing the precedent simplification one obtains the Landauer formula for perfectly transmitted channels [47]:

$$\begin{aligned} I = I_{\rightarrow} - I_{\leftarrow} &= \frac{e}{h}\int f_F(E - eV_L) - f_F(E - eV_R)\mathrm{d}E \\ &= \frac{e^2}{h}(V_L - V_R) \end{aligned} \tag{3.19}$$

The two wire conductance is thereby the conductance quantum $G_Q = e^2/h$ and the two wire resistance equals the resistance quantum $R_Q = h/e^2$.

Equilibrium currents: Following the same arguments, at equilibrium $V_L = V_R = V$ the chiral channels carry a local equilibrium current

$$I_{\rightarrow} = I_{\leftarrow} = \frac{e^2}{\hbar}V. \tag{3.20}$$

The net current $I = I_{\rightarrow} - I_{\leftarrow}$ is obviously null. However, the circulation of the equilibrium current around the sample perimeter is finite. These diamagnetic currents follow Le Chatelier's principle, and tend to oppose to the external magnetic flux.

Two wire resistance at arbitrary ν_L: For arbitrary integer filling factors $\nu_L \in \mathbf{N}^{*+}$, the system can be viewed as ν_L pairs of chiral edge channels in parallel. Following the arguments presented in the precedent paragraph, each channel carries the same currents defined by (3.17) and therefore the 2 wire resistance of the whole system is simply the parallel composition of ν_L resistance quanta [47, 57, 59]:

$$R_{\nu_L}^{2wire} = \frac{1}{\nu_L}\frac{h}{e^2}$$

The Hall Bar experiments

Chirality: What really makes the IQHE a unique system in quantum transport is the edge channel chirality: Namely, the edge channels having opposite propagation sense are spatially separated (see Figure 3.2). Therefore, backscattering is forbidden in macroscopic samples having a moderate disorder.Moreover, it permits to contact separately the edge channels having opposite chiralities. This is what is done in Hall bar geometries (Figure 3.5).

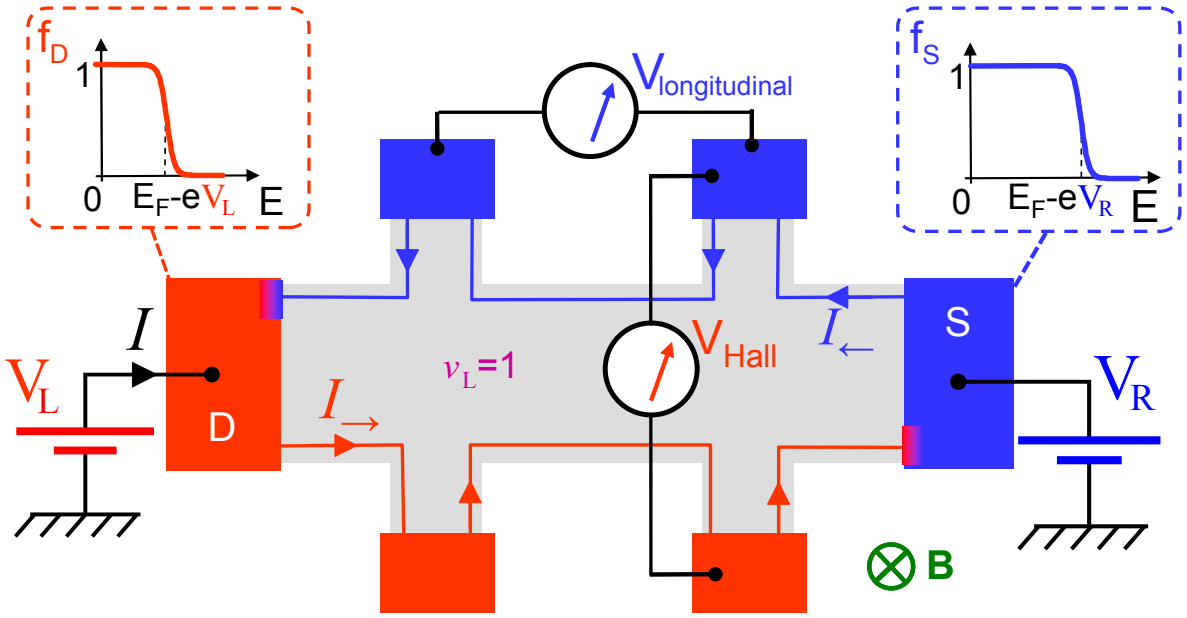

Figure 3.5: **Hall bar probing probing of the IQHE, ν_L= 1.** The edge channels chirality forbid backscattering and the edge channels maintain their initial potential along their propagation. The voltage drop due to the finite 2 wire resistance develops between opposite edges. Therefore, the Hall resistance matches the 2 wire resistance.

Longitudinal resistance: The first consequence of chirality is that the injected chiral currents $(I_{\rightarrow}, I_{\leftarrow})$ are conserved along the edge [64, 65]. Therefore, the electrochemical potential imposed by the reservoirs is kept the same all along the propagation. The longitudinal resistance vanishes as long as it is measured along the same edge. The edge chiral transport current without dissipation.

Hall resistance: However, there is a finite 2 wire resistance according to (3.19). Therefore, a voltage drop develops between the biasing contacts when a current flows through the sample. Because of the chirality, this voltage drop can only develop between edge channels on opposite edges [64, 65]. The Hall resistance is thereby equal to the two wire resistance: $R_{Hall} = \frac{1}{\nu_L}\frac{h}{e^2}$. And the Joule heating $R_{\rm Hall}I^2$ can only be dissipated in the reservoirs used to feed the sample [68] (see red and blue spots in Figures 3.4 and 3.5).

Spin: The precedent arguments apply for spinless particles. For spin resolved electrons, $\Delta_{\rm Z} > k_{\rm B}T$, they apply as well, but one has to keep in mind that the edge channels originate from spin split branches of the Landau levels. For spin degenerate electrons, $\Delta_{\rm Z} < k_{\rm B}T$, the spin degeneracy multiplies by two the conductances, and only even fractions arise.

Testing the edge-channel picture

The edge channel picture, combined to the scattering approach, gives the correct values of the multi terminal resistances measured in Hall experiments. But, can we consider that several co-propagating edge channels ($\nu_L \geq 2$) are well defined, distinct objects? One can perform more refined experiments based on the edge channel picture in order to test this. Such experiments were originally coined as anomalous quantum Hall effect [66, 67, 69].

The anomalous quantum Hall effect: The anomalous quantum Hall [66, 67, 69] effect arises in 2DEGs with small constrictions. Small enough constrictions can be used to transmit a sub-set of n edge channels, while reflecting the other $\nu_L - n$. Therefore, one can selectively bias and probe a sub-set of the edge channels. If the edge channels are distinct, they each carry their own potential, at least up to some equilibration length.

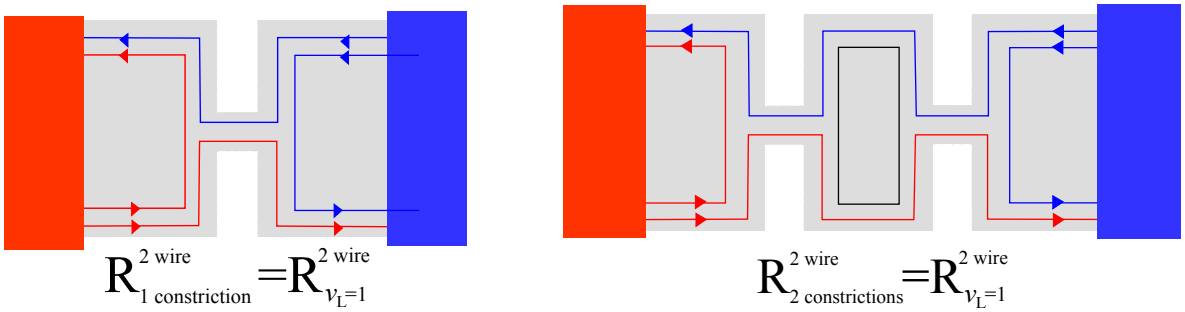

Figure 3.6: **Anomalous quantum Hall effect through small constrictions,** $\nu_L = 2$ Left: A small constriction fully transmits (reflects) the outer (inner) edge-channel. Since the current is transmitted by the outer edge channels edge-channels only, the 2 wire resistance matches the $\nu = 1$ Hall resistance. Right: Same argument applies to two constrictions in series ,if there is no electrochemical potential equilibration between the constrictions.

We consider the simplest case of two co-propagating edge channels ($\nu_L = 2$) and constrictions that fully transmit the outer edge channels while fully reflect the inner edge channels, which is depicted in Figure 3.6 left. Since only the outer edge channels transmit the current, the two wire resistance through the constriction matches the $\nu_L = 1$ resistance: $R^{2wire}_{1constriction} = R^{2wire}_{\nu_L=1}$. If two such constrictions are placed in series (Figure 3.6 right), the outer edge channel still connects opposite reservoirs and we obtain $R^{2wire}_{2constriction} = R^{2wire}_{\nu_L=1}$. This is a stark violation of classical impedance composition laws, by which one would expect $R^{2wire}_{2constriction} = 2R^{2wire}_{1constriction}$. Such effects where originally coined as anomalous quantum Hall effect and are a paradigm of ballistic transport effects. They are nothing but the consequence that distinct edge channels can carry their own potentials.

Equilibration length: If the distance between both constrictions is long enough, some of the charge injected in the outer edge channel will tunnel to the closed loop inner edge channel (black line in Figure 3.6). Eventually, the electrochemical potentials of the two counter propagating outer edge channels, and of the closed loop inner edge channel, equilibrate between the constrictions. In this limit, one recovers the classical result $R^{2wire}_{2constriction} = 2R^{2wire}_{1constriction}$. This scheme can be used to characterized the equilibration length between edge channels biased at different potentials [66, 67, 69], for instance by increasing the size of the loop until one reaches the classical impedance composition law.

The inter-channel charge equilibration lengths are long ($\gtrsim$ 100 µm in the sub Kelvin range) since the small overlapping between the different edge channels' wavefunctions exponentially suppresses it [56, 70]. At $\nu_L = 2$ the tunneling is further suppressed by the opposite spin polarization of the two copropagating edge channels. In this case, spin conservation imposes that the tunneling of an electron is accompanied by a nuclear spin flip. Such events take place at a low rate due to the small hyperfine coupling, which explains the very large equilibration lengths, up to the millimeter range, demonstrated at $\nu_L = 2$ below 0.1 K [71]. The two co-propagating edge channels have therefore well defined electron populations on nearly macroscopic distances.

3.3.4 Optical analogy

The unique properties of edge channels permit to develop an analogy with optics summarized in Figure 3.7. This analogy has led to a new branch of experiments, where quantum optics concepts are implemented with electron edge channels.

An edge channel mimics an optical fiber for electrons, since it can be used to propagate an injected charge without loss of (electrochemical) power. Moreover, constrictions can be used not only to selectively populate and probe the edge channels, but they can also be tuned to partially transmit and reflect a chiral pair of them. These tunable constrictions are called quantum point contacts [72, 73] (QPC) and are the edge channel analogue of a beam-splitter for light beams.

These tools are the building blocks for realizing interferential experiments with electrons propagating in edge channels. Fabry-Pérot resonances were first observed in the late 80's [50]. State of the art are the demonstration of electronic Mach-Zehnder interferometers (MZI) [8, 13, 15, 74], and of 2 particle electronic coherence using two coupled MZIs [9]. Last, an on demand single-electron source for edge channels has been realized [10].

The IQHE therefore opens avenues of investigation involving quantum optics concepts, the fermionic character of electrons and the many-body physics due to Coulomb interactions.

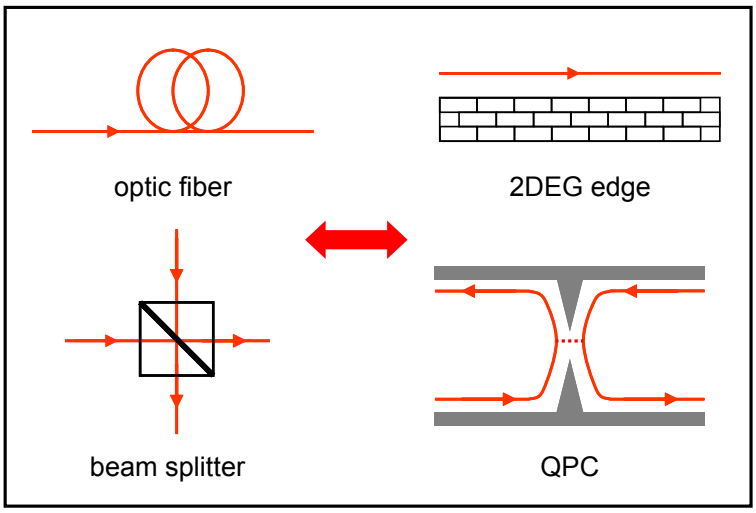

Figure 3.7: **Optical analogy in the IQHE between EC and light beams.** Top: Edge channels mimic optic fibers. Bottom: Partially transmitting small constrictions (quantum point contacts) mimic beam-splitters.

3.4 Interaction effects in the integer quantum Hall effect

Even if the IQHE was discovered nearly 30 years ago, the role of Coulomb interactions still causes an active debate since it is difficult to measure by usual experimental approaches. Here we highlight two main reasons:

Charge transport: In the precedent section we have seen in detail how the edge channels' chirality yields to the universal transport properties observed in Hall bar experiments. This universality has drawn much attention to the IQHE and is exploited on metrological purposes or in the optical analogy. But on the other side to the coin, it starkly limits what can be learned from usual charge transport experiments [16].

Optical probing: Kohn's theorem [75] shows that an homogeneous irradiation field only couples to the center of mass motion of the many cyclotron orbits. Since the center of mass dynamics are irrespective of Coulomb interactions, simple absorbtion measurements can only measure the non-interacting excitation gap.

However, Coulomb interactions can yield to dramatic effects on the very nature of the edge excitations. In the following we introduce the main effects that are expected to arise. We will conclude reviewing some experimental results giving some information on interaction effects.

3.4.1 Spontaneous spin polarization

Following the discussion on the spin degeneracy, the even integer fractions of Hall resistances arise only if the spin gap $\Delta_Z \sim \hbar\omega_C/80$ is larger than temperature and disorder. However, typical Hall resistance measurements, as in Figure 3.1, reveal that both even and odd fractions of the Hall resistance arise at the same magnetic fields so that both gaps should be comparable. This is the consequence that the exchange energy protects the spin polarization of completely filled Landau levels.

Let's see the simplest case of $\nu_L = 1$, where the ferromagnetic ground state reads:

$$|F>= \Phi(z_1, \ldots, z_N)|\uparrow, \ldots, \uparrow> . \tag{3.21}$$

Since the orbital part must be antisymmetric, two particles cannot be too close to each other diminishing the Coulombic repulsion. The exchange term thus lowers the interaction energy with respect to unpolarized states. Its energy scale per particle unit can be evaluated [62] to be $-\sqrt{\frac{\pi}{8}}\frac{e^2}{\epsilon l_B k_B} \sim 100$ K at $B \simeq 4$ T, which is two orders of magnitude higher than the Zeeman gap (3.7). The polarized states are therefore protected by the exchange energy for higher energies than those dictated the Zeeman coupling only.

Recent investigations at $\nu_L = 1$ have however revealed that the spin polarization at $\nu_L = 1$ decreases on a 200 mK scale [76]. The available theories on spin excitations (spin density waves [77] and spin topological textures [78]) fail to describe such behavior. The quantum ferromagnetism of the lowest Landau level is still an open problem.

3.4.2 Inter channel interactions

As long as the dispersion of non-interacting edge channels can be linearized, interactions within and between co-propagating 1D chiral fermions (1DCFs) can be handled by exact methods using the bosonization framework (see e.g. [55] and references therein). The key point is that the linearized hamiltonian of 1DCFs,

$$H_0 = \hbar v_D \int dk(k - k_F)\hat{c}_k^\dagger \hat{c}_k$$

can be expressed in terms of the local density operator

$$\hat{\rho}(x) = \hat{c}^\dagger(x)\hat{c}(x) - < \hat{c}^\dagger(x)\hat{c}(x) >_{\text{Fermi sea}}$$

so as to display the expression [38]:

$$H_0 = \pi\hbar v_D \int \hat{\rho}^2(x)\mathrm{d}x. \tag{3.22}$$

Naïve derivation

Since the bulk of the sample is incompressible, the only low energy excitations must be surface waves. Linearizing the confinement potential near the Fermi energy, the electrostatic energy of an edge displacement wave $\mathcal{E}$ can be expressed in terms of the bulk density $n_e = \frac{\nu_L}{2\pi l_B^2}$, the local electric field E and the transverse displacement per unit length, $h(x)$, caused by the local density change $h(x) = \frac{\rho(x)}{n_e}$:

$$\begin{aligned}\mathcal{E} &= \int \mathrm{d}x \int_0^{h(x)} neE y \mathrm{d}y \\ &= \int \frac{neE}{2} h^2(x) \mathrm{d}x \\ &= \frac{\pi\hbar v_D}{\nu_L} \int \rho^2(x) \mathrm{d}x. \end{aligned} \tag{3.23}$$

Quantizing the density operator yields directly to (3.22) for one IQHE edge-channel ($\nu_L = 1$). This naïve argument can be made rigorous by deriving the action of edge excitations [21]. It is found that the Fourier transform of the density operators follow bosonic commutation rules.

Local interactions within a channel

Departing from the expression (3.22), it is straightforward to see that local density-density interactions, within a branch of 1DCFs ($\nu_L = 1$), simply renormalizes their drift velocity:

$$\begin{aligned}\hat{H} = \hat{H}_0 + \hat{H}_{int} &= \pi\hbar v_D \int \hat{\rho}(x)^2 \mathrm{d}x + g \int \hat{\rho}(x)^2 \mathrm{d}x \\ \hat{H} &= \pi\hbar(v_D + \frac{g}{\pi\hbar}) \int \hat{\rho}(x)^2 \mathrm{d}x \end{aligned} \tag{3.24}$$

where g is the local interaction parameter. The final expression has the same form as (3.22), but with a drift velocity, v, renormalized by interactions:

$$v = v_D + \frac{g}{\pi\hbar} \tag{3.25}$$

Local inter-channel interactions, $\nu_L = 2$

We consider here the case of density-density interactions between co-propagating branches of 1DCFs [9]. The total hamiltonian is quadratic in the density fields of both edge channels labeled by the index $i = 1, 2$ and, following (3.25, interactions within the edge channels are hidden in the velocities v_i: [21]:

$$H = \pi\hbar \int \left\{ v_1 \hat{\rho}_1(x)^2 + v_2 \hat{\rho}_2(x)^2 + \frac{g_{12}}{\pi\hbar} \hat{\rho}_1(x)\hat{\rho}_2(x) \right\} dx \tag{3.26}$$

[9] Note that analytical solutions can also be obtained in the more general framework of non-chiral and non-Fermi 1D conductors, see e.g. [79].

Such hamiltonian can be easily diagonalized by a rotation in the density field spinor $(\hat{\rho}_1, \hat{\rho}_2)$, giving rise to eigenmodes $(\hat{\rho}_c, \hat{\rho}_n)$ which are linear combinations of the initial density fields [21, 22, 31, 80]:

$$\begin{aligned} H &= \pi\hbar v_c \int dx \hat{\rho}_c(x)^2 + \pi\hbar v_n \int dx \hat{\rho}_n(x)^2 \\ \hat{\rho}_c(x) &= \cos(\theta)\hat{\rho}_1(x) + \sin(\theta)\hat{\rho}_2(x) \\ \hat{\rho}_n(x) &= \sin(\theta)\hat{\rho}_1(x) - \cos(\theta)\hat{\rho}_2(x) \\ v_c &= \frac{v_1+v_2}{2} + \sqrt{\left(\frac{g_{12}}{\pi\hbar}\right)^2 + \left(\frac{v_1-v_2}{2}\right)^2} \\ v_n &= \frac{v_1+v_2}{2} - \sqrt{\left(\frac{g_{12}}{\pi\hbar}\right)^2 + \left(\frac{v_1-v_2}{2}\right)^2} \end{aligned} \tag{3.27}$$

where the pre-factors read:

$$\begin{aligned} \cos(\theta) &= \frac{1}{\sqrt{2}}\sqrt{1 + \frac{v_1-v_2}{\sqrt{4(\frac{g_{12}}{\pi\hbar})^2 + (v_1-v_2)^2}}} \\ \sin(\theta) &= \frac{1}{\sqrt{2}}\sqrt{1 - \frac{v_1-v_2}{\sqrt{4(\frac{g_{12}}{\pi\hbar})^2 + (v_1-v_2)^2}}} \end{aligned}$$

Large interaction limit: In the large interaction limit $g_{12} \gg \pi\hbar|v_1 - v_2|$, one finds $\theta = \pi/2$ and the eigenmodes are simply the symmetric, $\hat{\rho}_c(x)$, and antisymmetric, $\hat{\rho}_n(x)$, combinations of the initial density fields. In this limit the corresponding velocities read [21, 22, 31, 80]:

$$\begin{aligned} v_c &= \frac{v_1+v_2}{2} + \frac{g_{12}}{\pi\hbar} \\ v_n &= \frac{v_1+v_2}{2} - \frac{g_{12}}{\pi\hbar} \end{aligned} \tag{3.28}$$

and are different. The dynamics are therefore fully delocalized amongst both channels. Notably the symmetric mode, $\hat{\rho}_c(x)$, carries a charge while the antisymmetric mode, $\hat{\rho}_n(x)$, does not. Even if the structure of (3.28) implies that a negative velocity is possible for the neutral mode, it is not very physical since the initial velocities also contain the interaction term within the each channel (3.25). In the limit dominated by interactions, one would expect $g_1 \sim g_2 \sim g_{12} = g$ (see following section) and therefore:

$$\begin{aligned} v_n &= \frac{1}{\pi\hbar}\left(\frac{g_1+g_2}{2} - g_{12}\right) + \frac{v_{D1}+v_{D2}}{2} \simeq \frac{v_{D1}+v_{D2}}{2} \\ v_c &= \frac{1}{\pi\hbar}\left(\frac{g_1+g_2}{2} + g_{12}\right) \simeq \frac{2g}{\pi\hbar}. \end{aligned} \tag{3.29}$$

The charge mode velocity would measure the interaction parameter, whereas the neutral mode velocity would measure the mean drift velocity of the non-interacting problem.

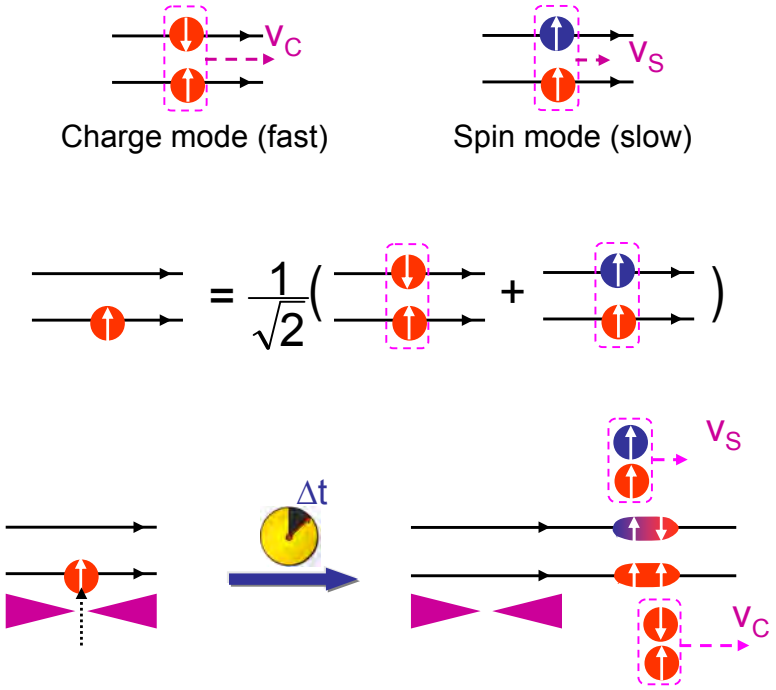

Figure 3.8: **Spin charge separation in $\nu_L = 2$ strongly interacting edge-channels.** Red/Blue: electron/hole like 1DCF excitations of an edge channel. Top: Strong interactions between edge channels yields to a spinless charge mode (fast) and a spin neutral (slow) mode. Middle: An electron like excitation of a single edge channel is a linear combination of the spin and charge modes. Bottom: The spin and charge modes, excited by the injection of a single electron in a single edge channel, spatially split due to their different drift velocities.

Spin-charge separation: In the particular case of $\nu_L = 2$, the edge channel index also labels the electron spin, as depicted in Figure 3.8. Thereby, the charge mode, $\hat{\rho}_c$, carries no spin, while the neutral mode, $\hat{\rho}_n$, carries a spin [21, 22, 31, 80]. In consequence, the spin and charge dynamics split in the strong interaction limit. However, DC charge transport cannot be sensible to such effect since it integrates (in time) amongst both charge and spin modes which globally carry the same amount of charge as two non-interacting channels.

3.4.3 Edge reconstruction

A confinement potential tends to shrink the electron fluid whereas the Coulomb electronic repulsion tends to expand it. This antagonistic forces lead to an instability of the non-interacting edges [18] that may deeply modify their physics. For moderate confinement potential gradients, such instability may give rise to additional co- and counter-propagating channels [19]. In the limit of smooth potentials, the self consistent edge-potential is expected

to reconstruct in an alternate series of compressible and incompressible strips [17]. As a result of this edge reconstruction, additional branches of acoustic excitations modes are predicted to arise within the compressible strips [20].

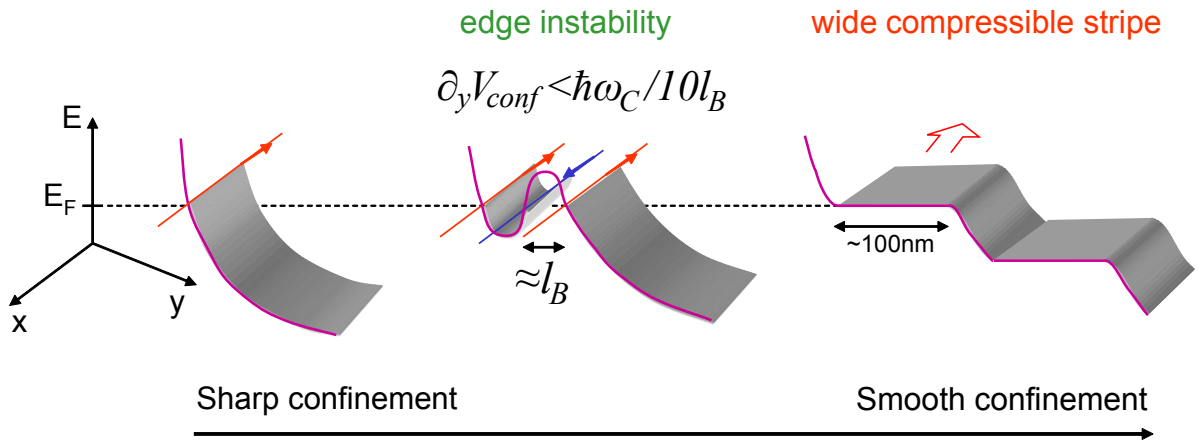

Figure 3.9: **Edge instability due to the Coulomb repulsion** Left: Sharp potential limit, non-interacting chiral edge channels (1DCFs) are well defined at the fermi energy E_F. Center: The self-consistent potential bends at a critical confinement potential gradient $\partial_y V$. This bending leads to additional co- and counter-propagating 1DCFs. Right: Smooth confinement potential limit. The self-consistent potential alternates wide compressible and small incompressible strips every time a Landau level crosses the Fermi energy.

Edge instability

In the sharp confinement limit, the confinement potential overpowers the Coulomb repulsion (hard wall limit). The non-interacting picture of edge channels described as one dimensional chiral fermions (1DCFs) (see Figure 3.9 Left) is well suited in this limit .

At a critical value of the confinement gradient, it is energetically favorable to bend the self-consistent potential. Indeed, the bending gives rise to additional co- and counter-propagating edge channels, which are spatially separated on a l_B scale (see Figure 3.9 Center). These additional 1DCFs permit to distribute spatially the charge originally carried by the non-interacting channel, thus increasing the self consistent capacitance. Numerical Hartree-Fock calculations of the self consistent potential profile predict a critical value at $l_B \partial_y V \sim \hbar\omega_C/10$ [19].

Since the current carried by 1DCFs does not depend on the microscopic parameters (3.19), the contribution to DC current of the co- and counter-propagating 1DCFs always cancel each other and are invisible in DC Hall bar experiments.

Edge reconstruction

In the smooth potential limit $l_B \partial_y V \ll \hbar\omega_C$, compressible electrons can rearrange their density in order to screen the confinement potential. At non-integer *local* filling fractions, the electrons completely screen the confinement potential, whereas at local integer values the incompressible electrons cannot. This yields to an alternation of compressible and incompressible strips parallel to the edge [81] (see Figure 3.9 Right), every time a Landau level crosses the Fermi energy.

Depletion length: We first assume a zero magnetic field. In a realistic model, the confinement potential follows from a voltage biased top metallic gate. The applied negative voltage, V_G, depletes the 2DEG beneath the gate and up to a transverse depletion length l_D in which the electron density is null. At distances higher than l_D the potential is completely screened, so that l_D fixes the screening length of the problem and must be larger than the Bohr radius $a_\mathrm{B} = \frac{4\pi\epsilon\hbar^2}{me^2}$ of the 2DEG. Neglecting the distance between the 2DEG and the top metallic gate planes, the electrostatic problem can be solved in terms of l_D [17]:

$$l_D = \frac{2V_G\epsilon}{e\pi n_\mathrm{e}} \tag{3.30}$$

The density profile is found as:

$$n(y) = \sqrt{\frac{y - l_D}{y + l_D}} n_\mathrm{e} \Theta_\mathrm{H}(y - l_D) \tag{3.31}$$

where y is the distance from the gate and Θ_H is the Heaviside step function.

For a typical bulk density $n_\mathrm{e} = 2\ 10^{15}\ \mathrm{m}^{-2}$, gate voltage $V_G = 1\,\mathrm{V}$ and taking $\epsilon = (\epsilon_0 + \epsilon_\mathrm{GaAs})/2 \simeq 7\epsilon_0$, the depletion length is about $l_D \sim 125$ nm which is much larger than $a_B \sim 6$ nm.

Dipolar strips: We first consider spinless Landau levels. At any reasonable magnetic field, the depletion length l_D (3.30) should remain the same since $\hbar\omega_c/eV_G$ is small. However, the density profile $n(y)$ may be slightly modified by the Landau levels. Indeed, at positions where all the Landau levels are fully occupied or empty, the incompressibility yields to a poor screening. But with incompletely filled Landau levels, the gas is locally compressible, and one should recover the low magnetic field density profile. This yields to an alternate series of compressible and incompressible strips parallel to the gate (Figure 3.9.right).

Labeling the incompressible stripes with the Landau levels i giving rise to them, they are located at the distances y_i from the gate defined by:

$$\begin{aligned} n(y_i) &= i\frac{B}{\Phi_0} \\ \Rightarrow y_i &= l_D \frac{\nu_L^2 + i^2}{\nu_L^2 - i^2} \end{aligned} \tag{3.32}$$

where the first equation follows from (3.15) and the second from (3.31). ν_L is the Landau level filling factor in the bulk and Φ_0 the flux quantum.

For a single Landau level at the Fermi energy, $1 < \nu_L < 2$, the width of the incompressible stripe u_1 is explicitly found [17] as:

$$\begin{aligned} u_1 &= \sqrt{\frac{4\epsilon\hbar\omega_C}{\pi e^2 \big(\partial n/\partial y\big)_{y=y_1}}} \\ &= \sqrt{\frac{8a_{\mathrm{B}}l_D}{\pi}}\frac{\nu_L}{\nu_L^2-1} \end{aligned} \tag{3.33}$$

which is much smaller than its distance to the gate y_1, since: $u_1/y_1 \propto \sqrt{\frac{a_{\mathrm{B}}}{l_D}}$. Therefore, the width a of the compressible stripe can be defined as

$$a = y_1 - l_D = \frac{2l_D}{\nu_L^2-1} \tag{3.34}$$

which is much wider than the incompressible strip width.

Spin polarized states The same arguments apply to spin splitted Landau levels. However, one should replace $\hbar\omega_C \to \Delta_{\mathrm{Z}} = g\mu_{\mathrm{B}}B$ in (3.33) in order to consider a Zeeman gap, rather than the cyclotron gap. The incompressible strips are smaller by a factor $\sqrt{80}$. However, the position of the incompressible stripes (3.4.3) does not change, and neither do the widths of the compressible stripes.

Incompressible bulks: At bulk filling factor $\nu_L = 2$, the outer compressible strip is about $\frac{2}{3}l_D \sim 85$ nm with the usual sample parameters. At integer bulk filling factors, the innermost incompressible strip position is singular in this model, since the original density (3.31) assumes a compressible bulk. However, the long range of Coulomb interaction will be cut at some other screening length which can be given by the distance to other gates. But, as a general rule, the innermost compressible stripe is wider than the outer one.

Additional excitation branches

In reconstructed edges, the compressible strips are the siege of transverse dynamics corresponding to density oscillations across the strip width. Because of the perpendicular magnetic field, these density oscillations are propagative and give rise to additional *acoustic* branches of edge excitations [20].

The starting point is the hydrodynamic description of a single compressible strip of width a. The dynamics are described by the Euler equation and the continuity equation which is

linearized in the electronic velocity $\vec{v}$:

$$\dot{\vec{v}} + \omega_C(\frac{\vec{z}}{|z|} \times \vec{v}) - \frac{e^2}{4\pi\epsilon m}\vec{\nabla}_{\vec{r}} \int \vec{r}_1 \frac{\delta n(\vec{r}_1)}{|\vec{r} - \vec{r}_1|} \mathrm{d}\vec{r}_1^2 \tag{3.35}$$
$$\delta\dot{n} + \vec{\nabla}_{\vec{r}} \cdot (n_0 \vec{v}) = 0$$

where δn is the density difference from its initial value $\delta n(y) = n(y) - n_0(y)$. These equations admit analytical solutions [20] in the long wavelength limit $ka \ll 1$, using the density profile

$$n_0(y) = \frac{2}{\pi}\bar{n} \arctan(\sqrt{\frac{y}{a}}) \tag{3.36}$$

where $\bar{n}$ is the bulk density. This model reproduces the main features of the density profile (3.31) found in [17].

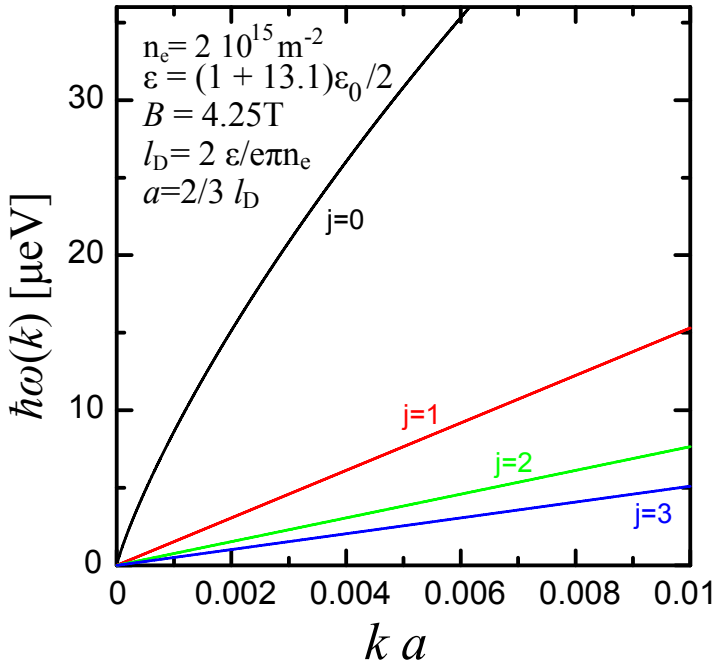

Figure 3.10: **Dispersion relation of the reconstructed edge modes.** The wave vector is normalized by the compressible strip width a. The charge mode $j = 0$ displays the same dispersion as classical edge magnetoplasmons [82, 83]. All additional modes $j > 0$ are gapless and acoustic. Inset: numerical values used for the calculation.

The solutions of (3.35) yield to an infinite series of *gapless* propagative excitation branches labeled by the number of nodes, j, of their transverse oscillations across the strip width [20]. Their dispersion relations read:

$$\epsilon(k)_{j=0} = \ln\left(\frac{e^{-\gamma}}{2|ka|}\right)\frac{2\bar{n}e^2}{4\pi\epsilon\omega_C}k \tag{3.37}$$
$$\epsilon(k)_{j>0} = \frac{2\bar{n}e^2}{4\pi\epsilon\omega_C}\frac{k}{j}$$

where γ is the Euler constant. These dispersion relations are plotted in Figure 3.10 for typical sample parameters.

Charge density mode j=0: The $j = 0$ mode [20] has no transverse dynamics. It is therefore a 1D charge density wave of finite width and can be pictured as a rigid displacement of the whole edge profile. Its dispersion (3.37) is the same as that of the classical edge magnetoplasmon [82, 83] of a non-degenerate electron gas.

The logarithmic term in the $j = 0$ mode (3.37) is the logarithmic correction due to the long range part of Coulomb interactions [55] taken into account by the last term in (3.35). Since top metallic gates screen this long range part on a 100 nm scale, the $j = 0$ mode can be linearized up to $k < 2\pi/100$ nm. This is also the limit where dispersion relations (3.37) hold since the strip width scales with the strip to gate distance (3.34).

Following the arguments of the bosonization section, the linearized charge mode can be mapped to the non-interacting 1D chiral fermion excitations of non-interacting edge-channels. This naïve argument can be made rigorous within a full quantum derivation of the compressible strip electrodynamics [84].

Internal transverse modes j>0: The $j = 1$ mode can be pictured as a propagative dipole, the $j = 2$ as a tripole and so on. These additional *acoustic* branches have slower drift velocities since they cost a smaller charging energy per unit length. Since the density profile within the stripe is not symmetric (3.36) across its width, they propagate a finite charge and may be observed in dynamical charge transport. However, applying a DC bias raises the electrochemical potential of the whole compressible strip so that it couples only to the charge j=0 mode. Therefore, the DC properties of reconstructed edges are the same as those of non-reconstructed edges.

3.4.4 Experimental signatures?

Time resolved charge transport experiments can be used to test the dynamic response of the ECs in time of flight experiments, but have never been able to demonstrate the existence of the predicted additional modes of reconstructed edges. Being sensitive to the single particle phase coherence, Mach-Zehnder interferometer (MZI) experiments provided strong evidence for interaction effects. There is currently an active debate in order to interpret the MZI results.

Time of flight experiments

Time of flight experiments are useful to probe the dynamical response of edge excitations. In the IQHE, time of flight experiments are implemented by applying a voltage pulse in a

contact and probing the the delay time before some current arrives to another contact linked by chirality some distance away [85, 86]. When the propagation distance is high enough, the applied pulse may split in several pulses carried by the edge excitations having different drift velocities. By knowing the (edge) propagation length between both contacts one can deduce the drift velocities of the current-carrying excitations.

Reported drift velocities of ν_L= 2: Several experiments carried at $\nu_L = 2$ with different geometries including chemically etched edges, gate defined edges and samples completely covered by a (screening) top gate, yield to a drift velocity for the fast mode in the range of[10] $v \in [5\,10^4, 5\,10^5]\mathrm{m.s}^{-1}$.

Testing the additional modes of reconstructed edges: Similar experiments have been used to test the existence of the additional transverse modes [87, 88] of the reconstructed edge, for which there are strong predictions [20] for the dispersion relation (3.37), and therefore their drift velocities. However, the number of time delayed pulses observed in these time of flight experiments has never been higher than the filling factor of the measured systems and can therefore be explained by (eventually interacting) ν_L co-propagating 1DCFs. Consequently, up to now there is still no direct signature of the *additional* reconstructed edge excitation branches.

Coulomb interaction dependence of drift velocity: Last, time of flight experiments can be used to investigate the effect of Coulomb interactions on the drift velocity of the edge excitations [89]. The idea is to probe the drift velocity for different values of the gate voltage used to define the edge of the sample. Different gate voltages result in different distances (3.30) between the edge channels and the gate that screens the Coulomb interactions within and between them. By modifying the interaction parameters, one tunes the renormalized drift velocities as expected by (3.25) and (3.27).

Such experiments demonstrate it is possible to tune the drift velocity by a factor of $\sim 2-3$ by changing the gate bias on the volt range [89, 90]. The results of [89] show that typical edge channels velocities at $\nu_L = 2$ are rather dominated by the interaction term.

Mach-Zehnder interferometers

Several observations in the recent Mach-Zehnder interferometers are incompatible with the non-interacting picture of edge channels:

- A multilobe structure arises in the visibility of the interference fringes when sweeping the energy bias of the edge channel impinging on the interferometer [11, 15, 74].

[10] See Chapter 4 for further details.

- It has been established that the current fluctuations in a co-propagating edge channel dephase the interfering edge channel [12, 23].

- The dephasing length, L_Φ, characterizing the propagation length after which the edge channel looses its quantum coherence has been obtained at $\nu_L = 2$ [14]. The resulting value is surprisingly low, $L_\Phi = 20\mu m$ at $20mK$, which is comparable to those found in diffusive metallic wires [91] where the elastic scattering with impurities increases interaction effects.

Such unexpected observations have yield to an active theoretical debate (e.g. [92, 93, 94, 95]). Even if a spin-charge separation model (3.27) explains the observed multilobe dependence of the interference fringes at $\nu_L = 2$ [93], or a mean-field treatment of the capacitive coupling [96] between edge channels explains the temperature dependence of the dephasing lengths also at $\nu_L = 2$ [23], a single theoretical framework able to explain all the observations is still missing. MZI interferometers are difficult to interpret since they are sensitive to the EC phase coherence and therefore to both inelastic mechanisms and purely dephasing mechanisms, but cannot directly discriminate between them.

3.5 Fractional quantum Hall effect

Before finishing this chapter, we introduce some basic aspects of the fractional quantum Hall effect (FQHE). In this regime, the bulk is incompressible and the low energy physics are also determined by the edge properties. We will see how Coulomb interactions give rise to an incompressible bulk for special values of the filling factory, which can be understood using a variational wave function introduced by Laughlin [34]. We will finally discuss the main differences between IQHE and FQHE edge channels.

3.5.1 Bulk incompressibility

The FQHE is observed for incompletely filled landau levels. Therefore, the Pauli principle alone cannot give rise to a bulk incompressibility. One needs to take into account Coulomb interactions.

Position of the problem

If the temperature and disorder are smaller than the cyclotron or spin gap[11] one can safely ignore any Landau level mixing. Since we are only dealing with a fixed Landau level, all electrons share the same kinetic energy. This constant removed from the problem, one

[11] Correctly renormalized to take into account the exchange energy.

faces a pure Coulomb interaction Hamiltonian in 2D. Traditional perturbative approach are therefore unappropriate.

Energy scales: Since the Coulomb interaction is the only energy scale, the energy scales arising in the FQHE will be proportional to

$$E_C(l_B) = \frac{e^2}{4\pi\epsilon l_B} \tag{3.38}$$

where the magnetic length $l_B = \sqrt{h/eB}$ is the only relevant length in the lowest Landau level. As a consequence, the energy scales arising in the FQHE must have a $\sqrt{B}$ dependence.

Electron hole symmetry: Since the partially filled band is fully flat, and that Coulomb interaction only depends on the charge squared, there is a perfect electron-hole symmetry. Therefore, if we understand the filling factors such as $\nu_L < 0.5$ of the lowest Landau level (LL), we obtain the properties of the $1 - \nu_L > 0.5$ by a charge conjugation transformation.

Laughlin trial wave function

Very soon after the FQHE discovery, Laughlin [34] found a trial many-body wave function that seized all the important aspects of the FQHE in the lowest Landau level. Laughlin's wavefunction reads as:

$$\Psi_q = \prod_{i>j}(z_i - z_j)^q e^{-\sum \frac{z_i^2}{4}} \tag{3.39}$$

where q is a positive integer, and $z = \frac{x+iy}{l_B}$ as in (3.10).

Equation (3.39) is a good trial wave function for the following reasons:

1. The exact wave function of the lowest Landau level must be a linear combination of slater determinants of the lowest Landau level eigenfunctions (see (3.10) in the symmetric gauge). This is the case of (3.39). For $q = 1$, the trial wave function is actually the exact slater determinant of the $\nu_L = 1$ IQHE.

2. Coulomb interactions conserve the angular momenta, and commute with the angular momenta operator. It can be therefore diagonalized in a basis of definite angular momentum. According to (3.39), all electrons in the Laughlin wave function have a definite angular momentum $q\hbar$.

3. The polynomial term in (3.10) nullifies the wave function when two electrons get close to each other, diminishing the repulsive energy.

Ground state properties: The Laughlin wave function describes a ground state having the following properties:

i) Since electrons have Fermi-Dirac statistics, Laughlin wave function must be antisymmetric under particle exchange. This fixes q to be an odd integer, and introduces the "magical" numbers $q \in \mathbf{N}^{*+}$.

ii) Even if it is a variational wavefunction, the variational parameter is found to be fixed by the bulk filling factor $1/q = \nu_L$ [34]. Laughlin wave function is fixed without performing any energy minimization! Moreover, it implies that it is a trial wave function for the following filling fractions of the lowest Landau level:

$$\nu_L = \frac{1}{q} \quad q \in \mathbf{N}^{+*} \tag{3.40}$$

iii) The electronic density is found squaring (3.39) and integrating the particles but one. This results in a uniform electron liquid, so there is no symmetry breaking (one does not expect gapless goldstone modes).

iv) One can find a Hamiltonian for which (3.39) is the exact ground state [97]. Such hamiltonian is essentially a close range interaction hamiltonian, for which a *finite gap* separates the ground state from excited states.

v) Exact diagonalization numerical calculations [98] of the interacting ground state yield to wave function overlaps with (3.39) better than 99%. Laughlin wave function is indeed a very good trial wave function.

Charged excitations: Single particle excitations can be directly obtained from the trial ground state [34]. By multiplying (3.39) by $\prod_i (z_0 - z_i)$ the local density is lowered at z_0. Developing the resulting polynomial part, one finds that this state is still an eigenstate of the angular momentum, and can be seen as a quasi-hole. Adding q quasi-holes at z_0 is equivalent to adding an electron in z_0, since one multiplies the wave function by $\prod_i (z_0 - z_i)^q$. Since the electronic density is uniform , q quasiholes are therefore neutralized by an electron. As a consequence, the resulting quasi-hole charge e^*_{qh} is fractional:

$$e^*_{qh} = \frac{e}{q} = \nu_L e \tag{3.41}$$

where ν_L is the filling factor of the parent ground state. Quasi-electrons are found using charge conjugation $e^*_{qe} = -\nu_L e$. Single-particle excitations carry therefore a fractional charge given by the the fractional filling factor.

Similar arguments link the quasihole/quasielectron densities ($n_{qh/qe}$) to the filling factors around the parent state filling factor $\nu_L = 1/q$:

$$n_{qh} = \frac{1}{2\pi l_B^2}(1 - q\nu_L), \quad \nu_L < 1/q \qquad n_{qe} = \frac{1}{2\pi l_B^2}(q\nu_L - 1), \quad \nu_L > 1/q \tag{3.42}$$

These quasiparticles cost a finite energy $\Delta_{qe/qh}$ [34], and therefore the ground state is *incompressible*. The excitation gap at fixed density $\Delta_{FQHE} = \Delta_{qe} + \Delta_{qh}$, scales with $\sqrt{B}$, and can be computed from the spatial dependence of Laughlin wave function. At filling factor 1/3, the excitation gap is typically found as [62] $\Delta_{1/3} \simeq 0.1\frac{e^2}{4\pi\epsilon l_B} = 3.7[\mathrm{K}/\sqrt{\mathrm{T}}]\sqrt{B}$. However, in real samples, there is a finite extension on the z direction which lowers the Coulomb repulsion, and the magnetic field is finite, so there is some contribution from other Landau levels. Numerical simulations taking into account both effects provide a reasonable agreement with the excitation gaps measured by thermal activated transport in high mobility samples [99].

Hierarchy The trial wave function provides directly the description of the $1/q$ fractions. At filling factors other than $1/q$, the quasiparticles may condense on a Laughlin ground state for quasiparticles [97] instead of electrons. Departing from a parent $1/q$ fraction, this gives rise to a whole hierarchy of similar incompressible states at the filling factors [97]:

$$\nu_L = \frac{2p}{2pq+1} \tag{3.43}$$

This hierarchy describes most of the measured features of Hall bar experiments performed in high mobility samples.

Composite fermions The $q = 1$ hierarchy can be found within a mean field approach due to Jain [100]. In this picture, 2 flux quanta are adiabatically attached to the electrons. Therefore, the resulting composite fermions see a reduced effective mean field $B_{eff} = B - 2n_e\Phi_0 = B - B_{\nu_L=1/2}$. The effective mean field cancels at bulk filling factor 1/2, which can be seen as a Fermi sea of composite fermions[12] [103].

In this approach, the hierarchy of filling factors $\nu_L(p) = \frac{p}{2p+1}$, and its hole conjugated hierarchy $1 - \nu_L(p)$, can be understood as the p^{th} Landau level resulting from the integer quantum Hall effect of composite Fermions. For instance the 1/3 FQHE is the first Landau level of the composite fermions. The corresponding activation gap is therefore:

$$\Delta_{1/3} = \hbar\omega_C^{eff} = \frac{\hbar e B_{eff}}{m_{eff}} \tag{3.44}$$

where m_{eff} is the composite Fermion mass. Since $\Delta_{\nu_L(p)}$ scales as $\sqrt{B}$, the corresponding effective mass m_{eff} has the same scaling according to (3.44).

This bold prediction has been experimentally demonstrated by measuring the Shubnikov-de Hass oscillations of composite fermions around their zero effective magnetic field ($B = B_{\nu_L=1/2}$). The composite fermions effective mass, and even their gyromagnetic factor [102,

[12] Strictly speaking it is not a normal Fermi liquid since its effective mass diverges at 1/2. It has nevertheless a well defined Fermi surface [101, 102].

104] have been measured around $\nu_L = 1/2$[102] and around $\nu_L = 3/2$ [104]. The resulting composite fermion giromagnetic factor is found very close to the electron g factor in GaAs, $g_{eff} = -0.4$.

3.5.2 Fractional edge channels

Since the FQHE is described by a ground state having a finite excitation gap, the low energy physics take place at the edge of the sample as in the IQHE. This is why their transport properties look so similar. However, FQHE edge-channels display some non-trivial correlations due to the Coulomb interactions giving rise to them, and exhibit different tunneling conductances or current fluctuations.

Hydrodynamic approach

Since the the bulk is incompressible, one can apply the same arguments as for the IQHE, and describe the edge excitations as chiral charge density waves [38]. The Hamiltonian describing a single fractional edge-channel $\nu_L = 1/q$ [13] reads :

$$\hat{H} = \frac{\pi v_D}{\nu_L} \int \mathrm{d}x \hat{\rho}^2(x). \tag{3.45}$$

A correct quantization of the density operator due to Wen [38] gives rise to a Kac-Moody algebra:

$$[\hat{\rho}_k, \hat{\rho}_{k'}] = \frac{\nu_L}{2\pi} k \delta_{k+k'} \tag{3.46}$$

$$[\hat{H}, \hat{\rho}_k] = v_D \hat{\rho}_k \tag{3.47}$$

The FQHE edge channel density fields are therefore a physical realization of the Tomonaga-Luttinger model [55] with (chiral) electrons moving in only one direction.

Transport properties

This model is exactly solvable, and has led to many strong predictions for the edge transport properties. We only cite three of them.

1. The two wire conductance at filling factors $\nu_L = 1/q$ are directly given by $G_{\nu_L} = \nu_L \frac{e^2}{h}$ [21] and explain accurately the fractional Hall resistance values measured in Hall bar experiments.

[13] Namely, for the Laughlin ground states $1/q$. In the hierarchies given by (3.43) there can be several edge channels, having fractional or integer interaction parameters and moving upstream or downstream the chirality. They are a consequence of the topological properties of the bulk, and are characterized by the topological matrices introduced by Wen [38].

2. The shot-noise due to the quantum partition of fractional edge channels has been predicted by Kane, Fischer and Matthew [105]. When a scatterer weakly transmits the incoming edge channels, the transmission events correspond to electron hoping and one recovers the poissonian shot-noise of electron tunneling barriers. But when a scatterer is tuned in a weak backscattering limit (its two point conductance is slightly smaller than $\nu_L \frac{e^2}{h}$), the quantum partitioning results from the (weak) backscattering events of the quasiparticles carried by the fractional edge. This results in a poissonian shot-noise renormalized by the quasiparticles charge. This scheme has been first used to measure the charge carried by Laughlin quasiparticles at $q = 3$ [35, 36], demonstrating a fractional charge $e^*_{qe/qh} = \mp\frac{e}{3}$.

3. The algebra (3.46) describes a correlated fluid displaying power law correlation functions [55] for $q \neq 1$. Therefore, the overlap with non-interacting electrons is not perfect and energy dependent. This results in nonlinear tunneling density of states, when injecting an electron to a fractional edge channel. The corresponding differential electron tunneling conductance $G = \partial I/\partial V$ is predicted to be universal and present a power law scaling $G \propto \{V^{1/\nu_L - 1}, T^{1/\nu_L - 1}\}$ [63]. However, the measurements systematically obtain a lower exponent $\alpha < 1/\nu_L - 1$ [106].

Some open questions: FQHE edge channels can be the siege of similar interaction effects as those introduced for the IQHE. For instance the inter-channel interactions for multiple co-propagating edge channels, or to edge reconstruction (changing the energy scale from $\hbar\omega_C$ to Δ_{FQHE}). Moreover, it it expected that for some hole conjugated fractions $0.5 < \nu_L < 1$, antichiral edge channels arise next to chiral ones [41, 107]. Interactions between them can give rise to antichiral neutral modes [42], and such interactions are expected to be important since they are necessary to obtain the correct values for the measured Hall resistances [108]. These interaction effects are non-universal and could be responsible to the systematic deviation between the universal prediction for tunneling conductances and the measured ones. But the debate is still open.

3.6 What are the low energy excitations?

Coulomb interaction can have deep effects on the dynamics of the QHE edge channels. In the IQHE, even the very nature of the edge-excitations can be starkly different from the non-interacting 1DCF. In the FQHE, they can modify the universal properties predicted for ideal edges. However, such effects are intrinsically difficult to track or to interpret with the existing experiments. This question is specially relevant regarding the optical analogy in the IQHE: Interactions between co-propagating edge channels not only may limit the

dephasing length of the 1DCF excitations of an edge channel, but also could yield to collective eigenmodes for which the constrictions used as beam-splitters in the optical analogy do not play this role anymore. On the other hand, the edge reconstruction constitues the basis for the theoretical understanding of the edge electrostatics, and yields to strong predictions by which additional acoustic excitations arise. Such additional modes could result in additional decoherence paths for the 1DCFs, but up to now there is none direct proof of their existence. They could also modify the tunneling density of states of FQHE, and explain the systematic mismatch between predictions and measurements.

The following chapters are devoted to describe and implement a new experimental approach permitting us to perform quantitative energy transport experiments in the IQHE. This new technique will be implemented in the $\nu_L = 2$ IQHE in order to probe its non-equilibrium dynamics and extract new information on the nature of edge excitations.

We will further present a preliminary investigation of the 4/3 FQHE using similar, yet qualitative, experimental approach. Even if this work is not concluded, it has already revealed a coupling between the FQHE edge channels and neutral bulk excitations, yet unidentified.

Chapter 4

Experimental approach

This chapter presents the experimental approach used to probe the low energy physics of the edge-channels arising in the integer quantum hall effect (IQHE). We argue that the inelastic mechanisms at work can be extracted from energy relaxation experiments for a propagative electronic system. We propose a voltage biased constriction, used as a beam splitter, to generate a non-equilibrium situation in an edge-channel. And propose a Coulomb blockaded island, used as an energy filter, to probe the local energy distribution. We finally discuss the link between the electronic energy distribution and heat current for 1D chiral systems.

4.1 What can be learned from energy relaxation experiments?

4.1.1 Testing the inelastic mechanisms at work

When a system is driven out of equilibrium, it can interact with its environment and relax to a local equilibrium. For a propagative system (see Figure 4.1. Top), the inelastic mechanisms taking place along the propagation modify the local energy distribution $f(E, L)$ until a limit $f(E)$ is reached ($\partial f(E, L)/\partial L = 0$). One can then compare the $f(E, L)$ evolution with different theories in order to discriminate between them. Such scheme has been successfully implemented in mesoscopic metallic wires [25, 91]. Even without a theory to test, important information can be obtained from the shape of $f(E)$ using very general arguments (see Figure 4.1) as was done in carbon nanotubes [26].

There are three limit cases where it is easy to link $f(E)$ to the inelastic mechanisms at work:

- **No relaxation:** When the inelastic mechanisms are negligible, the injected $f(E)$ remains the same during the propagation (Figure 4.1. 1).

- **Cold equilibrium:** When the system interacts with thermalized states at temperature T, $f(E)$ will relax towards[1] a cold equilibrium at temperature T. For electronic systems, this is a Fermi function

$$f_F(E) = 1/(1 + \exp[(E - \mu)/k_B T])$$

where μ is the electrochemical potential (Figure 4.1. 3).

- **Hot equilibrium:** Interactions within the electronic system conserve the injected excitation energy and $f(E)$ may relax to a hot electron regime characterized by a hot temperature Fermi function (Figure 4.1. 2, plain red curve). If the system interacts with co-propagating excitations, the injected excitation energy may redistribute between them yielding to a hot electron regime with a smaller hot temperature (but proportional to the square root of the injected power)[2] (Figure 4.1. 2, dotted red curve).

[1] Assuming that the coupling between them is not energy dependent.

[2] Interactions with thermalized states having a vanishing DOS (or in the coupling) at low energies would also yield to a hot electron regime. However, the hot temperature would saturate irrespective to the injected power.

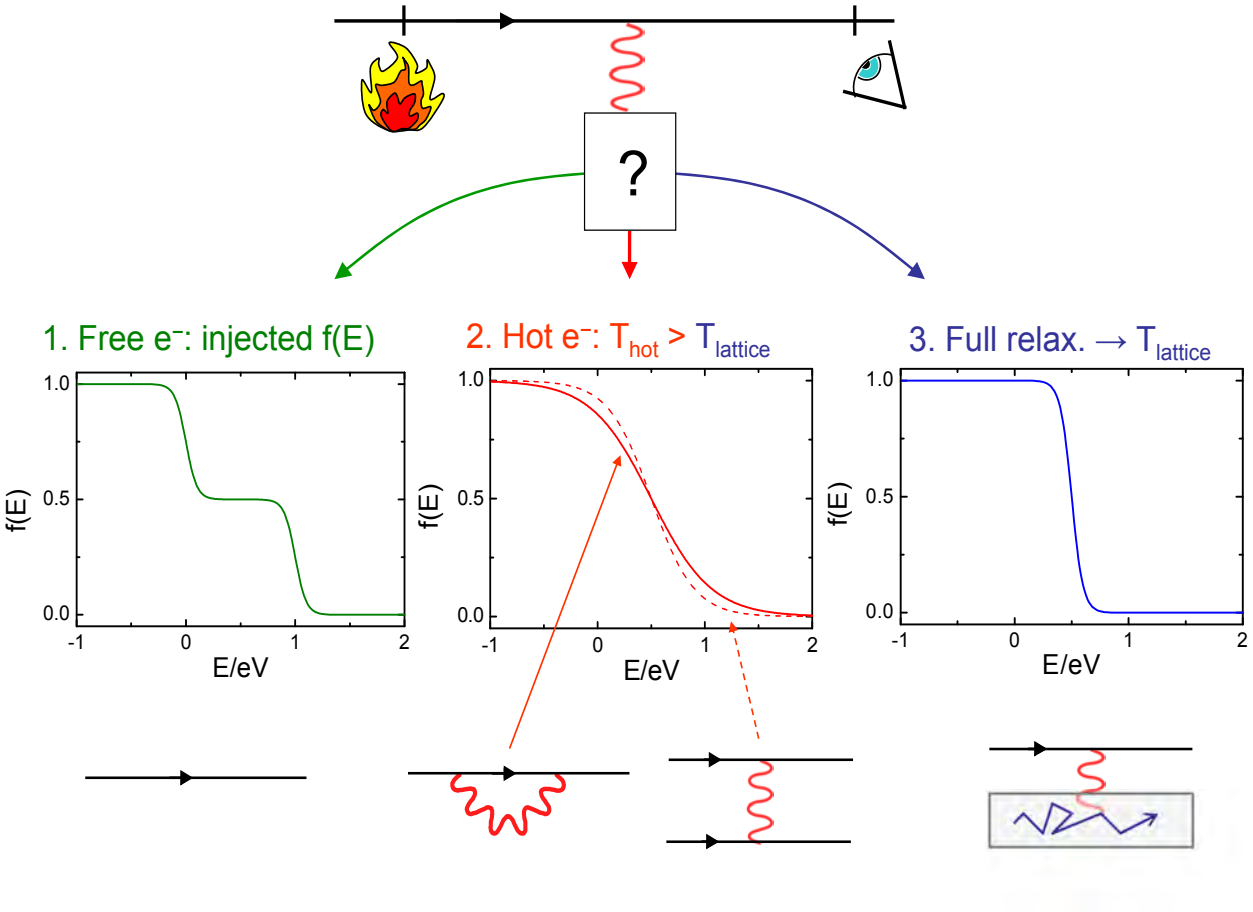

Figure 4.1: **3 simple limits of inelastic mechanisms.** Top: Scheme representing an energy relaxation experiment in a propagative edge-channel. A non-equilibrium edge-channel can relax during its propagation when interacting with its environment (question mark). Middle: Three $f(E)$ limits after propagation corresponding to three distinct situations (schematics at the bottom). 1. Non-interacting system, the injected non-equilibrium $f(E)$, here a non-equilibrium double-step, remains the same. 2. Relaxation due to interactions within the channel (plain red curve) yield to a hot electron regime conserving the injected energy. Relaxation due to interactions with co-propagative excitations (dotted red curve) redistribute the energy between them and yields to a hot electron regime having lost some energy. 3. Relaxation due to interactions with thermalized states yields to a cold $f(E)$, at thermal equilibrium with the base temperature.

4.1.2 Testing the nature of edge-excitations

The inelastic length, L_{inel}, characterizes the length before the local equilibrium $f(E)$ is reached. Since energy exchanges yield to orthogonal states, L_{inel} gives an upper limit to the phase coherence length, L_Φ. Moreover, L_{inel} can be used to derive an upper limit to the quantum lifetime, τ_{inel}, of the probed excitations, when knowing their drift velocity. Indeed an energy uncertainty, ΔE, is associated to the finite lifetime, by the Heisenberg relation:

$$\Delta E \cdot \tau_{inel} \geq \hbar/2.$$

Therefore, τ_{inel} can be used to test if the probed excitations have a well defined energy ($\Delta E/E << 1$).

If a single electronic excitation is injected above the Fermi sea, the corresponding energy uncertainty ΔE is directly the width of the single particle Green function Fourier transform (spectral width) [109]. When injecting a many-particle excited state, as we will do, one can still compare the energy uncertainty to the mean energy of the excited states.

4.2 Tuning an edge-channel out of equilibrium

When applying a bias to an electric system of finite resistance, R, a Joule heating $P_{Joule} = V\,I = V^2/R$ is dissipated. In the IQHE, the Joule heating resulting from the finite two wire resistance cannot be dissipated along the edge channels, since the longitudinal edge channel resistance is null. Therefore, the Joule heating is only dissipated at the reservoirs used to bias the sample [68], which are big enough to maintain a constant temperature. As a result, the edge channels are at local equilibrium with the contacts feeding them, and their resulting $f(E)$ are just Fermi functions at thermal equilibrium.

In order to drive an edge channel out of equilibrium, a voltage biased quantum point contact (QPC) is tuned to partially transmit/reflect the incoming edge channels. This results in a non-equilibrium (non Fermi) $f(E)$ by generating additional electron-hole excitations across the Fermi sea.

4.2.1 Quantum point contacts (QPC) in the regime of the integer quantum Hall effect

QPCs are small tunable constrictions realized in a 2DEG by voltage biased top metallic gates. The gates are capacitively coupled to the 2DEG so that a negative gate voltage depletes the 2DEG beneath and near the gates. In a split-gate geometry, it results in a 2DEG constriction whose width can be tuned by changing the applied gate voltage, V_{QPC}.

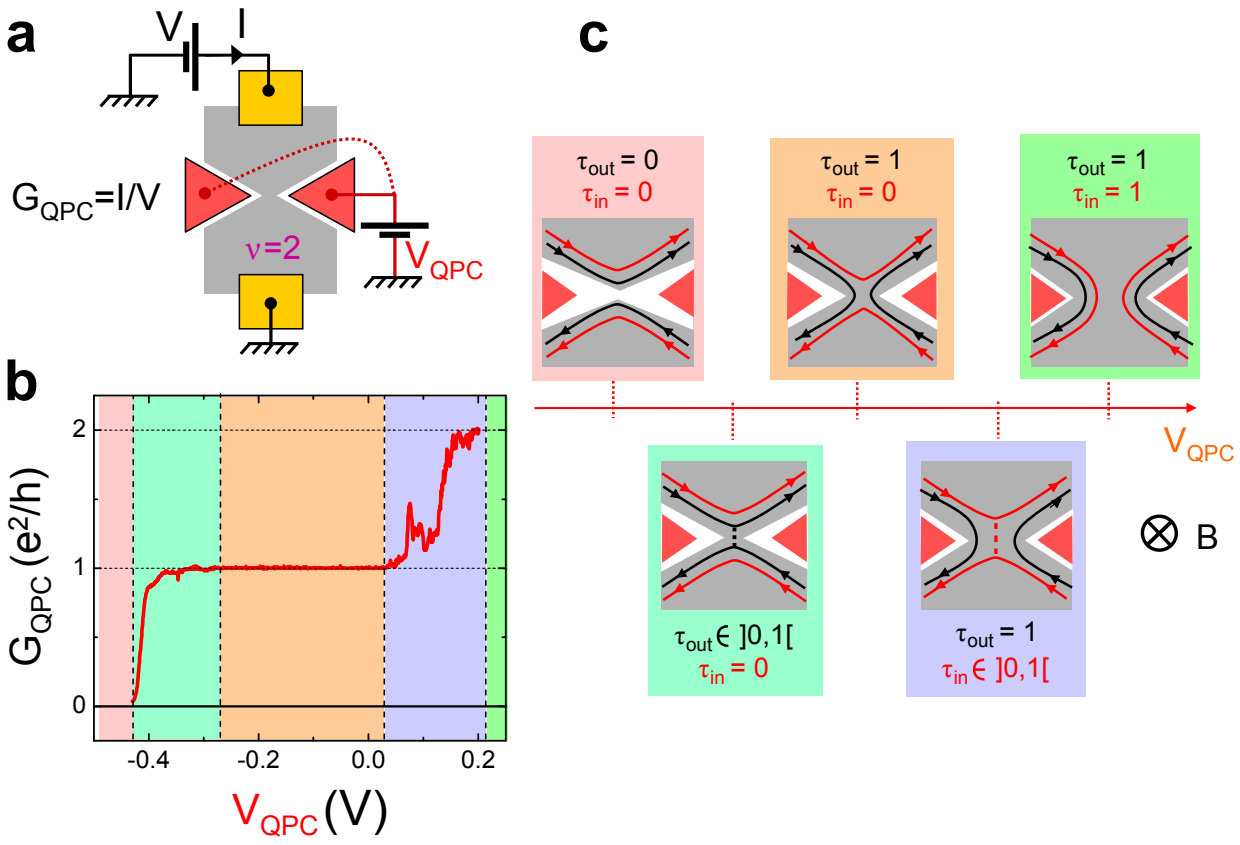

Figure 4.2: **QPCs in the IQHE,** $\nu_L = 2$. **a** Setup defining the two wire conductance of a QPC. **b** Two wire conductance of a QPC as a function of the gate voltage, revealing the transmission coefficients of the edge channels. The colored areas correspond to the situations depicted in c. A conductance measurement yields to the transmission sets for both edge channels. **c** Edge channel transmission through a QPC for different gate voltages yielding to different constriction widths.

In the IQHE, a small constriction will be able to couple the edge channels of opposite edges propagating, in opposite directions. The complete sequence from a wide constriction to a closed one, obtained by changing the gate voltage, is depicted in Figure 4.2.c for $\nu_L = 2$. For a wide enough constriction (large V_{QPC}), both edge channels are completely transmitted. For smaller values of V_{QPC}, the opposite inner edge channels are close enough so that an incoming electron can be either reflected on the opposite inner edge channel or transmitted within the same edge channel. For an even smaller width (V_{QPC}), the inner edge channels become completely reflected, while the outer ones are completely transmitted. For smaller widths (V_{QPC}) the same sequence repeats for the outer edge channels. Summing up, only a pair of opposite edge channels (having the same LL index) can be partially transmitted/reflected at a time, the other pair being fully reflected (or transmitted).

Within the sequential picture (Figure 4.2.c), the transmission coefficients can be obtained

from a simple conductance measurement. Indeed, the multichannel Landauer formula links the two wire conductance to the sum of the QPC transmission coefficients $G_{QPC} = \frac{e^2}{h}\sum_{i=1}^{\nu_L}\tau_i$, and from Figure 4.2.c, only one channel is partially transmitted $0 < \tau < 1$. The differential conductance measured through a QPC at $\nu_L = 2$ is plotted in Figure 4.2.b as a function of V_{QPC}. The conductance plateaus correspond to fully transmitted, or reflected, edge channels as depicted by the color matching schemes in Figure 4.2.c, and the transitions between conductance plateaus correspond to intermediate transmissions between 0 and 1 for a single pair of edge channels (Figure 4.2.c).

4.2.2 Consequences of the spatial separation of the incoming and outgoing channels

In the IQHE, the incoming edge channels are spatially separated from the outgoing ones. Therefore, it is not only possible to distinctly bias the incoming channels but also to distinctly probe the outgoing ones. It is this spacial separation between incoming and outgoing edge channels that is exploited in the optical analogy, where a partially transmitting QPC is the edge channel analogue of a beam-splitter.

We will exploit this spatial separation of the scattering modes to generate a non-equilibrium distribution function in a well defined edge channel that can be distinctly probed.

4.2.3 Energy distribution in the outgoing edge channel in the non-interacting models

The scattering approach goes beyond the conductance predictions, it also predicts the shape of the energy distribution function, $f(E)$, in the outgoing edge channels. The $f(E)$ in the incoming edge channels are Fermi functions, $f_F(E)$, of different electrochemical potentials shifted by the voltage bias $-eV$ applied to the corresponding electrode.

The electrons populating an edge channel, outgoing from the QPC, have the probabilities $\tau/1-\tau$ to be fed by the different sources. The resulting non-equilibrium distribution functions $f_D(E)$ read [28]:

$$f_D(E) \;=\; \tau f_F(E - eV_{D1}) + (1-\tau) f_F(E - eV_{D2}) \tag{4.1}$$

where $eV_{D1/2}$ label the electrochemical potentials of the transmitted/refelected incoming edge channels (see Figure 4.3). In consequence, voltage biased QPCs inject a non-equilibrium energy distribution in the coupled outgoing channels, displaying a double-step like shape (red insets in Figure 4.3). The perfectly transmitted/reflected edge channels maintain the original equilibrium (Fermi) $f(E)$.

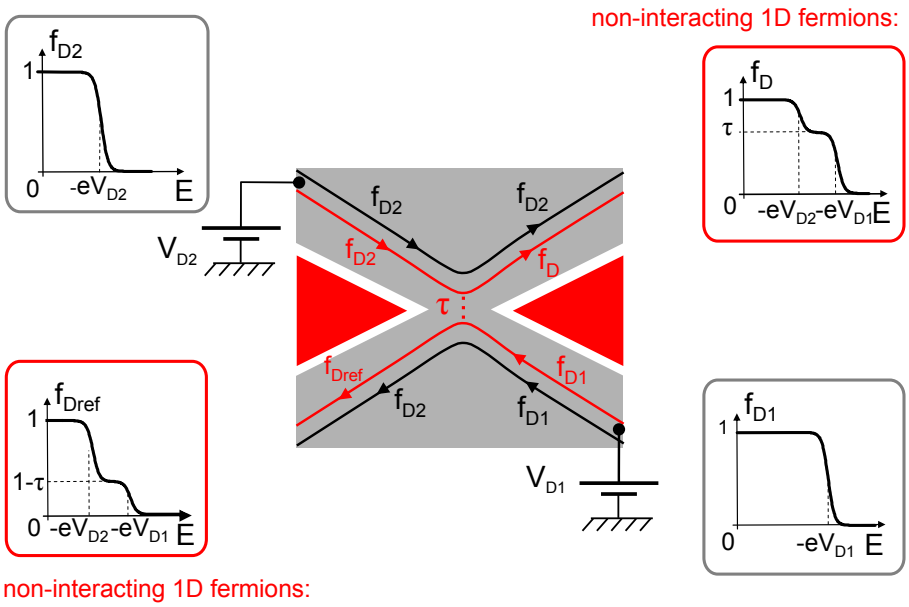

Figure 4.3: **Generating a non-equilibrium $f(E)$ with a voltage biased QPC.** A voltage biased QPC in the $\nu_L = 2$ IQHE set to partially transmit the outer edge channel (red), also fully reflects the inner edge channel (black). Within the scattering approach, outgoing outer edge channels present non-equilibrium $f(E)$s (Top right and bottom left insets), while outgoing inner edge channels present the incoming equilibrium (Fermi) $f(E)$ (top left and bottom right insets).

4.2.4 Energy injected by a QPC

The non-equilibrium $f_D(E)$ contains additional electron-hole excitations across the Fermi sea than those dictated by thermal fluctuations. Neglecting interactions, the energy of electron-hole excitations is simply additive and reads [29]:

$$E_{qp} = \nu \int dE(E-\mu)(f_D(E) - \Theta(\mu - E)) \tag{4.2}$$

where μ is the Fermi energy of the corresponding ground state, ν the density of states per unit length and energy (assumed constant on all relevant energy range), and $\Theta(E)$ is the Heaviside step function.

Neglecting the energy dependence on ν, the electrochemical potential μ of a double-step like $f_D(E)$ (see Figure refChap3noneqQPCs top-right inset) reads:

$$\mu = E_F = -eV_{D2} - e\tau(V_{D1} - V_{D2}). \tag{4.3}$$

Introducing (4.1) and (4.3) in (4.2), one finds that the energy of electron-hole excitations in each outgoing edge channels coupled by the QPC reads:

$$E_{qp} = \frac{\pi^2}{6}\nu(k_BT)^2 + \frac{\tau(1-\tau)}{2}\nu(eV_{D1} - eV_{D2})^2. \tag{4.4}$$

The first term in 4.4 is the equilibrium energy $E_{qp}^{eq} = \frac{\pi^2}{6}\nu(k_BT)^2$ due to the thermal occupations of electron-hole excitations. Therefore, a voltage biased QPC injects additional electron-hole excitations corresponding to an excess energy $E_{qp}^{excess} = E_{qp} - E_{qp}^{eq}$ given by:

$$\frac{E_{qp}^{excess}}{\nu} = \frac{\tau(1-\tau)}{2}(eV_{D1} - eV_{D2})^2. \tag{4.5}$$

4.2.5 Role of additional modes in reconstructed edges

The simple picture provided by the scattering approach, could be modified by the additional modes [20, 84] predicted to arise with smooth confinement potentials(see previous chapter). Indeed, an electron tunneling into the compressible strip could excite also these additional modes. This would yield to a non-linear $I-V$ curve [110, 111] in the low transmission limit $\tau << 1$. in practice, linear I-V characteristics are frequently observed at integer filling factors [106]. Therefore, it is assumed ad-hoc that only the rigid displacement of the compressible edge, namely the standard edge channel charge mode, is excited by tunneling events [112]. However, there are no predictions for intermediate transmissions. Therefore the possible excitations of additional edge modes remains an open question.

One could test the relevance of such modes by measuring the single particle excitations $f(E)$ at the output of a QPC. If additional modes were emitted, the resulting excitations energy E_{qp} would be smaller than (4.4).

4.3 f(E) spectroscopy with a quantum dot as an energy filter

4.3.1 Quantum dots

A quantum dot is a small electron box with a quantized electronic energy spectra. In 2DEGs, planar quantum dots [50] are realized with capacitively coupled top metallic gates (Figure 4.4.a). Applying a negative voltage to the top gates permits to confine an electronic droplet to a size smaller than the electronic wavelength.

Since the early 90's, quantum dots defined in 2DEGs have been extensively investigated. Because these quantum dots are highly tunable, many physical regimes can be realized and probed. To cite a few: coherent manipulation of a single electron spin [113], important Coulomb effects [114], or Kondo physics [115]. Although energy filtering with a quantum dot was demonstrated more than a decade ago [116, 117], we show that quantum dots can be used to extract the full $f(E)$ of the probed electrodes.

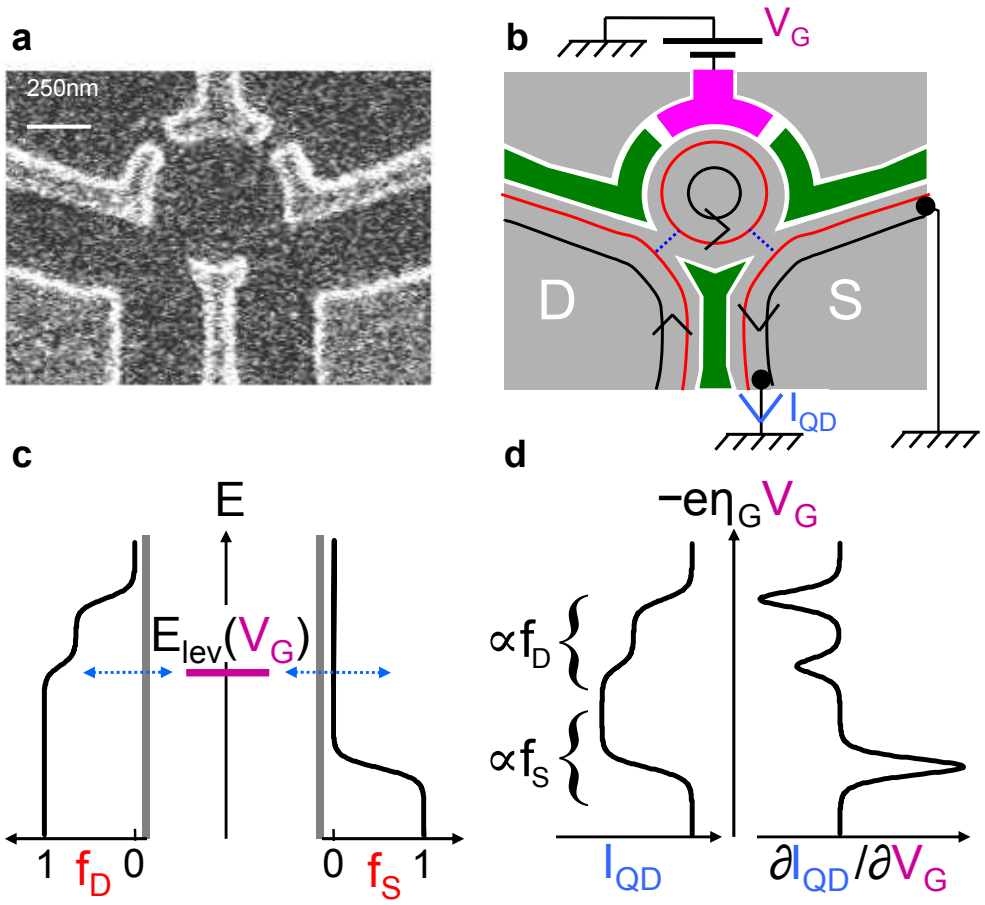

Figure 4.4: **Energy distribution spectroscopy with a quantum dot.** **a** Micrograph of a quantum dot (QD), where top metallic gates appear brighter (gates on the bottom corners are grounded and irrelevant). **b** Scheme of a QD in the IQHE at $\nu_L = 2$. Outer edge channels (EC) on both drain (D) and source (S) sides (red lines) are tunnel coupled to the QD, inner ECs (black lines) are fully reflected. A voltage biased side gate (magenta) is used to sweep the electrostatic energy of the confined states insides the QD. Incoming ECs on the source side are grounded. The current flowing through the QD, I_{QD} is probed in a contact on the bottom right side. **c** Schematic description of the incoming single particle $f(E)$ on both drain and source sides. The tunnel coupled QD has a single energy level, E_{lev}, within the transport window. **d** The current, I_{QD} (transconductance, $\partial I_{QD}/\partial V_G$) is proportional to $f_D - f_S$ ($\partial(f_D - f_S)/\partial E$), when the tunneling density of states is constant.

4.3.2 Resonant tunneling through a discrete level

We first consider the current flowing through a non-degenerate single electronic state, of energy E_{lev}, contacted by two electrodes (see Figure 4.4.c). When the transmission between

the electrodes and the quantum dot are small enough, electrons will tunnel through the quantum dot, one at a time. This is the sequential tunneling regime [45].

We define $P_{0/1}$ as the probability that the discrete level is respectively empty or occupied with one electron. We call $\tau_k^{D/S}$ the transmission probability between the discrete level and the state labeled by k in respectively the drain or source electrode. According to Fermi's golden rule, the mean current flowing from the drain/source electrode to the quantum dot read:

$$I_{D/S} = \frac{e}{h} \int \mathrm{d}\epsilon_k \rho_k^{D/S} \tau_k^{D/S} \{P_0 f_{D/S}(\epsilon_k) - P_1[1 - f_{D/S}(\epsilon_k)]\} \delta(\epsilon_k - E_{lev}) \tag{4.6}$$

where $\rho_k^{D/S}$ is the density of the coupled states at the drain/source electrode, and $f_{D/S}$ the energy distribution on the drain/source electrodes.

Assuming that the tunneling probabilities $\tau_k^{D/S}$ and the densities of states $\rho_k^{D/S}$ are constant, we define the couplings $\Gamma_{D/S} = \rho^{D/S}\tau^{D/S}/h$. The mean current flowing through the quantum dot in the stationary regime is $I_{QD} = I_D = -I_S$, where the second equality follows from charge conservation. Since the discrete level can be either full or empty, we have the second condition $P_0 + P_1 = 1$, and the stationary current can be found as [45]:

$$I_{QD} = e\frac{\Gamma_D \Gamma_S}{\Gamma_D + \Gamma_S}[f_D(E_{lev}) - f_S(E_{lev})]. \tag{4.7}$$

Therefore, the current flowing through the quantum dot is directly proportional to the difference of $f(E)$ on both sides to the quantum dot at the energy of the discrete level.

4.3.3 Energy distribution spectroscopy principle

For a single discrete level coupled in the sequential tunneling regime, we have according to (4.7), for energy independent couplings:

$$I_{QD} = I_{QD}^{max}(f_D(E_{lev}) - f_S(E_{lev})), \tag{4.8}$$

where I_{QD}^{max} encompasses the sample dependent parameters.

Sweeping the probed energy: E_{lev} can be easily swept by applying a voltage bias to a side gate capacitively coupled to the electronic confined state (magenta gate in Figure 4.4.b). E_{lev} is therefore directly proportional to the side gate voltage V_G:

$$E_{lev}(V_G) = E_0 - e\eta_G V_G \tag{4.9}$$

where E_0 is an unimportant constant depending on the quantum dot electrostatics, and η_G is the lever arm characterizing the capacitive coupling.

Resolving the drain/source contributions: In order to resolve the distinct contributions of the drain/source $f_{D/S}(E)$ to I_{QD}, it is sufficient to apply a high enough global electrochemical potential difference between them (situation depicted in Figure 4.4.c). The full $f_{D/S}(E)$ spectroscopy of both drain and source electrodes can be therefore accessed by probing I_{QD} as a function of the single level energy $E_{lev} \propto V_G$, in this situation (which is pictured in Figures 4.4.c and d).

Differential transconductance: In practice, it is useful to measure the differential transconductance $\partial I_{QD}/\partial V_G$. The corresponding raw signal reads:

$$\frac{\partial I_{QD}}{\partial V_G}(V_G) = -e\eta_G I_{QD}^{max}\left[\left(\frac{\partial f_D(E_{lev})}{\partial E_{lev}}\right)_{E_{lev}(V_G)} - \left(\frac{\partial f_S(E_{lev})}{\partial E_{lev}}\right)_{E_{lev}(V_G)}\right], \tag{4.10}$$

where we introduced the definition of the lever arm $\partial E_{lev}/\partial V_G = -e\eta_G$. We have plotted in Figure 4.4.d the differential transconductance resulting from an equilibrium source electrode, and a double-step like $f_D(E)$ in the drain side, whose electrochemical potential has been raised with respect to the source. The non-equilibrium $f_D(E)$ gives rise to a negative double dip, whereas the equilibrium f_S gives rise to a single peak.

Since V_G is the available experimental knob, it is crucial to characterize the proportionality lever arm, η_G. The lever arm can be characterized by probing the resonances in (4.10) at equilibrium for different temperatures. For instance, the contribution of the equilibrium source at temperature T (Fermi function) to (4.10) reads:

$$\frac{\eta_G e^2}{2k_B T}\frac{\Gamma_D\Gamma_S}{\Gamma_D+\Gamma_S}\frac{1}{\cosh^2\left(\frac{E_0-e\eta_G V_G}{k_B T}\right)}, \tag{4.11}$$

whose amplitude scales with $1/T$ and its width at half maximum is about $\Delta V_G = 3.55 k_B T/e\eta_G$. Moreover, single electron effects, arising from the smallness of the quantum dot, can also be exploited to extract η_G.

4.3.4 Single electron electrostatics

The quantum dot must be small in order to have a well defined discrete spectra, in consequence its capacitance, C_Σ, is small too and the corresponding single electron charging energy $E_C = \frac{e^2}{2C_\Sigma}$ is large. In the sequential tunneling regime, the charge in the quantum dot defined by an integer number of electrons, n, can only change by one.

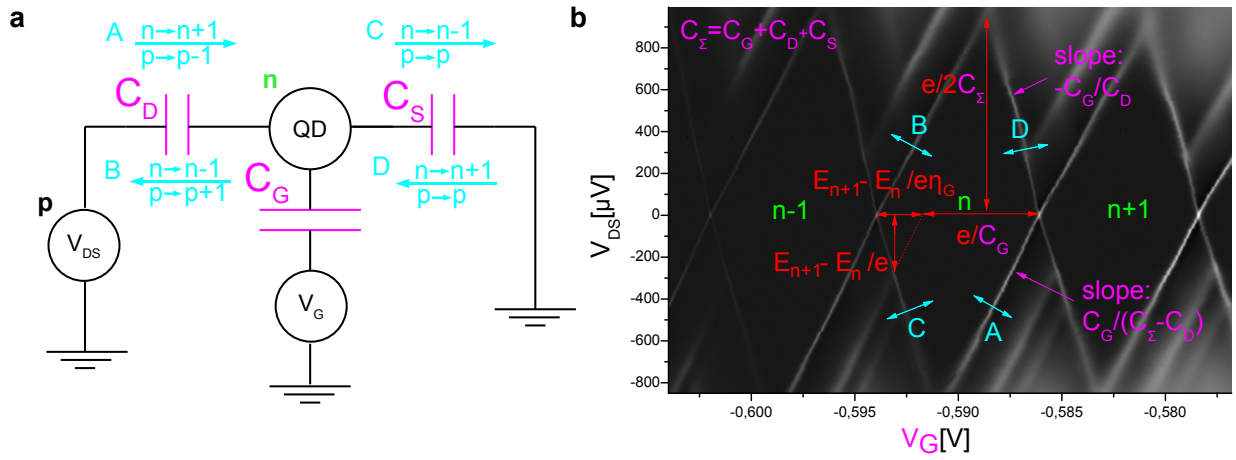

Figure 4.5: **Single electron stability diagram and Coulomb diamonds. a** Electrostatic scheme of a quantum dot, taking into account the voltage source. Electrons inside the quantum dot are labeled by n, electrons furnished by the source by p. 4 different tunneling events (blue) can modify the circuit energy. **b** $\partial I_{QD}/\partial V_{DS}$ conductance plot of a quantum dot, as a function of voltage bias V_{DS} and gate voltage V_G. Three consecutive Coulomb diamonds ($n-1$, n, $n+1$) are shown. The diamonds frontiers are linked to the tunneling processes described in a (blue).The frontiers' slopes depend on the quantum dot capacitances (magenta).

Single charge electron circuit: When n is large, the Coulombic repulsion between the confined electrons can be treated within a mean field approach. In this limit, the electrostatic energy can be taken as independent of n and be encompassed within the capacitance C_Σ. The total energy of the circuit is the sum of the quantum dot electrostatic energy and the work supplied by the voltage source [118]. At zero temperature it reads:

$$E_{n,p}(V_{DS}, V_G) = \frac{(-ne + C_D V_{DS} + C_G V_G)^2}{2C_\Sigma} - peV + \sum_{i=1}^{n} E_i + \epsilon(V_{DS}, V_G), \tag{4.12}$$

where n and p are integers labeling the electron number inside the dot, n, and the electrons supplied by the voltage source, p. $\epsilon(V_{DS}, V_G)$ is a function that only depends on the voltages (and is therefore irrelevant to single electron tunneling) and $\sum_{i=1}^{n} E_i$ is the energy due to

the occupation of the first n^{th} discrete levels inside the quantum dot. The circuit parameters are depicted in the circuit schematic (Figure 4.5), and $C_\Sigma = C_D + C_S + C_G$.

Sequential tunneling regime: In the large charging energy E_C limit, $E_C >> k_\text{B}T$, and moderate biases, $E_C \gtrsim |eV_{DS}|$, only one electron can tunnel at a time [45]. The corresponding tunneling events changing the number n of charges trapped within the dot are pictured in Figure 4.5.a. Electrons can tunnel in the charge degeneracy points, where the n and $n \pm 1$ charge states have the same energy:

$$
\begin{aligned}
&\mathbf{A}: \quad \mathbf{E_{n+1,p-1} - E_{n,p} = 0} \\
&\Rightarrow V_{DS} = \frac{C_G}{C_\Sigma - C_D} V_G - \frac{n + 1/2}{C_\Sigma - C_D} - \frac{C_\Sigma [E(n+1) - E(n)]}{e(C_\Sigma - C_D)} \\
&\mathbf{B}: \quad \mathbf{E_{n-1,p+1} - E_{n,p} = 0} \\
&\Rightarrow V_{DS} = \frac{C_G}{C_\Sigma - C_D} V_G - \frac{n - 1/2}{C_\Sigma - C_D} - \frac{C_\Sigma [E(n) - E(n-1)]}{e(C_\Sigma - C_D)} \\
&\mathbf{C}: \quad \mathbf{E_{n-1,p} - E_{n,p} = 0} \\
&\Rightarrow V_{DS} = -\frac{C_G}{C_D} V_G + \frac{n - 1/2}{C_D} + \frac{C_\Sigma [E(n) - E(n-1)]}{eC_D} \\
&\mathbf{D}: \quad \mathbf{E_{n+1,p} - E_{n,p} = 0} \\
&\Rightarrow V_{DS} = -\frac{C_G}{C_D} V_G + \frac{n + 1/2}{C_D} + \frac{C_\Sigma [E(n+1) - E(n)]}{eC_D}
\end{aligned}
\tag{4.13}
$$

Inside these frontiers of the (V_G, V_{DS}) plane, the current is blocked since there is not enough available energy to afford the single electron charging energy. Therefore n is fixed. Outside these frontiers, the current is constant (if the couplings $\Gamma_{D/S}$ are energy independent) until an excited (electron or hole) discrete state enters in the transport window. The corresponding degeneracy points are found replacing $E(n \pm 1) - E(n)$ by $E(n \pm 2) - E(n)$ in the precedent conditions. The resulting stability diagram can be probed by plotting the conductance of the quantum dot as a function of V_G and V_{DS}. It can be used to characterize the quantum dot electrostatic parameters as highlighted in Figure 4.5.b.

Lever arm and stability diagram: The side gate lever arm is simply related to the quantum dot capacitances [118] and can be found from the slopes of the Coulomb diamonds $s_{neg} = -C_G/C_D$ and $s_{pos} = C_G/(C_\Sigma - C_D)$:

$$\eta_G = \frac{C_G}{C_D + C_S + C_G} \tag{4.14}$$

$$= (s_{pos}^{-1} - s_{neg}^{-1})^{-1} \tag{4.15}$$

Selecting the probed electrodes: The processes A and B in Figure 4.12 only couple to the drain electrode, while C and D to the source electrode. Since A and B (C and D) yield

to a positive (negative) slope in the (V_G, V_{DS}) plane, one can easily identify what electrode is probed by the quantum dot for a given (V_G, V_{DS}). Negative slopes in the stability diagram probe $f_D(E)$, while negative slopes probe $f_S(E)$

4.3.5 Sequential tunneling through multiple discrete levels

When multiple discrete levels lie in the transport window, non-intuitive dynamical effects can arise. In the sequential tunneling regime, the strong Coulomb energy impedes changes of more than one electron. Therefore, the many electron paths due to the many levels do not add in parallel. The resulting expression for the mean current can be starkly different [119] from the one found for a single level (4.8), which *limits its application range*. Moreover, dynamical effects can modify the sharp features of the stability diagrams plots at finite temperature, see appendix for more details. Both effects will *limit the experimental accuracy on the lever arm experimental calibration*, when using the simple single level model (4.8).

The general problem of non symmetric multiple levels with energy dependent couplings (A.1) and (A.4) can be handled numerically [119], when the couplings to the discrete levels and their energy spacings are known. However, using this scheme to probe an unknown $f(E)$ would need an independent calibration of the couplings which cannot be done by DC measurements alone, and complicates the analysis. In order to probe an unknown $f(E)$, it is therefore desirable use a quantum dot with a single active level within the transport window needed to probe the relevant energy scales.

4.3.6 Metallic islands

A quantum dot is in the Coulomb blockaded "metallic" regime when the discrete level spacing is small, $E_{i+1} - E_i << k_{\mathrm{B}}T$, but the single electron charging energy is large $E_C > k_{\mathrm{B}}T$. This regime can be pictured as the continuous limit of the multiple level quantum dot $E_{i+1} - E_i << 1$. The current is therefore blocked inside the Coulomb diamonds provided by the conditions (4.13). But since the density of states in the confined region is continuous, the current also evolves continuously outside the charge degeneracy limits (4.13). For energy independent couplings at zero temperature, and assuming full relaxation between tunneling events, I-V curves are linear for biases outside (4.13) [45]. These systems can be used as a high pass energy filter to probe the electrodes electronic excitations at energies higher than (4.13). Therefore, the energy cut-off for the probed excitations can be swept with the gate voltage V_G.

4.4 Energy transport in 1D systems and $f(E)$

This section details the strong link between the single particle $f(E)$, and the energy currents carried by 1D chiral non-interacting fermions (1DCFs). We show, that the knowledge of $f(E)$ fully defines the energy current [24], using the very same arguments that yield to the universal transport results for ballistic transport [57].

The chiral energy current, J_{qp}, carried by non-interacting electron-hole excitations in a chiral 1D channel reads [24]:

$$J_{qp} = \int \mathrm{d}E v(E)\nu(E)(E-\mu)(f(E)-\Theta(\mu-E)), \tag{4.16}$$

where introduced the drift velocity $v(E)$, the density of states per unit length ν, the Fermi energy μ and the Heaviside step function $\Theta(E)$. Since in 1D systems, the product $v(E)\nu(E) = 1/h$ is universal and energy independent, the energy flow is fully characterized by $f(E)$:

$$J_{qp} = \frac{1}{h}\int \mathrm{d}E(E-\mu)(f(E)-\Theta(\mu-E)) \tag{4.17}$$

which is directly contained within $f(E)$.

It is useful to define the non-equilibrium temperature T_{qp} as the temperature needed to obtain an equilibrium chiral energy current equal to J_{qp}:

$$J_{qp} = \frac{1}{h}\int \mathrm{d}E(E-\mu)(f_{\mathrm{F}}(E,T_{qp},\mu)-\Theta(\mu-E)) \tag{4.18}$$

$$\tag{4.19}$$

where we introduced the Fermi function $f_{\mathrm{F}}(E,T,\mu)$, describing the electron-hole occupations at temperature T and Fermi energy μ. Since the integral in (4.18) gives $\frac{\pi^2}{6}(k_B T_{qp})^2$ [24, 29] one obtains:

$$J_{qp} = \frac{\pi^2}{6h}(k_{\mathrm{B}}T_{qp})^2. \tag{4.20}$$

The non-equilibrium temperature, T_{qp}, is therefore a (quadratic[3]) measure of the energy current carried by the electron-hole excitations. According to (4.17) and (4.20), it can be directly extracted from $f(E)$ without sample dependent parameters. Moreover, it has a direct physical interpretation, when the non-equilibrium $f(E)$ describes a broadband excited state and the density of states is energy independent. In this limit, the whole excitation energy is roughly $\nu(k_{\mathrm{B}}T_{qp})^2$ while the number of excited states is roughly $\nu k_{\mathrm{B}}T_{qp}$. Therefore, $k_{\mathrm{B}}T_{qp}$ is roughly the mean energy of the electronic excitations.

[3]But since the excitation energy is always positive, it is a well defined bijective measure.

Chapter 5

Non-equilibrium edge-channel spectroscopy

5.1 Experimental demonstration in the $\nu_L = 2$ quantum Hall effect

This section reproduces an article we have published in Nature Physics [1] where we demonstrate experimentally the non-equilibrium edge channel spectroscopy. For this purpose, we have probed the energy distribution $f(E)$ generated by a voltage biased quantum point contact (QPC) after a short propagation path. These measurements, also permit to discard that the predicted additional [20] modes of reconstructed edges [17] are not emitted by voltage biased QPCs at finite transmissions.

LETTERS
PUBLISHED ONLINE: 25 OCTOBER 2009 | DOI: 10.1038/NPHYS1429
nature physics

Non-equilibrium edge-channel spectroscopy in the integer quantum Hall regime

C. Altimiras, H. le Sueur, U. Gennser, A. Cavanna, D. Mailly and F. Pierre*

The study of heat transport has the potential to reveal new insights into the physics of mesoscopic systems. This is especially true of those that show the integer quantum Hall effect[1], in which the robust quantization of Hall currents limits the amount of information that can be obtained from charge transport alone[2]. As a consequence, our understanding of gapless edge excitations in these systems is incomplete. Effective edge-state theory describes them as prototypical one-dimensional chiral fermions[3,4]—a simple picture that explains a large body of observations[5] and suggests the use of quantum point contacts as electronic beam splitters to explore a variety of quantum mechanical phenomena[6–8]. However, this picture is in apparent disagreement with the prevailing theoretical framework, which predicts in most situations[9] extra gapless edge modes[10]. Here, we present a spectroscopic technique that addresses the question of whether some of the injected energy is captured by the predicted extra states, by probing the distribution function and energy flow in an edge channel operated out-of-equilibrium. Our results show it is not the case and therefore that regarding energy transport, quantum point contacts do indeed behave as optical beam splitters. This demonstrates a useful new tool for heat transport and out-of-equilibrium experiments.

The integer quantum Hall effect, discovered nearly thirty years ago[1], has recently experienced a strong revival driven by milestone experiments towards quantum information with edge states[7,11,12]. Beyond Hall currents, new phenomena have emerged that were unexpected within the free one-dimensional chiral fermions (1DCFs) model. The ongoing debate triggered by electronic Mach–Zehnder interferometer experiments[7,13–15] vividly illustrates the gaps in our understanding. Coulomb interaction is seen as the key ingredient. In addition to its most striking repercussion, the fractional quantum Hall effect[16], the edge reconstruction turns out to have deep implications on edge excitations. This phenomenon results from the competition between Coulomb interaction that tends to spread the electronic fluid, and the confinement potential: as the latter gets smoother, the non-interacting edge becomes unstable[17]. Theory predicts new branches of gapless electronic excitations in reconstructed edges[10,18], which breaks the mapping of an edge channel onto 1DCFs and, possibly, the promising quantum optics analogy. For most edges realized in semiconductor heterojunctions (except by cleaved edge overgrowth[19]), edge reconstruction results in wide compressible edge channels separated by narrow incompressible strips[9] and the new excited states are overall neutral internal charge oscillations across the edge channels' width[10].

In practice, the predicted extra neutral modes are transparent to Hall currents. More surprisingly, a linear I–V characteristic is frequently observed for tunnel contacts (different behaviours were also reported, for example, ref. 20), whereas a nonlinear characteristic is predicted[21–23]. This contradiction is resolved by assuming *ad-hoc* that only rigid displacements of compressible edge channels are excited by tunnel events, and not internal excitations[10,21,22,24]. The rigid displacement model arguably relies on the overriding strength of Coulomb interaction that tends to orthogonalize bare tunnelling electrons and correlated electronic fluids[24]. However, the above argument does not hold at arbitrary transmission probabilities, where several electron processes occur. Therefore, the role of predicted internal excitations has to be determined experimentally. The present work provides such a test. An edge channel is driven out-of-equilibrium with a quantum point contact (QPC) of arbitrary transmission, possibly exciting internal modes. A short distance away, the resulting energy distribution $f(E)$ is measured with a tunnel-coupled quantum dot expected to probe only rigid displacement excitations, hereafter called quasiparticles. Consequently, the amount of energy injected into internal modes at the QPC would appear as an energy loss in $f(E)$.

Measurements of the energy distribution in mesoscopic devices were first carried out in 1997 on metallic circuits using a superconducting tunnel probe[25]. In two-dimensional electron-gas systems, non-Fermi energy distributions could not be measured because transferring the techniques developed for metal circuits is technically challenging (although hot electrons have been detected, for example, ref. 26). Regarding the quantum Hall regime, the state of the art is the very recent qualitative probe of heating[27]. Here, we demonstrate that $f(E)$ can be fully extracted from the tunnel current across a quantum dot. In the sequential tunnelling regime, the discrete electronic levels in a quantum dot behave as energy filters[28], as previously demonstrated with double quantum dots[29]. Assuming a single active quantum-dot level of energy E_{lev}, and ignoring the energy dependence of tunnel rates and tunnelling density of states in the electrodes, the quantum-dot current reads

$$I_{\mathrm{QD}} = I_{\mathrm{QD}}^{\max}(f_{\mathrm{S}}(E_{\mathrm{lev}}) - f_{\mathrm{D}}(E_{\mathrm{lev}})) \qquad (1)$$

where the subscript S (D) refers to the source (drain) electrode; $f_{\mathrm{S,D}}$ are the corresponding energy distributions and $I_{\mathrm{QD}}^{\max}$ is the maximum quantum-dot current. In practice, $f_{\mathrm{S,D}}$ are obtained separately by applying a large enough source–drain voltage (Fig. 1a,b) and the probed energy $E_{\mathrm{lev}} = E_0 - e\eta_{\mathrm{G}}V_{\mathrm{G}}$ is swept using a capacitively coupled gate biased at V_{G}, with η_{G} being the gate voltage-to-energy lever arm and E_0 an offset. Raw data $\partial I_{\mathrm{QD}}/\partial V_{\mathrm{G}}$ measured by lock-in techniques are proportional to $\partial f_{\mathrm{D,S}}(E)/\partial E$.

A tunable non-Fermi energy distribution is generated in an edge channel with a voltage-biased QPC. Similar set-ups were used previously to create imbalanced electron populations between co-propagating edge channels[30], each characterized by a cold Fermi distribution. Only in a very recent experiment[27] was an edge

CNRS, Laboratoire de Photonique et de Nanostructures (LPN)—Phynano team, route de Nozay, 91460 Marcoussis, France.
*e-mail: frederic.pierre@lpn.cnrs.fr.

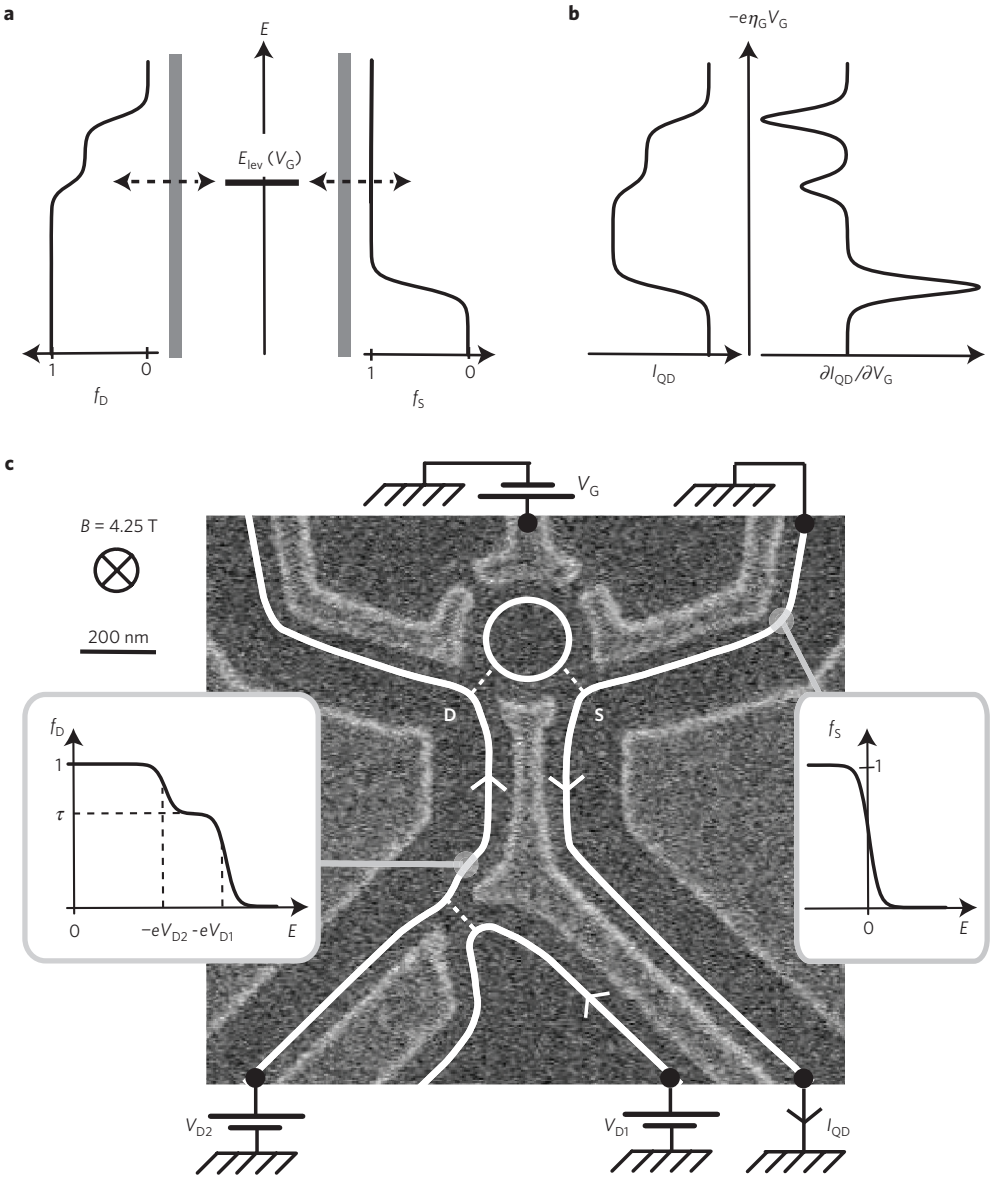

Figure 1 | Experimental implementation of non-equilibrium edge-channel spectroscopy. a, Schematic description of the energy distributions' $f_{D,S}(E)$ spectroscopy with a single active electronic level of tunable energy $E_{lev}(V_G)$ in the quantum dot. **b**, The current I_{QD} ($\partial I_{QD}/\partial V_G$) is proportional to $f_S(E)-f_D(E)$ ($\partial(f_S(E)-f_D(E))/\partial E$) ignoring variations in tunnel rates and tunnelling density of states. **c**, Electron-beam micrograph of the sample. Surface metal gates appear brighter. Electronic excitations propagate anticlockwise along two edge channels of the quantum Hall regime. The outer edge channel (solid white lines) is partly transmitted (dashed lines) across the QPC and the quantum dot. The inner edge channel (not shown) is always reflected. The QPC is used to drive out-of-equilibrium the drain outer edge channel. Gates partly covered by the insets are grounded and do not influence the electron paths. Left inset: Non-interacting electrons prediction for $f_D(E)$ in the outer edge channel at the output of the QPC. Right inset: Equilibrium Fermi function f_S emitted by a cold ground.

channel heated up. Beyond heating, $f(E)$ is here controllably tuned out-of-equilibrium. Let us consider one edge channel and assume it can be mapped onto non-interacting 1DCFs. According to the scattering approach[5], the energy distribution at the output of a QPC of transmission τ is a tunable double step (Fig. 1c, left inset)

$$f_D(E) = \tau f_{D1}(E) + (1-\tau) f_{D2}(E) \qquad (2)$$

where f_{D1} (f_{D2}) is the equilibrium Fermi distribution function in the partially transmitted (reflected) incoming edge channel of electrochemical potential shifted by eV_{D1} (eV_{D2}). In the presence of edge reconstruction, the above energy distribution applies to the quasiparticles if internal modes are not excited at the QPC. On the other hand, if internal modes are excited, there are no theoretical predictions because a QPC is very difficult to treat non-perturbatively in their natural bosonic formalism.

The sample shown in Fig. 1c was tailored in a two-dimensional electron gas realized in a GaAs/Ga(Al)As heterojunction, set to filling factor two and measured in a dilution refrigerator of base temperature 30 mK. The experiment detailed here focuses on the outer edge channel represented as a white line. The inner edge channel (not shown) is fully reflected by the QPC and the quantum dot. We checked that charge tunnelling between edge channels is negligible along the 0.8 μm propagation length from the QPC to the quantum dot.

We first carry out a standard nonlinear quantum-dot characterization[28] (Fig. 2, top left inset). The two large signal stripes

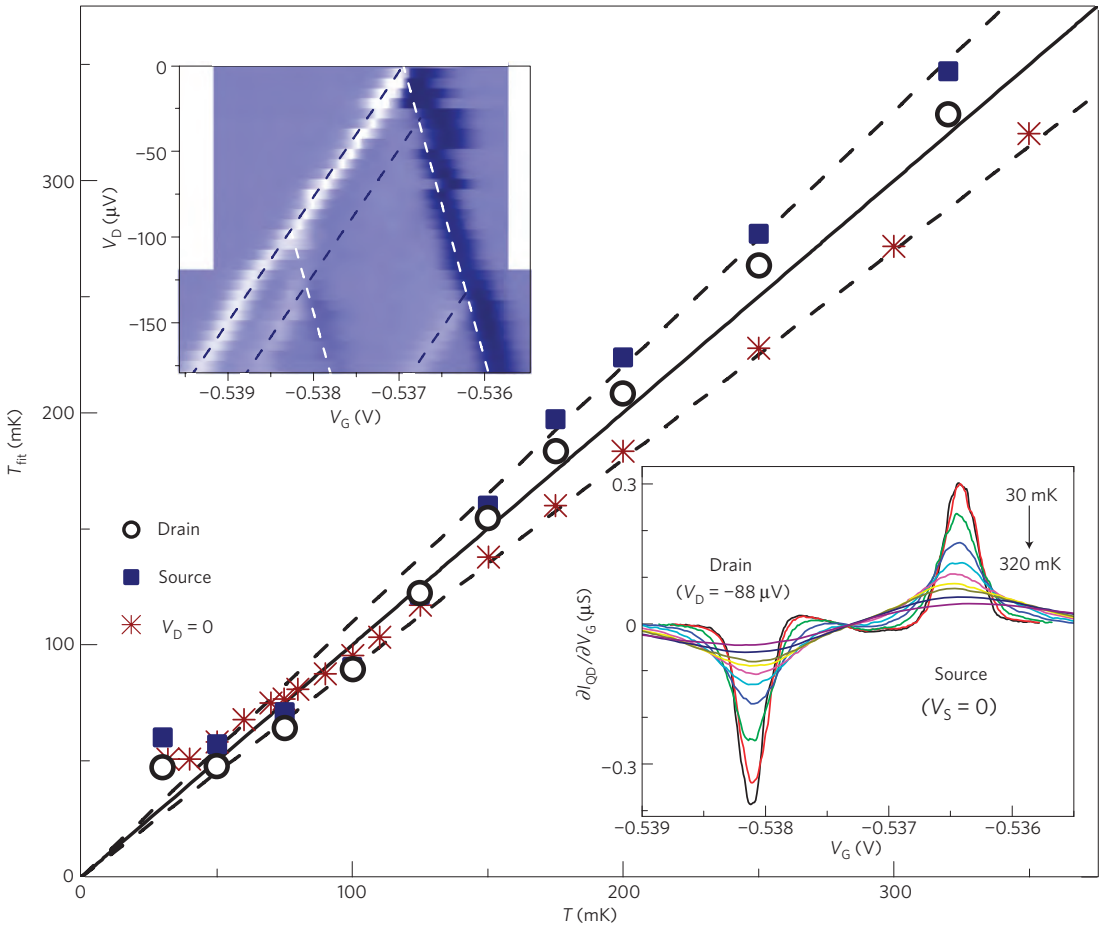

Figure 2 | Equilibrium edge-channel spectroscopy and quantum-dot characterization. Temperatures T_{fit} are obtained by fitting the quantum-dot drain dip and quantum-dot source peak in $\partial I_{QD}/\partial V_G$ (respectively, left and right peaks in bottom right inset), and from the single $\partial I_{QD}/\partial V_D$ peak at $V_D = 0$ (raw data not shown) with $\eta_G = 0.057$. We assumed a single active level in the quantum dot and Fermi energy distributions in source and drain. Errors within $T \pm 10\%$ are enclosed between the dashed lines. Top left inset: Surface plot of $\partial I_{QD}/\partial V_G$ (negative is brighter, positive darker) measured at $T = 30$ mK for an outer (inner) drain edge channel biased at V_D (−88 μV). The intense stripes' slopes yield $\eta_G = 0.052 \pm 9\%$. The enclosed dashed lines outline the small contributions of other electronic levels. Bottom right inset: $\partial I_{QD}/\partial V_G$ measured at $V_D - V_S = -88$ μV for several temperatures.

are frontiers of consecutive Coulomb diamonds and are accounted for by a single active quantum-dot level. Small contributions of three extra levels of relative energies $\{-95, 30, 130\}$ μeV are also visible. The lever arm extracted from the stripes' slopes is $\eta_G \simeq 0.052 \pm 9\%$.

Then, we test the spectroscopy with known Fermi functions by measuring $\partial I_{QD}/\partial V_G(V_G)$ at $V_{D1} = V_{D2} = -88$ μV for several temperatures (Fig. 2, bottom right inset). By fitting these data with equation (1) using Fermi functions, we extract a fit temperature scaled by the lever arm T_{fit}/η_G. The value $\eta_G = 0.057$, compatible with the nonlinear quantum-dot characterization, is found to reproduce best the mixing-chamber temperature T with T_{fit}. The drain and source fit temperatures are shown in Fig. 2, together with T_{fit} obtained using the standard procedure[28] from $\partial I_{QD}/\partial V_D(V_G)$ at $V_D \simeq 0$. We find deviations mostly within ±10% (dashed lines in Fig. 2) except for a saturation at $T_{fit} \approx 50$ mK possibly owing to a higher electronic temperature. In the following, we use $\eta_G = 0.057$ obtained here in the same experimental configuration as to measure unknown $f(E)$s.

Electrons are now driven out-of-equilibrium in the drain outer edge channel. In the following, the electrode D2 and the inner drain edge channel are voltage biased at $V_{D2} = -88$ μV and the source edge channels are emitted by a cold ground.

First, the bias voltage across the QPC is set to $\delta V_D \equiv V_{D1} - V_{D2} = 36$ μV and its conductance $G_{QPC} = \tau e^2/h$ is tuned by applying V_{QPC} to the bottom left gate in Fig. 1c (see Fig. 3a). Note that at 30 mK, we find the transmission τ is constant within 2% with the QPC voltage bias below 36 μV. Typical sweeps $\partial I_{QD}/\partial V_G(V_G)$ and the corresponding $f_D(E)$ are shown in Fig. 3b and e, respectively. The quantum-dot drain negative contribution transforms from a single dip at $\tau = \{0, 1\}$ into two dips separated by a fixed gate voltage and with relative weights that evolve monotonously with $\tau \in]0, 1[$. The solid lines are fits with equation (2) using for $f_{D1,D2}$ two Fermi functions shifted by a fixed energy and weighted by the factors τ_{fit} and $1 - \tau_{fit}$. The values of τ_{fit} are found to deviate by less than 0.03 from the measured transmission τ (Fig. 3c), in accurate agreement with the free 1DCF model. The plus symbols in Fig. 3 correspond to data obtained in a second cooldown.

In a second step, the QPC transmission is fixed to $\tau \approx 0.5$ and the bias voltage δV_D is changed. Typical raw data are shown in Fig. 4a. These were obtained in a third cooldown with a quantum dot renewed by the thermal cycle showing no signs of extra quantum-dot levels in the probed energy range. The single dip in the quantum-dot drain contribution (bright) at $\delta V_D = 0$ splits into two similar dips that are separated by a gate-voltage difference proportional to δV_D. In contrast, the quantum-dot source peak (dark) is mostly unchanged but slowly drifts parallel to one quantum-dot drain dip owing to the capacitive coupling between the drain and the quantum dot. In the first cooldown, V_{D1} was kept within $[-106, -34]$ μV to minimize

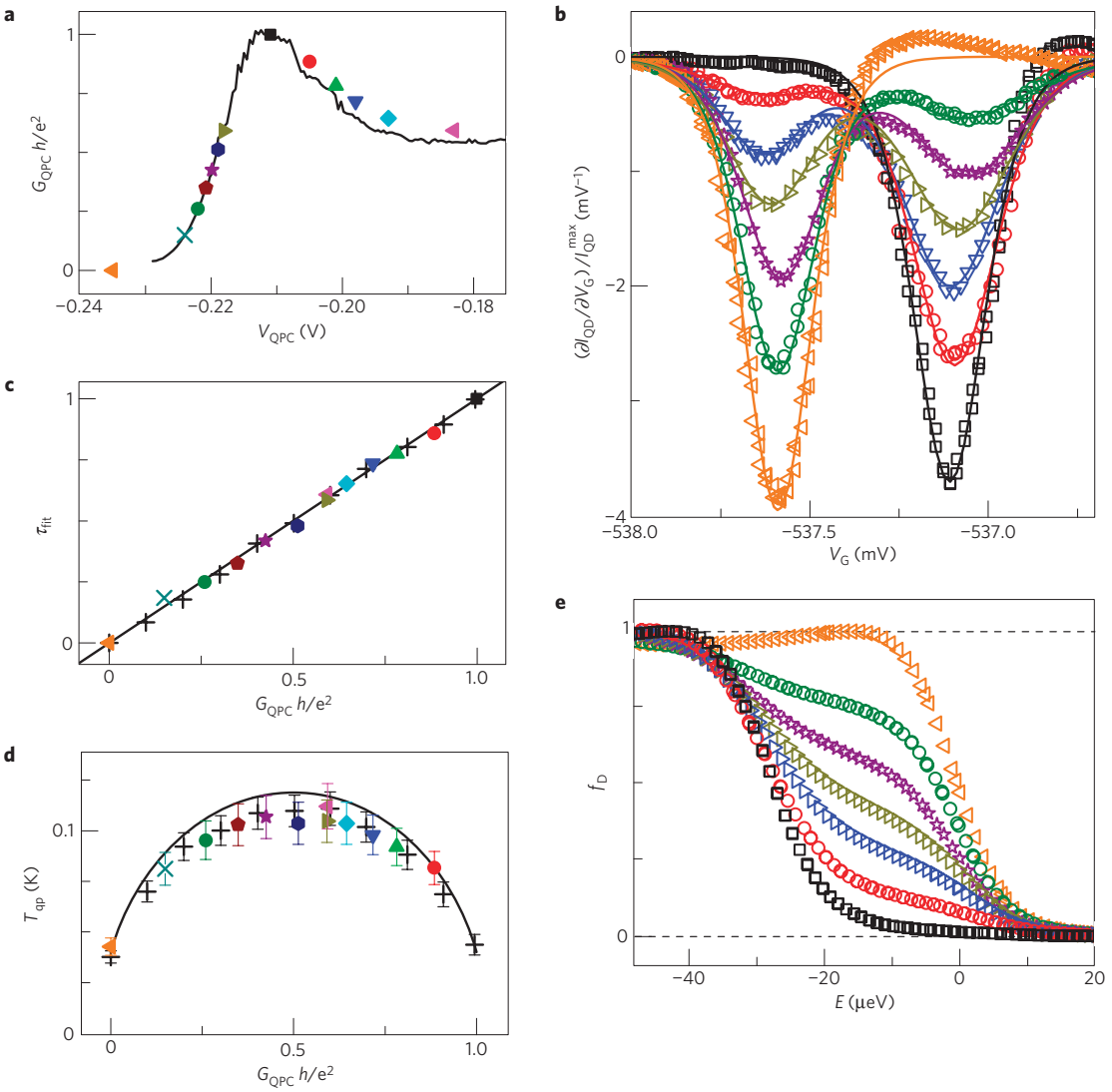

Figure 3 | Spectroscopy of an edge channel tuned out-of-equilibrium with the conductance of a QPC. The QPC's voltage bias is here fixed to $\delta V_D \equiv V_{D1} - V_{D2} = 36\,\mu V$. The data shown as plus symbols in **c**,**d** were obtained in a second cooldown with a renewed $\eta_G = 0.059 \pm 7\%$. **a**, Measured G_{QPC} versus V_{QPC} applied to the lower left metal gate in Fig. 1c. The symbols are data points obtained during the corresponding edge-channel spectroscopy. The solid line was measured earlier with $\delta V_D = 0$. **b**, Measured $\partial I_{QD}/\partial V_G$ (symbols) for the quantum-dot drain contribution (data have been aligned in V_G and normalized to I_{QD}^{max}). The two dips correspond to a double-step energy distribution $f_D(E)$. **c**, The symbols are τ_{fit} obtained from fits of the data (solid lines in **b**) assuming $f_D(E)$ is the weighted sum of two Fermi functions. We find an accurate agreement with the non-interacting 1DCF model prediction $\tau_{fit} = G_{QPC}h/e^2$. **d**, Generalized non-equilibrium temperature (symbols, see text) extracted from the data and theoretical prediction for free 1DCFs (solid line). The error bars are dominated by uncertainties on η_G. **e**, Energy distributions obtained by integrating the data in **b**.

complications related to extra quantum-dot levels (lower bound) and to ensure well-separated source and drain contributions (upper bound). The symbols in Fig. 4b and e are, respectively, data and extracted $f_D(E)$ for the quantum-dot drain contribution at $\delta V_D = \{-18, 0, 18, 27, 36, 45, 54\}\,\mu V$ and $\tau = 0.58$. The solid lines in Fig. 4b are fits with equation (2) using the measured τ and for $f_{D1,D2}$ two Fermi functions shifted in energy by the fit parameter $-e\eta_G\delta V_G$. The resulting $\eta_G\delta V_G$ are plotted as symbols versus δV_D in Fig. 4c. Those obtained in the third cooldown are shown as purple star symbols using the renewed lever arm $\eta_G = 0.062$. We find $\eta_G\delta V_G \simeq \delta V_D$ as expected from the non-interacting 1DCF model. Deviations are always smaller than 8 μV (5 μV) for the first (third) cooldown, a reasonable agreement regarding uncertainties in η_G of ±10% (±5%).

In the two experiments above, we found the measured quasiparticle $f(E)$s verify predictions of the scattering approach. To establish the QPC/beam-splitter analogy one also needs to demonstrate that internal edge-channel modes are not excited. A direct test consists of extracting the quasiparticle heat current J_E^{qp} from the data, and comparing it with the full edge-excitations' heat current J_E obtained from power-balance considerations (see Supplementary Information for details):

$$J_E(T=0) = \frac{(e\delta V_D)^2}{2h}\tau(1-\tau)$$

The cancellation $\nu v = 1/h$ of velocity (v) and density of states per unit length and energy (ν) that applies to the 1DCF quasiparticles permits us to obtain J_E^{qp} from the measured $f(E)$ without any sample-specific parameters:

$$J_E^{qp} = \frac{1}{h}\int (E-\mu)(f(E) - \theta(\mu - E))\,dE \qquad (3)$$

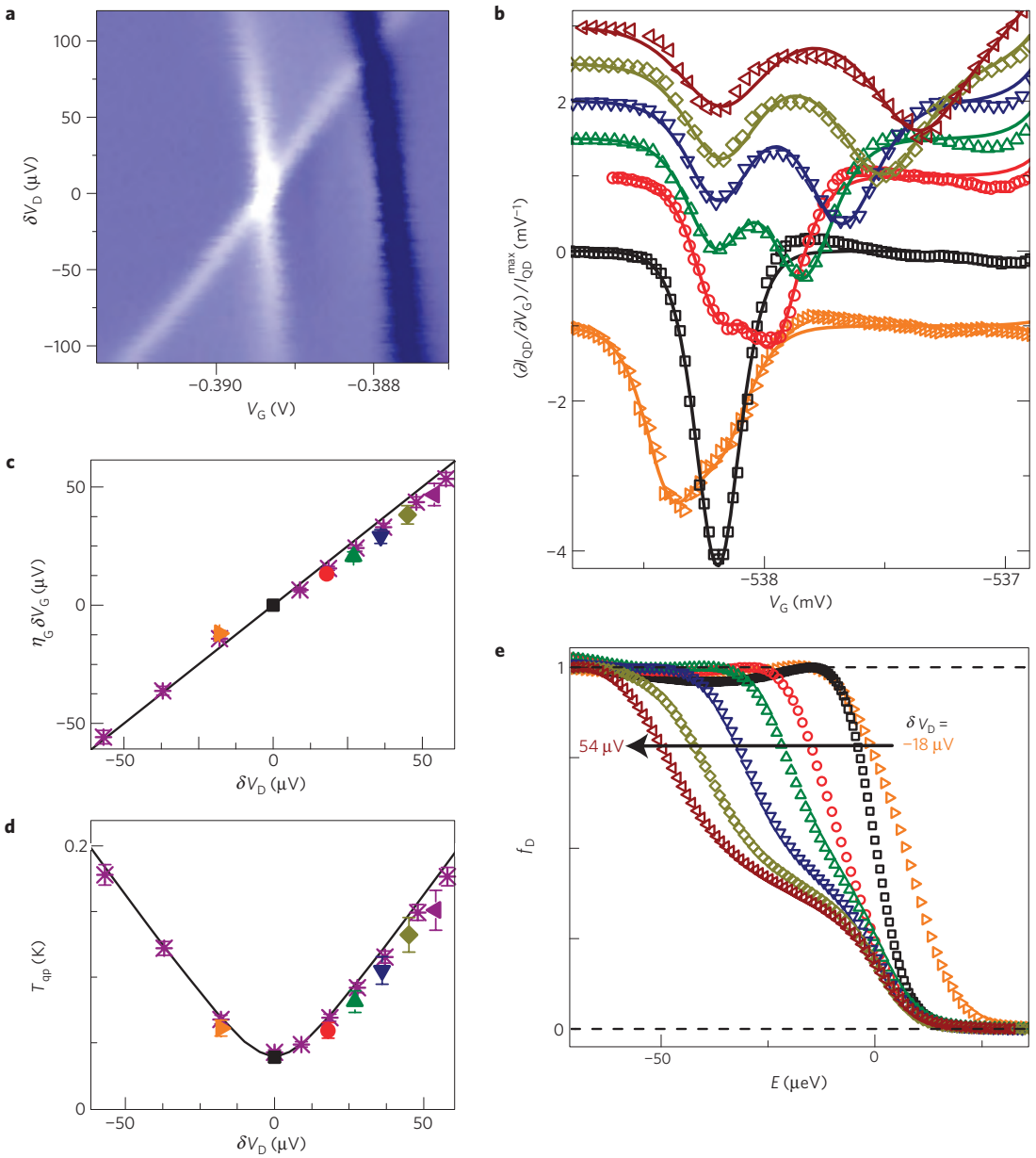

Figure 4 | Spectroscopy of an edge channel tuned out-of-equilibrium with the voltage across a QPC. The QPC's conductance is here fixed to $G_{QPC} \approx 0.5e^2/h$. The data in **a** and the purple star symbols in **c** and **d** were obtained in a third cooldown with a renewed $\eta_G = 0.062 \pm 5\%$. **a**, Surface plot of $\partial I_{QD}/\partial V_G(\delta V_D, V_G)$. The quantum-dot drain contribution (brighter) splits into two similar dips separated by a gate-voltage difference proportional to δV_D. **b**, Measured $\partial I_{QD}/\partial V_G$ (symbols) for the quantum-dot drain contribution. Data have been shifted vertically for clarity, and horizontally to align the peak corresponding to the fixed potential V_{D2}. The solid lines are fits assuming $f_D(E)$ is the weighted sum of two Fermi functions. **c**, The symbols are the fit parameters $\eta_G \delta V_G$. The solid line is the prediction for non-interacting 1DCFs. **d**, Generalized non-equilibrium temperature (symbols) and theoretical prediction for free 1DCFs (solid line). The good data–prediction agreement demonstrates that internal modes are not excited at the QPC within our experimental accuracy. **e**, Energy distributions obtained by integrating the data in **b**.

where μ is the electrochemical potential and $\theta(E)$ is the step function. Consequently, we measure quantitatively the quasiparticle heat current. The result of this procedure is shown as symbols in Figs 3d and 4d using the generalized non-equilibrium temperature $T_{qp} \equiv \sqrt{6hJ_E^{qp}/\pi k_B}$ together with the prediction $T_{1DCF} = \sqrt{T^2 + \tau(1-\tau)3(e\delta V_D/\pi k_B)^2}$ if none of the injected power is carried on by internal modes (solid lines). We find a good agreement $T_{qp} \simeq T_{1DCF}$ without fitting parameters and essentially in or close to error bars. Hence, within our experimental accuracy, the propagative internal modes do not contribute to heat transport and therefore are not excited. Note that the relatively small observed deviations are cooldown dependent, which suggests that the quantum-dot detector is responsible for these deviations. Indeed, the data can be more accurately accounted for including a second active quantum-dot level (see Supplementary Information). Last, preliminary data show a significant energy redistribution with the inner edge channel for propagations longer than 2 μm in the probed energy range. Therefore, the observed small discrepancies could also result from the finite 0.8 μm propagation length.

Overall, we demonstrate that QPCs in the quantum Hall regime are tunable electrical beam splitters for one-dimensional fermions, that is, rigid edge-channel displacements, (1) by comparing the energy distribution at a QPC output with predictions of the scattering approach[5], and (2) by showing that internal edge-channel

modes are not excited. This does not only rule out non-ideal QPC behaviours to explain the surprising phenomena observed on electronic Mach–Zehnder interferometers[7,13–15], it also establishes a solid ground for future quantum information applications with edge states. Finally, an essential part of this work is the demonstration of a new technique to measure the fundamental energy-distribution function. It makes $f(E)$ accessible for most systems where quantum dots can be realized. We expect it will trigger many new experiments dealing with heat transport, out-of-equilibrium physics and quantum decoherence.

Received 15 April 2009; accepted 9 September 2009; published online 25 October 2009

References

1. Klitzing, K. v., Dorda, G. & Pepper, M. New method for high-accuracy determination of the fine-structure constant based on quantized hall resistance. *Phys. Rev. Lett.* **45,** 494–497 (1980).
2. Fertig, H. A. A view from the edge. *Physics* **2,** 15 (2009).
3. Halperin, B. I. Quantized Hall conductance, current-carrying edge states, and the existence of extended states in a two-dimensional disordered potential. *Phys. Rev. B* **25,** 2185–2190 (1982).
4. Wen, X.-G. Theory of the edges states in fractional quantum Hall effects. *Int. J. Mod. Phys B* **6,** 1711–1762 (1992).
5. Büttiker, M. Absence of backscattering in the quantum Hall effect in multiprobe conductors. *Phys. Rev. B* **38,** 9375–9389 (1988).
6. Ionicioiu, R., Amaratunga, G. & Udrea, F. Quantum computation with ballistic electrons. *Int. J. Mod. Phys. B* **15,** 125–133 (2001).
7. Ji, Y. *et al.* An electronic Mach–Zehnder interferometer. *Nature* **422,** 415–418 (2003).
8. Samuelsson, P., Sukhorukov, E. V. & Büttiker, M. Two-particle Aharonov–Bohm effect and entanglement in the electronic Hanbury Brown–Twiss setup. *Phys. Rev. Lett.* **92,** 026805 (2004).
9. Chklovskii, D. B., Shklovskii, B. I. & Glazman, L. I. Electrostatics of edge channels. *Phys. Rev. B* **46,** 4026–4034 (1992).
10. Aleiner, I. L. & Glazman, L. I. Novel edge excitations of two-dimensional electron liquid in a magnetic field. *Phys. Rev. Lett.* **72,** 2935–2938 (1994).
11. Fève, G. *et al.* An on-demand coherent single-electron source. *Science* **316,** 1169–1172 (2007).
12. Neder, I. *et al.* Interference between two indistinguishable electrons from independent sources. *Nature* **448,** 333–337 (2007).
13. Roulleau, P. *et al.* Direct measurement of the coherence length of edge states in the integer quantum Hall regime. *Phys. Rev. Lett.* **100,** 126802 (2008).
14. Litvin, L. V., Tranitz, H. P., Wegscheider, W. & Strunk, C. Decoherence and single electron charging in an electronic Mach–Zehnder interferometer. *Phys. Rev. B* **75,** 033315 (2007).
15. Bieri, E. *et al.* Finite-bias visibility dependence in an electronic Mach–Zehnder interferometer. *Phys. Rev. B* **79,** 245324 (2009).
16. Tsui, D. C., Stormer, H. L. & Gossard, A. C. Two-dimensional magnetotransport in the extreme quantum limit. *Phys. Rev. Lett.* **48,** 1559–1562 (1982).
17. MacDonald, A. H., Yang, S. R. E. & Johnson, M. D. Quantum dots in strong magnetic fields: Stability criteria for the maximum density droplet. *Aust. J. Phys.* **46,** 345–358 (1993).
18. Chamon, C. de C. & Wen, X. G. Sharp and smooth boundaries of quantum Hall liquids. *Phys. Rev. B* **49,** 8227–8241 (1994).
19. Chang, A. M., Pfeiffer, L. N. & West, K. W. Observation of chiral Luttinger behavior in electron tunneling into fractional quantum Hall edges. *Phys. Rev. Lett.* **77,** 2538–2541 (1996).
20. Roddaro, S., Pellegrini, V., Beltram, F., Pfeiffer, L. N. & West, K. W. Particle-hole symmetric Luttinger liquids in a quantum Hall circuit. *Phys. Rev. Lett.* **95,** 156804 (2005).
21. Conti, S. & Vignale, G. Collective modes and electronic spectral function in smooth edges of quantum Hall systems. *Phys. Rev. B* **54,** R14309–R14312 (1996).
22. Han, J. H. & Thouless, D. J. Dynamics of compressible edge and bosonization. *Phys. Rev. B* **55,** R1926–R1929 (1997).
23. Yang, K. Field theoretical description of quantum Hall edge reconstruction. *Phys. Rev. Lett.* **91,** 036802 (2003).
24. Zülicke, U. & MacDonald, A. H. Periphery deformations and tunneling at correlated quantum Hall edges. *Phys. Rev. B* **60,** 1837–1841 (1999).
25. Pothier, H., Guéron, S., Birge, N. O., Esteve, D. & Devoret, M. H. Energy distribution function of quasiparticles in mesoscopic wires. *Phys. Rev. Lett.* **79,** 3490–3493 (1997).
26. Heiblum, M., Nathan, M. I., Thomas, D. C. & Knoedler, C. M. Direct observation of ballistic transport in GaAs. *Phys. Rev. Lett.* **55,** 2200–2203 (1985).
27. Granger, G., Eisenstein, J. P. & Reno, J. L. Observation of chiral heat transport in the quantum Hall regime. *Phys. Rev. Lett.* **102,** 086803 (2009).
28. Kouwenhoven, L. P. *et al.* in *Mesoscopic Electron Transport Series E: Applied Sciences* Vol. 345 (eds Sohn, L. L., Kouwenhoven, L. P. & Schön, G.) 105–214 (Kluwer Academic, 1997).
29. van der Vaart, N. C. *et al.* Resonant tunneling through two discrete energy states. *Phys. Rev. Lett.* **74,** 4702–4705 (1995).
30. van Wees, B. J. *et al.* Anomalous integer quantum Hall effect in the ballistic regime with quantum point contacts. *Phys. Rev. Lett.* **62,** 1181–1184 (1989).

Acknowledgements

The authors gratefully acknowledge discussions with M. Buttiker, P. Degiovanni, C. Glattli, P. Joyez, A. H. MacDonald, F. Portier, H. Pothier, P. Roche and G. Vignale. This work was supported by the ANR (ANR-05-NANO-028-03).

Author contributions

Experimental work and data analysis: C.A., H.l.S. and F.P.; nanofabrication: C.A. and F.P. with input from D.M.; heterojunction growth: A.C. and U.G.; theoretical analysis and manuscript preparation: F.P. with input from coauthors; project planning and supervision: F.P.

Additional information

The authors declare no competing financial interests. Supplementary information accompanies this paper on www.nature.com/naturephysics. Reprints and permissions information is available online at http://npg.nature.com/reprintsandpermissions. Correspondence and requests for materials should be addressed to F.P.

5.1.1 Ruling out additional modes emission by QPCs

The difference of the measured $f_D(E)$ with the non-interacting prediction are small, but it is however difficult to rule out, from a direct comparison, the influence of the additional modes [20] predicted in reconstructed edge channels [17]. Nevertheless, the power carried by the probed 1DCFs can be extracted from the measured $f_D(E)$ (article equation 3) and very general power balance considerations can rule out any energy leak from the probed 1DCFs (up to our incertitude in the extracted T_{qp}).

Figure 5.1 recapitulates the logical structure that permits us to discard the emission of energy towards additional modes by the voltage biased QPCs.

Heat flow injected by the QPC

From general power balance considerations, we obtain the heat flow injected at the QPC output. We consider the simplified circuit at filling factor 1 (one edge channel) shown in Figure 5.2.

The total power $P = VI = V^2\tau e^2/h$, with τ the quantum point contact transmission, dissipated in the source (S) and drain (D) electrodes (nearby the hot spots shown as red areas in Figure 5.2, see e.g. [68]), can be decomposed into two contributions [24]:

$$P = V^2\tau e^2/h = P_{\delta\mu} + P_{edge}. \tag{5.1}$$

The first one ($P_{\delta\mu}$) corresponds to the energy injected into the drain and source electrodes due to the electrochemical potential difference $\delta\mu$ between the electrodes and the corresponding incoming edge. The edge electrochemical potential is defined as that of a floating electrode inserted in its path (Figure 5.3), in the spirit of the 'measurement reservoir' model (see e.g. [24]). At unity transmission $\tau = 1$, this 'electrochemical power' is the only contribution to the dissipated power $P_{\delta\mu}(\tau = 1) = P = (eV)^2/h$. In general, the electrochemical power injected by each edge in its output electrode is $(\delta\mu)^2/2h$ and gives the same information as the DC current. At arbitrary transmission τ, the electrochemical potential difference at the input of both the source and drain electrodes is $|\delta\mu| = \tau e|V|$ and one finds:

$$P_{\delta\mu} = (\tau eV)^2/h. \tag{5.2}$$

The second contribution $P_{edge} = 2(J_E^{in} - J_E^{out})$ corresponds to the difference between the incoming J_E^{in} and outgoing J_E^{out} energy current carried on by *all edge excitations, even by the predicted additional modes*, respectively in and out the corresponding electrode. The factor two here accounts for the two electrodes. Note that P_{edge} corresponds to the amount of energy that would be absorbed by two floating reservoirs inserted along the path of the edges incoming to source and drain electrodes and thermalized at the same temperature as

Working hypothesis

H1: Tunnel contacts do not couple to internal EC modes

H2: "Quasiparticles" can be described as 1D chiral fermions (quasiparticles = rigid EC displacement excitations)

H3: Internal EC modes are propagative

Implications of hypothesis

H1 $\Rightarrow$ **I1**: f(E) measured with a tunnel coupled QD is that of quasiparticles

H2 + I1 $\Rightarrow$ **I2**: Quasiparticle heat current J_E^{qp} given by Eq. 4

H3 $\Rightarrow$ **I3**: If $\exists$ excited internal states at QPC then this implies excess J_E^{qp} < excess edge excitations heat current J_E

Experimental observations

E1: Measured f(E) complies with Eq. 1

E2 (using **I2**): Excess J_E^{qp} ~ excess J_E

Conclusions

E1 + I1 $\Rightarrow$ **C1**: Quasiparticles f(E) obey the scattering model of QPCs

E2 + I3 $\Rightarrow$ **C2**: Internal modes are not excited at the QPC

C1 + C2 $\Rightarrow$ **C3**: Regarding energy transport, QPCs in int. QHR are electrical analogues for quasiparticles of tunable beam splitters

Figure 5.1: **Logical structure of the arguments ruling out the emission of additional reconstructed edge modes by voltage biased QPCs.** The hypothesis H1 relies on the linear I-V characteristic for tunnel contacts that is mostly observed (including here) in the integer quantum Hall effect [20, 84, 110, 111, 112]. The hypothesis H2 holds for each edge channel's 1DCFs quasiparticle branch according to [20, 38, 84, 110]. Note that the hydrodynamic approach considers specifically rigid edge channel displacements [38]. The hypothesis H3 is a prediction for internal edge channel modes [19, 20, 84, 110].

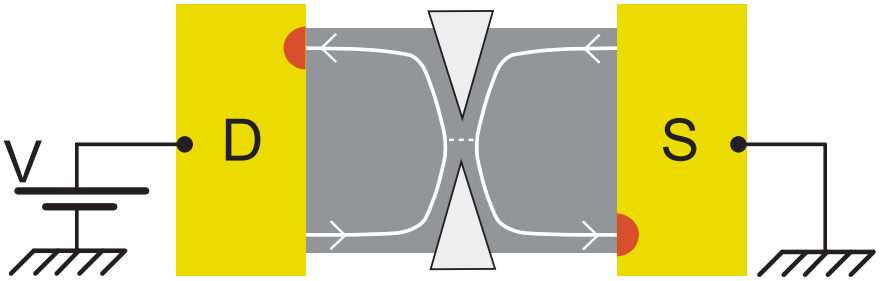

Figure 5.2: **Simplified schematic circuit used for power balance considerations.** The Landau level filling factor is here set to one. The edge channel is shown as a white line and the propagation direction of electronic excitations is indicated by an arrow. The dissipated power $V^2 G_{QPC} = V^2 \tau e^2/h$ is injected into the source (S) and drain (D) electrodes by the corresponding incoming edge channels.

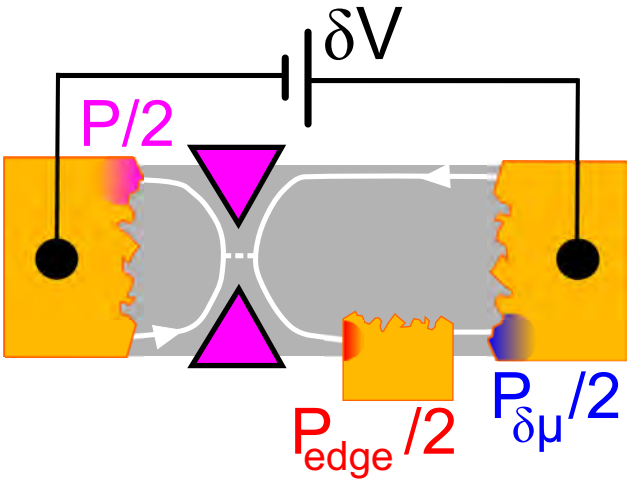

Figure 5.3: **Electrochemical power $P_{\delta\mu}$ and excitation power P_{edge} injected by a QPC.** Scheme of setup permitting to distinguish the electrochemical power $P_{\delta\mu}$ from the excitation power P_{edge}. The excitation power P_{edge} is dissipated by all ohmic contacts, even a floating contact (red spot the bottom floating contact). The electrochemical power $P_{\delta\mu}$ is dissipated only in contacts having a different electrochemical potential from the incoming edge channel (blue spot in the right ohmic contact).

their corresponding electrode (figure 5.3). This contribution vanishes at zero transmission and also at unity transmission, as long as the drain and source electrodes are at the same temperature since in that case $J_E^{in} = J_E^{out}$. At intermediate transmissions, P_{edge} is obtained from Equations 5.1 and 5.2:

$$P_{edge} = P - P_{\delta\mu} = \tau(1-\tau)\frac{(e\delta V_D)^2}{h}. \tag{5.3}$$

This last quantity is identical to the one obtained from the double step distribution function

(using the J_E^{in} following from Equation 4.1 and article Equation 3, and the equilibrium heat current $J_E^{out} = \frac{\pi^2}{6h}(k_B T)^2$). Therefore the observed agreement between measured quasiparticle $f(E)$ and the prediction of Equation 4.1 already implies that the excess energy current is carried on by quasiparticles and not internal edge channel modes. However, the most straightforward evidence is to extract the energy current directly from the measured quasiparticle energy distribution function. The predicted internal modes being propagative, the observation that excess quasiparticle energy current and full excess edge current are similar (see article Figures 3d and 4d) implies internal edge channel states are not excited by a voltage biased QPC of arbitrary transmission within our experimental accuracy on T_{qp}.

5.1.2 Supplementary Data

In this section we present supplementary data regarding other cooldowns, that were not shown in the article. Since the quantum dot is renewed by the thermal cyclings (see Figure 5.4), these additional measurements test the robustness of our findings. Indeed, Article Figures 3.d and 4.d show that the excess temperatures (and therefore quasiparticle heat currents) measured for different cooldowns (and renewed quantum dots) match within our experimental uncertainty. Different cooldowns also agree in the transmission and QPC biases used to fit our experimental data, shown in Article figures 3.c and 4.c, with the non-interacting formula given by Article Equation 2.

For completeness, we show here:

1. The quantum dot calibration data in Figure 5.4.

2. Data obtained in cooldown two with a fixed bias voltage $\delta V_D = -36$ μV and several values of the QPC conductance are shown in Figure 5.5. These data correspond to symbols (+) in article Figure 3.c and d. Note that here V_{D2} and the inner edge channel potential are set to -129 μV.

3. Data obtained in cooldown three with a fixed QPC conductance $G_{QPC} \simeq 0.5e^2/h$ and several values of the QPC voltage bias δV_D are shown in Figure 5.6. As for cooldown one, V_{D2} and the inner edge channel potential are here fixed to -88 μV.

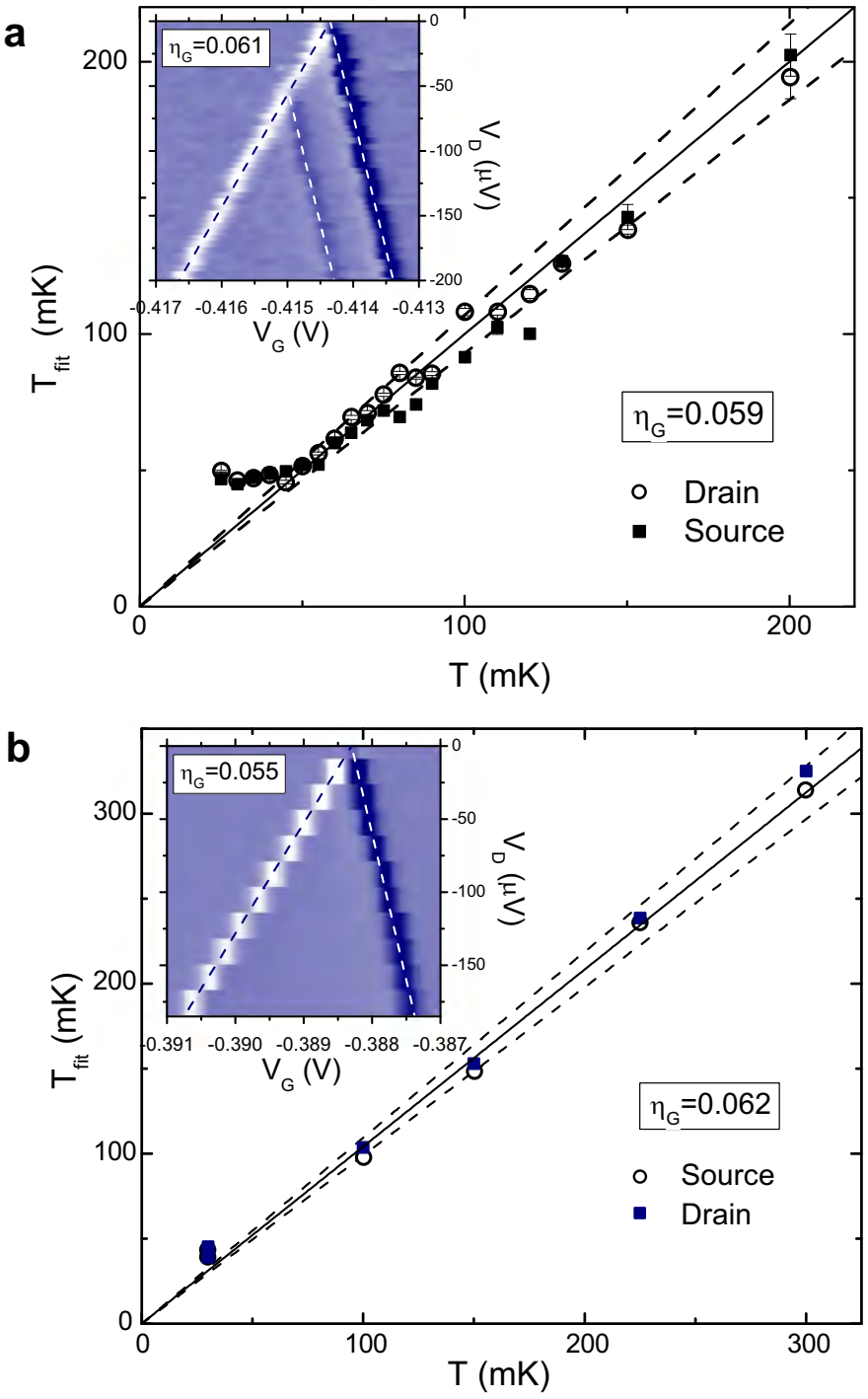

Figure 5.4: **Quantum dot calibration in cooldowns two and three.** This figure complements Figure 2 that focused on cooldown one. (**a**) and (**b**) are calibration data for cooldowns two and three, respectively. Errors in T_{fit} within $\pm 7\%$ for cooldown two (**a**) and within $\pm 5\%$ for cooldown three (**b**) are enclosed between the black dashed lines. Note that an additional quantum dot level of relative energy -56 μeV for cooldown two is visible in the top left inset of (**a**).

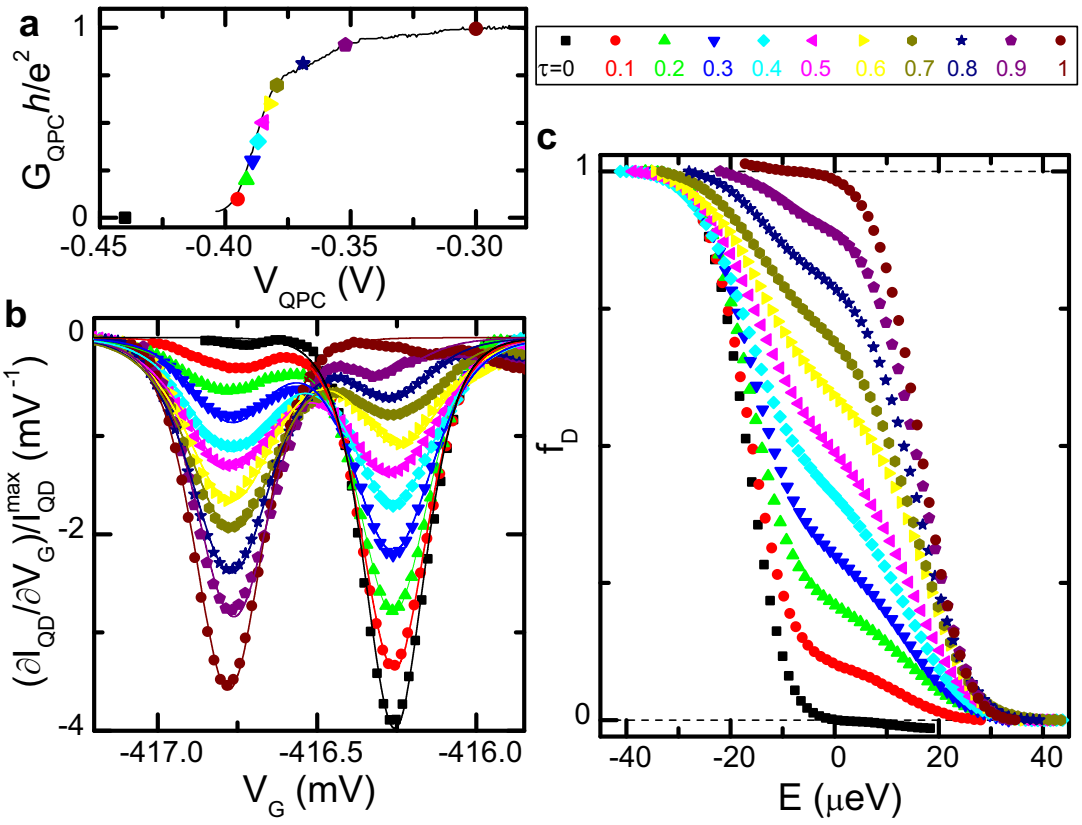

Figure 5.5: **Spectroscopy of an edge channel tuned out-of-equilibrium with the conductance of a QPC in cooldown two.** The QPC's voltage bias is here fixed to $\delta V_D \equiv V_{D1} - V_{D2} = -36$ μV. **a**, Measured $G_{\rm QPC}$ versus $V_{\rm QPC}$ applied to the lower left metal gate in Figure 1c. Symbols are data points obtained during the corresponding edge channel spectroscopy. The continuous line was measured with $\delta V_D = 0$. **b**, Measured $\partial I_{\rm QD}/\partial V_G$ (symbols) for the quantum dot-drain contribution (data have been aligned in V_G and normalized to $I_{\rm QD}^{max}$). Continuous lines are fits assuming $f_D(E)$ is the weighted sum of two Fermi functions. The detailed set of used fit parameters is given in Table 5.3. **c**, Energy distributions obtained by integrating the data in (**b**) and using $\eta_G = 0.059$.

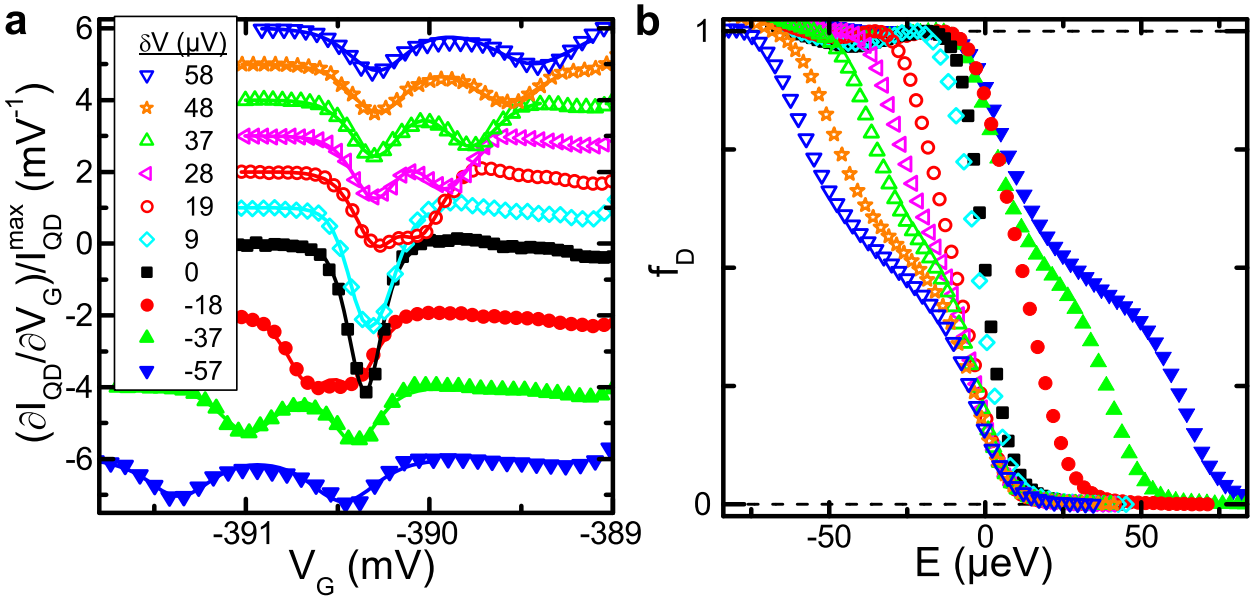

Figure 5.6: **Spectroscopy of an edge channel tuned out-of-equilibrium with the voltage across a QPC in cooldown three.** The QPC's conductance is here fixed to $G_{\mathrm{QPC}} = 0.5e^2/h$. **a**, Measured $\partial I_{\mathrm{QD}}/\partial V_G$ (symbols) for the quantum dot-drain contribution. Data have been shifted vertically for clarity, and horizontally to align the peak corresponding to the fixed potential V_{D2}. Continuous lines are fits assuming $f_D(E)$ is the weighted sum of two Fermi functions (see Table 5.4). **b**, Energy distributions obtained by integrating the data in (**a**) and using $\eta_G = 0.062$.

5.2 Experimental procedures

5.2.1 Extraction of the energy distribution function

The distribution functions $f(E)$ are obtained by integrating with V_G the normalized data $-(\partial I_{\mathrm{QD}}/\partial V_G)/I_{\mathrm{QD}}^{max}$ from a charge stability zone ($I_{\mathrm{QD}} = 0$) on the negative side up to $V_G = -(E - E_0)/e\eta_G$.

5.2.2 Extraction of the electrochemical potential

The electrochemical potential μ enters in the evaluation of the energy density, and consequently in the heat current J_E^{qp} and in the generalized quasiparticle temperature T_{qp}. The parameter μ is here obtained very directly from the measured $f(E)$ since the density of states has a negligible energy dependence in the probed range:

$$\mu = E_{min} + \int_{E_{min}}^{E_{max}} f(E)dE, \tag{5.4}$$

with E_{min} (E_{max}) an energy under (above) which we assume $f(E) = 1$ ($f(E) = 0$). Note that μ is obtained up to the same unknown constant offset E_0 as $f(E)$, however this has no impact since only the difference $E - \mu$ plays a role.

5.2.3 Estimation of uncertainties on the lever arm η_G

Uncertainties in the gate voltage-to-energy lever arm conversion factor η_G are mostly responsible for our error bars on energy related quantities (e.g. article Figures 3.d and 4.c and 4.d).

This parameter is extracted from two independent calibration procedures: First, we perform a non-linear characterization of the quantum dot [120] and extract η_G from the slopes of the Coulomb diamond $\partial I_{\mathrm{QD}}/\partial V_G(V_G, V_{\mathrm{D}})$ (hereafter called procedure 1). Second, we measure $\partial I_{\mathrm{QD}}/\partial V_G(V_G)$ at several temperatures and extract η_G from the scaling between fit temperatures (using Fermi functions in Equation 1) and measured mixing chamber temperatures (hereafter called procedure 2).

In procedure 1, uncertainties on η_G are obtained from the change in slopes corresponding to displacements equal to the full width at half maximum of the peaks at the highest drain-source voltage. This gives $\eta_G = 0.052 \pm 9\%$, $0.062 \pm 8\%$ and $0.055 \pm 9\%$ for, respectively, cooldowns one, two and three.

In procedure 2, uncertainties in η_G are obtained from the dispersion in fit temperatures T_{fit} around measured temperatures T of the dilution refrigerator mixing chamber. We evaluate roughly the uncertainty by finding the range of η_G that permits us to account for most T_{fit} at $T > 50$ mK. The reader can get a direct idea of the used uncertainties

in Figure 2 and Supplementary figure 5.4, where the expected fit temperatures using the considered extremal values of η_G are shown as dashed lines. This gives $\eta_G = 0.057 \pm 10\%$, $0.059 \pm 7\%$ and $0.062 \pm 5\%$ for, respectively, cooldowns one, two and three.

In the article, we have chosen to use the values of η_G and the associated uncertainties extracted using procedure 2, in the same experimental configuration as to measure unknown $f(E)$s.

5.2.4 Estimation of error bars

The error bars in the figures take into account the finite signal to noise and reproducibility (i.e. the standard error in the average value), and, if it applies, uncertainties in the lever arm.

Regarding the finite signal to noise and reproducibility our approach is very straightforward. We perform a statistical analysis on the considered quantity extracted from up to a hundred different V_G sweeps in the exact same experimental configuration. The corresponding standard error is then plus/minus the mean deviation per sweep divided by the square root of the number of sweeps. This is the only contribution for the parameter τ_{fit} whose typical error bars are found to be about 0.02, small compared to the symbol size in Figure 3.c. Note that in practice, we acquired the large number of sweeps necessary for an accurate statistical analysis in only a few realizations per experiment. In other realizations of a given experiment (i.e. when changing only the QPC conductance or the applied voltage bias), we assumed that the observed mean deviation per sweep is unchanged and estimate the standard error using the corresponding number of sweeps (generally more than five).

It turns out that, except for the immune τ_{fit}, error bars are mostly dominated by uncertainties on the lever arm η_G and therefore are proportional to the overall energy (namely, T_{qp} or δV_D). Indeed, the standard error on T_{qp} was always found smaller than 1 mK for cooldowns one and three, and 4 mK for cooldown two. Nevertheless, the full error bars shown in figures include both contributions, taken as independent from each other.

5.2.5 Fit procedures

We fitted the measured $(\partial I_{\mathrm{QD}}/\partial V_G)/I_{QD}^{max}$ using article Equations 1 and 2, with Fermi functions for f_{D1} and f_{D2}. The full set of fit parameters is not only constituted of τ_{fit} and $\eta_G \delta V_G$ shown in article Figures 3c and 4c, respectively. It also includes the temperatures T_{D1} and T_{D2} of the corresponding Fermi functions. We recapitulate the full set of used fit parameters in Tables 5.1, 5.2, 5.3 and 5.4.

G_{QPC} (e^2/h)	τ_{fit}	$T_{D1}(K)$	$T_{D2}(K)$
0	0	0.042	0.042
0.15	0.18	0.158	0.042
0.26	0.25	0.078	0.046
0.35	0.33	0.071	0.049
0.43	0.42	0.067	0.050
0.51	0.48	0.062	0.054
0.59	0.58	0.064	0.054
0.59	0.61	0.067	0.056
0.65	0.65	0.062	0.056
0.72	0.73	0.061	0.053
0.78	0.77	0.056	0.059
0.88	0.86	0.053	0.073
1	1	0.045	0.045

Table 5.1: **Summary of parameters used to fit the data shown in article Figure 3.b (cooldown one).** The conductance G_{QPC} is measured. Note that near zero and full transmission, the fit temperature of the small corresponding peak is not very significant. In order to focus on the fit parameter τ_{fit}, we chose to fix $\eta_G \delta V_G = 30$ μV. If $\eta_G \delta V_G$ is set free, we find values within 30 ± 1 μV, except at $G_{QPC} = 0.9e^2/h$ where $\eta_G \delta V_G = 39$ μV. Note that τ_{fit} is not affected more than ± 0.03 by whether $\eta_G \delta V_G$ is fixed or free.

δV_D (μV)	T_{D1} (K)	$T_{D2}(K)$	$\eta_G \delta V_G$ (μV)
-18	0.049	0.049	-12
0	0.040	0.040	0
18	0.048	0.045	13
27	0.054	0.054	20
36	0.061	0.056	29
45	0.074	0.063	38
54	0.076	0.073	46

Table 5.2: **Summary of parameters used to fit the data shown in article Figure 4.b (cooldown one).** Here δV_D is the applied voltage bias and the parameter τ_{fit} is set to the measured $G_{QPC} h/e^2 = 0.58$.

G_{QPC} (e^2/h)	τ_{fit}	$T_{D1} = T_{D2}$(K)	$\eta_G \delta V_G$ (μV)
0	0	0.043	-36
0.10	0.08	0.046	-30
0.20	0.18	0.050	-31
0.30	0.28	0.057	-30
0.40	0.41	0.062	-30
0.50	0.49	0.065	-30
0.60	0.61	0.063	-31
0.70	0.71	0.063	-30
0.81	0.80	0.057	-30
0.91	0.89	0.054	-28
1	1	0.049	-36

Table 5.3: **Summary of parameters used to fit the data shown in Figure 5.5.b (cooldown 2).** The conductance G_{QPC} is measured. The applied QPC voltage bias is here $\delta V_D = -36$ μV. The lever arm is $\eta_G = 0.059$.

$\delta V_D(\mu V)$	T_{D1} (K)	T_{D2}(K)	$\eta_G \delta V_G$ (μV)
-57	0.089	0.077	-56
-37	0.073	0.061	-36
-18	0.055	0.054	-15
0	0.044	0.044	0
9	0.046	0.043	7
19	0.057	0.052	15
28	0.064	0.055	24
37	0.073	0.060	32
48	0.088	0.070	44
58	0.094	0.080	53

Table 5.4: **Summary of parameters used to fit the data shown in Figure 5.6.a (cooldown 3).** Here δV_D is the applied voltage bias and the parameter τ_{fit} is set to the measured $G_{QPC}h/e^2 = 0.5$. The lever arm is $\eta_G = 0.062$.

5.3 Limits and constraints on the spectroscopic technique

5.3.1 Additional quantum dot levels

The simple procedures used to extract $f(E)$ from the quantum dot signal follow from the simple model used to describe the quantum dot article Equation 1, in which only a single energy lies within the transport window. However at least one energy level is close to the resonances used to perform the $f_D(E)$ spectroscopy. One could be naïvely tempted to this simple model in a multilevel case, but this simple form does not hold when Coulomb blockade effects are important (see e.g. Appendix and [119]). Coulomb interactions build in strong constraints on the available states, namely a single electronic state can be occupied at once, so that when multiple discrete levels lie in the transport window it does not result in multiple transport paths in parallel. One has to solve the sequential tunneling rate equations in order to compute the resulting current which can result in non-intuitive dynamical effects (even in the stationary regime). In particular, it was shown that the gate voltage position of a Coulomb peak can be shifted by about its width when the temperature changes [119]. We found a similar phenomenon could change the gate voltage separation between the two dips observed in presence of a double step energy distribution.

By solving the master equation with non-equilibrium energy distributions, using a slightly modified version of the code provided by [119], and with a second level of energy ε nearby the first active level, we could reproduce the observed difference between $\eta_G \delta V_G$ and δV_D shown in article Figure 4.d. Such second level for cooldown one is not visible in the top left inset of article Figure 2 but its existence is suggested by data taken in slightly different conditions (not shown) and by the observed $T_S > T_D$ at $T = 30$ mK (see article Figure 2). The presence of such a level can reduce $|\delta V_G|$ by a constant offset for $|e\delta V_D| > |\varepsilon|$ if asymmetrically coupled to the source and drain electrodes. Figure 5.7 shows $\eta_G \delta V_G$ extracted from cooldown one (data also shown in Figure 4c) together with dashed lines of slopes as expected from $\eta_G = 0.057$ but offset by ± 7 μV which is compatible with a second level located at $\varepsilon \approx -10$ μeV, below the first level.

Even in the presence of multiple levels, one could in principle extract the energy distribution by solving the corresponding rate equations. However, a full characterization of the tunneling rates linking the discrete levels to the electrodes should be carried which complicates the analysis and implies longer characterization work.

5.3.2 Energy relaxation

Last, the probe quantum dot and the injection QPC have a finite propagation length between them. Changes in $f(E)$ can therefore result from the energy relaxation arising during this

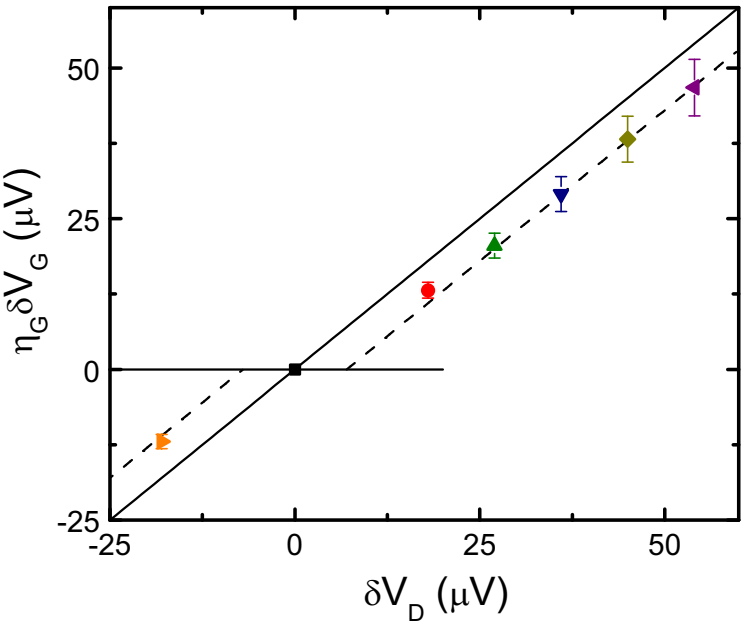

Figure 5.7: **Possible explanation with additional quantum dot levels of observed small deviations on cooldown one.** Data shown as symbols are those obtained in cooldown one and also displayed in article Figure 4c. Dashed lines correspond to the slope predicted by $\eta_G = 0.057$ but shifted horizontally by ± 7 μV. Such shifts are compatible with the presence of a second active quantum dot level located at $\varepsilon \approx -10$ μeV, below the first level.

finite propagation. This effect, although probably small for the short 0.8 μm propagation length considered here, could explain the also small deviation observed between the free 1D chiral fermions model and our data in article Figures 3d and 4d. Another indication that energy relaxation along the edge is not fully negligible is the observed increase in the fit temperatures T_{D1} and T_{D2} with injected power (see Supplementary tables 5.1, 5.2, 5.3 and 5.4). A detailed analysis of the energy relaxation along the propagation path is shown in the next chapter.

Chapter 6

Energy exchanges in the integer Quantum Hall effect

The possibility to probe the electronic $f(E)$ in out-of-equilibrium situations in 2DEGs opens the path to performing energy relaxation experiments in the IQHE. A similar approach, using Normal-Insulator-Superconductor (N-I-S) junctions as quantitative $f(E)$ probes, has already been used to test the inelastic mechanisms at work in mesoscopic metallic wires [25] (the high magnetic field regime has also been probed using the non-linearities of a dynamical Coulomb blockaded tunnel junction [121]) and in carbon nanotubes [26]. However Josephson junctions and dynamical Coulomb blockade are technically challenging to implement in the IQHE. Up to now, only a very qualitative probing of energy transport in the $\nu_L = 1$ IQHE was performed using narrow wires as local heaters and heat probes [122]. Although it was possible to test the chirality of heat transport using this simple scheme, the lack of control on the generated non-equilibrium situation and on the heat probe energy sensitivity could not permit to discriminate between different possible inelastic mechanisms[1].

In the precedent chapter, we have demonstrated that a well controlled and tunable non-equilibrium situation can be created in an edge-channel with the help of a voltage biased QPC, and that the non-equilibrium $f(E)$ can be directly extracted from the transconductance measured through a tunnel coupled quantum dot. In this chapter we are going to exploit these tools in order to perform quantitative energy relaxation and energy exchange experiments in the $\nu_L = 2$ IQHE. We find a strong energy relaxation, *without inter-channel particle exchanges*, towards a hot electron regime in a 3 μm scale that challenges the usual non-interacting 1DCF picture of edge-channels. Interactions within the edge-channel and with thermalized states[2] are found to be irrelevant to the relaxation dynamics, whereas in-

[1]For instance, the article claims that there is a significant energy relaxation towards (bulk) thermalized stated, but a relaxation towards a hot electron regime within the non-equilibrium edge-channel could also give rise to their measured signal if their heat probe signal is dominated by the highest energy excitations.

[2]Such as lattice vibrations, or the electronic states of the metallic gates used to define the edge-channel

ter edge-channel interactions play a dominant role. Last, an energy leakage from the two edge-channel system within the 1DCF basis suggests the presence of other co-propagative excitations, yet unidentified.

6.1 Experimental setup

How to tune the relaxation length: In order to perform energy relaxation experiments on edge-channels, we have chosen to use a single quantum dot as an $f(E)$ probe, and various QPCs to create a non-equilibrium $f(E)$ in distinct places (see Figures 6.1 and 6.2). Indeed, it is easier (and faster) to characterize a QPC rather than a quantum dot. We have also used two top metallic plates surrounding the quantum dot in order to screen the capacitive coupling between the quantum dot and the gates used to define the QPCs and the different propagation paths (Figures 6.1 and 6.2). Since these plates are grounded, they do not influence the electron paths. Figures 6.2 shows the 0.8, 2.2, 10 μm edge-channel paths between the QPC and the quantum dot. A further 4 μm path can be used using the left QPC, while closing the other ones. And a 30 μm path can be realized similarly to the 10 μm path (Figure 6.2.d), but using the right gate shown in Figures 6.1 to reflect the edge-channels towards the QPC.

Addressing energy relaxation and energy exchanges: We will always probe $f(E)$ in the outer edge-channel since our quantum-dot is optimized for doing so[3]. However, the double step like non-equilibrium $f(E)$ can be injected in the outer edge-channel (tuning the QPC at $G_{QPC} = 0.5e^2/h$, see Figure 4.2) in order to perform energy relaxation experiments within the outer edge-channel. Or the same non-equilibrium $f(E)$ can be injected in the inner edge-channel (tuning the QPC at $G_{QPC} = 1.5e^2/h$, see Figure 4.2) in order to test directly the energy exchanges between both edge-channels.

Power injected by QPCs: The non-equilibrium $f_D(E)$ in either the inner or outer edge-channels are always injected through a QPC having a 0.5 transmission for the partially transmitted edge-channel. So the excess power injected by the QPC, J^{QPC}_{excess}, in the non-

paths.

[3]In order to probe the inner edge-channel, the outer one should be fully transmitted. The quantum dot should be wider and therefore have smaller excitation energy gaps when used to probe the outer edge-channel, limiting the voltage range in which it can be safely used (multiple level complications). Moreover, since the edge-channels exchange energy (see further sections) the perfectly transmitted outer edge-channel would be more noisy ([12, 23]) and could perturb the resolution of the inner edge-channel spectroscopy.

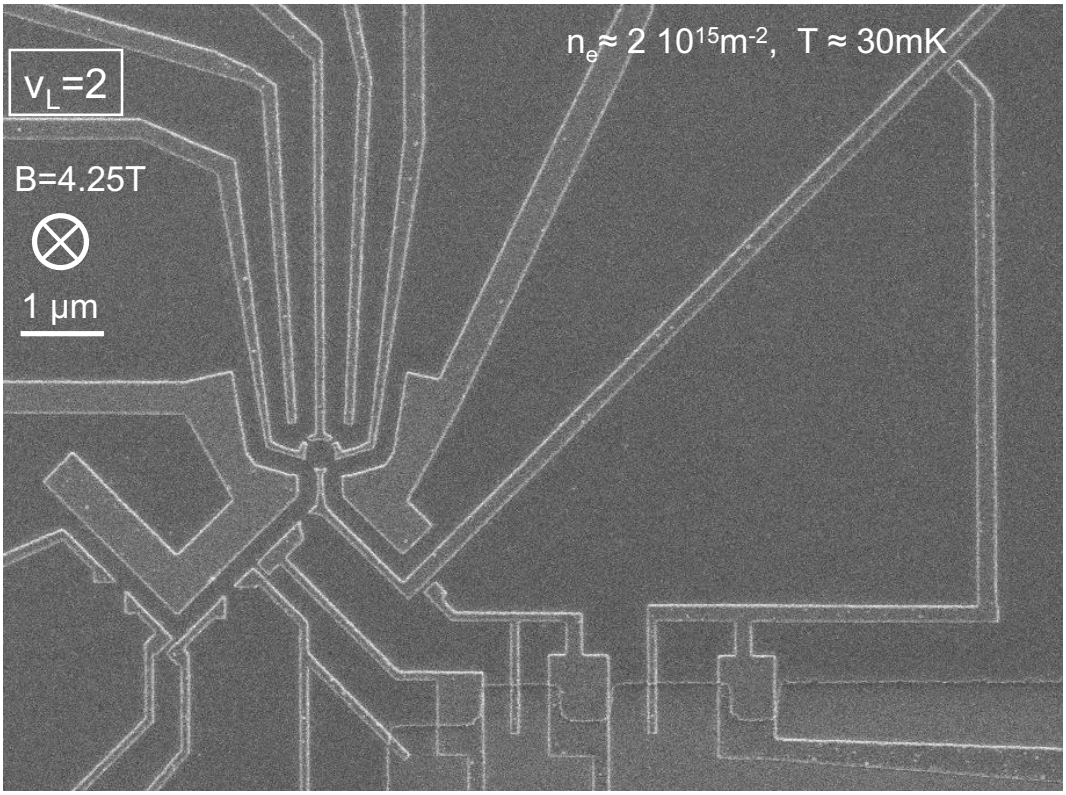

Figure 6.1: **Measured sample micrograph.** All top metallic gates (appearing brighter) that are used in the following experiments are visible. A magnetic field of $4.25T$ is applied entering the picture, defining two co-propagative edge-channels having an anticlockwise chirality. The mesa edge is visible at bottom right of the micrograph, chemically defined edge paths are short compared to the gate defined edges. 3 QPCs (bottom-left) can be used to generate a non-equilibrium $f(E)$ in 3 distinct places, and a quantum dot (middle-top) is used to probe $f(E)$ after the edge-channel propagation. The propagation length is selected with the help of top metallic gates (see figure 6.2). The top metallic plates surrounding the quantum dot are grounded and do not influence the electron paths.

equilibrium edge-channel reads (Equations 4.16 and 4.1):

$$J_{excess}^{QPC} = \frac{e^2}{4h}\delta V_D^2 \tag{6.1}$$

characterized by an excess temperature T_{excess}^{QPC} which is linear in the QPC voltage bias $|\delta V_D|$:

$$k_B T_{excess}^{QPC} = \frac{\sqrt{3}e}{2\pi}|\delta V_D| \tag{6.2}$$

All measurements are performed at a base temperature of $30mK$.

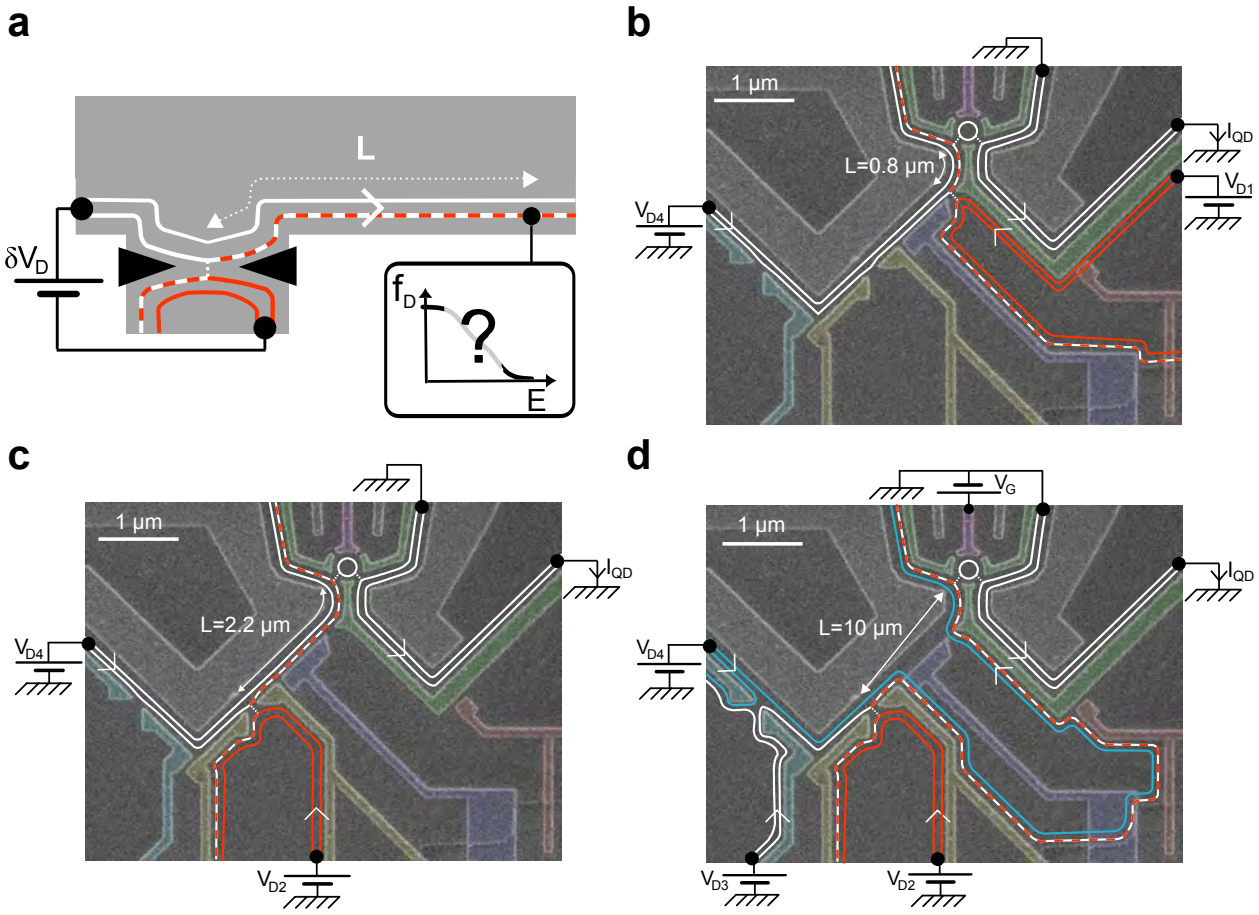

Figure 6.2: **Selecting the propagation length with top metallic gates. a** Schematic principle of the energy relaxation experiment. **b** The $0.8\mu m$ edge-channel path is selected by injecting a non-equilibrium $f(E)$ in the QPC, closest to the quantum dot, biased by voltage sources V_{D1} and V_{D4}. **c** The $2.2\mu m$ edge-channel path is selected by injecting a non-equilibrium $f(E)$ in the QPC, second closest to the quantum dot, biased by voltage sources V_{D2} and V_{D4}, while the closest QPC is fully closed ($G_{QPC} = 0$). **d** The $10\mu m$ edge-channel path is selected by injecting a non-equilibrium $f(E)$ in the QPC, second closest to the quantum dot, biased by voltage sources V_{D2} and V_{D4}, while the closest QPC fully transmits both edge-channels ($G_{QPC} = 2e^2/h$). The red gate (bottom-right) is tuned to reflect both edge-channels to the quantum dot, defining the $10\mu m$ path.

Measuring $f(E)$

We follow the methods introduced in Chapter 2, to measure the non-equilibrium $f(E)$ after the several propagation paths on the drain side of the quantum dot (left in Figure 6.1). The lever arm calibration is here slightly different:

Lever arm calibration: The lever arm η_G, permitting to link the side gate voltage V_G to the electrostatic energy inside the dot has been extracted using a method slightly different from Chapter 2. This issue is here more stringent since several calibrations where needed each time the bias of the surrounding gates where significantly modified within the same cooldowns. This results from the capacitive coupling between quantum dot and the gates defining the several paths[4] a more straightforward method was needed.

We first performed a characterization of the QD in the non-linear regime [120] and extracted η_G from the slopes of the Coulomb diamond $\partial I_{\mathrm{QD}}/\partial V_G(V_G, V_D)$ (hereafter called method 1).

We also measured $\partial I_{\mathrm{QD}}/\partial V_G(V_G, V_D = -88\ \mu\mathrm{V})$ at several temperatures and extracted η_G from the scaling between the measured mixing chamber temperatures and the fit temperatures T_S (T_D) of the source peak (drain dip) obtained assuming Fermi functions (hereafter called method 2 (method 3)) (see Chapter 2 article Figure 2 [1]).

We defined η_G as the average of the three values obtained with these methods, and used the corresponding standard error to define uncertainty on η_G. The average values of η_G used in the present work are recapitulated in Table 6.1 with their relative standard errors. Note that we found small variations between the various average values of η_G, well within standard errors. This suggests that the relative error bars between experimental configurations is smaller than the absolute error bar displayed in all figures.

6.2 Energy relaxation along the edge-channels

This section shows our energy relaxation measurements: the *same* outer edge-channel is driven out of equilibrium and probed after a selected propagation length (setup depicted in Figure 6.2.a). The raw quantum dot signal $\partial I_{QD}/\partial V_G \propto \partial f_E/\partial E$ for the different propagation length shows a strong energy relaxation on a few μm scale. We further provide quantitative information on the corresponding inelastic mechanisms by extracting the generalized temperature T_{qp} (see Equation 4.20), and analyze its dependence with the propagation length and QPC voltage bias.

The experiment principle is recalled in Figure 6.2.a and the practical implementations of several propagation paths is depicted in Figures 6.1.b, c, and d.

[4] Despite the presence of the screening plates. But it is hard to screen 3D fields with 2D plates.

$\{L, G_{QPC}\}$ $\{(\mu\text{m}), (e^2/h)\}$	η_G	$\Delta\eta_G/\eta_G$ (%)
$\{0.8, 0.5\}^+$	0.0593	5.3
$\{4, 1.5\}^+$	0.0610	3.5
$\{4, 0.5\}$	0.0610	3.5
$\{2.2, 0.5\}$	0.0610	3.5
$\{2.2, 1.5\}$	0.0610	3.5
$\{10, 0.5\}^+$	0.0606	5.7
$\{30, 0.5\}$	0.0606	5.7
$\{10, 1.5\}^+$	0.0598	6.3

Table 6.1: Used lever arms η_G and their relative standard errors $\Delta\eta_G/\eta_G$. The symbol ($^+$) points out experimental configurations, characterized by $\{L, G_{QPC}\}$, for which the full QD calibration was performed.

6.2.1 f(E) vs propagation length

We first measure the non-equilibrium $f_D(E)$ after several propagation lengths, and several QPC biases. Figure 6.3 shows the quantum dot signal $\propto \partial f_E/\partial E$ measured during a same cooldown for the propagation lengths L={0.8, 2.2, 4, 10, 30 μm} and a QPC voltage bias[5] $\delta V_D = 36\mu V$.

Energy exchanges: The double-dip measured at $0.8\mu m$ corresponds to the energy derivative of a double-step like $f_D(E)$ close to the $f_D(E)$ injected by the QPC (see Chapter 2). It is found to evolve towards an equilibrium like single dip reached within 10 μm (continuous lines are fits using the derivative of a Fermi function). The mere fact that the quantum dot signal, and therefore $f_D(E)$, evolves with the propagation length is the signature that energy exchanges take place along the edge-channels propagation.

Small inelastic length: The initial double-dip structure is already washed out between the 2.2 μm and the 4 μm propagation paths. This defines roughly a characteristic scale for the $f_D(E)$ evolution of about 3 μm. This inelastic length corresponds to a characteristic input energy per injected excitation of about $k_B T^{QPC}_{excess}(\delta V_D = 36\ \mu\text{V}) \simeq 10\ \mu\text{eV}$ (Equation 6.2).

[5] δV_D is defined as the difference between the potential applied to the transmitted edge-channel towards the quantum dot and the potential applied to the reflected edge-channel. For the $0.8\mu m$ path, it is defined as $\delta V_D = V_{D1} - V_{D4}$ (see Figure 6.2.b). For the $2.2\mu m$ path it is $\delta V_D = V_{D2} - V_{D4}$ (Figure 6.2.b, and so on.)

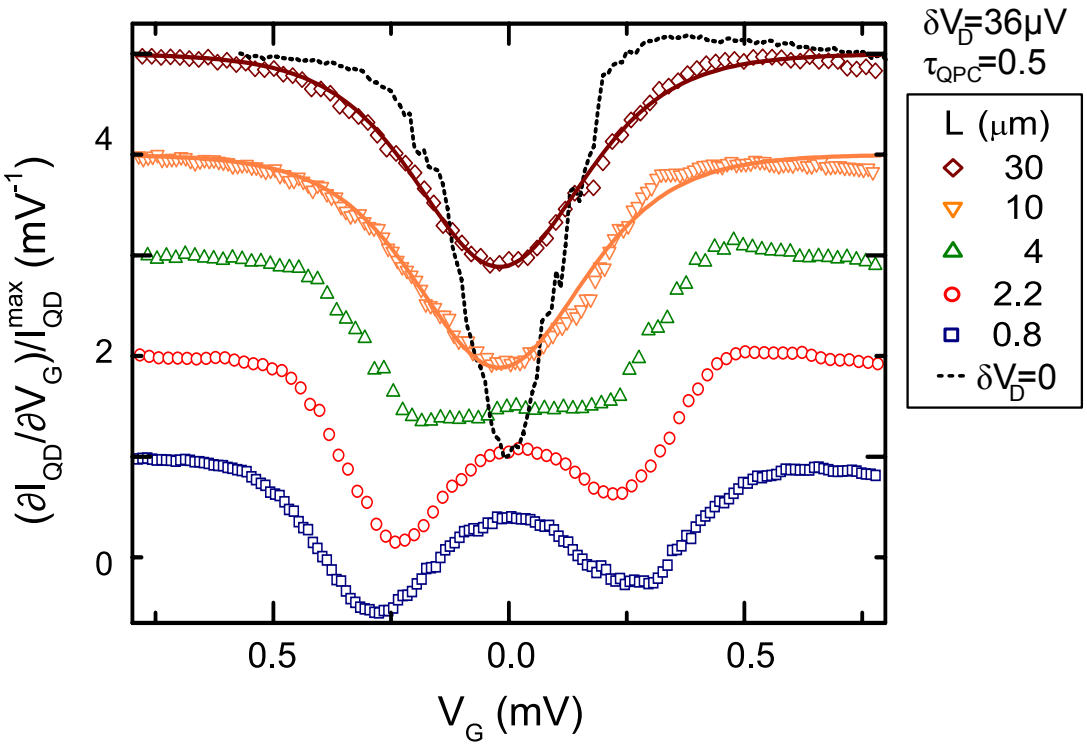

Figure 6.3: **Quantum dot signal ($\propto \partial f_D(E)/\partial E$) as a function of the propagation length for non-equilibrium situation defined by** δV_D =36 μV **and** $\tau_{QPC} = 0.5$ Vertical offsets applied for clarity, horizontal offsets are applied to align the chemical potentials in V_G. The initial non-equilibrium double-dip signal evolves towards a stationary single dip ($L = 10$ and 30 μm) in a characteristic length scale of about3 μm. The stationary dip is wider than the equilibrium signal (dotted lines) indicating that a hot electron regime is reached. This conclusion is strengthened by the hot Fermi function derivative fits (continuous lines) yielding to the same fit temperature of $T_{Hot} = 85$ mK at both $L = 10$ and 30 μm, ~ 2 times the equilibrium dip temperature $T_{eq} = 40$ mK.

Saturation in a hot electron regime: The signal evolution saturates between the 10 μm and 30 μm, indicating that a stationary regime is reached regarding energy exchanges. Both signals can be fitted with the same Fermi function confirming that a local equilibrium is reached (continuous lines in Figure 6.3). However, both Fermi fits gives a fit temperature of $T_{Hot} = 85$ mK whereas the base temperature is 30 mK. The non-equilibrium edge channel relaxes to a hot electron regime. The difference between the saturation and the equilibrium signal is stark (dotted line in Figure 6.3 is the signal measured at $\delta V_D = 0$).

Fitting the equilibrium dip at $\delta V_D = 0$ using a Fermi function gives an equilibrium temperature $T_{eq} = 40$ mK, similar to the low temperature limit of the quantum dot calibrations

shown in Chapter 2 (e.g. article Figure 1). The resonance is larger than the base temperature 30 mK, measured by a calibrated Ruthenium oxide resistance thermally anchored to the cold finger. This is possibly due to a unperfect electron thermalization at high magnetic fields[6]. It could also result from capacitively coupled charge fluctuations around the quantum dot which could make oscillate the discrete level energy at faster rates than our integration time (~ 0.8 s). Anyway, it defines our temperature (energy) resolution limit, so that we will refer to T_{eq} when extracting the excess energy carried by the probed edge channel.

6.2.2 Discarding experimental artifacts

We have performed some supplementary checks in order to ascertain that the measured propagation length evolution of the quantum dot signal is unambiguously due to energy exchanges. First, one can ask whether the observed evolution with the propagation length could be attributed to the different QPCs used. Second, changes on $f_D(E)$ could result from charge transfer between the edge-channels (through tunneling across the incompressible strip separating both edge-channels). Third, the quantum dot could be perturbed by the interaction mechanisms at work. We have checked that neither of these scenarii takes place.

Different QPCs?

(i) Experimental configurations $L \in \{2.2, 10, 30\}$ μm use the same voltage biased QPC but the signal is different.
(ii) Similar hot Fermi dips (not shown) as those measured at $L = \{10, 30\}$ μm were obtained at $L = \{12, 32\}$ μm with a different QPC (light blue metallic gates in Figure 6.2, also used here for the $L = 4$ μm propagation path).
(iii) These results have been reproduced in three different cooldowns (data not shown), with renewed quantum dots and QPCs.

No particle exchanges

It is known that the electrochemical potentials of co-propagating ECs equilibrate only on large propagation distances [66, 67, 69]. At low temperatures and filling factor $\nu_L = 2$, macroscopic equilibration lengths of 1 mm were reported [123]. We have nevertheless verified that no particle exchanges take place along our smaller propagation paths.

Direct inter-channel charge equilibration test: First, the most straightforward approach to test the presence of tunneling is to perform an anomalous quantum Hall effect

[6] At low magnetic fields, we find an excellent agreement on the temperature dependence of the dynamical Coulomb blockade correction to the conductance of a QPC (Chapter 9). Which demonstrates good electron thermalization at low magnetic fields.

measurement [66], namely biasing the two edge channels at different potentials and measuring them separately after some propagation distance. This can be done by using injection and measurement QPCs set to the conductance $G_{QPC} = e^2/h$ to separate the two edge-channels. We did this measurement, and also a variation of this measurement in which the injection QPC was set to $G_{QPC} \simeq 0.5e^2/h$, for $L = 30$ μm and for the largest applied bias voltage $\delta V_D = \pm 54$ μV. We found, at base temperature $T = 30$ mK, that tunneling between co-propagating edge channels was always negligible (less than 1% of the population difference).

Direct coupling vs gating: Second, in order to perform this test, simultaneously to data acquisition, we made use of the fact that in absence of charge tunneling between edge-channels, the inner edge-channel is only capacitively coupled to the quantum dot, as is if it were a plunger gate. Therefore, the presence of tunneling between co-propagating edge-channels shows up as deviations from a strict proportionality between $\partial I_{\rm QD}/\partial V_{in}(V_G)$ and $\partial I_{\rm QD}/\partial V_G(V_G)$, where V_{in} is the potential applied to the inner edge channel. We systematically applied an AC modulation $e\delta V_{in}$ to the inner edge-channel electrochemical potential at a specific frequency, different from the outer edge-channel's and quantum dot gate modulation frequencies. We could do this by separating the two edge-channels upstream of the injection QPC (see Figure 6.2 with $V_{in} = V_{D4}$), except for $L = 4$ μm, where the injection QPC is the foremost upstream. We then measured $\partial I_{\rm QD}/\partial V_{in}$ by lock-in techniques, and checked that there were no such deviations at the largest applied bias voltage in each experimental configurations which is shown in Figure 6.4.a.

Both tests agree: We verified the pertinence of this second test at a larger fridge temperature $T = 190$ mK, where the first test (i.e. anomalous quantum Hall effect measurements) showed the presence of tunneling between co-propagating edge-channels (8.7%, 5.0% and 2.3% equilibration at $\delta V_D = 54$ μV, 36 μV and 0 V, respectively, after a propagation distance 30 μm). The fact that we also observed significant deviations from $\partial I_{\rm QD}/\partial V_{in} \propto \partial I_{\rm QD}/\partial V_G$ demonstrates the pertinence of this second test.

No energy resolution loss

The quantum dot could be perturbed by the non-equilibrium edge-channel and loose some of its energy sensitivity. For instance, the capacitive coupling between the quantum dot discrete level and the non-equilibrium (noisy [31]) channel could yield to higher electronic temperatures when measuring the width of the quantum dot resonance. This is difficult to track in the non-equilibrium drain signal, since we do not have definite prediction for the relaxed $f_D(E)$. However, the equilibrium source peak can be *used as a witness* of the energy

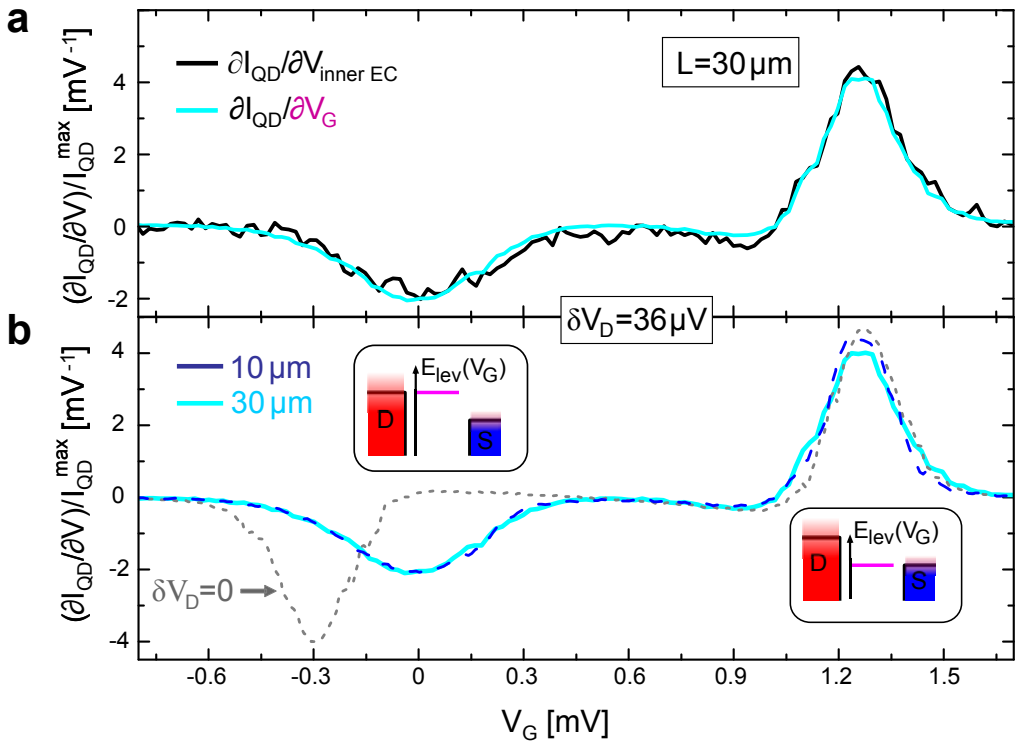

Figure 6.4: **Discarding experimental artifacts for the energy relaxation a** Quantum dot transconductances with respect to the gate voltage, V_G and with respect to the inner edge-channel potential, $V_{innerEC}$, for a relaxation path of 30 µm. The gate voltage range permits to see both drain and source contributions to the quantum dot signal. $\partial I_{QD}/\partial V_{innerEC}$ has been rescaled in amplitude. The strict proportionality between both signal demonstrates the inner edge-channel is only capacitively coupled with the quantum dot, even in non-equilibrium situations and for the longest probed path. **b** Relaxation, $\partial I_{QD}/\partial V_G$ measurements, for the longest propagation paths and at equilibrium (dotted line), showing both the non-equilibrium drain (left, left inset) and the cold equilibrium source (right, right-inset) contributions to the quantum dot signal. The source contribution is not affected by the energy relaxation. The quantum dot energy resolution is not perturbed by interaction effects.

resolution, since it is fed by an equilibrium cold ground. Figure 6.4.b shows the full gate voltage sweep of the quantum dot signal at equilibrium and for the relaxation paths of 10 and 30 µm, where both the drain (left) and source (right) electrode contributions to the quantum dot signal can be seen. The source peak remains essentially unchanged between the equilibrium and long path non-equilibrium situations. The small changes in the source peak are within 10% of its initial width, corresponding to about 5 mK in temperature. This is negligible in front of the saturation hot temperature found in the drain signals ($T_{Hot} = 85$ mK).

The quantum dot energy sensitivity can therefore be considered as constant when com-

pared to the strong energy exchanges observed.

6.2.3 Energy currents

We define the excess temperature T_{exc}, characterizing the excess heat current with respect to the equilibrium chiral heat flow $J_eq = \frac{\pi^2}{6h}(k_B T)^2$. The QPC bias and propagation length dependence of T_{excess} permit to discuss the possible inelastic mechanism responsible for the relaxation shown in Figure 6.3.

Excess energy current and excess temperature

Definition: We define the excess temperature T_{excess} as:

$$J_{qp}(T_{excess}) = J_{qp}(T_{qp}) - J_{qp}(T_{eq}) \tag{6.3}$$

$$\Longleftrightarrow T_{excess} = \sqrt{T_{qp}^2 - T_{eq}^2}, \tag{6.4}$$

which measures the energy current carried by the excitations additional to the thermal excitations giving rise to equilibrium (chiral) energy currents. T_{excess} permits to compare different quantum dot configurations yielding to slightly different drain equilibrium temperatures T_{eq} (due to quantum dot imperfections), and to compare the data obtained in different experimental runs (measured base temperatures range between 30 and 40 mK).

Extraction of T_{excess}: We have extracted T_{qp} with the same method describes in Chapter 3. We therefore obtain T_{excess} from Equation 6.3, where T_{eq} is the Fermi fit temperature of the equilibrium drain signal at $\delta V_D = 0$. However, in order to limit artifacts related to the finite signal-to-noise ratio[7], to the finite energy window probed and to the simple quantum dot model used, we also always tried to fit the data assuming that f_D is the weighted sum of two Fermi functions. This yielded an alternative value for T_{excess}. First, at equilibrium, the Fermi fit gave an estimate of deviations of our detector from the simple quantum dot model (Chapter 2 last section). Second, as long as the accuracy of the non-equilibrium fits was found equal to or better than that of the reference at equilibrium (most often the case), T_{excess} was taken as the average value of the fit and the integral (Chapter 3) procedures. Displayed error bars on T_{excess} include the two independent contributions of the standard deviation between extraction procedures for T_{excess} and for η_G. In practice, we found in most cases that the error is dominated by the latter contribution.

Figure 6.5 presents the resulting excess temperatures for the different propagation lengths and voltage biases.

[7] The signal to noise ratio is minimal when $\partial I_{QD}/\partial V_G$ approaches zero. Since the corresponding energy ranges correspond to the large energy single particle excitations, small fluctuations can impact the integrated energy current.

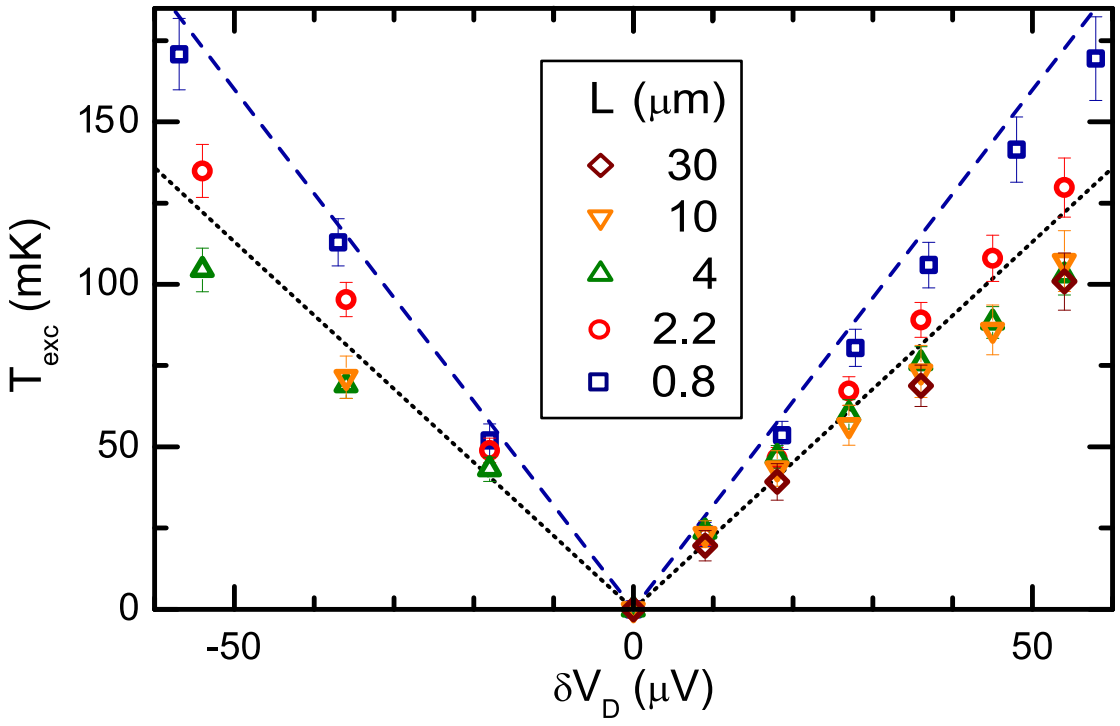

Figure 6.5: **Excess temperature for several relaxation path lengths and QPC voltage biases** The outer edge-channel cools down (symbols) as the relaxation propagation length is increased and saturates to values roughly proportional to the injected T_{excess}^{QPC} (dashed line: prediction at QPC output). The saturation values are found below the expectations for two interacting edge-channels (Dotted line: Lower bound accessible for two interacting 1D channels).

Possible inelastic mechanisms

No coupling towards thermalized states: For every fixed non-equilibrium situation, the excess temperature decreases with the propagation length and saturates in rough proportionality to the excess temperature,

$$T_{excess}^{QPC} = \sqrt{\frac{3e^2}{(\pi k_B)^2}\tau(1-\tau)|\delta V_D|},$$

injected by the QPC: $T_{excess} \approx (0.61 \pm 0.04) \times T_{excess}^{QPC}$. Since the saturation (hot electron regime) excess temperature scales with the injected power, *the relaxation dynamics are incompatible with a relaxation driven by interactions with thermalized excitations*. In particular, the relaxation due to the coupling with thermalized acoustic phonons is found negligible in agreement with theoretical expectations [56, 70]

Weak energy exchanges within the excited edge-channel: Moreover, energy exchanges within the 1DCFs of the same edge-channel are *relatively weak* compared to the dominant mechanism. Indeed, they preserve T_{excess}, instead we find $f_D(E)$ (Figure 6.3) and T_{excess} (Figure 6.3) evolve on the same length scale.

Co-propagating excitations Our data is nevertheless compatible with a relaxation induced by interactions with co-propagative excitations. The simplest case of all would correspond to interactions with the co-propagating inner edge-channel initially at equilibrium. This mechanism is most plausible since it is known that at $\nu_L = 2$ the low frequency current fluctuations of the inner edge-channel couple to the outer one, making it loose its coherence [12, 23][8]. In the steady state for two interacting co-propagating channels only, both edge-channels should exhibit the same saturation T_{excess}. Power conservation on the two-channel system further constraints T_{excess} to match:

$$T_{excess} \rightarrow \frac{T_{excess}^{QPC}}{\sqrt{2}} \tag{6.5}$$

which is plotted in Figure 6.5 as a dotted line.

Since the saturation values of T_{excess} are found below this limit[9] our relaxation data suggests that *more than one co-propagative excitations branches are coupled to the non-equilibrium outer edge-channel* [30, 31].

Self consistency of single particle excitations

Our measurements show a rather fast relaxation towards a hot electron regime. The inelastic length, L_{inel}, characterizing the energy loss from the non-equilibrium edge-channel can be used to test the self consistency of the single particle 1DCFs picture: The finite quantum lifetime corresponding to L_{inel} can be used to extract the energy uncertainty of single particle excitations. By comparing it to their mean energy, we can show that single particle excitations have an ill-defined energy.

Inelastic lengths: We have extracted the quantity $L_{inel}(\delta V_D)$ by fitting $T_{\rm exc}(L)$ at a fixed non-equilibrium situation, defined by the QPC bias δV_D, with the exponential function

$$T_{excess}^{fit}(L) \equiv (T_{excess}^{QPC} - T_{excess}^{sat}) \exp\left(-L/L_{inel}\right) + T_{excess}^{sat}, \tag{6.6}$$

where $T_{\rm exc}^{sat}$ is a second fit parameter that corresponds to the excess temperature at large propagation lengths.

[8] Note that low frequency noise induced dephasing demonstrates a capacitive coupling, but does not demonstrate energy exchanges.

[9] Three different cooldowns with renewed quantum dots and QPCs validate this statement.

The values of $L_{inel}(\delta V_D)$ extracted by this procedure are recapitulated in Table 6.2. Error bars ΔL on L_{inel} are standard errors obtained taking into account error bars in the extracted T_{excess}. $T^{fit}_{excess}(L)$ corresponding to L_{inel} shown in Table 6.2 are displayed as continuous lines in Figure 6.6.

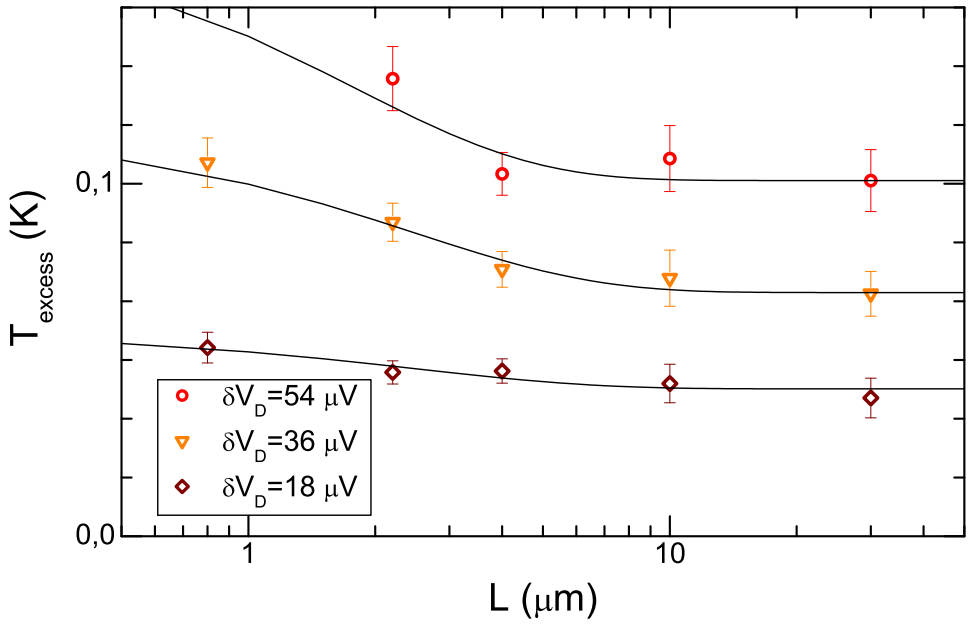

Figure 6.6: **Fits of $T_{excess}(L)$ used to extract L_{inel}.** The resulting fit parameters are shown in Table 6.2.

δV_D (μV)	L_{inel} (μm)	ΔL (μm)
18	2.5	0.85
36	2.5	0.4
54	1.8	0.65

Table 6.2: L_{inel} and corresponding standard error obtained by fitting $T_{\rm exc}(L)$ (see text).

Quantum lifetime: A lower bound for the 1DCF's lifetime can be obtained from L_{inel}, by using the range of drift velocities $v_D \in [0.5, 5]\ 10^5$ m/s measured in similar structures at $\nu_L = 2$ [89]. Applying the time-energy uncertainty relation, one finds for $\delta V_D = 36\ \mu$V that the energy linewidth of 1DCF states $\Delta E > \hbar v_D / 2L_{\rm inel} \in [6, 70]\ \mu$eV is of the same order or larger than their characteristic energy $k_B T^{\rm qpc}_{\rm exc}(\delta V_D = 36\ \mu{\rm V}) \approx 10\ \mu$eV, and therefore are *ill-defined electronic edge excitations*.

Ref.	v_D (10^5 m/s)	n (10^{15}m^{-2})	μ (m^{2}V^{-1}s^{-1})	d (nm)
[124]	0.85	1.9	70	120
[124]	0.55	2.3	50	90
[125]	1	1	75	130
[90]	[1,3]	1.2	100	
[89]	[2.8,4.3]	3.2	170	110
[11]	> 1	~ 1.5		85

Table 6.3: Drift velocities at $\nu_L = 2$ with metal gates. The main sample parameters are given when known (n: electron density, μ: mobility, d: depth of 2DEG). Samples in [124, 125] are fully covered by a metallic gate at the surface, others have metallic side gates. The range of values in [89, 90] was obtained by changing the metal side gate voltage bias (more negative voltages give larger velocities). The data in [11] permits to obtain a lower bound for v_D from the observed phase rigidity up to an energy of at least 10 μeV in an electronic Mach-Zehnder with an extra length of 2.4 μm along a metal side gate in one of the interferometer's two paths (using Eq. 2 in [11] with $\varphi < 1$ rad).

Consequently, although the 1DCF representation of edge states is very powerful at short distances, the observed short L_{inel} challenges the description of quantum Hall excitations as quasiparticles localized in one edge channel.

Range of drift velocities in similar systems: The range of drift velocities $v_D \in [0.5, 5]$ 10^5 m/s used is obtained from different sources that are recapitulated in Table 6.3. We focus on GaAs/Ga(Al)As devices set to display the integer quantum Hall effect at $\nu_L = 2$. Furthermore, the above range of v_D concerns only devices that are either fully covered by surface metal gates or with edges defined by voltage biased metal gates. Note that similar devices without metal gates have a drift velocity typically one order of magnitude larger (e.g. [89]), which would result in an even more stringent failure of the self consistent test described in the last paragraph.[10].

6.2.4 Summing up

First, our energy relaxation data on the outer edge-channel demonstrate strong energy exchanges challenging the single-particle 1DCF picture.

[10]Note that all used values, excepting the last one, are extracted from time of flight experiments. Strictly speaking, they measure the drift velocity of the charge magnetoplasmon mode and are sensitive to the interactions between ECs (see Equations 3.27). But if 1DCFs are well defined, it should be similar to the 1DCFs' velocity, and can be used to perform a self consistent test of the 1DCF picture.

Moreover, the energy relaxation dependence on the QPC bias yields to strong constraints to the possible inelastic mechanisms. For instance, coupling thermalized excitations (such as phonons, or the electronic states within the metallic gates used to define the edge-paths) are ruled out by our data. Interaction within the 1DCFs of the outer edge-channel are found to be not the dominant mechanism, if relevant at all. Finally, our data is compatible with interactions with al least more than one co-propagative excitation branch. In the following section we will directly test the energy exchages between the 1DCFs excitation of both co-propagating edge-channels.

6.3 Energy exchanges between edge-channels

It is most natural to assume the 1DCFs of the two co-propagating ECs exchange energy. This hypothesis can be tested directly by generating a non-equilibrium energy distribution in the *inner* EC ($G_{QPC} \simeq 1.5e^2/h$), with $f_D(E)$ still being measured in the *outer* EC (see Figure 6.7.a).

6.3.1 Inter channel energy exchanges measurements

Inter-channel energy exchanges: Figure 6.7.b shows the raw data obtained in this configuration at $\delta V_D = 54$ µV for several propagation lengths L. We find that the initial equilibrium dip broadens as L is increased, and therefore that the outer edge-channel heats up[11] when propagating next to the non-equilibrium inner edge-channel. This unambiguously demonstrates energy exchanges between edge-channels. Figure 6.7.c shows T_{excess} in the outer edge-channel (symbols), which increases with L as expected from the raw data.

Energy currents equilibration: It is noteworthy that at $L = 10$ µm, T_{excess} is approximately independent of which of the inner or the outer edge-channel is driven out-of-equilibrium (compare full and open symbols ($\triangledown$) in Figure 6.7.c), and therefore the energy currents carried by both inner and outer edge-channel single particle excitations equilibrate at long distances. Disregarding the energy leakage from the 2 edge-channel 1DCFs system and disorder, this finding would imply [31] that the edge-channels interact in the strong coupling limit ($g_{12} \gg \hbar|v_1 - v_2|$ using Equation 3.27's notations), strengthening the finding that 1DCFs single particle excitations within a single edge-channel are ill-defined already on a $\sim$ µm scale.

[11] The dip's width is proportional to the outer edge-channel temperature.

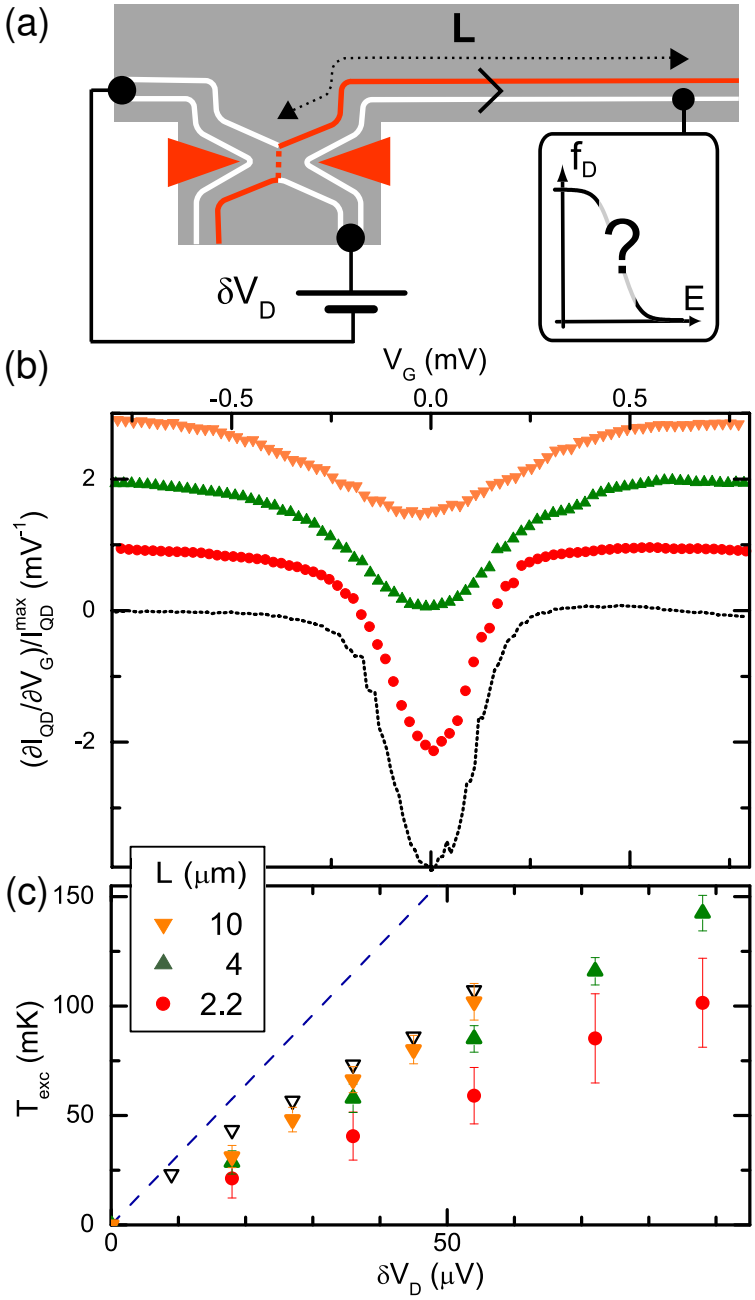

Figure 6.7: **Inter channel energy exchanges setup and measurements.** (a) The *inner* EC is driven out-of-equilibrium. (b) Raw data at $\delta V_D = 0$ (dotted line) and $\delta V_D = 54$ μV (symbols), shifted vertically for several L. The dip broadens as L is increased. (c) Excess temperatures extracted from the data (full symbols) and prediction at the QPC output (dashed line). The outer EC heats up as L is increased, up to an excess temperature close to that when driving the outer EC out-of-equilibrium ($T_{excess}(L = 110$ μm) in Figure 6.5 are shown here as open symbols (▽)).

Comparison to Mach-Zehnder experiments: These results are in qualitative agreement with the recent investigations of dephasing at $\nu_L = 2$, which established that current noise in the inner edge-channel reduces the phase coherence in the outer edge-channel [12, 23]. The dephasing length $L_\phi(T) \simeq 20\ \mu\text{m}/(T/20\ \text{mK})$ [14] can be compared to our inelastic length, L_{inel}. Using the injected excess temperature $T_{exc}^{QPC} = 115$ mK at $\delta V_D = 36\mu$V , we find an $L_\phi(115\ \text{mK}) \simeq 3.5\ \mu$m, which is similar to the corresponding $L_{inel} = 2.5 \pm 0.4\ \mu$m (see Table 6.2). This strengthens the hypothesis that a same physical mechanism is at the root of both dephasing and energy exchanges. However, contrary to dephasing [23], energy exchanges cannot be accounted for by low frequency noise within perturbation theories [96].

6.3.2 Comparison with recent theories

Two recent theories [30, 31] have been developed in order to understand our experimental findings:

Disorder assisted perturbative coupling: Within the widespread picture of 1DCF quasiparticles, the minimal approach is to include interactions between co-propagating edge-channels as a small perturbation. However, in absence of disorder, energy exchanges between 1DCFs of different drift velocities v_D would be essentially suppressed, due to combined energy and momentum conservations. Therefore, it is crucial to assume a sufficient disorder to break momentum conservation. Motivated by the present work, Lunde *et al.* modeled inter edge-channel interactions as a density-density coupling, where disorder changes the coupling coefficient along the edge with a correlation length ℓ [30]. Within this model, $T_{exc}(L/L_0, \delta V_D)$ was obtained up to an unknown length scaling factor L_0. Comparing with the relaxation experiment data, it was found that the non-linear shape of $T_{exc}(\delta V_D)$ can be reproduced using a reasonable micron-scale ℓ [30] (Figure 6.8.left). However, since two weakly interacting 1DCF branches cannot result in $T_{exc} < T_{exc}^{QPC}/\sqrt{2}$ at saturation, and we find that T_{exc} at long L saturates about $\approx 13\%$ *below* this lower bound (displayed as a dotted line in 6.5), this two channel theory cannot reproduce the absolute value of T_{exc}. Such discrepancy is significantly larger than experimental error bars. Although a good agreement data-theory was reached in [30] assuming *ad-hoc* the presence of a hidden third EC, one may wonder if the discrepancy results from the perturbative treatment of interactions. Importantly, the weak interaction hypothesis could not be checked in [30], due to the unknown length scaling factor in the theory.

Plasmon approach: Alternatively, density-density interactions between co-propagating 1DCFs can be handled non-perturbatively using the bosonization technique [55]. Motivated by the present experiment, T_{exc} was recently calculated in the bosonization framework [31].

Assuming strong interactions and a standard drift velocity 10^5 m/s, calculations are found to reproduce the measured non-linear shape of $T_{\rm exc}(\delta V_D)$ and also the energy relaxation length scale, without the need to introduce disorder [31] (Figure 6.8.right). However, the same lower bound $T_{\rm exc}^{\rm qpc}/\sqrt{2}$ was confirmed for arbitrary interaction strength between two 1DCF branches. In [31], the data are reproduced quantitatively by assuming *ad-hoc* 25% of the energy leaks out toward other degrees of freedom.

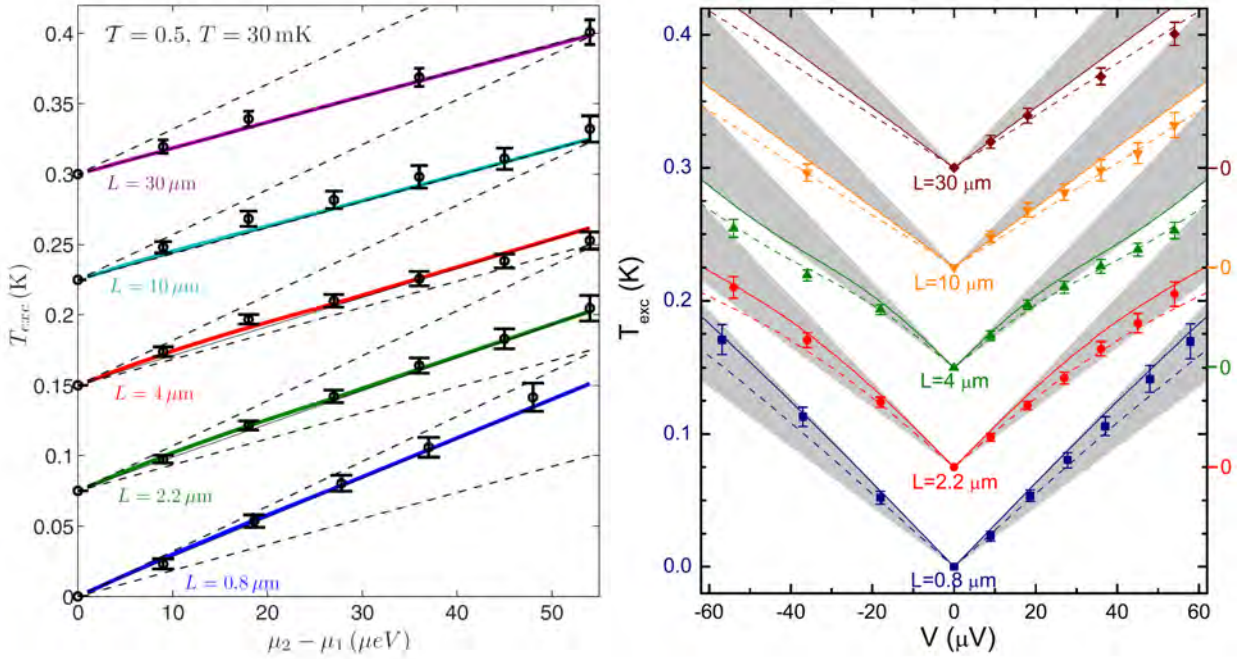

Figure 6.8: **Comparison of the energy relaxation data with two recent theories (see text).** Left: Figure extracted from [30] Right: Figure extracted from [31]. Both theories reproduce the non-linear shape and the energy relaxation length scale. The energy leak with respect to the predictions of both two channel models suggest a coupling towards additional co-propagating modes.

The main outcome of the data-theory comparisons strengthen the case that additional co-propagative excitations need to be taken into account.

6.3.3 Summing up

We have demonstrated that co-propagating edge-channels are *directly exchanging energy* without particle exchanges. This inelastic mechanism is efficient and the *energy currents carried by both edge-channels equilibrate* on about 10 µm. But even if is the main inelastic path, the observed energy leakage from the two channel, within the 1DCF basis, suggests that additional co-propagative additional excitations do step in.

These results are seemingly bad news regarding the quantum information potentialities of edge-channels following from the optical analogy since both rely on the non-interacting picture. However, we will further see it is possible to tune the energy relaxation in both up and down, recovering this seemingly lost potential.

Energy Relaxation in the Integer Quantum Hall Regime

H. le Sueur, C. Altimiras, U. Gennser, A. Cavanna, D. Mailly, and F. Pierre*

CNRS, Laboratoire de Photonique et de Nanostructures (LPN)—Phynano team, route de Nozay, 91460 Marcoussis, France

(Received 22 March 2010; published 27 July 2010)

We investigate the energy exchanges along an electronic quantum channel realized in the integer quantum Hall regime at a filling factor of $\nu_L = 2$. One of the two edge channels is driven out of equilibrium and the resulting electronic energy distribution is measured in the outer channel, after several propagation lengths 0.8 μm $\leq L \leq$ 30 μm. Whereas there are no discernible energy transfers toward thermalized states, we find efficient energy redistribution between the two channels without particle exchanges. At long distances $L \geq 10$ μm, the measured energy distribution is a hot Fermi function whose temperature is lower than expected for two interacting channels, which suggests the contribution of extra degrees of freedom. The observed short energy relaxation length challenges the usual description of quantum Hall excitations as quasiparticles localized in one edge channel.

DOI: 10.1103/PhysRevLett.105.056803 PACS numbers: 73.43.Fj, 72.15.Lh, 73.23.Ad, 73.43.Lp

The basic manifestation of the quantum Hall effect is a quantized Hall resistance $R_H = h/e^2\nu_L$, accompanied by a vanishing longitudinal resistance. In this regime, quantization of the two-dimensional cyclotron motion opens a large gap separating Landau levels in the bulk of the sample from the Fermi energy. The only available low energy excitations propagate along the edges, where the Landau levels cross the Fermi energy. The effective edge state theory suggests these excitations are prototypal one-dimensional chiral fermions (1DCF) [1], each of the ν_L edge channels (EC) being identified with a one-dimensional conductor. Because backscattering is forbidden by chirality, ECs are considered to be ideal ballistic quantum channels. Their similitude with light beams has inspired electronic analogues of quantum optics experiments [2–5] and proposals for quantum information applications [6]. However, the nature and decoherence of edge excitations are poorly understood, as highlighted by unexpected results obtained with electronic Mach-Zehnder interferometers: an unusual energy dependence of the interference fringes' visibility [2,7], a non-Gaussian noise [8], and a short coherence length [9,10]. Interactions between ECs and with their environment are seen as the key ingredient to explain these results (see, e.g., [11,12]).

In the present experimental work, we investigate the interaction mechanisms taking place along an EC through the energy exchanges they induce. A similar approach was previously used on mesoscopic metal wires [13] and on carbon nanotubes [14]. Here we focus on the filling factor $\nu_L = 2$, where two copropagating ECs are present, and at which the above unexpected results were observed. Our experiment relies on the techniques we recently demonstrated to drive out of equilibrium an EC and to measure the resulting energy distribution $f(E)$ of 1DCF quasiparticles [15]. There, we drove out of equilibrium only the outer EC, and $f(E)$ was measured in the same EC after a short 0.8 μm propagation distance, for which the energy redistribution is negligible. Here, we drive out of equilibrium selectively either the inner or the outer EC and probe $f(E)$ in the outer EC after various, much longer, propagation paths, up to 30 μm. The electronic energy transfers, including those within and between the ECs, are revealed through changes in $f(E)$ along the edge. This gives us access to the underlying interaction mechanisms.

The measured sample displayed in Fig. 1 was tailored in a two-dimensional electron gas realized in a GaAs/Ga(Al)As heterojunction of density 2×10^{15} m^{-2}, mobility $\mu = 250$ m^2 V^{-1} s^{-1}, and measured in a dilution refrigerator of base temperature 30 mK [16]. The relevant ECs are defined by voltage biased surface metallic gates

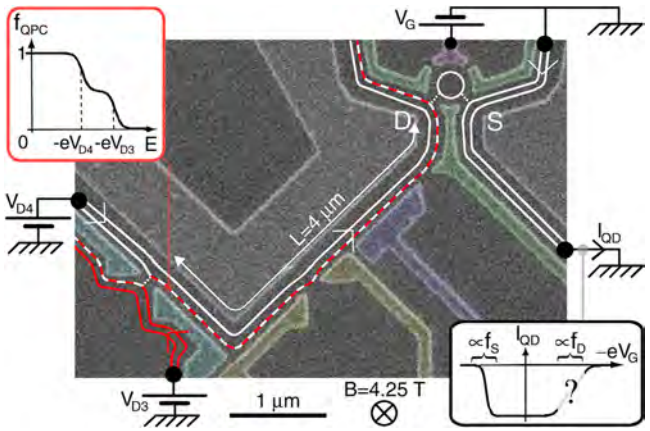

FIG. 1 (color online). Sample micrograph: metallic gates appear bright; the two widest gates (not colorized) are grounded. The current propagates counterclockwise along two edge channels (EC) depicted by lines. White dashed lines indicate intermediate EC transmissions. At the output of the voltage biased quantum point contact (left in figure), the electronic energy distribution is a double step (left inset) in the partly transmitted EC (dashed outer EC in figure). After an adjustable propagation distance ($L = 4$ μm in figure), the energy distribution f_D in the outer EC is measured using a quantum dot (white circle, see right inset).

(except a small portion defined by mesa etching for the longest propagation paths, see [16]). The energy distribution $f_D(E)$ in the outer EC at the drain (D) side of a quantum dot (QD, white circle in Fig. 1) is probed using the QD as an energy spectrometer, as has already been described in [15]: We record the differential conductance $\partial I_{\rm QD}(V_G)/\partial V_G \propto \partial f_D(E)/\partial E$, with $I_{\rm QD}$ the tunnel current across the small QD set to have a single active electronic level, while sweeping the voltage V_G applied to a capacitively coupled gate [15]. The path length $L \in \{0.8, 2.2, 4, 10, 30\}$ μm is tuned *in situ* by first choosing the pair of metallic gates that define the quantum point contact (QPC) at which a nonequilibrium energy distribution $f_{\rm QPC}$ is induced, and then by applying a negative voltage to selected gates to define the path between the QPC and the QD. A nonequilibrium smeared double step $f_{\rm QPC}(E)$ [15] is induced at the output of the voltage biased QPC selectively in the outer or inner EC by adjusting the QPC's conductance to $0.5e^2/h$ or $1.5e^2/h$, which are illustrated in Figs. 2(a) and 3(a), respectively.

First, we generate a nonequilibrium energy distribution in the measured *outer* EC [Fig. 2(a)]. The raw $\partial I_{\rm QD}/\partial V_G$ data are shown in Fig. 2(b) for several lengths L, at fixed QPC voltage bias $\delta V_D = 36$ μV. For the shortest propagation length $L = 0.8$ μm, we find a double dip close to expectations for noninteracting ECs and, consequently, that energy exchanges are small on this scale [15]. As L is increased the signal evolves toward a single dip. This demonstrates energy exchanges, which occur here on a characteristic length $L_{\rm inel} \approx 3$ μm [16]. At the two longest propagation paths, we find the *same* broad dip within experimental accuracy. It corresponds to a drain Fermi distribution of temperature $T_{\rm hot} = 85$ mK (solid lines on top of data at $L = 10$ and 30 μm), much larger than the equilibrium dip's temperature $T_{\rm eq} = 40$ mK (data at $\delta V_D = 0$ are shown for comparison as a dotted line). Complementary tests were performed to ascertain the observed energy exchanges are not artifacts [16].

We now investigate the interaction mechanisms responsible for the established energy exchanges. A simple mechanism could be the tunneling of charges between copropagating ECs, but we found it is here negligible [16]. In particular, anomalous quantum Hall effect measurements [17] showed that there is here no equilibration along the considered paths between the different electrochemical potentials of the two copropagating ECs. Important information to elucidate the interaction mechanisms can be obtained from the total energy $E_{\rm out}$ of the probed outer EC's 1DCFs. Let us consider several scenarios. (i) If interactions are essentially between 1DCFs in the same EC, then energy conservation in the stationary regime implies $E_{\rm out}$ is unchanged along the propagation path. On the other hand, (ii) if there is a significant interaction with thermalized states, such as the many quasiparticles within the surface metal gates along sample edges or the phonons, then $E_{\rm out}$ should relax toward its cold equilibrium

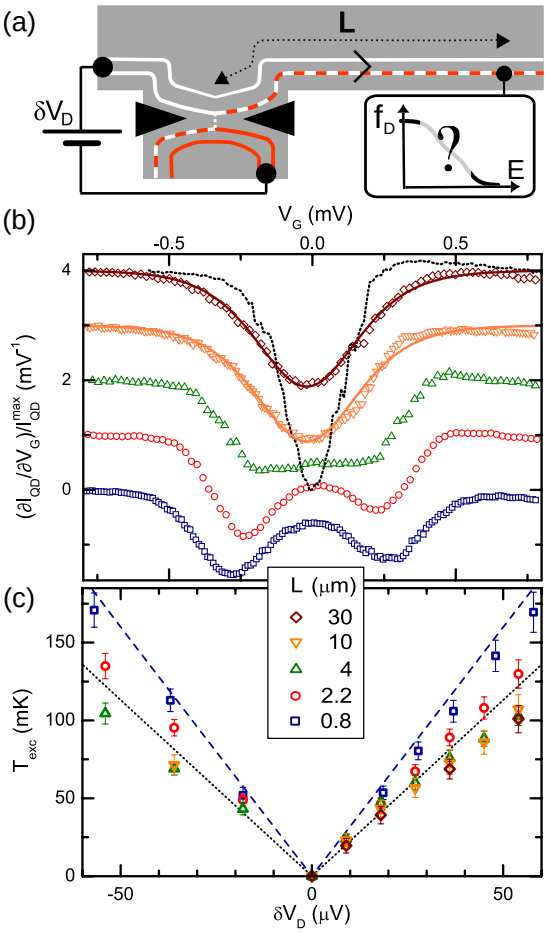

FIG. 2 (color online). (a) The outer EC is driven out of equilibrium. (b) Raw data (symbols) at $\delta V_D = 36$ μV, shifted vertically for several L. The nonequilibrium double dip relaxes over $L_{\rm inel} \approx 3$ μm toward a dip broader than the equilibrium dip at $\delta V_D = 0$ (dotted line). Solid lines are calculations with a Fermi distribution at 85 mK. (c) Excess temperatures extracted from the data (symbols) and prediction at the QPC output (dashed line). The outer EC cools down as L is increased and saturates at a value below expectations for two interacting ECs (dotted line, see text).

value $E_{\rm out}(\delta V_D = 0)$, or, if either the coupling constant or the density of these states vanishes at low energies, toward a fixed value at large δV_D. Last, (iii) if interactions are essentially with other copropagating states, then the injected energy redistributes. Therefore $E_{\rm out}$ should decrease to a value above $E_{\rm out}(\delta V_D = 0)$ by an amount proportional to the injected energy. The copropagating states could be the inner EC's 1DCFs or/and additional internal EC modes [18] that are predicted to exist in most situations due to edge reconstruction [19].

Figure 2(c) shows the outer EC's energy for various L and δV_D as the generalized excess temperature $T_{\rm exc} \equiv \sqrt{6[E_{\rm out} - E_{\rm out}(\delta V_D = 0)]/\nu\pi^2 k_B^2}$ (symbols), with ν the outer EC's density of states per unit length and energy. The ratio $E_{\rm out}/\nu$ can be obtained from f_D using

$$E_{\mathrm{out}}/\nu = \int (E-\mu)[f_D(E) - \theta(\mu - E)]dE, \quad (1)$$

with $\theta(E)$ the step function and μ the electrochemical potential (the full procedure to extract T_{exc} is detailed in [16]). We find T_{exc} relaxes as L increases, from a value very close to the QPC output prediction $T_{\mathrm{exc}}^{\mathrm{qpc}} = \sqrt{3}e|\delta V_D|/(2\pi k_B)$ (dashed line) at $L = 0.8$ μm, down to $T_{\mathrm{exc}} \approx (0.61 \pm 0.04)T_{\mathrm{exc}}^{\mathrm{qpc}}$ at $L = 10$ and 30 μm for $|\delta V_D| > 20$ μV. The saturation of T_{exc} at long propagation lengths to a value proportional to $T_{\mathrm{exc}}^{\mathrm{qpc}}$ at the QPC output is incompatible with significant dissipation toward thermalized states on the probed length scales [scenario (ii)]. Instead, this observation corresponds to expectations for interactions with copropagating states [scenario (iii)]. Last, energy exchanges between 1DCFs of the same EC [scenario (i)] are relatively weak compared to the dominant mechanism. Indeed, they preserve T_{exc}, whereas we find f_D and T_{exc} evolve on the same length scale, as seen in Figs. 2(b) and 2(c). Additional experiments not shown here further demonstrate that this energy exchange mechanism is negligible for $L \leq 10$ μm [20].

The data are compatible with energy redistribution with copropagating states, but which states? It is most natural to assume the 1DCFs of the two copropagating ECs exchange energy. This hypothesis can be tested directly by generating a nonequilibrium energy distribution in the inner EC ($G_{\mathrm{QPC}} \simeq 1.5e^2/h$), with f_D still being measured in the outer EC [see Fig. 3(a)]. Figure 3(b) shows raw data obtained in this configuration at $\delta V_D = 54$ μV for several L. We find that the dip broadens as L is increased, and therefore that the outer EC heats up. This unambiguously demonstrates energy exchanges between ECs. Figure 3(c) shows T_{exc} in the outer EC (symbols), which increases with L as expected from the raw data. Note that $T_{\mathrm{exc}}(L = 10$ μm) is approximately independent of which of the inner or the outer EC is driven out of equilibrium, as would be expected for a complete energy current equipartition between ECs.

These results are in qualitative agreement with recent investigations of dephasing at $\nu_L = 2$, which established current noise in one EC reduces phase coherence in the second EC [8,21]. The dephasing length $L_\phi(T) \simeq 20$ μm$/(T/20$ mK) [10] can be compared to the inelastic length. Using the injected excess temperature $T_{\mathrm{exc}}^{\mathrm{qpc}} = 115$ mK at $\delta V_D = 36$ μV, we find $L_\phi(115\ \mathrm{mK}) \simeq 3.5$ μm, similar to the corresponding $L_{\mathrm{inel}} = 2.5 \pm 0.4$ μm [16]. This strengthens the case for a same physical mechanism at the root of both dephasing and energy exchanges. However, contrary to dephasing [21], energy exchanges cannot be accounted for by low frequency noise within perturbation theories.

We now discuss different theoretical models aiming at explaining the present data. Within the widespread picture of 1DCF quasiparticles, the minimal approach is to include interactions between copropagating ECs as a small perturbation. However, in absence of disorder, energy exchanges between 1DCFs of different drift velocities v_D would be essentially suppressed, due to combined energy and momentum conservations. Therefore, it is crucial to assume a sufficient disorder to break momentum conservation. Motivated by the present work, Lunde *et al.* modeled inter EC interactions as a density-density coupling, where disorder changes the coupling coefficient along the edge with a correlation length ℓ [22]. Within this model, $T_{\mathrm{exc}}(L/L_0, \delta V_D)$ was obtained up to an unknown length scaling factor L_0. Comparing with the data, it was found that the nonlinear shape of $T_{\mathrm{exc}}(\delta V_D)$ can be reproduced using a reasonable micron-scale ℓ [22]. On the other hand, general arguments imply that two weakly interacting 1DCF branches cannot result in $T_{\mathrm{exc}} < T_{\mathrm{exc}}^{\mathrm{qpc}}/\sqrt{2}$ at saturation [16,22]. Surprisingly, we find T_{exc} at long L saturates about $\approx 13\%$ below this lower bound [displayed as a dotted line in Fig. 2(b)]. Such a discrepancy is significantly

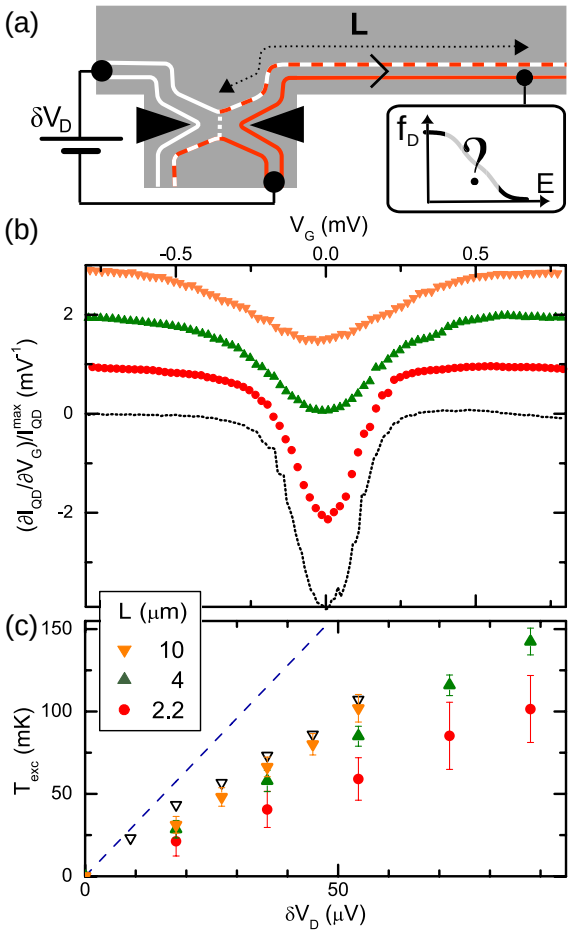

FIG. 3 (color online). (a) The inner EC is driven out of equilibrium. (b) Raw data at $\delta V_D = 0$ (dotted line) and $\delta V_D = 54$ μV (symbols), shifted vertically for several L. The dip broadens as L is increased. (c) Excess temperatures extracted from the data (full symbols) and prediction at the QPC output (dashed line). The outer EC heats up as L is increased, up to an excess temperature close to that when driving the outer EC out of equilibrium [$T_{\mathrm{exc}}(L = 10$ μm) in Fig. 2(c) are shown here as open symbols ($\bigtriangledown$)].

larger than experimental error bars. Although a good agreement data theory was reached in [22] assuming *ad hoc* the presence of a hidden third EC, one may wonder if the discrepancy results from the perturbative treatment of interactions. Note that the weak interaction hypothesis could not be checked in [22], due to the unknown length scaling factor in the theory.

Alternatively, density-density interactions between copropagating 1DCFs can be handled nonperturbatively using the bosonization technique [23]. Within this framework, edge states are depicted as collective magnetoplasmon modes. For strong enough interactions, these are fully delocalized over the ECs [12,24]. At filling factor 2, where the two ECs have opposite spin polarities, this yields spinless charge waves and chargeless spin waves propagating at different velocities. These edge states appear strikingly different from quasiparticles, where both charge and spin propagate at the same speed. Motivated by the present experiment, $T_{\rm exc}$ was recently calculated in the bosonization framework [25]. Assuming strong interactions and a standard drift velocity 10^5 m/s, calculations are found to reproduce the measured nonlinear shape of $T_{\rm exc}(\delta V_D)$ and also the energy relaxation length scale, without the need to introduce disorder [25]. However, the same lower bound $T_{\rm exc}^{\rm qpc}/\sqrt{2}$ was confirmed for arbitrary interaction strength between two 1DCF branches. In [25], the data are reproduced quantitatively by assuming *ad hoc* 25% of the energy leaks out toward other degrees of freedom.

The main outcome of the data-theory comparisons is that additional states need to be taken into account. Experimental observations, in particular, the saturation at the same hot Fermi distribution for both $L = 10$ and 30 μm, put stringent constraints on these states. The predicted internal EC modes mentioned in scenario (iii) seem plausible candidates. However, additional experiments not shown here demonstrate that 1DCFs and internal modes localized in the same outer EC do not exchange energy [20]. Although this weakens the internal modes hypothesis, note that energy exchanges with the inner EC's internal modes were not dismissed.

One conceptually important question concerns the nature of the pertinent edge excitations. Are these better described as Fermi quasiparticles localized in an EC or as delocalized bosonic collective states? The above comparison with theories did not permit discrimination. Nevertheless, the experimental results can be used to test whether the quasiparticle description is self-consistent. Indeed, a lower bound for the 1DCF's lifetime can be obtained from $L_{\rm inel}$, by using the range of drift velocities $v_D \in [0.5, 5] \times 10^5$ m/s measured in similar structures at $\nu_L = 2$ [16,26]. Applying the time-energy uncertainty relation, one finds for $\delta V_D = 36$ μV that the energy linewidth of 1DCF states $\Delta E > \hbar v_D/2L_{\rm inel} \in [6, 70]$ μeV is of the same order or larger than their characteristic energy $k_B T_{\rm exc}^{\rm qpc}(\delta V_D = 36\ \mu{\rm V}) \approx 10$ μeV, and therefore are ill-defined electronic edge excitations. Consequently, although the 1DCF representation of edge states is very powerful at short distances, the observed short $L_{\rm inel}$ challenges the description of quantum Hall excitations as quasiparticles localized in one edge channel.

The authors gratefully acknowledge discussions with A. Anthore, M. Büttiker, P. Degiovanni, C. Glattli, P. Joyez, I. Neder, F. Portier, H. Pothier, P. Roche, and E. Sukhorukov. This work was supported by the ANR (ANR-05-NANO-028-03).

*Corresponding author.
frederic.pierre@lpn.cnrs.fr

[1] B. I. Halperin, Phys. Rev. B **25**, 2185 (1982); M. Büttiker, *ibid.* **38**, 9375 (1988).
[2] Y. Ji *et al.*, Nature (London) **422**, 415 (2003).
[3] P. Samuelsson, E. V. Sukhorukov, and M. Büttiker, Phys. Rev. Lett. **92**, 026805 (2004).
[4] S. Ol'khovskaya *et al.*, Phys. Rev. Lett. **101**, 166802 (2008).
[5] I. Neder *et al.*, Nature (London) **448**, 333 (2007).
[6] R. Ionicioiu, G. Amaratunga, and F. Udrea, Int. J. Mod. Phys. B **15**, 125 (2001); T. M. Stace, C. H. W. Barnes, and G. J. Milburn, Phys. Rev. Lett. **93**, 126804 (2004).
[7] E. Bieri *et al.*, Phys. Rev. B **79**, 245324 (2009).
[8] I. Neder *et al.*, Nature Phys. **3**, 534 (2007).
[9] L. V. Litvin *et al.*, Phys. Rev. B **75**, 033315 (2007).
[10] P. Roulleau *et al.*, Phys. Rev. Lett. **100**, 126802 (2008).
[11] G. Seelig and M. Büttiker, Phys. Rev. B **64**, 245313 (2001); J. T. Chalker, Y. Gefen, and M. Y. Veillette, *ibid.* **76**, 085320 (2007); E. V. Sukhorukov and V. V. Cheianov, Phys. Rev. Lett. **99**, 156801 (2007); S.-C. Youn, H.-W. Lee, and H.-S. Sim, *ibid.* **100**, 196807 (2008); P. Degiovanni, Ch. Grenier, and G. Fève, Phys. Rev. B **80**, 241307(R) (2009).
[12] I. P. Levkivskyi and E. V. Sukhorukov, Phys. Rev. B **78**, 045322 (2008).
[13] H. Pothier *et al.*, Phys. Rev. Lett. **79**, 3490 (1997).
[14] Y.-F. Chen *et al.*, Phys. Rev. Lett. **102**, 036804 (2009).
[15] C. Altimiras *et al.*, Nature Phys. **6**, 34 (2010).
[16] See supplementary material at http://link.aps.org/supplemental/10.1103/PhysRevLett.105.056803 for additional experimental details, data, and analysis.
[17] B. J. van Wees *et al.*, Phys. Rev. Lett. **62**, 1181 (1989).
[18] I. L. Aleiner and L. I. Glazman, Phys. Rev. Lett. **72**, 2935 (1994); C. de C. Chamon and X. G. Wen, Phys. Rev. B **49**, 8227 (1994).
[19] D. B. Chklovskii, B. I. Shklovskii, and L. I. Glazman, Phys. Rev. B **46**, 4026 (1992); A. H. MacDonald, S. R. E. Yang, and M. D. Johnson, Aust. J. Phys. **46**, 345 (1993).
[20] C. Altimiras *et al.*, arXiv:1007.0974.
[21] P. Roulleau *et al.*, Phys. Rev. Lett. **101**, 186803 (2008).
[22] A. M. Lunde, S. E. Nigg, and M. Büttiker, Phys. Rev. B **81**, 041311(R) (2010).
[23] T. Giamarchi, *Quantum Physics in One Dimension* (Oxford University Press, USA, 2003).
[24] X. G. Wen, Phys. Rev. Lett. **64**, 2206 (1990).
[25] P. Degiovanni *et al.*, Phys. Rev. B **81**, 121302(R) (2010).
[26] H. Kamata *et al.*, Phys. Rev. B **81**, 085329 (2010).

Chapter 7

Tuning the relaxation of integer quantum Hall edge-channels

This chapter shows it is possible to tune the energy relaxation in both increasing it or freezing it [3]. First, we show it is possible to increase the relaxation up to full relaxation towards thermal equilibrium, by diverting a non-equilibrium edge-channel towards a voltage probe through an intermediate QPC . Such a scheme could be used to perform fast resets of flying Q-bits [126]. More surprisingly, we demonstrate it is possible to freeze the relaxation dynamics by closing the inner edge-channel in a small loop. We obtain inelastic lengths more than 4 times longer that could yield to a phase coherence length in the 1DCF basis beyond 100 μm at 20 mK, therefore recovering the potentialities of the optical analogy.

7.1 Driving the relaxation up with a voltage probe

We show it is possible to drive the system up to full relaxation by diverting the non-equilibrium edge channel towards a floating ohmic contact. The ohmic contact here plays the role of the so-called 'voltage probe' introduced by theorists to account for decoherence and energy relaxation within the scattering approach to quantum transport [32].

7.1.1 A voltage probe as a heat sink

Voltage probes act as reservoirs that absorb all incoming electronic quasiparticles and emit new quasiparticles with a Fermi statistics at the electrochemical potential dictated by current conservation or voltage bias. These absorption/emission processes mimic both the finite quantum lifetime and the energy relaxation toward thermal equilibrium of electronic excitations. In practice, the voltage probe is realized by a large ohmic (metallic) contact connected to the outer edge-channel (the setup schematic shown Figures 7.1 and 7.2.a). The impact of similar floating Ohmic contacts on current noise has previously been investigated [127]. More

recently, their dephasing properties were characterized using an electronic Mach-Zehnder interferometer [128]. Here we use an experimental setup that permits us to fully explore the relaxation of energy with such a voltage probe.

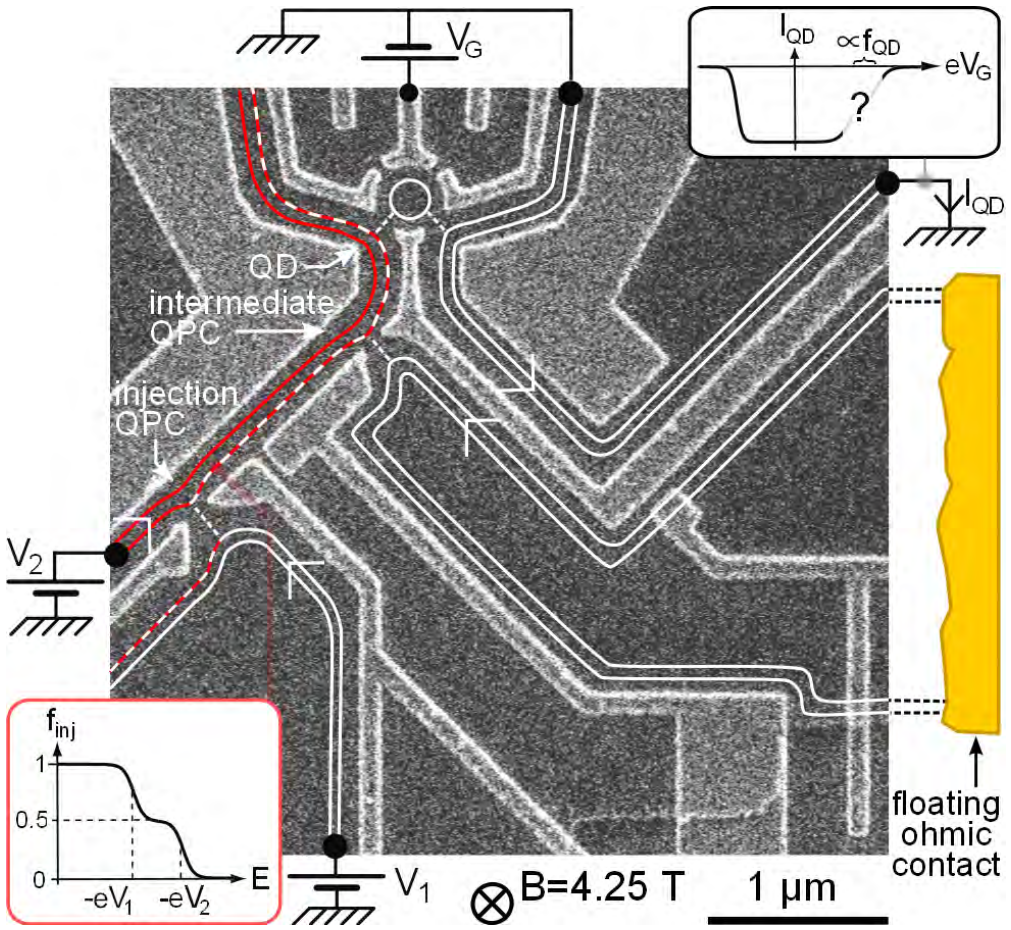

Figure 7.1: **Voltage probe setup.** Sample e-beam micrograph: metallic gates appear bright; the wide gates on the left and right of the quantum dot (QD) are grounded and can be ignored. Electronic excitations propagate counter clockwise along two edge channels (EC), depicted by lines. Dashed lines connecting ECs indicate transmission through quantum point contacts (QPC). At the output of the injection QPC, the energy distribution f_{inj} is a double step (left inset) in the half transmitted outer EC. Electronic excitations travel along adjustable paths from the injection QPC to the QD, and part of the outer EC can be diverted toward a floating ohmic contact by tuning the intermediate QPC's transmission. Right inset: the tunnel current I_{QD} through the QD is proportional to the energy distribution f_{QD} probed at the QD in the left outer EC.

7.1.2 Experimental principle

The experiment performed is as follows, see Figures 7.1 and 7.2.a. The injection QPC located $L = 2.2$ μm upstream of the quantum dot drives the outer edge-channel out of equilibrium at a voltage bias $\delta V = V_1 - V_2 = 36$ μV. The resulting non-equilibrium outer edge-channel propagates for 1.4 μm along the edge before it reaches the intermediate QPC across which it is partly transmitted, with a probability $\tau_{\rm im} = G_{\rm im}h/e^2 \in [0, 1]$, toward the floating ohmic contact (connected to the bottom right edge-channels in Figure 7.1). The energy distribution in the outer edge-channel is measured at the quantum dot, 0.8 μm downstream of the intermediate QPC.

7.1.3 Tuning $f(E)$ relaxation by changing the coupling to a voltage probe

Figure 7.2.b shows the raw data $(\partial I_{\rm QD}(V_G)/\partial V_G)/I_{\rm QD}^{\rm max}$ obtained for different intermediate QPC transmissions τ_{im} spanning from zero to full transmission (symbols). At $\tau_{im} = 0$, we observe a double dip that corresponds to significant but incomplete energy redistributions (see $L = 2.2$ μm in 6.3; note that the data shown here in Figure 7.2.b were obtained in a different cooldown). In contrast to this non-equilibrium double dip, the energy derivative of a Fermi function is a single dip whose width and inverse amplitude are proportional to the temperature. In the opposite limit, $\tau_{im} = 1$, we observe a narrow single dip fitted using a cold Fermi function at $T = 36$ mK (continuous line). This shows that edge-channels emitted by the floating ohmic contact are fully thermalized, and that they are not heated up along their way back to the intermediate QPC by the (nearby) opposite/counter-propagating hot edge states (see Fig. 7.1). At incomplete transmissions, the signal in Fig. 7.2.b exhibits a more complex shape that we now compare to predictions of the scattering approach.

Comparison to scattering approach predictions: The scattering approach predicts the energy distribution at the intermediate QPC's output is the sum of the distribution functions in the two incoming edge-channels weighted by their respective transmission probabilities τ_{im} and $1 - \tau_{im}$ [32]. Since interactions are ignored in this approach, it applies only if energy relaxation along the 0.8 μm path between the intermediate QPC and the quantum dot is small, which was shown to be the case in Chapter 3's article [1]. Energy relaxation occurring upstream of the intermediate QPC is taken into account by using the data at $G_{im} = 0$ as the reference signal that originates from the injection QPC.

The scattering approach predictions, shown as continuous lines in Figure 7.2.b, are the sum of the data measured at $G_{im} = 0$ and at $G_{im} = e^2/h$ weighted, respectively, by the independently measured reflection $1 - G_{im}h/e^2$ and transmission $G_{im}h/e^2$ probabilities of

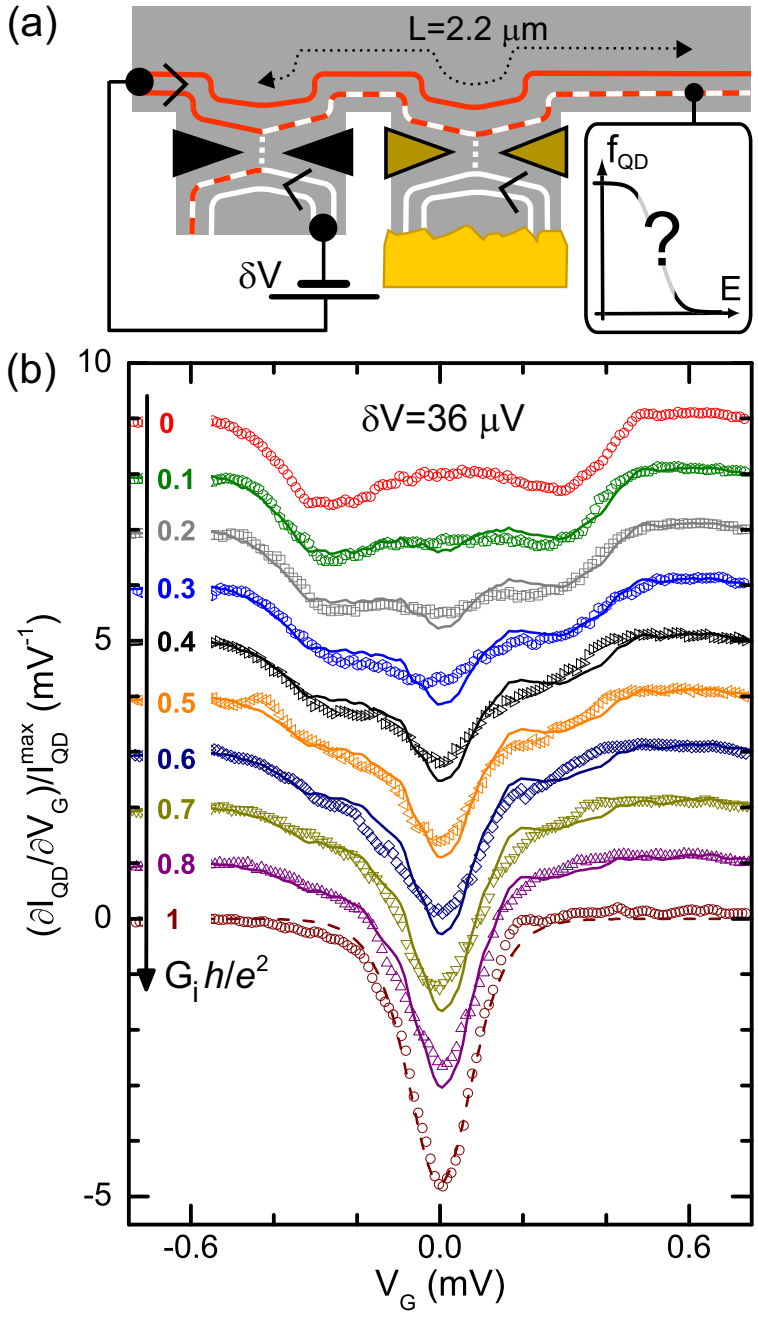

Figure 7.2: **Driving the relaxation with a voltage probe** (a) Experiment schematic: the outer edge channel's relaxation is forced by partly diverting it toward a floating ohmic contact, through the intermediate QPC (middle split gate) of conductance $G_\mathrm{i} \in [0, 1]\ e^2/h$. (b) Raw data (symbols) at $\delta V = 36$ μV are shifted vertically for different values of G_i. The dashed line is a Fermi fit ($T_\mathrm{fit} = 36$ mK). Continuous lines are the weighted sums of the data at $G_\mathrm{i} = 0$ and e^2/h, as predicted by the scattering theory.

the intermediate QPC. We find a good agreement, without fitting parameters, with the data.

This shows energy exchanges can be *tuned up to full relaxation* toward equilibrium, in

quantitative agreement with the scattering theory.

Regarding the inelastic mechanisms at work, the full thermalization measured at $G_{im} = e^2/h$, is found irrespective to the presence of the (nearby) opposite/counter-propagating hot edge states. This observation ensures that the energy loss found in the relaxation experiments cannot be accounted by a coupling towards opposite/counter-propagating edge-channels that could carry away the injected power.

7.2 Freezing the relaxation with a small loop

We now show that energy exchanges can be strongly reduced at $\nu_L = 2$, by closing the inner edge channel on itself along the outer edge channel's path.

7.2.1 Localized vs propagative edge-channels

When an edge-channel is closed to form a loop, it becomes a localized state. Therefore it cannot absorb energy in the stationary regime, unless it is coupled to thermalized excitations. Moreover, for small enough loops, the periodic boundary conditions yield to a discrete electronic spectra, which is expected to diminish the phase space available to the inter-channel interactions that were found to be the dominant interaction mechanism. We have implemented a closed loop setup in order to investigate the impact of such closed loops to the $\nu_L = 2$ relaxation dynamics.

7.2.2 Closed loop setup

The experiment schematic is shown in Fig. 7.4.a. For the intermediate QPC's conductance set to $G_{\rm im} = e^2/h$, the outer edge-channel is fully transmitted while the inner edge-channel is fully reflected at the QPC.

Defining a closed loop edge channel: Contrary to the previous setup to enhance energy relaxation, the transmitted outer edge-channel does not reach the floating ohmic contact. Instead, it is reflected toward the quantum dot by applying a sufficiently negative voltage to a surface metal gates barring the way (bottom right gate Fig. 7.1, or another gate further away: right gate in Figure 6.1). As a result, for $G_{\rm im} = e^2/h$ the inner edge-channel propagates on a shorter distance from injection QPC to quantum dot (set to $L_{in} = 2.2$ µm) than the outer edge-channel (selected between $L_{out} \simeq 10$ or 30 µm). The extra outer edge-channel propagation path takes place along *a closed inner edge-channel loop* of perimeter $L_{loop} = L_{out} - L_{in} \simeq 8$ µm or 28 µm.

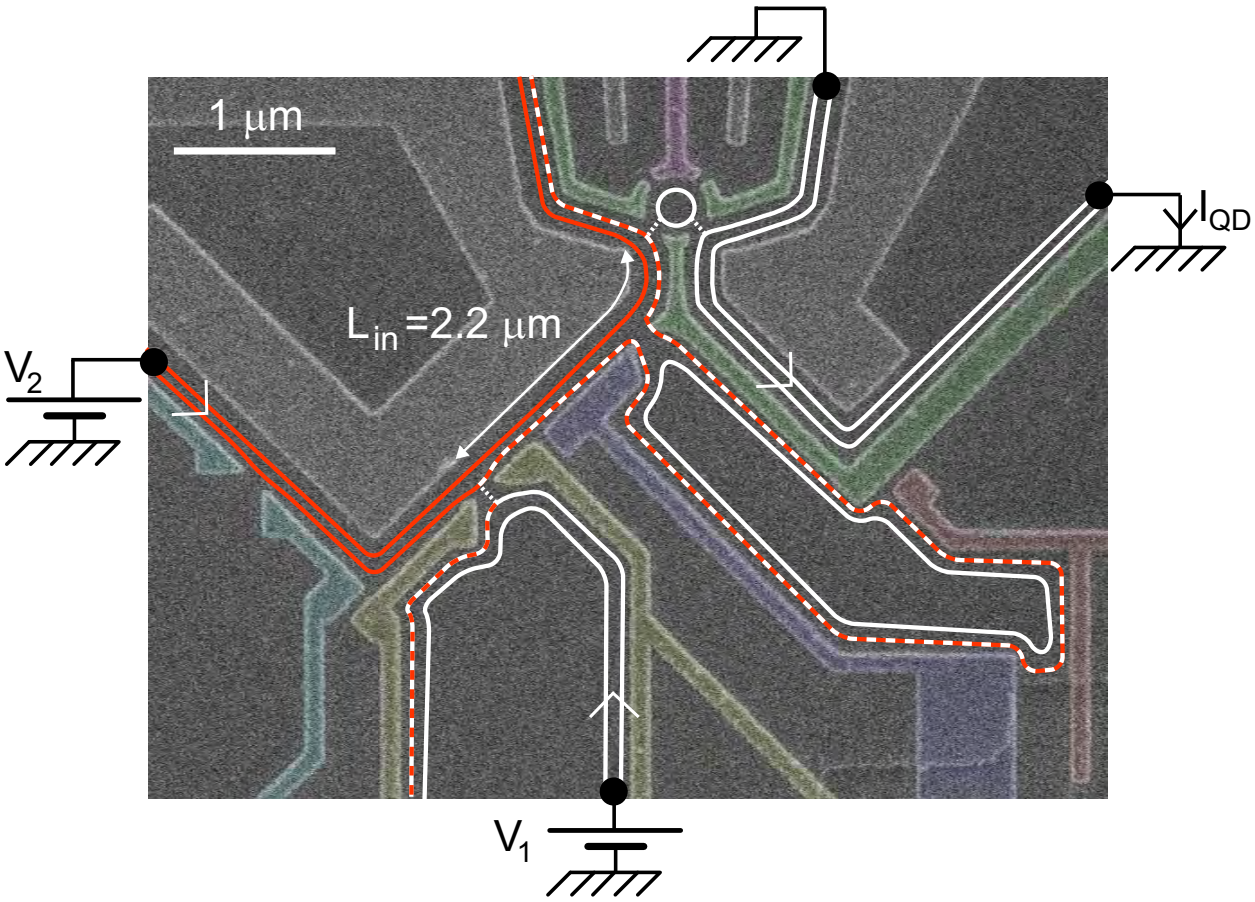

Figure 7.3: **Experimental realization of a closed loop setup** A non-equilibrium situation is generated in the outer edge-channel at a QPC (yellow gates) situated 2.2 µm uphill the quantum dot used to probe $f_D(E)$ in the outer edge-channel. An intermediate QPC (blue and green gates) tuned at $G_{QPC} = e^2/h$ fully reflects the inner edge-channel, while fully transmitting the outer edge-channel. The transmitted outer edge-channel is reflected by a second gate (red gate) towards the probe quantum dot, defining an extra propagation path along an inner-edge channel closed in a loop. The corresponding schematic is shown in Figure 7.1.a and the corresponding raw data, ($L_{in} = 2.2$ µm, $L_{out} = 10$ µm) in Figure 7.1.b.

Fully propagative geometries: For $G_{\rm im} = 0$ or $2e^2/h$, both the inner and outer edge-channels co-propagate along the same length $L = L_{in} = L_{out} \in \{2.2, 10\}$ µm.

In the following, we characterize the experimental configuration by the two propagation lengths (L_{in} (µm), L_{out} (µm)).

7.2.3 Small loop vs large loop

Relaxation measurements along a small loop: Figure 7.4.b shows as symbols the raw data obtained for $\delta V = -36$, 36 and 54 µV applied to the injection QPC. The striking

feature is that the data for $(2.2, 2.2)$ and those for $(2.2, 10)$ are *essentially identical*, up to our experimental resolution. This demonstrates directly that the energy distributions in the probed outer edge-channel remain unchanged in the extra 8 μm path along the inner edge-channel closed loop. The contrast is stark when compared to $(10, 10)$, where the outer edge-channel propagates on the same length as $(2.2, 10)$, but along a fully co-propagative (open) inner edge-channel path. Indeed, in the latter configuration the non-equilibrium double dip structure, that remained apparent for $(2.2, 2.2)$ and $(2.2, 10)$, is completely washed out and the energy distributions have relaxed toward hot Fermi functions (as stressed in Figure 6.3, continuous lines are the hot electron Fermi fits).

Therefore, closing the inner edge-channel on a 8 μm loop switches the intensity of energy exchanges in the outer edge-channel *from complete energy redistribution, to negligible*!

Relaxation measurements along a large loop: For the increased loop size of 28 μm obtained in the configuration $(2.2, 30)$, $f_D(E)$ now ends up similar to a hot Fermi function: the raw signal evolves towards a single dip that can be fitted by a Fermi function (Figure 7.4.b).

This shows energy exchanges reappear for 28 μm inner edge-channel's loops.

Energy currents: As in the precedent chapter, we obtain further quantitative information, by extracting the excess energy currents, carried by the single-particle excitations, characterized by the excess temperature T_{exc} (Equation 6.3).

Figure 7.5 shows as symbols the excess temperatures extracted from the data with a closed inner edge-channel as well as in the corresponding configurations with a fully co-propagative inner edge-channel. For completeness, we also give in Table 7.1 the Fermi fit temperatures corresponding to the continuous lines shown in Figure 7.4.b.

(L_{in}, L_{out}) (μm)	δV μV	$T_{\rm fit}$ (mK)
$(10, 10)$	-36	81
$(10, 10)$	36	83
$(10, 10)$	54	129
$(2.2, 30)$	-36	101
$(2.2, 30)$	36	108
$(2.2, 30)$	54	145

Table 7.1: **Fit temperatures corresponding to the continuous lines shown in Fig. 7.4.b.**

The main result is that the excess temperature *is identical*, at our experimental accuracy, in the configurations $(2.2, 2.2)$ and $(2.2, 30)$ despite the important energy exchanges taking

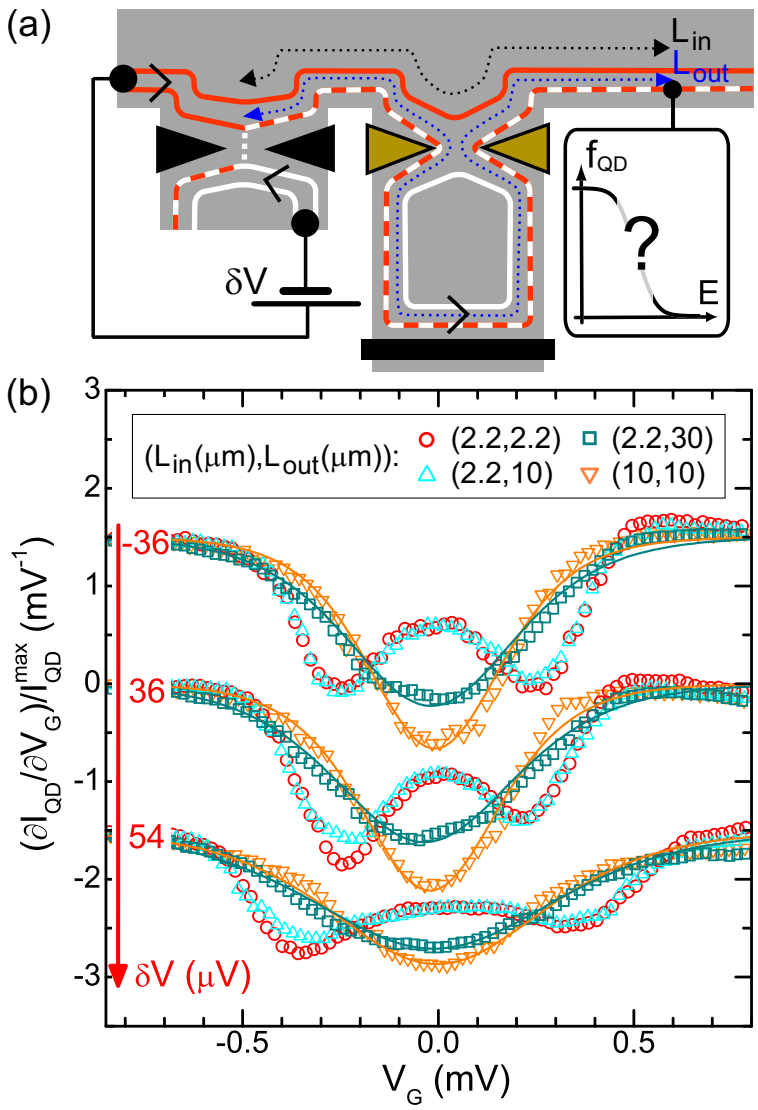

Figure 7.4: **Freezing the relaxation dynamics with a closed loop a** The non-equilibrium outer edge channel propagates partly along a closed inner edge channel's loop, except when $L_{in} = L_{out}$. **b** Raw data (symbols) for various (L_{in} (μm), L_{out} (μm)) are shifted vertically for the different $\delta V \in \{-36, 36, 54\}$ μV. The data for $(2.2, 10)$ are mostly unchanged from those for the short direct path $(2.2, 2.2)$. This implies that *energy exchanges are negligible* in the outer edge-channel along the 8 μm closed inner edge-channel loop. The contrast is stark with the data for the corresponding direct path $(10, 10)$, which exhibit a broad Fermi dip (continuous lines are fits with hot Fermi functions). The observed energy relaxation toward a broad dip for the larger 28 μm inner edge-channel loop of $(2.2, 30)$ shows the above freezing of energy exchanges depends on the loop's dimensions.

place in the latter (seen in Figure 7.4.b).

On the contrary, the full propagation configuration $(10, 10)$ displays substantially smaller excess temperatures.

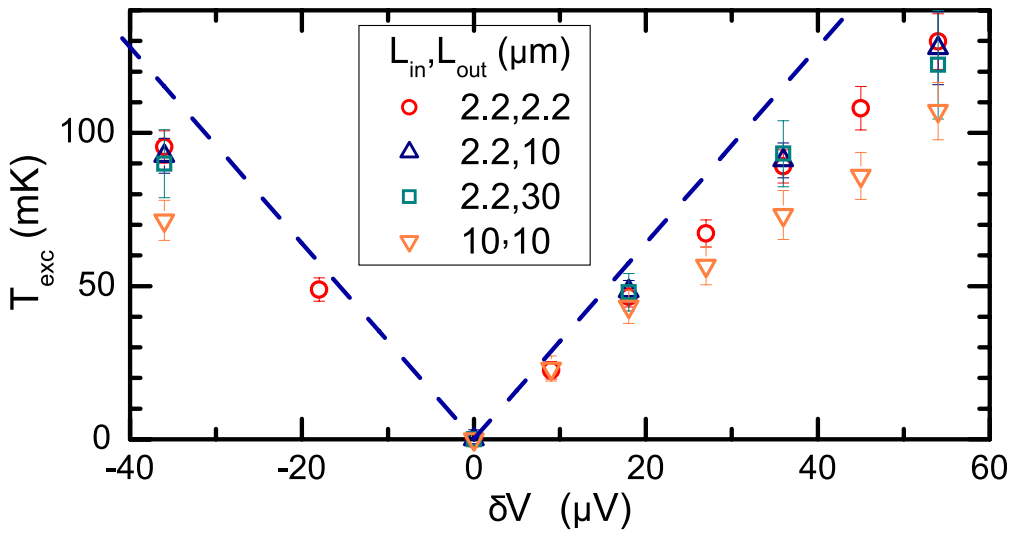

Figure 7.5: **Excess temperatures extracted from the raw data for various** $(L_{\rm in}, L_{\rm out})$ **configurations.** Fig. 7.4 shows some of the corresponding raw data. Both small $(2.2, 10)$ and large $(2.2, 30)$ closed loops yield to the same excess temperature found at $(2.2, 2.2)$, up to our experimental incertitude, so that the outer edge-channel does not loose its excess power along both small and large loops. The full propagation $(10, 10)$ excess temperature is sensibly lower.

7.2.4 Interactions vs. available phase space

We find experimentally that energy exchanges can be frozen over along a 8 μmloop, but recovered for a longer 28 μm loop. We attribute this behavior to the discreteness of energy levels in the closed inner edge-channel loop, whose spacing competes with the available energy. Indeed, for a 8 μm closed loop and using the standard $\nu_L = 2$ drift velocity $v_D \approx 10^5$ m/s (obtained from references in 6.3), the energy spacing $\delta E_{in} \approx 52$ μeV, is larger than or comparable to $e|\delta V|$. Since the available energy in the outer edge-channel is not sufficient to excite the discrete inner edge-channel's energy levels, energy exchanges between edge-channels, which were shown in the precedent chapter to be the dominant inelastic mechanism at $\nu_L = 2$, are frozen. This analysis is consistent with the observation of important energy exchanges for a 28 μm inner edge-channel closed loop: the corresponding spacing $\delta E_{in} \approx$ 15 μeV is smaller than $e|\delta V|$, therefore there is enough available energy to excite the discrete inner edge-channel's energy levels. This analysis is implicitly perturbative in interactions since the above estimates of available energy assume two-body collisions. However, similar conclusions can be reached within the non-perturbative bozonisation framework [1].

[1] P. Degiovanni, private communication.

7.2.5 Consequences on the inelastic mechanisms

The observation of frozen energy exchanges also provides important information regarding the inelastic mechanisms at work along the edge-channels at filling factor $\nu_L = 2$. These informations complement those obtained in the precedent chapter. In particular, the relaxation freezing implies that internal energy exchanges within the outer edge-channel are not only smaller than those with the inner edge-channel, but are *incontrovertibly negligible* on an 8 *um* length scale at the probed energies (while a complete energy redistribution was found at this length scale for both co-propagating edge-channels, Figure 6.3). This conclusion encompasses interaction with additional modes of the *outer* reconstructed edge-channel.

Second, it also encompasses energy exchanges between the outer edge-channel and bulk states located within the closed inner edge-channel loop, for instance due to disorder induced inhomogeneities in the density. Indeed, Figure 7.5 shows that the overall electronic energy probed at the quantum dot in the outer edge-channel is identical in the configurations $(2.2, 2.2)$ and $(2.2, 30)$, despite the important changes observed in the shape of $f_D(E)$. It also shows that energy redistribution with the predicted additional modes of the outer edge-channel are small also on the 28 µm propagation length.

Chapter 8

Conclusions and perspectives, $\nu_L = 2$ edge-channels

8.1 Non-interacting picture challenged

The single particle excitations of $\nu_L = 2$ exhibit *a strong energy relaxation* characterized by an inelastic length $L_{inel} = 2.5$ µm for non-equilibrium situations with an excess energy $k_B T_{exc} \simeq 10$ µeV. The corresponding higher bound to the single particle excitation quantum lifetime (found using the drift velocities measured in similar systems) yields to an excitation spectral width comparable to the characteristic excitation energy. *Therefore, our data strongly suggest that the single-particle particle excitations of $\nu_L = 2$ edge-channels have an ill-defined energy.*

8.2 Inelastic mechanisms at $\nu_L = 2$

Inter-channel interactions between 1DCFs excitations, *without particle exchanges*, are found to be the *dominant inelastic mechanism*, yet not the only one since we find an energy leak from the two channel system. This energy leak is compatible with interactions towards additional co-propagating modes, yet unidentified.

However, energy exchanges with the following excitations are ruled out by our observations:

- Thermalized excitations, such as lattice vibrations, spin states or electronic states in the metallic gates used to define the edge paths.

- Interactions within the outer edge-channel (including the predicted additional modes of the reconstructed outer edge-channel).

- Interactions with counter-propagating cold edge states flowing on opposite edges at about a 0.5 μm distance.

8.3 Towards macroscopic phase coherence?

We have found that the small closed loop technique freezes the relaxation dynamics for lengthes at least 4 times longer than the "natural" inelastic length, L_{inel}. We also expect it to increase the dephasing length, L_Φ, since closing the inner edge channel on a loop also suppresses its low frequency current fluctuations, which have been demonstrated to dephase the outer edge-channel [12, 23].

Moreover, the observed L_{inel} is comparable to L_Φ found at $\nu_L = 2$ [14], strengthening the hypothesis that a same physical mechanism is at the root of both dephasing and energy exchanges. Therefore, we expect that L_Φ would be increased by the same factor of 4, yielding to 80 μm dephasing lengths at 20 mK (4 times L_Φ found in [14]).

In practice, inner edge-channel loops are easily implementable by top-metallic gates in a comb geometry as presented in Figure 8.1.a, and are even compatible with optical lithographic techniques. Experiments relying on the optical analogy of the 1DCFs, could therefore be carried on the outer edge-channel for nearly macroscopic distances.

8.4 Towards plasmon interferometry?

Last, the energy currents redistribution found at 10 μm suggests a strong coupling between 1DCFs of both edge-channels. Since other excitations also step in, the system cannot be simply described with the charge and neutral plasmon modes predicted for two interacting channels. Nevertheless, these bosonic modes can be longer lived than the single particle excitations, and could be used as quantum channels [31] to perform quantum information experiments.

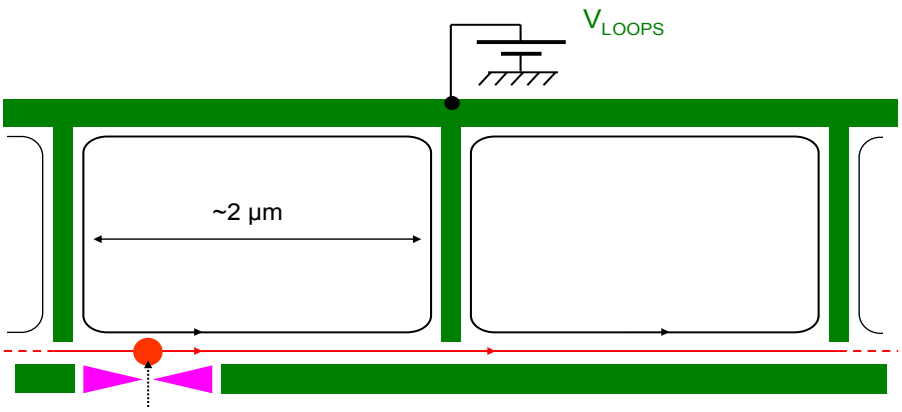

Figure 8.1: **Possible implementation of the the closed loop technique.** Inner edge-channel forming a series of small quantizing loops (of about 2 μm diameter) realized with a top-metallic gate in a comb geometry are expected to yield to higher dephasing lengths for the 1DCFs excitations in the outer edge-channel.

Chapter 9

Energy transport in the fractional quantum Hall effect

9.1 Introduction

As stressed in the introductive chapter to this part, very little is known about the detailed microscopic features of fractional quantum Hall (FQHE) edge channels. The 2DEG used to investigate the $\nu_L = 2$ integer quantum Hall effect (IQHE) has a high enough electron mobility, $\mu_e \simeq 2\ 10^6$ m.s^{-1}, and develops clear 4/3 and 5/3 plateaus, as can be seen in Figure 3.1. In this chapter, we present an investigation of the edge dynamics at $\nu_L = 4/3$, from the viewpoint of energy transport, similar to that realized at $\nu_L = 2$. Although, this work is still in progress, the first results already illustrate the power of our experimental approach. In particular, our preliminary investigations of the $\nu_L = 4/3$ FQHE demonstrate a coupling between edge channels and neutral bulk excitations.

9.1.1 Edge channels at $\nu_L = 4/3$

The edge dynamics of the $\nu_L = 4/3$ fractions have been described theoretically by a series of articles by Kane and Fischer [42, 43], within the chiral Luttinger liquid (CLL) formalism [38]. The $\nu_L = 4/3$ fraction has two co-propagating edge-channels:

- The outer edge-channel results from the completely filled $S = +1/2$ spin branch of the lowest Landau level. It can be pictured as a non-interacting branch of one dimensional chiral fermions (1DCFs).

- The opposite spin branch of the lowest Landau level has a $\nu_{L,\downarrow} = 1/3$ filling factor. It gives rise to a co-propagating edge-channel described as a CLL of Laughlin quasiparticles with $q = 3$ (a 1/3 fractional charge density wave, in the hydrodynamic picture).

The (electrochemical) equilibration length between both co-propagating edge channels, l_μ, is expected to diverge at low temperatures [108], even in the presence of impurity assisted scattering. Therefore, each edge channel is expected to carry its own potential on large distances.

9.1.2 Experimental approach

In order to probe the low energy physics of FQHE edge channels, we follow the proposal of Kane and Fischer [43] of using energy transport experiments. Our setup will be slightly different from their proposal though.

Heat transport properties of $4/3$ edge channels

Heat currents in the FQHE: As a general rule, Kane and Fischer found [43] that in the FQHE, the chiral heat current carried by edge channels, J_H, at temperature T reads:

$$J_H = \nu_H \frac{\pi^2}{6h} T^2 \tag{9.1}$$

where ν_H is the difference between the number of chiral and antichiral edge channels at one edge. The quantity ν_H is a topological invariant characterizing the fractional edges [38] and is independent of the microscopic parameters of the sample. The heat conductance simply reflects the difference between chiral and antichiral modes.

Heat current in $4/3$ edges: Since the FQHE at $\nu_L = 4/3$ presents two co-propagating edge channels, it corresponds to $\nu_H = 2$, and the edge chiral heat current $J_H^{4/3}$ reads:

$$J_H^{4/3} = \frac{\pi^2}{3h} T^2. \tag{9.2}$$

If the edge channels are uncoupled to other excitations, heat transport is ballistic, and gives no more information (even less) than charge transport. However, it can reveal acoupling with other states.

Experimental tools

We have used a non-equilibrium toolkit similar to the one demonstrated in the precedent chapters to probe edge dynamics, in the $\nu_L = 4/3$ FQHE. A voltage biased quantum point contact (QPC), of partial transmission, is used to create a non-equilibrium situation in the coupled edge channels. Second, the energy at a different location is probed with an energy filter. Since we are mainly interested in testing the chirality of the heat current, a qualitative heat filter is sufficient. We have used a tunnel coupled island, displaying a Coulomb blockade gap, as a high pass energy filter.

One may wonder why we do not use exactly the same setup as for the $\nu_L = 2$ experiments, since it has proved to give quantitative results in the IQHE. However, we did not manage to operate the quantum dot in a canonical regime at $\nu_L = 4/3$, since we systematically found multiple resonant levels with a $\sim k_B T$ spacing forbidding us to extract quantitative information.

Experiment description

We have used two QPCs tuned to half transmission as heat sources. A 3rd QPC displaying Coulomb diamonds is used as high pass energy filter. Therefore, even if the energy filter only provides qualitative information on the probed excitations, the setup permits us to perform a direct, one to one, comparison of the local heating for an edge channel driven out-of-equilibrium upstream and downstream the probe. The setup is depicted in Figure 9.1.

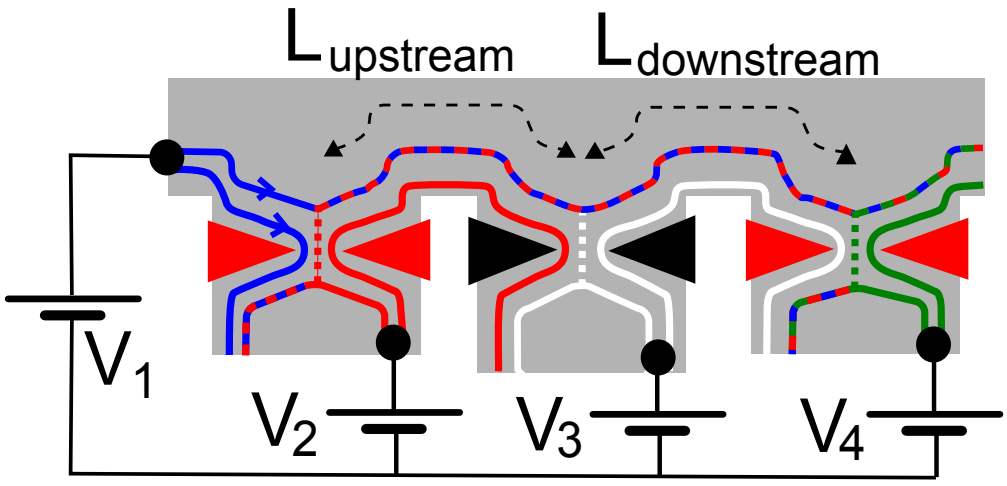

Figure 9.1: **Experimental principle.** Two QPCs tuned to half transmission (red) locally drive out of equilibrium an edge channel upstream and downstream an intermediate QPC (black). The intermediate QPC is used as an energy filter to probe qualitatively the local energy in between the sources. This scheme permits to compare the chiral and antichiral heat currents contributions to the probed energy.

We have implemented this setup at $\nu_L = 4/3$, where the edge heat currents are expected to be chiral. Already this "simple" fractional state has revealed new surprising features. First, we have observed an anti-chiral energy current in non-equilibrium situations, whereas the charge current flows downstream with the expected chirality. Second, we demonstrate that this anti-chiral heat current is not due to a plain local "killing" of the local FQHE(for instance, due to local thermally activated transport). Last, we show that the antichiral heat current is carried by neutral bulk excitations.

In the following, we first characterize the 4/3 FQHE properties of our sample. Next we will show that in our sample, a QPC exhibits a Coulomb blockaded gap when tuned in the tunneling regime. We will exploit this energy dependence on its transmission signal in order to perform the energy transport experiments.

9.2 Sample characterization

In this section we characterize the 4/3 FQHE properties of our sample, which is the same sample used to investigate the $\nu_L = 2$ IQHE in the previous chapters. First, we extract the transport fractional gap $\Delta_{4/3}$ from thermally activated transport measurements. Second, we show that the co-propagative edge-channels can be selectively biased and probed with QPCs. Last, we show that they can carry their own potentials in the active region of our sample.

Bulk characterization

Measurement setup: We have measured the Hall and longitudinal resistance with a three contact measurement. We label the contacts following the edge chirality (Figure 9.2.a). The current I is injected in contact (3) and flows along the perimeter before impinging on contact (1). The intermediate contact (2) is connected to a cold ground.

The potential V_1 equals the current impinging on contact 1 times its 2 wire resistance to the ground $R_{4/3} = \frac{3}{4}\frac{h}{e^2}$. The resistance $(V_3 - V_1)/I$ measures the "longitudinal" resistance plus the polarization wire resistance R_S. In the $\nu_L = \{3, 2, 4/3\}$ plateaus, it saturates at low temperature to a finite value $R_S = 290\ \Omega$ corresponding to the series wire resistance at high magnetic fields. Therefore, the longitudinal resistance reads $R_L = \frac{V_3 - V_1}{I} - R_{sat}$.

Thermally activated transport measurements: In the thermally activated regime $k_B T \lesssim \Delta_{4/3}$, thermal fluctuations yield to a moderate population of single particle excitations across the fractional gap $\Delta_{4/3}$. In consequence, the longitudinal resistance follows an Arrhenius activation law $R_L(T) \propto \exp(-\Delta_{4/3}/2k_{\mathrm{B}}T)$. Figure 9.2.b presents the Arrhenius plot of the longitudinal resistance in two distinct regions of the sample. Region 1 is homogeneous, and we find no residual backscattering from contact 3 to 2, while region 2 is not homogeneous due to sample processing[1] (there is a small backscattering, 2% of the polarization current[2], from contact 3 to 2). From the Arrhenius plot, we identify a linear dependence in the range of $T \in [100, 300]$ mK, corresponding to a fractional gap $\Delta_{4/3}/k_{\mathrm{B}} = 315 \pm 10$ mK and $\Delta_{4/3} = 335 \pm 10$ mK respectively for regions 1 and 2.

[1] After processing we find a dark shape in the middle of region 2, but nowhere else.

[2] Which increases the "series resistance" to $\sim 600\ \mathrm{k}\Omega$

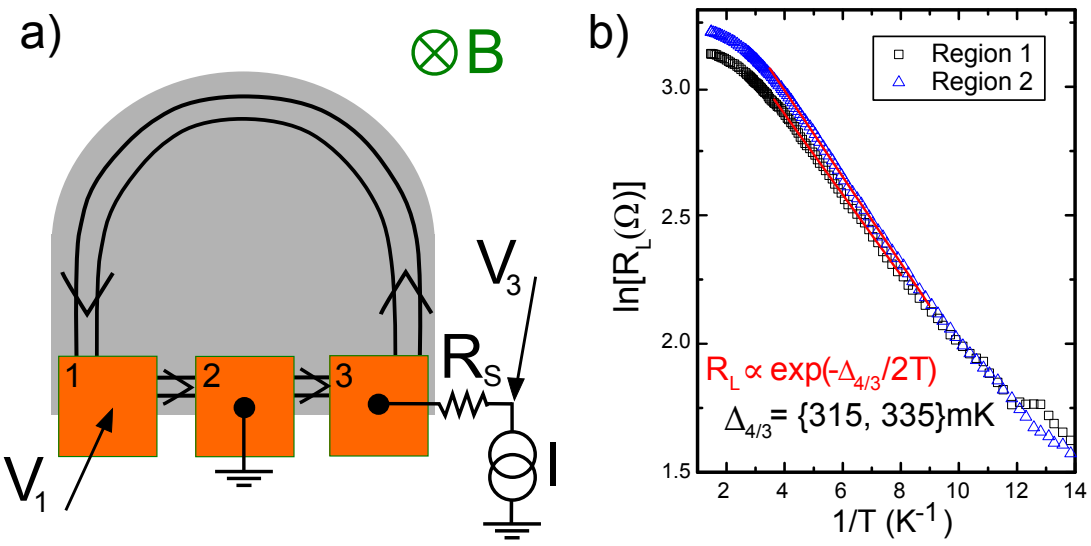

Figure 9.2: **Determination of the thermal activation transport gap. a)** Schematic of the three contact scheme used to measure the longitudinal resistance R_L B) Arrhenius plot of the longitudinal resistance measured in two distinct regions of the sample (see text). The Arrhenius plot reveals an activated transport dependence $R_l(T) \propto \exp(\Delta_{4/3}/2k_{\mathrm{B}}T)$ in the $T \in [100, 300]$ mK range. Linear fits give the activation gaps $\Delta_{4/3}/k_{\mathrm{B}} = \{315, 335\} \pm 10$ mK.

These thermal activation measurements integrate over the sample surface and are sensitive to disorder. The resulting transport excitation gap $\Delta_{4/3}$ is therefore smaller than the intrinsic excitation gap Δ characterizing the FQHE. This is due to the disorder energy enlargement Γ of the discrete energy levels, so that $\Delta = \Delta_{4/3} + \Gamma$ [102]. We can roughly estimate the Landau level broadening Γ from the onset of the measured Hall plateaus. We measure an offset at about $B^* \simeq 200$ mT, so that the Landau level broadening $\Gamma \simeq \hbar\omega_C(B^*)$ is about $\Gamma/k_B \simeq 2.5$ K. The resulting fractional gap reads:

$$\Delta/k_{\mathrm{B}} = (\Delta_{4/3} + \Gamma)/k_{\mathrm{B}} \simeq 2.8\mathrm{K} \tag{9.3}$$

and is in rough agreement with the 4/3 fractional gap extracted from the 3/2 composite fermion masses found in the literature [104]. For this, we extrapolate the $\sqrt{B}$ dependence of the composite fermion mass, m_{eff}, found at $B = 2.9$ T in [104]. This leads to an effective mass in our working conditions:

$$m_{eff}(B = 6\ \mathrm{T}) = \sqrt{\frac{6}{2.9}} 0.42 m_{\mathrm{e}}, \tag{9.4}$$

which corresponds to the fractional gap:

$$\frac{\Delta}{k_{\mathrm{B}}} = \frac{\hbar e B_{eff}}{k_{\mathrm{B}} m_{eff}} = 2.89\ \mathrm{K}$$

where B_{eff} is the effective magnetic field seen by the composite fermions: $B_{eff} = 3(B - B_{\nu_L=3/2})$. This value is compatible with our transport characterization (9.3).

Edge characterization

We first check that our QPCs can be used to selectively populate either co-propagating edge-channel. We further verify that both co-propagating channels can carry their own potentials in the active region of our sample (shown in Figure 6.1).

Selective population by a QPC: Using a similar scheme as depicted in Figure 9.2.a, we have probed the current reflected, I_{ref}, by a QPC as a function of its gate bias V_{QPC}. The corresponding plot (Figure 9.3) reveals two current steps. The most negative gate voltage current step matches the $\frac{3}{4}$ step expected from the reflection of the integer outer edge channel. While the higher voltage conductance step matches the expected contribution 1/4 of a fully reflected fractional inner edge channel. The large gate voltage range of the intermediate plateau ~ 0.35 V ensures that the integer and fractional edge channels can be distinctly populated by a voltage biased QPC.

Anomalous quantum Hall effect measurement: By tuning two consecutive QPCs in the intermediate plateau, we have selectively populated and probed the chemical potentials of the co-propagating edge-channels in the active region of our sample (see Anomalous Hall effect in Chapter 2). Even in non-equilibrium situations and electrochemical potential differences between co-propagating channels up to 200 μeV we find no electrochemical equilibration in the tested 2 μm paths (two consecutive QPCs in the region surrounded by a grounded gate in Figure 6.1).

9.3 Coulomb blockade in a quantum point contact

Our approach to probe a local energy relies on the non-linearity of a mesoscopic conductor. In our samples, the QPCs exhibited Coulomb diamonds when the fractional outer edge channel is in the low transmission regime. This can be seen when plotting their inner edge channel transmission as a function of the QPC's gate and bias voltage, (Figure 9.4). This feature results most probably from the residual disorder present in our sample. If a local scatterer is found close to the QPC, it may create a small resonant level sensitive to charging effects.

The transmission remains null up to a charging energy ΔE_C, and after a sharp increase evolves slowly (Figure 9.4. right inset). Such abrupt change can be used as a high pass energy

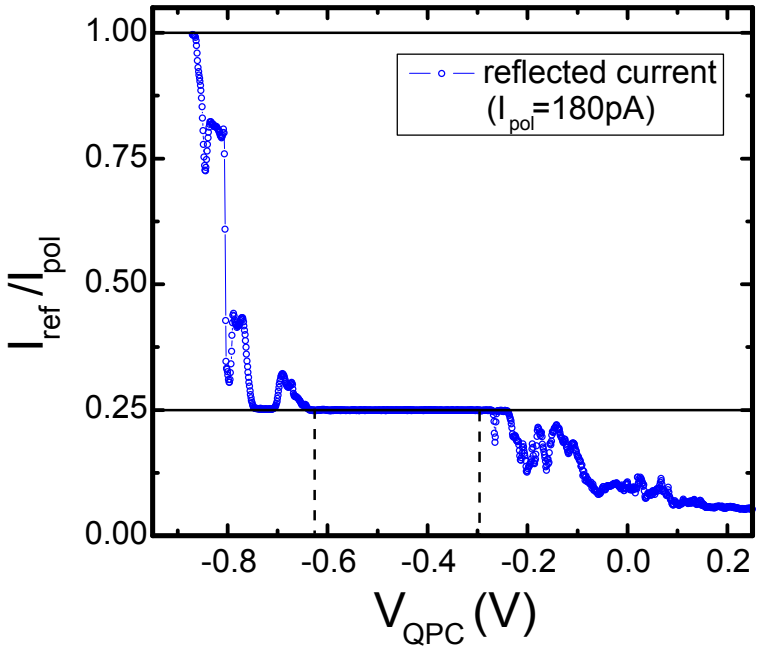

Figure 9.3: **Current reflected by a QPC vs its gate voltage in the 4/3 FQHE.** The reflected current reveals two successive steps. Full reflection of the inner edge channel saturates at 1/4 of the polarization current, I_{pol}. Full reflection of the outer edge channel increases the reflected current by $0.75I_{pol}$. The (fractional) inner edge channel yields to a $1/3e^2/h$ two wire conductance, while the (integer) outer edge channel to e^2/h. The large intermediate plateau ensures that both edge channels can be selectively populated.

filter. Most notably, the addition gap ΔE_C can be tuned by sweeping the gate voltage (V_G). This permits to sweep the energy range of the probed excitations.

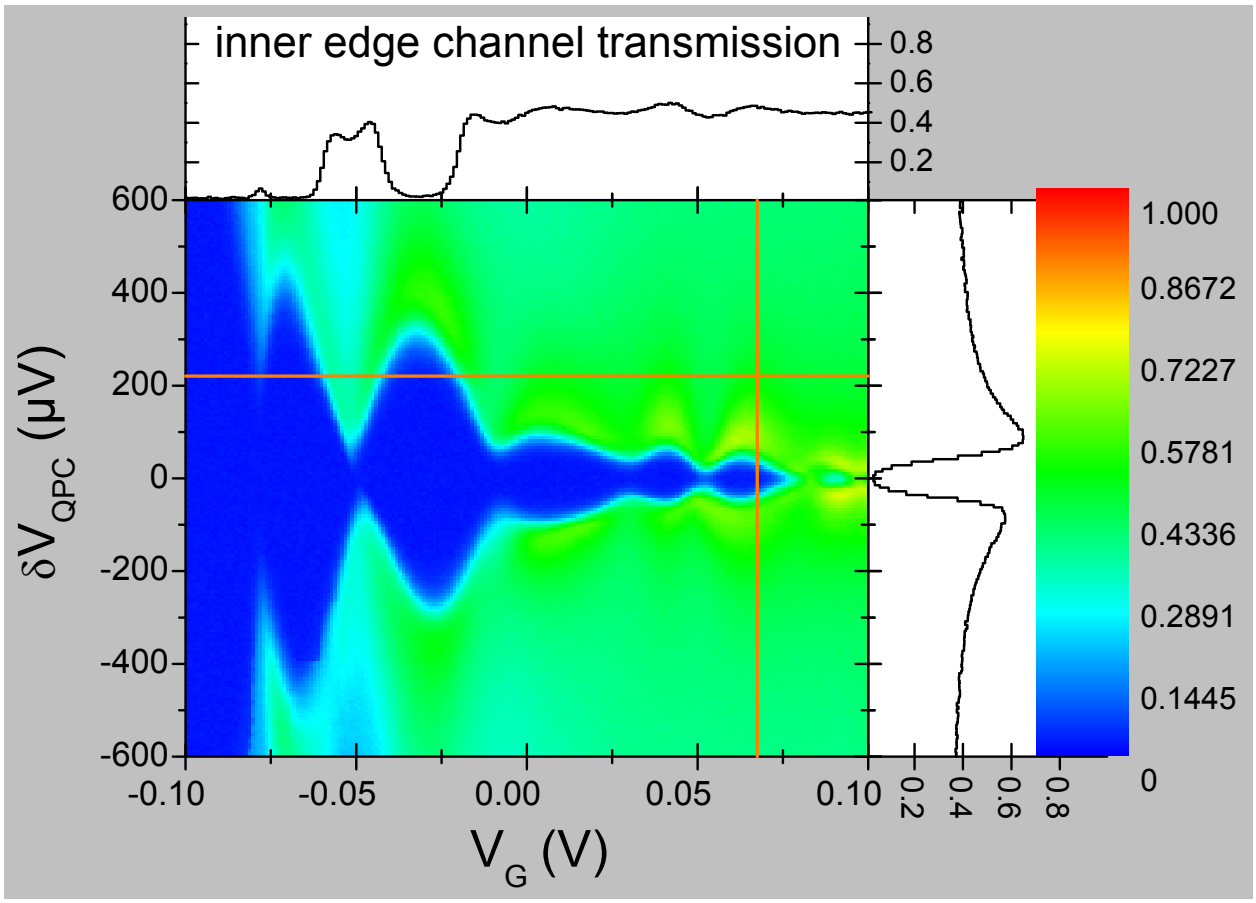

Figure 9.4: **Coulomb diamonds in a QPC.** Color plot of the inner edge channel transmission by a QPC in the high backscattering regime (blue: vanishing transmission, red: unity transmission). The inner edge channel transmission presents sharp Coulomb diamonds as a function of gate and bias voltages. In most of the probed range, the transmission only presents sharp feature across the diamonds. The resulting energy dependent transmissions (right inset for a representative gate voltage) can be used as high pass energy filter. The energy cut-off is given by the edges of the blockaded region diagram, and can be tuned by sweeping the gate voltage.

9.4 Energy transport measurements

9.4.1 Charge vs heat chirality

Setup: We first tune the energy filter to a small addition gap $\Delta E_C \simeq 30$ μeV. The energy filter probes the electronic excitations at energies higher than the addition gap.

We tune both injection QPCs to half transmission for the inner edge channel. They are tuned to display the smallest possible energy dependence in the used bias windows. We systematically checked that the resulting reflected DC current is linear up to 5% changes in the slope. We name QPC1 and 2 the injection QPCs placed respectively upstream and downstream the energy filter.

The "as the crow flies" distance between the QPC 1(2) to the energy filter is 1.5 μm (1.4 μm). The three QPCs are directly connected by chiral edge channels as pictured in Figure 9.1. The edge distance along the edge channel path connecting the QPC 1(2) to the energy filter is l_{edge} =1.8 μm (1.4 μm).

Anti-chiral heat flow: We bias the injection QPC 1(2) at $\delta V_{1(2)}$, while keeping the voltage difference across the energy filter null[3]. We show in Figure 9.5 the color plot of the energy filter transmission τ as a function of δV_1 and δV_2. The energy filter increases with the upstream bias δV_1 as expected from the edge channels chirality. The striking feature is that it depends on the downstream bias δV_2. This demonstrates the presence of an anti-chiral heat flow.

Chiral charge flow: All along the energy transport measurement, we test the charge flow chirality. We do so, by injecting a small AC current $I_{AC} = 9.1$ pA across QPC 2 at small frequency f (< 100 Hz). This modulation permits to trace the origin of the injected current. Performing lock-in measurements, we find that the current impinging, at frequency f, to a contact connected by chirality to QPC 2 matches I_{AC} (at our absolute accuracy of 0.1 pA). Moreover, we find that no current at frequency f impinges in the contacts situated beneath QPC 1 and beneath the energy filter (contacts recovering the chiral edge channels at the bottom of Figure 9.1). Therefore, charge transport follows the edge chirality in the non-equilibrium situations.

Thermal killing? One may wonder if the anti-chiral heat flow is due to a plain thermal killing of the FQHE on the heated regions, since $\Delta_{4/3} \sim \Delta E_C$. However, it can be discarded with the following arguments. First, the observation of a chiral charge transport

[3]We neglect the $\lesssim 5\%$ energy dependence of QPC 1 transmission for doing so.

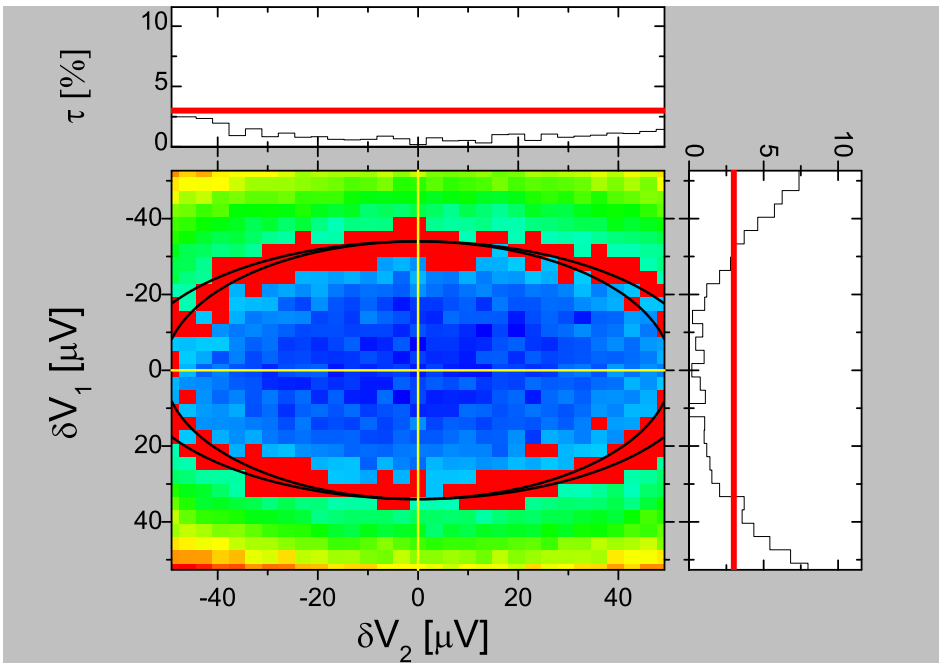

Figure 9.5: **Antichiral heat flow.** Color plot and projections of the energy filter transmission for the inner edge channel, as a function of the bias applied to the heat injection QPCs 1 and 2. The transmission depends on the bias applied to QPC2 placed downstream the detection point, revealing an antichiral heat flow. Red points: intercept of the data with a $\tau = 0.03 \pm 20\%$ plane. The signal presents an elliptical symmetry $\tau = f(V_1^2 + \alpha V_2^2)$. Continuous lines: ellipses of aspect ratio $\alpha = 2.5 \pm 0.3$, and small axis R_1 =34 μV.

seems incompatible with a thermally activated transport. More importantly, the signal symmetry manifest in Figure 9.5 permits to discard this mechanism. Indeed the energy filter transmission presents an elliptical geometry with respect to the injection QPC biases. Such particular geometry implies that the energy filter signal is a function of $\delta V_1^2 + \alpha \delta V_2^2$ only, with an aspect ratio α.

We estimate the aspect ratio by intercepting the data with a $\tau = 0.03 \pm 20\%$ plane (red points in Figure 9.5. right), and adjusting the corresponding graph with an elliptic function. Note that only the signal in the low transmission limit is meaningful, since at finite transmissions the energy filter itself perturbs significantly the probed edge channel. We find an aspect ration $\alpha = 2.5 \pm 0.3$.

Now, since the energy injected by QPCs 1 and 2, $E_{QPC\,1/2}$, scale with $\delta V_{1/2}^2$, we find that the energy filter signal is a function of $E_{QPC\,1} + \alpha E_{QPC\,2}$ only:

$$\tau(E_{QPC\,1}, E_{QPC\,2}) = f(E_{QPC\,1} + \alpha E_{QPC\,2}).$$

Therefore, the antichiral heat flow contribution to the energy filter signal appears to be *unsensitive* to the energy injected upstream.

9.4.2 Coupling to bulk excitations

Setup: In order to test wether the antichiral heat current is carried by edge or bulk excitations, we set the QPC2-energy filter direct distance "as the crow flies" to d =2.2 µm, but change the edge path between them with the help of top metallic gates. We can use an intermediate QPC to fully transmit[4] both co-propagating edge channels towards a floating ohmic contact (Figure 9.6.b). When the intermediate QPC is closed, we have l_{edge} = 2.2 µm (Figure 9.6.a). Therefore, we can change the edge channel path linking the probe QPC to the injection QPC. The ohmic contact path permits us to perform a stringent test of wether the antichiral heat flow is carried by edge excitations: Since the ohmic contact forces the relaxation of the incoming edge excitations, there can be no counter propagating heat flow along the edge in this configuration.

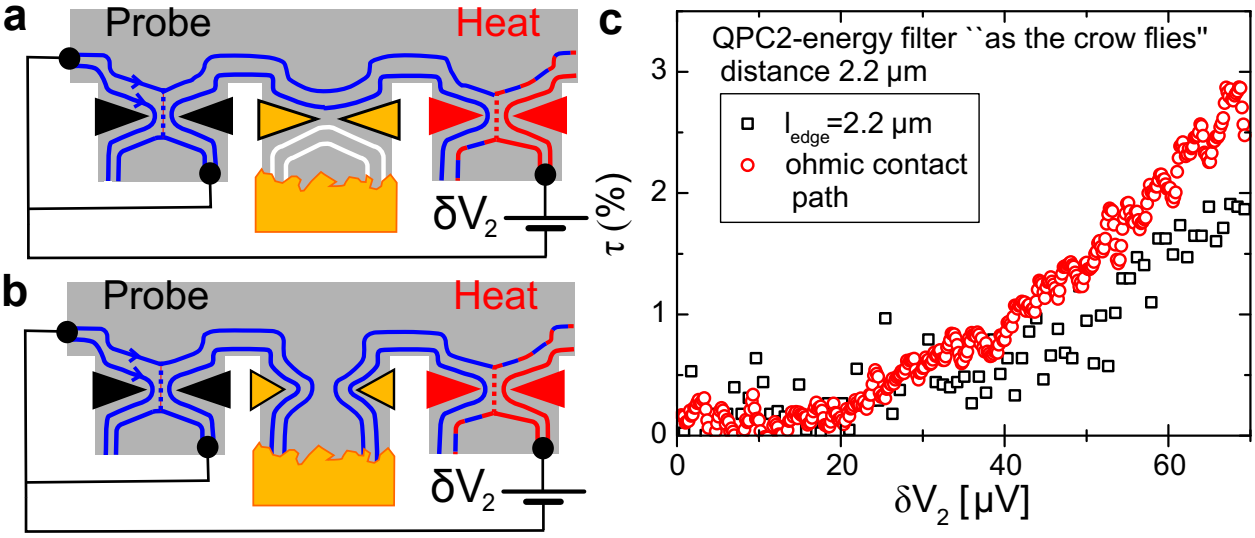

Figure 9.6: **Coupling to bulk excitations.** **a** Schematic of the $l = edge$ =2.2 µm setup. **b** Schematic of the ohmic contact setup. **c** Energy filter transmission τ as a function of the downstream QPC 2 bias δV_2 in four distinct situations. The distance "as the crow flies" between QPC2 and energy filter is set to d =2.2 µm. QPC 2 is tuned to half transmission for the inner edge channel. □: The edge channel linking the energy filter to QPC2 has a propagation length l_{edge} =2.2 µm. ▽: the edge channel is fully diverted to a floating ohmic contact between QPC2 and the probe QPC (see b). Both setups give similar antichiral heat flow signals.

Measurements: We show in Figure 9.6.b the probe QPC transmission, τ, as a function of the downstream QPC bias δV_2, for the four edge path situations: l_{edge} = 2.2 µm and the ohmic contact path. The fact that the probe QPC signal depends on the downstream bias in

[4]Inner edge channel transmission > 92% even in non-equilibrium situations.

the ohmic contact path setup, shows directly that some energy is carried by bulk excitations. Note that a direct comparison with the $L_{edge} = 2.2\mu$m is not possible, since the probe QPC is not exactly the same[5]. The main point is that we find at l_{edge} =2.2 μm a similar counter propagating heat flow signal.

These measurements give evidence for a coupling between the non-equilibrium edge channel and bulk excitations. Since no antichiral charge flow was found, these bulk excitations are neutral.

9.4.3 Energy dependence of the antichiral heat current

We further characterize the bulk excitations carrying the antichiral heat current by investigating the dependence of the aspect ratio α as a function of the low energy cut-off ΔE_C. The energy dependence is found compatible with spin excitations or neutral quasielectron/hole collective excitations.

Setup: We come back to the initial setup depicted in Figure 9.1, but tuning the energy filter to different addition gaps ΔE_C. This yields to different low energy cut-offs for the the probed excitations (changing V_G in Figure 9.4).

Measurements: Figure 9.7 shows the energy filter transmission, as a function of the upstream and downstream QPC biases, $\tau(\delta V_1, \delta V_2)$, for different addition gaps ΔE_C. We have intercept all measurements data with a same plane[6] $\tau = 0.03 \pm 20\%$, that we adjust with an ellipse of aspect ratio α and principal axis $R = \delta V_2(\tau = 0.03)$. The aspect ratio, α, characterizes the relative contribution to the local energy signal of the downstream heating with respect to the upstream heating. The principal axis, R, characterizes the applied bias on the downstream QPC to achieve an energy signal $\tau = 3\%$. We present the addition gap dependence of α and R in Figure 9.8.

We find that the bias needed to obtain a 3% transmission signal roughly scales linearly with the addition gap: $R \sim 2\delta V_2$ (Figure 9.8.b), validating that indeed, we are probing energies higher than the addition gap. As we increase the probed energies, the aspect ratio diminishes (Figure 9.8.a). The exact energy dependence is difficult to interpret, since the geometry is quite complicated (for instance, the edge channel driven out of equilibrium may not only couple to the bulk excitations, but also to the outer edge channel too which is fully transmitted besides the probe QPC). However, we observe that the aspect ratio diminishes

[5]Due to the capacitive coupling between the probe QPC and the intermediate QPC. A large gate voltage range had to be swept between a fully transmitting QPC situation, and a fully reflecting situation (see e.g. Figure9.3)

[6]The value of 3% is high enough to achieve a reasonable signal to error ratio, while slow enough so that the measurement does not perturb the probed edge channel.

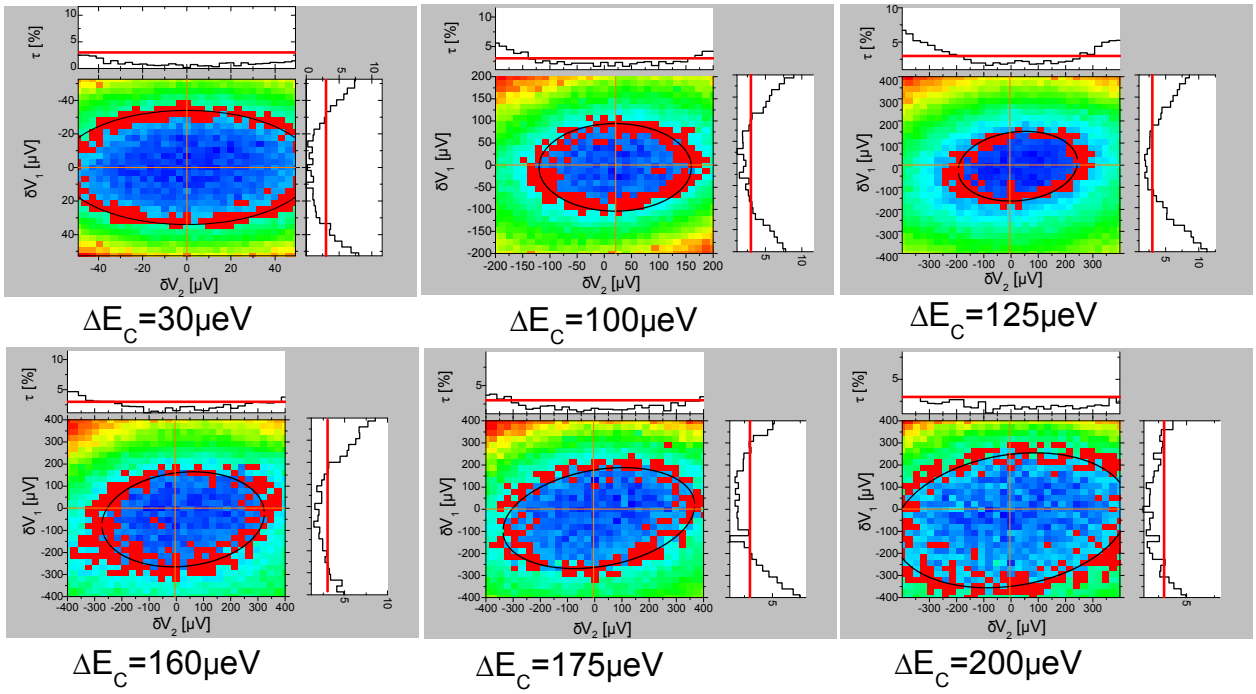

Figure 9.7: Raw data $\tau(\delta V_1, \delta V_1)$ for different addition gaps $\Delta E_C \in \{30\ \mu\text{eV}, 200\ \mu\text{eV}\}$. The "as the crow flies"distance between energy filter and QPC 1(2) is $d_{1(2)} = 11.5\ \mu\text{m}(1.4\ \mu\text{m})$. The aspect ratio diminishes as the addition gap increases.

at higher energies. Therefore, the upstream and downstream contributions to the probed energies tend to equilibrate at higher energies.

Nature of the coupled bulk states? Assuming, as predicted, that bulk excitations are gapped [77, 129], no bulk excitations should contribute in the zero energy limit. Therefore, the aspect ratio should diverge[7] at low energies. We use $\alpha = 2$ to define the characteristic energy scale. It corresponds to a chiral heating two times more effective than the antichiral heating. The characteristic energy scale is about 100 μeV.

What could be these bulk states? The presence of quasielectron/hole neutral collective bulk excitations [129], and neutral spin density waves [77] are predicted. We now compare these excitation gaps to our findings:

i) The 4/3 FQHE is spin polarized [76], since the upper spin branch ($s = -1/2$) of the lowest partial level is partially filled, while the lower spin branch is completely filled ($s = +1/2$). This spontaneous symmetry breaking gives rise to gapless spin excitations in the small Zeeman coupling limit [77]. However, the Zeeman energy imposes a spin excitation gap $\Delta_S = g\mu_B B$ imposed by Larmor's theorem. The Zeeman gaps for plain electrons and

[7] We cannot probe energies lesser than ~ 30 μeV, since when the probe QPC has sharp features within this energy range, the transmission is not in the $\tau << 1$ limit.

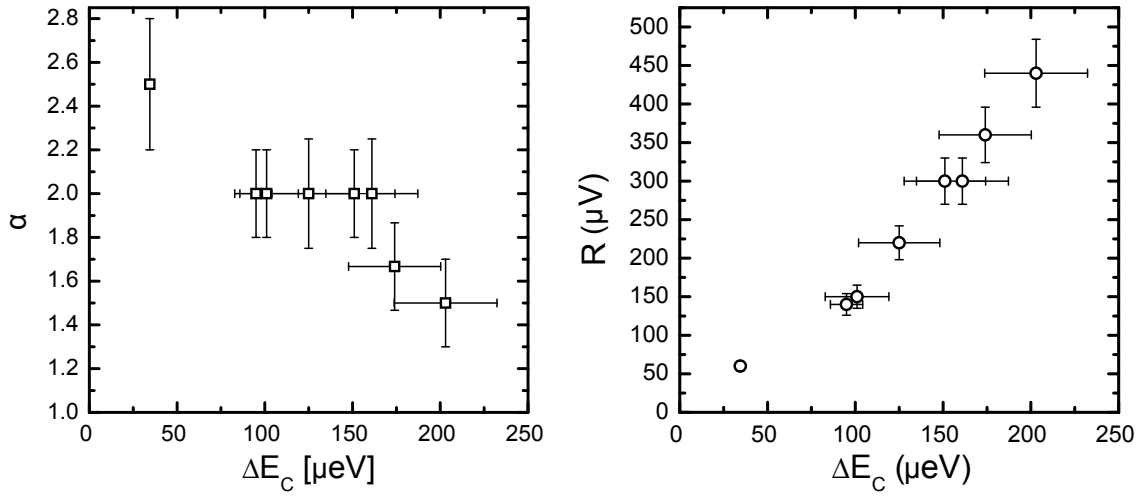

Figure 9.8: **Energy dependence of the aspect ratio α and the principal ellipse radius** $R = \delta V_2(\tau = 0.03)$ Black squares: ellipse aspect ratio, decreases with the energy filter addition gap. Red circles: Principal ellipse axis $R = \delta V_2(tau = 0.03)$, represents the downstream bias δV_2 needed to obtain a significant energy filter signal, at a given ΔE_C. We find roughly scales with the addition gap. Horizontal error bars reflect the bias asymmetry of the Coulomb diamonds (see Figure 9.4, where $\Delta E_C(V_D > 0) \neq \Delta E_C(V_D < 0)$). Vertical error bars reflect the uncertainty on adjusting the data at $\tau = 0.03 \pm 20\%$ with an ellipse. They are typically about 20%.

composite fermions are respectively $\Delta_S^e = g\mu_B B \simeq 150$ μeV and $\Delta_S^{CF} = g_{eff}\mu_B 3(B - B_{\nu_L=3/2}) \simeq 30$ μeV. For composite fermions, we took the effective mass (9.4) and the same gyromagnetic factor as for plain electrons [104].

ii) Quasielectron/hole bulk collective excitations display a magneto-roton minima at about the 10% of the fractional gap Δ [129]. The magneto-roton minima corresponding to our bulk characterization, $\Delta(9.3)$, is about 25 μeV (9.3).

All expected gapped excitations are therefore compatible with the observed energy dependence of α.

Ellipse bending: A second feature we can see in Figure 9.8 is that the elliptic shape bends for higher addition gaps. We remind that all outer edge channels are fully transmitted, that δV_1 is the voltage difference of QPC1 symmetrically voltage biased, while $\delta V_2 = (\frac{3}{4} + 0.5\frac{1}{4})R_Q I^{pol}_{QPC2}$ is the voltage difference of QPC2 which is current polarized. Therefore, if the QPC1 transmission where different from 1/2 for the inner edge channel, the real voltage difference across QPC2 would depend on both δV_2 and δV_1 as we have defined. This would result on a rotation in the $\delta V_1, \delta V_2$ plane. However, we systematically checked that the differential transmission of QPC1 remains close to 1/2 up to 10% and that the 2 wire voltage

drop across QPC2 matches $(\frac{3}{4}+0.5\frac{1}{4})R_Q I^{pol}_{QPC2}$ up to the percent. We have therefore no good explanation for such bending.

Reproducibility: All the observed features have been reproduced in several runs (different cool downs) and with a second sample within the same chip.

Similar effects arise when heating the outer edge channels upstream and downstream QPCs (QPC two wire conductance set to $0.5e^2/h$), but measuring the inner edge channel[8]. These measurements are sensitive to direct energy exchanges between co-propagating edge-channels heated upstream, and to energy exchanges with bulk excitations in both upstream and downstream injections. We find that the aspect ratio evolves from 1.2 to 1 in a similar same energy range.

9.5 Conclusion and perspectives

The investigation of the 4/3 FQHE had to be stopped since our sample was deadly injured by a voltage source disfunction. Our results are therefore preliminary and incomplete. However, our data illustrates the power of our experimental approach since it already reveals a coupling between edge channels and neutral bulk excitations. But, we have not been able to carry a systematic investigation on such bulk excitations.

Further work would need to extract a quantitative heat transport measurement (with a quantum dot for instance), at least on the outer edge channel which is expected to have linear tunneling density of states. This could be used to extract a reliable value for the corresponding coupling. A systematic distance dependence on the bulk signal should can performed with well suited geometries in order to characterize the transport regime of these bulk excitations.

On another direction, our approach is already well suited to the probe the chirality of energy currents. It can be directly implemented to investigate the elusive neutral antichiral modes predicted for some special filling factors [42] like 2/3 or 5/3. If bulk excitations were also excited in these regimes, a setup using an ohmic contact would permit to separate the antichiral heat flows carried by bulk and edge excitations.

[8] We only observed Coulomb diamonds in the low tunneling regime of the inner edge channel. Not in the outer edge channel, whose transmission step is much more abrupt than for the inner one (see Figure 9.3).

Part II

Dynamical Coulomb blockade in a model short coherent conductor

Chapter 10

Dynamical Coulomb blockade in short coherent conductors

10.1 Impedance composition laws in quantum circuits

A central question of quantum electronics is how do quantum conductors behave when placed in an electric circuit. This is important since the possibility to combine different quantum conductors in a same circuit may open the path to new functionalities. However, it is a problem far more complex than its classical counterpart for two main reasons.

First, if two conductors are composed in a circuit within distances shorter than the phase coherence length L_Φ, the non locality of the electronic wave function impedes to distinguish them as distinct conductors. In consequence, one has to solve the full quantum problem in order to predict the circuit's dynamics. This can be dealt within the scattering approach to quantum transport in the DC [47] and AC [130] responses. For example, we can cite the Aharonov-Bohm oscillations arising in small rings [131], the Fabry-Pérot resonances arising in double-barriers [50] or even the universal relaxation times arising in mesoscopic RC circuits [132].

The second reason is important even for well defined conductors, separated by distances longer than L_Φ. When taking into account the Coulomb interaction, the quantum fluctuations of charge arising in quantum conductors may couple them to their electromagnetic environment. In quantum circuits the main electromagnetic environment is the series impedance seen by the conductor. Therefore, the transport properties of a quantum conductor depend on the circuit in which it is embedded. This interaction effect is called dynamical Coulomb blockade [133, 134] and can be handled within a (phenomenological) quantum description of the whole electric circuit (see [46] and references therein).

In order to understand how the dynamical Coulomb blockade modifies the usual impedance composition laws, I will briefly remind the description of classical circuits. I will further show how to describe a quantum circuits: First, by presenting the scattering approach to quantum transport across a quantum conductor. Second, by presenting the quantum description of a macroscopic circuit. Last, I will discuss the mechanism by which the microscopic quasiparticles flowing through a quantum conductor couple to the macroscopic degrees of freedom of the surrounding circuit.

10.1.1 Classical circuits

In classical circuits [135] a circuit element is fully characterized by the constitutive relation linking its dynamical degrees of freedom, namely the current flowing through it, I, and the voltage drop across it V. The constitutive relations are usually encapsulated in the frequency dependent impedances $Z(\nu)$, by $V(\nu) = Z(\nu)I(\nu)$, or admittances $Y(\nu)$, by $I(\nu) = Y(\nu)V(\nu)$. The dynamics of a complex circuit follow from the linearity of Maxwell's equations and Kirschoff's laws (the nodal law for currents and the string law for voltages). These constraints determine the classical circuit composition laws: Impedances add in series, while admittances add in parallel.

Kirschoff's laws can be seen as kinematic constraints on the circuit's dynamical degrees of freedom and should not change in a quantum circuit. Indeed, the nodal law follows from charge conservation, while the string law follows from energy conservation. Nevertheless, it is the circuit dynamics, and the very description of a single circuit element, that change in a quantum circuit.

10.1.2 Scattering description of a quantum conductor

A quantum coherent conductor is a conductor whose dimensions are smaller than the electronic phase coherence length, L_Φ[1]. At this scale, electron transport can be seen as a scattering problem for the electronic (Schrodinger) waves [47, 57, 59]. A complete review on this approach can be found in [48] and [49].

Scattering matrix

As stressed in the introduction, it is a good approximation to neglect Coulomb interactions in a good conductor, since the low energy quasiparticles of a Fermi liquid are long lived [29]. Strictly speaking, it is therefore a scattering problem for the non-interacting quasiparticles's, that obey Fermi statistics and carry a discrete charge, e. Nevertheless, transport is fully

[1] In GaAS/Ga(Al)As 2DEGs, $L_\Phi \simeq 20\ \mu$m at 20 mK.

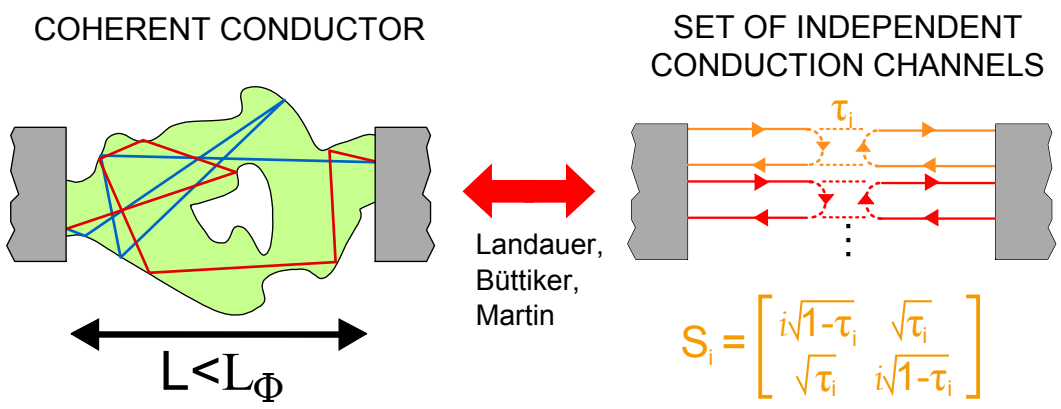

Figure 10.1: **Scattering description of a quantum conductor** Left: Schematic picture of a quantum conductor. Contacts appear grey, the conductor in green. Two electron paths are represented (blue, red). Right: Schematic picture of the decomposition in independent conduction channels [59]. Transmission probability, τ_i, is represented for an independent channel's modes block. Within an arbitrary global phase, the scattering matrix block of a single independent channel mode, i, can be described by the matrix S_i.

described by a scattering matrix, S, linking the incoming and outgoing quasiparticles on both sides to the conductor:

$$|\Psi_{out,R}, \Psi_{out,L} >= S|\Psi_{in,R}, \Psi_{in,L} > \tag{10.1}$$

where R/L label the right and left side of the conductor, out/in label the outgoing and incoming waves. And where Ψ can be eventually a tensor product over all the relevant quantum numbers[2], for example:

$$|\Psi_{out,R} >= \otimes_n |\psi_{out,R,n} > \tag{10.2}$$

where n represents the relevant quantum numbers spanning the Hilbert space of the outgoing waves on the right side.

Neglecting interactions, S can be (block) diagonalized [57, 59] in a basis of independent conduction channels, irrespectively of the complexity of the sample's geometry. This is pictured in Figure 10.1, where i labels the independent conduction modes. In this basis any incoming mode is transmitted or reflected within the same mode, avoiding any mode mixing. Namely, the anihilation operators of the outgoing independent mode i, $\hat{b}_{i,L/R}$, are only related to the incomming fields in the same mode, $\hat{a}_{i,L/R}$, through:

$$\begin{pmatrix} \hat{b}_{i,L} \\ \hat{b}_{i,R} \end{pmatrix} = S_i \begin{pmatrix} \hat{a}_{i,L} \\ \hat{a}_{i,R} \end{pmatrix} \tag{10.3}$$

[2]Whose dimensions can be different on either side.

where S_i is the independent mode block matrix shown in Figure 10.1. S_i is hermitian due to time inversion symmetry, and unitary due to charge conservation. S_i is therefore completely characterized by the transmission amplitude $\sqrt{\tau_i}$ whose square gives the transmission probability for the incoming modes $\hat{a}_{i,L/R}$.

Current operator

The strong consequence of this decomposition is that the current operator results from a simple summation over the independent channels' contributions, $\hat{I} = \sum_i \hat{I}_i$. The Heisenberg representation of the particle current carried by mode i, $\hat{I}_i$, reads (see e.g. [58]):

$$\begin{aligned}
\hat{I}_i &= \frac{e}{h}\int \mathrm{d}\epsilon_1 \mathrm{d}\epsilon_2 \Big[\hat{a}^\dagger_{i,L}(\epsilon_1)\hat{a}_{i,L}(\epsilon_2) - \hat{b}^\dagger_{i,L}(\epsilon_1)\hat{b}_{i,L}(\epsilon_2)\Big] e^{i(\epsilon_1-\epsilon_2)t/\hbar} \\
\hat{I}_i &= \frac{e}{h}\int \mathrm{d}\epsilon_1 \mathrm{d}\epsilon_2 \Bigg\{ \tau\Big[\hat{a}^\dagger_{i,L}(\epsilon_1)\hat{a}_{i,L}(\epsilon_2) - \hat{a}^\dagger_{i,R}(\epsilon_1)\hat{a}_{i,R}(\epsilon_2)\Big] + \\
&\quad + i\sqrt{\tau(1-\tau)}\Big[\hat{a}^\dagger_{i,R}(\epsilon_1)\hat{a}_{i,L}(\epsilon_2) - \hat{a}^\dagger_{i,L}(\epsilon_1)\hat{a}_{i,R}(\epsilon_2)\Big]\Bigg\} e^{i(\epsilon_1-\epsilon_2)t/\hbar}
\end{aligned} \tag{10.4}$$

Therefore, $\hat{I}$ depends only on the transmission probabilities of the independent channels's modes $\{\tau_i\}$, and on the boundary conditions determining the incoming modes. The microscopic complexity of the sample is simply encapsulated in $\{\tau_i\}$. However, it does not depend on the density of states $\rho(E)$, or velocity $v(E) = (\frac{\partial E}{\partial k})_E)$, which results from the decomposition in 1D modes for which $\rho(E)v(E) = 1/h$ [47].

Boundary conditions: reservoirs When the quantum conductor is fed by voltage biased electron reservoirs, the boundary conditions impose the statistical averages (labeled by $<>_\beta$):

$$< \hat{a}^\dagger_{i,A}(\epsilon_1)\hat{a}_{j,B}(\epsilon_2) >_\beta = \delta_{ij}\delta_{AB}\delta(\epsilon_1-\epsilon_2) f_{F,A}(\epsilon) \tag{10.5}$$

where $f_{F,L/R}$ are the Fermi-Dirac energy distribution functions at equilibrium with the electrochemical potentials, $eV_{L/R}$, applied to the left and right reservoirs: $f_{F,L/R}(E) = 1/(1+\exp[\beta(E-eV_{L/R})])$ and $\beta = \frac{1}{k_\mathrm{B}T}$. For simplicity, we will define $V_L = V$ and $V_R = 0$.

Dynamics of a quantum conductor

Since the current is now a quantum operator and conduction is probabilistic, the full dynamics of the quantum conductor cannot follow anymore from a simple constitutive relation. However, all statistical cummulants of the current operator can be computed from the scattering matrix. They define the Full Counting Statistics of charge transfer [136] and provide

a complete description of the probabilistic conductor's dynamics. In this sense, the conductance is the first cummulant, the correlation of current fluctuations the second, and so on.

Conductance Nevertheless, the mean current is still simply related to the voltage bias:

$$\begin{aligned} < \hat{I} >_\beta &= \frac{e}{h} \sum_i \int \mathrm{d}E \tau_i [f_{F,L}(E) - f_{F,R}(E)] \\ &= \frac{e^2}{h} \sum_i \tau_i V \\ &= GV, \end{aligned} \tag{10.6}$$

where the energy dependencies of τ_i are neglected. The final expression defines the multichannel Landauer formula of conductance [47, 57]

$$G = \frac{e^2}{h} \sum_i \tau_i. \tag{10.7}$$

where it can be seen that conductance is simply the transmission of the incoming modes.

Quantum noise The noise of electron current is characterized by the spectral density of the symmetrized correlation of current fluctuations

$$S^{II}(V, \omega) = \int \mathrm{d}t e^{i\omega t} < \Delta\hat{I}(t)\Delta\hat{I}(0) + \Delta\hat{I}(0)\Delta\hat{I}(t) >_\beta \tag{10.8}$$

where $\Delta\hat{I}$ are the current fluctuations $\Delta\hat{I} = \hat{I} - < \hat{I} >_\beta$. By introducing (10.4) in (10.8), simplifying using Wick's theorem and using the correlation relations provided by (10.5), one finds that in the low frequency limit S^{II} reads [58, 59] (for a review see [48, 49]):

$$\begin{aligned} S^{II}(V,0) =& 2\frac{e^2}{h} \sum_i \int \mathrm{d}E \Big\{ \tau_i(1-\tau_i)\big[f_F(E-eV) - f_F(E)\big]^2 + \\ &+ \tau_i\big[f_F(E)(1-f_F(E)) + f_F(E-eV)(1-f_F(E-eV))\big] \Big\}. \end{aligned} \tag{10.9}$$

The first term is null at equilibrium, when $eV = 0$. Using the property of Fermi functions $f(1-f) = -k_\mathrm{B}T\partial f/\partial E$, the equilibrium noise reads:

$$\begin{aligned} S^{II}(0,0) &= 4\frac{e^2}{h} \sum_i \int \mathrm{d}E \tau_i \big[f_F(E)(1-f_F(E))\big] \\ &= 4k_\mathrm{B}T \frac{\partial < \hat{I} >_\beta}{\partial V} \\ &= 4k_\mathrm{B}TG. \end{aligned} \tag{10.10}$$

The equilibrium noise only traces the thermal fluctuations of the reservoirs and follows the fluctuation-dissipation theorem.

A zero temperature, only the first term in (10.9) contributes. In this limit, noise is pure shot noise due to the discrete charge partitioning by the scatterer. Such noise is the result of the quantum correlations build in by the scattering of undistinguishable fermionic quasiparticles. Neglecting energy dependencies on τ_i, it reads:

$$\begin{aligned} S^{II}(V,0)_{T=0} =& 2\frac{e^2}{h}\sum_i \int \mathrm{d}E \tau_i(1-\tau_i)\big[f_F(E-eV)-f_F(E)\big]^2 \\ &= 2\frac{e^3|V|}{h}\sum_i \tau_i(1-\tau_i) \\ &= 2eF|<\hat{I}>_\beta|. \end{aligned} \tag{10.11}$$

The last expression defines the Fano factor F as:

$$F = \frac{\sum_i \tau_i(1-\tau_i)}{\sum_i \tau_i}. \tag{10.12}$$

Since $\tau_i < 1$, F verifies $F < 1$ and shot noise is sub-Poissonian. This is a result of the strong correlations build by the Pauli principle that tend to regularize the electron flow [59]. In particular, perfectly transmitted or reflected modes do not give rise to shot noise [52, 53].

In conclusion, the scattering approach provides a complete description of non-interacting quantum conductors. For instance, we have seen that conductance is simply the transmission of incoming quasiparticles, or that perfectly transmitting conductors do not give rise to additional current fluctuations.

Now that we dispose of a powerful approach to describe a quantum conductor, let's see how we can provide a quantum description of a classical linear circuit.

10.1.3 Quantum description of a linear macroscopic circuit

The classical description of electric circuits is already a phenomenological approach that encapsulates the complexity of Maxwell's equations in continuous media, in discrete elements. For instance, a capacitor can be seen as an "electric field box" while an inductor as a "magnetic field box" [137]. This phenomenology can be pushed forward to the quantum level by identifying the canonical dynamical variables of the circuit and applying to them Dirac's correspondence principle. Raw as it may seem, this approach can be derived from microscopic electrodynamic considerations (see Appendix in [46]). We will follow [46] to provide the quantum description of an LC circuit and extend it to general linear circuits. We refer the reader to [46] for further details.

LC circuits

The dynamics of a closed LC circuit can be described with a phase ϕ defined as

$$\phi(t) = \frac{e}{\hbar}\int_{-\infty}^{t} \mathrm{d}t' U(t'), \tag{10.13}$$

where U is the voltage drop across the capacitor $U = Q/C$, Q the influence charge deposited on the capacitor plates and C its capacitance. With these notations, the Lagrangian of an LC circuit, $\mathfrak{L}$, reads

$$\mathfrak{L} = \frac{C}{2}\left(\frac{\hbar}{e}\dot{\phi}\right)^2 - \frac{1}{2L}\left(\frac{\hbar}{e}\phi\right)^2. \tag{10.14}$$

which permit to identify ϕ and Q as the canonical degrees of freedom. Applying Dirac's correspondence principle to them results in a commutation relation to their quantum operators:

$$[\hat{\phi}, \hat{Q}] = ie. \tag{10.15}$$

The Hamiltonian of an LC circuit therefore reads

$$\hat{H} = \frac{\hat{Q}^2}{2C} + \frac{1}{2L}\left(\frac{\hbar}{e}\hat{\phi}\right)^2 \tag{10.16}$$

so that the charge (or phase) dynamics are those of an harmonic oscillator of pulsation $\omega = \frac{1}{\sqrt{LC}}$. The Hilbert space is spanned by the occupation number of the oscillator mode.

General linear circuits

A macroscopic linear circuit is characterized by its complex impedance $Z(\omega)$ and can be dissipative, so that switching on to the Hamiltonian formalism is not straightforward. However, already in Nyquist's treatment of equilibrium noise [138], a dissipative circuit of resistance R was modeled by a transmission line whose characteristic impedance matched R. As a transmission line can be seen as a series composition of LC circuits, it can be treated within a conservative framework. More generally, the Caldeira-Leggett theorem [139] ensures that any linear circuit of arbitrary impedance, $Z(\omega)$, can be decomposed in an eventually infinite series of LC circuits of frequencies $\{\omega_n\}$, whose density is given by $\Re e[Z(\omega_n)]$. The Hamiltonian of a capacitor in parallel with a general impedance therefore reads:

$$\hat{H}_{C//Z} = \frac{\hat{Q}^2}{2C} + \sum_n \frac{\hat{q_n}^2}{2C_n} + \frac{1}{2L_n}\left(\frac{\hbar}{e}\hat{\phi_n}\right)^2. \tag{10.17}$$

As a consequence of the string law, (10.17) is constrained by $\hat{\phi} = \sum_n \hat{\phi}_n$, so that the phase across the capacitor $\hat{\phi}$ is bilinearly coupled to the oscillator bath . A general linear circuit is therefore described by a bosonic oscillator bath, whose Hilbert space is spanned by the occupation numbers of the different oscillator modes.

Now that we know how to describe a macroscopic circuit within a quantum mechanical framework, we can discuss how do the microscopic excitations flowing through a quantum conductor may couple to the macroscopic degrees of freedom of the electric circuit.

10.1.4 Coupling the microscopic to the macroscopic

The coupling between the microscopic and macroscopic degrees of freedom of an electric circuit is a consequence of the granularity of charge and Coulomb interactions. In the following we illustrate this coupling in the simplest case where the quantum conductor is a tunnel junction defined in a good conductor. With this picture in mind, and with the tools presented in the previous sections, we will be able to introduce a phenomenological coupling.

Microscopic picture of tunneling events

A tunnel junction, depicted in Figure 10.2, consists on a insulating barrier separating two conducting electrodes. The barrier is thin enough so that the incoming quasiparticles have a (small) probability to tunnel through. Within the scattering approach, such conductor is in the limit $\forall i \quad \tau_i << 1$. According to (10.11) and (10.12), its shot noise is Poissonian, so that tunneling events are scarce and uncorrelated.

For our present purposes, it is however simpler to describe tunnel junctions within a tight-binding model defined by the Hamiltonian

$$\hat{H} = \hat{H}_L + \hat{H}_R + \hat{H}_T^e \tag{10.18}$$

where $\hat{H}_{L/R} = \sum_k \epsilon_{k,L/R} \hat{a}^\dagger_{k,L/R} \hat{a}_{k,L/R}$ describe free quasiparticle on the left/right electrodes and where the barrier is modeled by a point like tunneling hamiltonian

$$\hat{H}_T^e = \sum_{kl} T_{kl} \hat{a}^\dagger_{k,R} \hat{a}_{l,L} - T^\dagger_{kl} \hat{a}^\dagger_{k,L} \hat{a}_{k,R} \tag{10.19}$$

where the transmission T_{kl} amplitudes are small.

Since we are dealing with a good conductor, electric fields within the electrodes are screened and the quasiparticles can be pictured as plain electrons dressed by a neutralizing polarization cloud. However, the polarization cloud results from the influence of many electrons, and the transmissions $|T_{kl}|^2$ are low, so that only the plain electrons can tunnel through the barrier. By taking a look to Figure 10.2, one can see that, in consequence, an influence charge Q matching the discrete charge e is deposited on the barrier plates, at every tunneling event.

Phenomenological coupling

Environment hamiltonian The insulating barrier defines a geometrical capacitance C, so that Q sees an electric circuit defined by the parallel composition of the geometrical capacitance C and the series impedance, $Z_{series}(\omega)$, characterizing the circuit used to bias the barrier. Therefore, the hamiltonian describing the macroscopic environment of the tunneling electrons, $\hat{H}_{env}$, is given by (10.17).

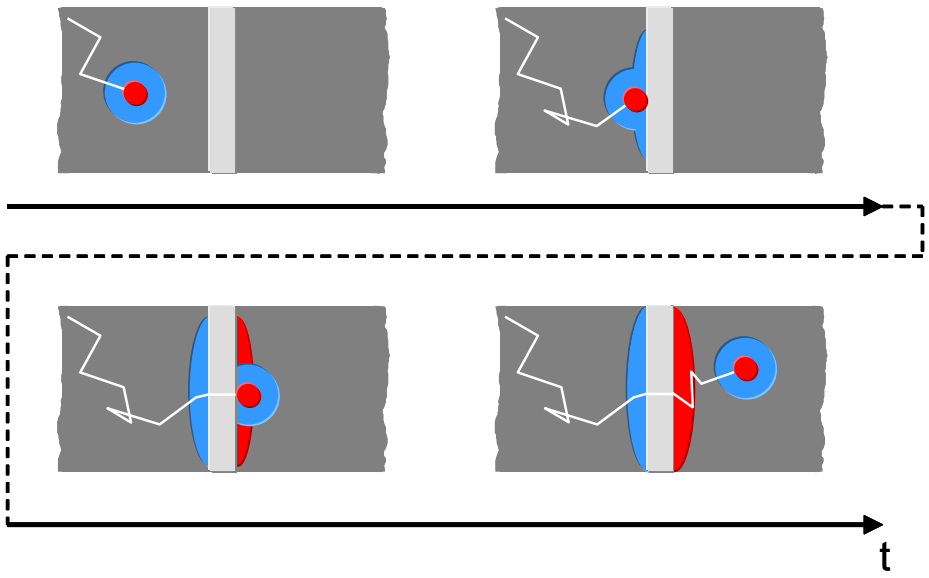

Figure 10.2: **Microscopic picture of a charge transfer across a tunneling barrier.** Schematic description of a quasiparticle (plain electron: red, polarization cloud: blue) tunneling through a barrier (light gray). After the single charge transfer, the incoming polarization cloud is deposited on one side to the barrier, while the same amount is removed on the opposite plate. An influence charge e is deposited on the plates of the barrier, thus charging its geometrical capacitance.

Coupling According to the commutation relation (10.15), a charge kink of discrete value e on $\hat{Q}$ is described by the translation operator in charge space $e^{-i\hat{\phi}}$. Therefore, the coupling between the tunneling quasiparticles and their electromagnetic environment can be simply obtained by introducing this translation operator in $\hat{H}_T^e$ (10.19):

$$\hat{H}_T = \sum_{kl} T_{kl} \hat{a}^\dagger_{k,R} \hat{a}_{l,L} e^{-i\hat{\phi}} - T^*_{kl} \hat{a}^\dagger_{k,L} \hat{a}_{k,R} e^{+i\hat{\phi}} \tag{10.20}$$

The resulting problem for tunnel junctions is described by the total Hamiltonian

$$\hat{H} = \hat{H}_L + \hat{H}_R + \hat{H}_T + \hat{H}_{env}, \tag{10.21}$$

where $\hat{H}_T$ not only couples quasiparticles on both electrodes, but also couples the quasiparticle tunneling to the electromagnetic modes of the circuit described by $\hat{H}_{env}$. In this model, the influence of a voltage source, V, manifests in the electrode hamiltonians $\hat{H}_{L/R}$ so that

$$\epsilon_{k,L} = \epsilon_{k,R} + eV \tag{10.22}$$

The canonical theory of the dynamical Coulomb blockade permits to calculate the mean current of this problem, which we are going to see in the following section.

Range of validity Note that this approach can be built upon microscopic considerations of the electrodynamics triggered by tunneling events, but does not hold for all possible geometries (Appendix in [46]). First, the approach is justified if the characteristic time that takes to homogenize the influence charge Q on the capacitor plates is smaller than the other characteristic timescales. Second, it applies only in the case of "short" junctions, so that the tunneling time can be also be neglected. If it is not the case, the effective impedance seen by the tunneling electrons is renormalized [140].

10.2 Dynamical Coulomb blockade

The dynamical Coulomb blockade theory was initially developed for tunnel junctions in the early 90's [133, 134] and has been thoroughly investigated in small [141, 142] and large [143, 144] tunnel junctions during the 90's. Anticipating the results, the single charge transfers across the barrier may excite the modes of the electromagnetic environment. Quasiparticle tunneling becomes inelastic and therefore there are fewer available states to tunneling. The current is blocked so that the differential conductance exhibits a dip at low biases and temperatures. Since higher impedance lead to stronger dissipation, the conductance dip is deeper for higher environment impedance. At the end of this section, we will discuss the general case of an arbitrary quantum conductor which has only been predicted recently [5, 6] in the limit of low impedance environments.

10.2.1 Dynamical Coulomb blockade of tunnel junctions

Tunnel junctions are easy to deal with theoretically since the coupling Hamiltonian H_T defined by (10.20) is "small" and can be taken as a perturbation to the total hamiltonian $\hat{H}$. This means that the quasiparticle transition rates across thee barrier, $\overrightarrow{\Gamma(V)}$ and $\overleftarrow{\Gamma(V)}$, can be computed from the Fermi golden rule. Finally, the mean current is simply obtained from the transition rates through $< I(V) >= e\big[\overrightarrow{\Gamma(V)} - \overleftarrow{\Gamma(V)}\big]$.

Transition rates

In order to calculate the transition rates, we follow reference [46]. The starting point is the Fermi golden rule with respect to $\hat{H}_T$ giving the rate for the $i \to f$ transition:

$$\Gamma_{i\to f} = \sum_{i,f} \frac{2\pi}{\hbar} | < f|\hat{H}_T|i > |^2 \delta(E_i - E_f) \tag{10.23}$$

This expression can be calculated assuming that $|i/f >$ are equilibrium states. This approximation means that the charge relaxation time should be shorter than the time between two tunneling events. In this limit, $|i/f >= |E > |R >$ are tensor products of equilibrium

quasiparticle states $|E>$, labeled by their energy, and equilibrium environment states $|R>$ spanned by thermal occupations of the oscillator bath (10.17).

The transition rate for electrons tunneling from left to right therefore reads:

$$\overrightarrow{\Gamma}(V) = \frac{2\pi}{\hbar}\sum_{E,E'}\sum_{k,l}| < E'|T_{kl}\hat{a}^{\dagger}_{k,R}\hat{a}_{l,L}|E >_{\beta}|^2 \times \\ \times \sum_{R,R'}| < R|e^{-i\hat{\phi}}|R' >_{\beta}|^2\delta(E + E_R - E' - E_{R'}). \tag{10.24}$$

which is a product of a quasiparticle and an environment terms constrained by energy conservation.

A straightforward calculation shows that the quasiparticle term is

$$\int \mathrm{d}\epsilon_k \mathrm{d}\epsilon_l \sum_{k,l} |T_{kl}|^2 f_{F,L}(\epsilon_l)[1 - f_{F,R}(\epsilon_k)]. \tag{10.25}$$

It is the simple summation over the joint probabilities to find a quasiparticle in state l and energy ϵ_l on the left electrode, to find an empty space on state k and energy ϵ_k on the right electrode, weighted by the transmission probability between both states. The summation over k, l can be averaged when neglecting the energy dependencies on tunneling probabilities. This defines a tunneling conductance

$$G_T = \frac{2\pi e^2}{\hbar}\sum_{k,l}|T_{k,l}|^2. \tag{10.26}$$

The environment term is more engaging. Nevertheless, it is simply a function of $\epsilon_l - \epsilon_k$, so that (10.24) can be written in the appealing form:

$$\overrightarrow{\Gamma}(V) = \frac{G_T}{e^2}\int \mathrm{d}\epsilon_l \mathrm{d}\epsilon_k f_{F,L}(\epsilon_l)[1 - f_{F,R}(\epsilon_k)]P(\epsilon_l - \epsilon_k) \tag{10.27}$$

Where $P(\epsilon)$ encompasses the environment term, and where following (10.22), we have $f_{F,L}(\epsilon_l) = f_F(\epsilon_l - eV)$ and $f_{F,R}(\epsilon_k) = f_F(\epsilon_k)$. This equation shows that $P(\epsilon)$ is the probability that a tunneling electron gives an amount of energy ϵ to the environment, as depicted in Figure 10.3. On the contrary, $P(-\epsilon)$ is the probability that it receives an energy ϵ from the environment. This probability can be expressed with the help of the phase correlation function[3] $J(T)$:

$$J(T) =< \hat{\phi}(t)\hat{\phi}(0) - \hat{\phi}(0)^2 >_{\beta} \tag{10.28}$$

so that $P(\epsilon)$ is the Fourier transform of $e^{J(t)}$ [46]:

$$P(\epsilon) = \frac{1}{2\pi}\int \mathrm{d}t e^{J(t)}e^{i\epsilon t/\hbar}. \tag{10.29}$$

[3]Since the equilibrium density matrix of the environment has a gaussian measure in the ϕ representation, all equilibrium dynamical quantities can be expressed by the first and two moments of $\hat{\phi}$.

The phase correlation function $J(t)$ can be obtained [46] from the fluctuation-dissipation theorem, yielding to:

$$J(t) = 2\int_0^\infty \frac{\mathrm{d}\omega}{\omega}\frac{\Re e[Z_{env}(\omega]}{R_Q}\left\{\coth\left(\frac{1}{2}\beta\hbar\omega\right)[\cos(\omega t)-1] - i\sin(\omega t)\right\}, \tag{10.30}$$

where $R_Q = \frac{h}{e^2} \simeq 25.8\,\mathrm{k}\Omega$, and where the environment impedance Z_{env} is the parallel composition of the barrier's capacitance, C, and the series impedance, $Z_{series}(\omega)$, describing the circuit used to bias the junction:

$$Z_{env} = \frac{Z_{series}(\omega)}{1 + i\omega Z_{series}(\omega)C} \tag{10.31}$$

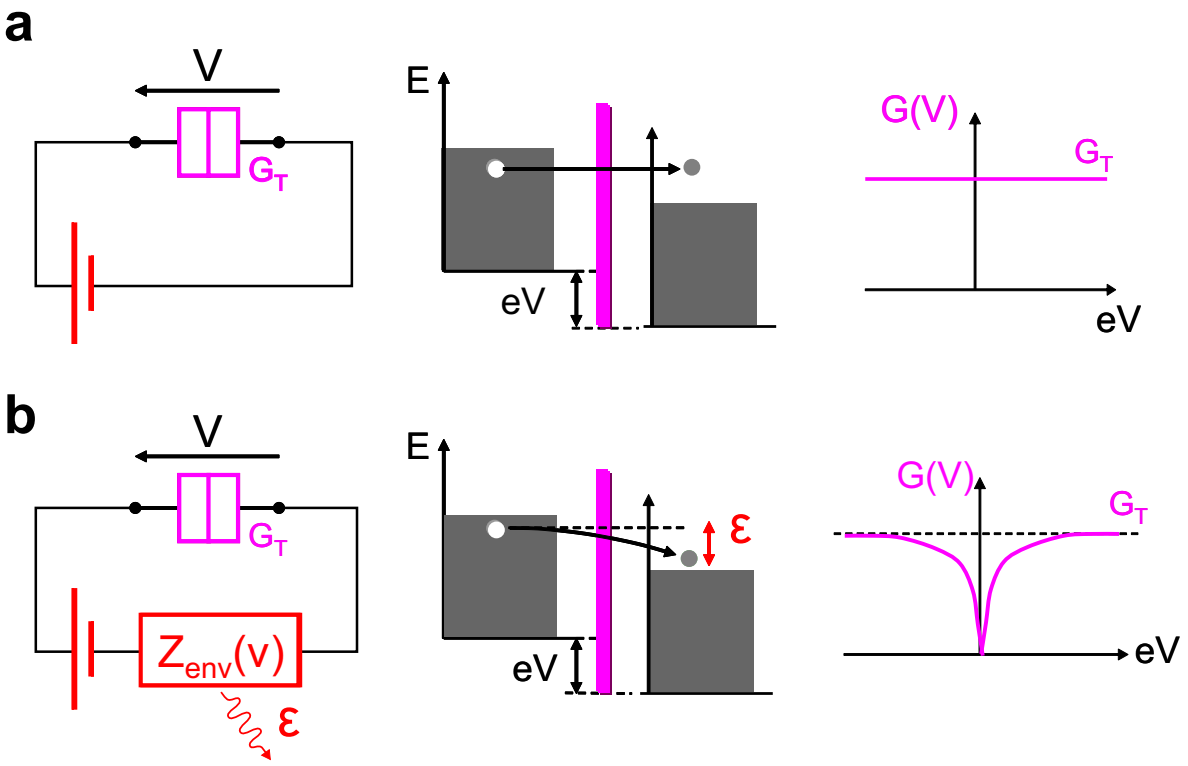

Figure 10.3: **Transport across tunnel junctions.** **a** *Tunnel junction biased through perfect leads. Left:* electric scheme. *Middle:* Tunneling events are elastic, their number is proportional to the transport window defined by the reservoir populations. *Right:* The resulting differential conductance $G_T = \partial I/\partial V$, defined by (10.26), is independent of the bias. **b** *Tunnel junction biased through a series impedance. Left:* electric scheme, the series impedance dissipates some of the energy carried by the tunneling electrons. *Middle:* Tunneling events are inelastic, reducing the phase space available to transport at low energies. *Right:* The resulting differential conductance $G(V)$ develops a dip at low energies. At high energies, the intrinsic G_T is recovered.

Properties of $P(\epsilon)$

Normalized $P(\epsilon)$ can indeed be considered a probability since it is correctly normed

$$\int \mathrm{d}\epsilon P(\epsilon) = e^{J(0)} = 1.$$

Charging energy $P(\epsilon)$ obeys the sum rule

$$\int \mathrm{d}\epsilon \epsilon P(\epsilon) = i\hbar J'(0) = \frac{e^2}{2C}.$$

The maximum energy that a tunneling electron can exchange with its electromagnetic environment is indeed given by the single electron charging energy of the capacitor.

Detailed balance $P(\epsilon)$ obeys a detailed balance equation

$$P(-\epsilon) = e^{-\beta\epsilon} P(\epsilon). \tag{10.32}$$

The probability for a tunneling electron to excite the environment is therefore larger than the probability for the opposite energy transfer by a Boltzmann factor. In particular, a tunneling electron cannot absorb any energy from a zero temperature environment.

Direct bias When the junction is biased by perfect leads, the phase ϕ is fixed by the voltage source, V, $\phi = \frac{e}{\hbar}Vt$ and displays no quantum fluctuations (there is no dissipation). $J(t)$ is therefore null and $P(\epsilon) = \delta(\epsilon)$ so that electron tunneling is elastic. One recovers the usual tunneling rates for elastic tunneling:

$$\overrightarrow{\Gamma}(V) = \frac{G_T}{e^2} \int \mathrm{d}\epsilon f_F(\epsilon - eV)[1 - f_F(\epsilon)] \tag{10.33}$$

Low impedance limit In the low impedance limit, $\Re e[Z_{env}(\omega)] << R_Q$, $P(\epsilon)$ can be simplified by expanding the exponential to its first order $e^{J(t)} \simeq 1 + J(t)$. This expansion consists in neglecting all multi-photon energy transfers.

$P(\epsilon)$ reads in this limit:

$$P(\epsilon) = \delta(\epsilon) + \frac{2}{\epsilon} \frac{\Re e[Z_{env}(\epsilon/\hbar)]}{R_Q} \frac{2}{1 - e^{-\beta\epsilon}} \tag{10.34}$$

which is the sum of an elastic and a single photon emission contributions.

Conductance

The mean current is obtained using $< I(V) >= e[\overrightarrow{\Gamma}(V) - \overleftarrow{\Gamma}(V)]$ where $\overleftarrow{\Gamma}(V) = \overrightarrow{\Gamma}(-V)$ by the symmetry of the problem. The differential conductance $G(V) = \frac{\partial I}{\partial V}$ is therefore obtained from (10.27):

$$\frac{G(V)}{G_T} = \iint \mathrm{d}E\mathrm{d}E' f_F(E)\Big[- \frac{\partial f_F}{\partial E}(E' - eV) - \frac{\partial f_F}{\partial E}(E' + eV)\Big] P(E - E') \tag{10.35}$$

It is useful to define the environment corrections to the tunneling conductance $\delta G \equiv G(V) - G_T$. Using (10.35) one gets:

$$\frac{\delta G}{G_T}(V) = \int \mathrm{d}E f_F(E) \int \mathrm{d}\epsilon P(\epsilon) \frac{\partial[f_F(E+eV+\epsilon) - f_F(E+eV-\epsilon)]}{\partial E}. \tag{10.36}$$

Zero temperature limit Using the detailed balance relation (10.32) it can be shown [46] that in the zero temperature limit:

$$G(V) = G_T \int_{-\infty}^{e|V|} \mathrm{d}\epsilon P(\epsilon) \tag{10.37}$$

where it is clear that $G(\pm\infty) = G_T$. The consequent dynamical Coulomb blockade correction to the tunneling conductance is therefore:

$$\frac{\delta G}{G_T}(V) = -\int_{e|V|}^{+\infty} \mathrm{d}\epsilon P(\epsilon). \tag{10.38}$$

This relations result from the fact that a zero temperature: i) The environment can only absorb energy (10.32). ii) Tunneling electrons cannot emit energies higher than eV due to their Fermi-Dirac statistics. It also demonstrates that the corrections to conductance, which is a DC property, depend on the environment's impedance at the high frequencies defined by $h\nu > eV$.

Zero bias conductance drop: low impedance limit Using the low impedance limit of $P(\epsilon)$, the conductance correction (10.36) can be found at zero bias :

$$\frac{\delta G}{G_T}(V=0,T) = \int_0^{+\infty} \mathrm{d}\epsilon\beta \frac{\Re e[Z(\epsilon/\hbar)]}{\epsilon R_Q} \frac{\sinh(\beta\epsilon) - \beta\epsilon}{\sinh^2(\beta\epsilon/2)} \tag{10.39}$$

It is noteworthy that in this single photon exchange limit, the temperature dependence of $\delta G/G_T$ only depends on the quasiparticle Fermi functions. One sees in (10.39) that the blockade is due to the environment impedance at frequencies $h\nu > k_\mathrm{B}T$.

Temporal representation Following equations (10.29), (10.30) and (10.35) one needs to perform four successive integrals in order to calculate $G(V)$ from the environment impedance Z_{env}. However, the conductance can be directly related to $J(t)$ [145], reducing the number of integrations to two:

$$\frac{\delta G}{G_T}(V) = 2\int_0^{+\infty} \frac{\mathrm{d}t}{\hbar\beta} \frac{\pi t}{\hbar\beta} \frac{\Im m\left[e^{J(t)}\right] \cos(\frac{eVt}{\hbar})}{\sinh^2(\frac{\pi t}{\hbar\beta})} \tag{10.40}$$

RC circuits

When the tunnel junction is biased through a series resistance $Z_{env}(\omega)$ simply reads:

$$Z_{env}^{RC}(\omega) = \frac{R}{1 + i\omega RC} \tag{10.41}$$

Zero temperature limit In the limit of zero temperature, the conductance correction (10.38) corresponding to the environment impedance (10.41) can be found analytically. It yields to:

$$\left(\frac{\delta G}{G_T}\right)_{RC}(V, T=0) = -\frac{R}{R_Q}\ln\left(\sqrt{1+\left(\frac{\hbar}{eRCV}\right)^2}\right) \tag{10.42}$$

The conductance therefore develops a dip at low biases having a logarithmic bias dependence. The zero temperature dip's amplitude is found to scale with the series resistance.

Zero bias conductance drop: low impedance limit In a low resistance RC circuit, we can use (10.39) for the evaluation of the conductance drop at zero bias. It depends only on the normalized temperature βE_C, with $E_C = \frac{e^2}{2C}$ being the single electron charging energy of the barrier and on the ration R/R_Q. It reads:

$$\frac{\delta G}{G_T}(V=0,T)_{RC} = \int_0^{+\infty} \frac{R}{R_Q}\frac{1}{1+\left(\pi\frac{R}{R_Q}\frac{\epsilon}{\beta E_C}\right)^2}\left(\frac{\coth(\epsilon/2)}{\epsilon} - \frac{1}{\sinh^2(\epsilon/2)}\right)\mathrm{d}\epsilon \tag{10.43}$$

where it can be seen that the blockade correction is null in the high temperature limit $k_{\mathrm{B}}T >> E_C$. A typical dilution fridge temperature 30 mK corresponds to a capacitance of about 30 fF.

Approximating the RC dependence by a hard low pass dependence $\left(1+\left(\pi\frac{R}{R_Q}\frac{\epsilon}{\beta E_C}\right)^2\right)^{-1} \sim 1-\Theta(\epsilon-\frac{\beta E_C}{\pi R/R_Q})$ one obtains the approximate expression:

$$\frac{\delta G}{G_T}(V=0,T)_{RC} \simeq 2\frac{R}{R_Q}\ln\left(\frac{\beta E_C}{\pi R/R_Q}\right)+\alpha, \tag{10.44}$$

where α is independent of temperature. The logarithmic dependence can be used to make quick estimations of the RC circuit parameters from a measured temperature dependence of $\delta G(V=0)$.

The canonical dynamical Coulomb blockade theory is found to provide a complete comprehension of the impedance composition laws for a tunnel junction embedded in a generic linear circuit. This theory can be extended in order to take into account finite size effects corresponding to long tunnel junctions, where the capacitor's charge homogenization time cannot be neglected [143], or to take into account the transversal time of tunneling electrons [140]. However, it cannot be applied to general quantum conductors having arbitrary (not small) transmission probabilities. In the following we are going to see a recent generalization to quantum conductors that works in the low impedance environment limit.

10.2.2 Dynamical Coulomb blockade of quantum conductors

Only recently the dynamical Coulomb blockade has been worked out for the case of a short quantum conductors whose transversal time can be neglected. Since a general conductor

cannot be treated as a perturbation it is a difficult problem. This difficulty has been circumvented [5, 6] by taking the limit of a low impedance circuit, for which the quantum fluctuations of phase are small (see equations (10.28) and (10.30)). In this limit, the corrections to the conductance of a quantum conductor are found to exhibit the same bias, temperature and environment impedance dependence as those found for tunnel junctions (10.35) or (10.26). However, they are renormalized in amplitude by the same Fano factor F (10.12) that also renormalizes the amplitude of shot noise (10.11) with respect to that of a tunnel junction (for which $F = 1$).

Coupling hamiltonian for small phase fluctuations

In order to sketch the derivation of this strong result, we are going to follow [51] in the simplest case of a single scattering mode. Using the notations of the scattering approach, the coupling hamiltonian can be written as:

$$\hat{H}_{scatt} = \iint \mathrm{d}\epsilon_1 \mathrm{d}\epsilon_2 \sqrt{\tau}\big[\hat{b}_R^\dagger(\epsilon_1)\hat{a}_L(\epsilon_2)e^{-i\phi} + \hat{b}_L^\dagger(\epsilon_1)\hat{a}_R(\epsilon_2)e^{+i\phi}\big]. \tag{10.45}$$

where the electromagnetic environment is introduced as a C-number. The particle current operator found in (10.4) therefore follows the Hamilton equation $\hat{I} = \frac{e}{\hbar}\big(\frac{\partial \hat{H}_{scatt}}{\partial \phi}\big)_{\phi=0}$. In consequence, if the phase fluctuations ϕ are small we have $\hat{H}_{scatt} = \hat{H}_{scatt}(\phi = 0) + \delta\hat{H}_{scatt}(\phi)$. In order to obtain the quantum fluctuations of ϕ we treat it as an operator and obtain

$$\delta\hat{H}_{scatt} = \frac{\hbar}{e}\hat{\phi}\left[\hat{I}_0 + \frac{\hat{\phi}^2}{2}\Big(\frac{\partial \hat{I}}{\partial \phi}\Big)_{\phi=0}\right], \tag{10.46}$$

so that the final problem reads

$$\hat{H} = \hat{H}_0 + \delta\hat{H}_{scatt} \tag{10.47}$$

where H_0 is the hamiltonian describing uncoupled conductor and environment.

The current operator is also perturbed by the phase fluctuations:

$$\hat{I}(\phi) = \frac{e}{h}\int \mathrm{d}\epsilon_1 \mathrm{d}\epsilon_2 e^{i(\epsilon_1-\epsilon_2)t/\hbar}\Bigg\{\tau\Big[\hat{a}_{i,L}^\dagger(\epsilon_1)\hat{a}_{i,L}(\epsilon_2) - \hat{a}_{i,R}^\dagger(\epsilon_1)\hat{a}_{i,R}(\epsilon_2)\Big] + \tag{10.48}$$

$$+ i\sqrt{\tau(1-\tau)}\Big[\hat{a}_{i,R}^\dagger(\epsilon_1)\hat{a}_{i,L}(\epsilon_2)e^{-i\phi} - \hat{a}_{i,L}^\dagger(\epsilon_1)\hat{a}_{i,R}(\epsilon_2)e^{+i\phi}\Big]\Bigg\}$$

which can be expanded as $\hat{I}_0 + \delta\hat{I}$

$$\delta\hat{I} = \hat{\phi}\Big(\frac{\partial \hat{I}}{\partial \phi}\Big)_{\phi=0} + \frac{\hat{\phi}^2}{2}\Big(\frac{\partial^2 \hat{I}}{\partial \phi^2}\Big)_{\phi=0} \tag{10.49}$$

The first and second derivatives of $\hat{I}$ are simply found from (10.48).

$$\Big(\frac{\partial \hat{I}}{\partial \phi}\Big)_{\phi=0} = \frac{e}{h}\int \mathrm{d}\epsilon_1 \mathrm{d}\epsilon_2 e^{i(\epsilon_1-\epsilon_2)t/\hbar}\sqrt{\tau(1-\tau)}\Big[\hat{a}_{i,R}^\dagger(\epsilon_1)\hat{a}_{i,L}(\epsilon_2) + \hat{a}_{i,L}^\dagger(\epsilon_1)\hat{a}_{i,R}(\epsilon_2)\Big]$$

$$\Big(\frac{\partial^2 \hat{I}}{\partial \phi^2}\Big)_{\phi=0} = i\frac{e}{h}\int \mathrm{d}\epsilon_1 \mathrm{d}\epsilon_2 e^{i(\epsilon_1-\epsilon_2)t/\hbar}\sqrt{\tau(1-\tau)}\Big[\hat{a}_{i,R}^\dagger(\epsilon_1)\hat{a}_{i,L}(\epsilon_2) - \hat{a}_{i,L}^\dagger(\epsilon_1)\hat{a}_{i,R}(\epsilon_2)\Big] \tag{10.50}$$

Correction to current

Since δH_{scatt} is "small" we can calculate the correction to the mean current of the coupled problem $< \delta\hat{I}(t) >=< e^{-i\hat{H}t/\hbar}\delta\hat{I}e^{i\hat{H}t/\hbar} >$ with a perturbative expansion on $\delta\hat{H}_{scatt}$. Up to second order on ϕ, it reads [51]:

$$< \delta\hat{I}(t) > =< \delta\tilde{I}(t) >_\beta + \frac{1}{i\hbar}\int_0^\infty \mathrm{d}\tau < \big[\tilde{I}_0(t+\tau) + \delta\tilde{I}(t+\tau), \delta\tilde{H}_{scatt}(t)\big] >_\beta + \\ - \frac{1}{\hbar^2}\int_0^\infty\int_0^\tau \mathrm{d}\tau\mathrm{d}\tau' < \big[\big[\tilde{I}_0(t+\tau), \delta\tilde{H}_{scatt}(t+\tau')\big], \delta\tilde{H}_{scatt}(t)\big] >_\beta \qquad (10.51)$$

where $<>_\beta$ denotes an average on the uncoupled equilibrium states, and where the tilde denotes the interaction representation $\tilde{A} = e^{-i\hat{H}_0 t/\hbar}\hat{A}e^{i\hat{H}_0 t/\hbar}$. In order to carry this calculation, we assume a stationary state.

The first term is null according to (10.50). Realizing that $[\hat{I}_0(t_1), \hat{I}_0(t_2)] = 0$ for an energy independent transmission, the second term also vanishes. The last term yields to the final expression for the correction to the mean current:

$$\delta I = \tau(1-\tau)\frac{e}{\hbar}\int_{-\infty}^{+\infty}\mathrm{d}t\Bigg[e^{-i(\epsilon_1-\epsilon_2)t/\hbar} < \tilde{\phi}(t)\tilde{\phi}(0) - \tilde{\phi}(0)^2 >_\beta \times \\ \times \iint \mathrm{d}\epsilon_1\mathrm{d}\epsilon_2\Big\{f_L(\epsilon_1)\big[1-f_R(\epsilon_2)\big] - f_R(\epsilon_1)\big[1-f_L(\epsilon_2)\big]\Big\}\Bigg]. \qquad (10.52)$$

Realizing that $\frac{e^2}{h}\tau$ is the conductance of the uncoupled scatterer, and that the first term is the Fourier transform of $J(t)$, this correction is directly proportional to the one that would exhibit a tunnel junction in a low impedance environment, which can be directly extracted from (10.27). The proportionality factor is simply the Fano factor for one mode $F = 1-\tau$.

This result can be generalized to a multimode scatterer resulting in the relation [5, 6]:

$$\Big(\frac{\delta G}{G}\Big)_{\{\tau_i\}} = F(\{\tau_i\})\Big(\frac{\delta G}{G}\Big)_{\{\tau_i \ll 1\}}. \qquad (10.53)$$

The relative corrections to the conductance of a quantum conductor are those that would arise for a tunnel junction in the same environment, but renormalized in amplitude by the conductor's Fano factor $F(\{\tau_i\}) = \frac{\sum_i \tau_i(1-\tau_i)}{\sum_i \tau_i}$.

This strong prediction has been tested in atomic contacts [51] where it was found that the corrections to conductance due to an electromagnetic environment where starkly reduced when the contact's transmission probabilities approached one. However, a quantitative test of the full transmission dependence of the theory has been missing.

10.3 Experimental test of the dynamical Coulomb blockade theory for short coherent conductors

In order to test the dynamical Coulomb blockade theory for short coherent conductors, we have used a model quantum conductor (we have chosen a quantum point contact, QPC)

whose transmission coefficients, and therefore its Fano factor, can be tuned in situ. We have embedded it in a tunable circuit whose series resistance can be selected between two different resistances and a high frequency shorting path. By selecting the short circuit path, we have been able to characterize the QPC transmissions when the corrections due to the environment are negligible. After this, we have been able to trigger and measure the environment corrections by selecting a higher series resistance. We have measured the resulting changes in the QPC conductance as a function of its Fano factor F. We obtain a quantitative agreement with the theory, giving solid grounds to our understanding of impedance composition laws in quantum circuits.

10.3.1 Published article

I hereby reproduce the article published in the Physical Review Letters detailing our experiment.

Our approach is novel in the sense that we do not extract the dynamical Coulomb blockade from $G(V)$ curves as is usually done in tunnel junctions or atomic contacts. We measure instead how different electromagnetic environments modify the zero bias conductance of the same conductor $\delta G(V = 0, T)$. This allows us to extract the environment corrections without biasing, and therefore without heating the sample. The electronic temperature being known, it is easier to compare our signal to the theoretical prediction (10.53).

I will afterwards give further details on the capacitive cross-talks and the universal conductance fluctuations arising in our sample and limiting our approach. I will further detail the the numerical estimation of the QPC geometric capacitance needed to perform a quantitative comparison with the theories predictions.

Experimental Test of the Dynamical Coulomb Blockade Theory for Short Coherent Conductors

C. Altimiras, U. Gennser, A. Cavanna, D. Mailly, and F. Pierre*

Phynano team, Laboratoire de Photonique et de Nanostructures (LPN)-CNRS, route de Nozay, 91460 Marcoussis, France

(Received 12 September 2007; published 19 December 2007)

We observed the recently predicted quantum suppression of dynamical Coulomb blockade on short coherent conductors by measuring the conductance of a quantum point contact embedded in a tunable on-chip circuit. Taking advantage of the circuit modularity we measured most parameters used by the theory. This allowed us to perform a reliable and quantitative experimental test of the theory. Dynamical Coulomb blockade corrections, probed up to the second conductance plateau of the quantum point contact, are found to be accurately normalized by the same Fano factor as quantum shot noise, in excellent agreement with the theoretical predictions.

DOI: 10.1103/PhysRevLett.99.256805 PACS numbers: 73.23.Hk, 72.70.+m

A tunnel junction exhibits a drop of its conductance at low voltages and temperatures when it is embedded in a resistive circuit, in violation of the classical impedances composition laws. This quantum phenomenon, known as dynamical Coulomb blockade (DCB), results from the excitation of the circuit's electromagnetic modes by the current pulses associated with tunnel events. The theory is well understood and verified experimentally for tunnel junctions [1–5], but it is only recently that it has been extended to short coherent conductors [6]. The strong recent prediction is that DCB corrections are simply reduced by the *same* normalization factor as quantum shot noise, as a consequence of electron flow regulation by the Pauli exclusion principle [7,8]. The aim of this work is to perform an accurate experimental test of the DCB theory for coherent conductors and thereby to provide solid grounds to our knowledge of impedances composition laws in mesoscopic circuits.

A powerful description of coherent conductors in absence of interactions is provided by the scattering approach, which encapsulates the complexity of transport mechanisms into the set $\{\tau_n\}$ of transmission probabilities across the conduction channels indexed by n. In short conductors, the energy dependence of $\{\tau_n\}$ can be neglected provided that $h/\tau_{\mathrm{dwell}} \gg k_B T, eV_{\mathrm{SD}}$, where τ_{dwell} is the dwell time in the conductor, T the temperature and V_{SD} the applied voltage [9]. The conductance then reads $G = G_Q \sum_n \tau_n$, with $G_Q = 2e^2/h$ the conductance quantum, and the current shot noise at zero temperature is $S_I = 2eIF$, where $2eI$ is the Poissonian noise and $F = \sum_n \tau_n(1-\tau_n)/\sum_n \tau_n$ is the Fano factor. More generally, the full counting statistics of charge transfers can be formulated with $\{\tau_n\}$ [8]. How is this picture modified by Coulomb interaction? First, the low energy excitations are transformed from electrons to Fermion quasiparticles of finite lifetime which thereby limits the coherent extent of conductors [10]. Second, Coulomb interaction couples a coherent conductor to the circuit in which it is embedded, which results in the DCB. In practice, DCB corrections reduce the transmission probabilities at low energies. The theory of DCB has first been worked out for small tunnel junctions of resistance large compared to the resistance quantum $R_K = h/e^2 \simeq 25.8\ \mathrm{k}\Omega$ and embedded in macroscopic linear circuits characterized by a frequency dependent impedance $Z_{\mathrm{env}}(\nu)$ [1,3]. The theory has been found in excellent agreement with experiments [2], and, more recently, extended to low impedance [4] and long [5] tunnel junctions. From a theoretical standpoint, tunnel junctions are easy to deal with since they can be treated perturbatively. The generalized DCB theory to short coherent conductors, whose transmission probabilities can take any value between 0 and 1, assumes instead that quantum fluctuations are small. This hypothesis limits its validity to low environmental impedance $\mathrm{Re}[Z_{\mathrm{env}}(\nu)] \ll R_K$. The striking prediction is that the amplitude of DCB corrections to the conductance of coherent conductors is reduced relative to tunnel junctions by the same Fano factor as quantum shot noise [6]. Further theoretical investigations concluded that a similar relation holds more generally between the Coulomb corrections to the nth cumulant of current fluctuations and the $(n+1)$th cumulant [11]. Experimentally, a pioneer work performed on an atomic contact showed that DCB corrections are strongly reduced when the transmission probability approaches 1, in qualitative agreement with the theory [12]. However, as pointed out by the authors of [12]: "it (was) not possible to conclude whether or not (the theory) is quantitatively correct." Indeed, at large transmissions, relatively large universal conductance fluctuations were superimposed on the DCB signal whereas, in the tunnel regime, the set of transmission probabilities could not be extracted reliably due to significant DCB corrections. Up to now a quantitative test of the dynamical Coulomb blockade theory for a coherent conductor was missing. The present experiment fills this gap.

In this experiment, we have measured the variations in the resistance of a quantum point contact (QPC) realized in a 2D electron gas (2DEG) while changing the adjustable on-chip circuit in which it is embedded. The conduction channels of a QPC are directly related to the 1D subbands

quantized by the transverse confinement [13]. By reducing the confinement with voltage biased top gates, the transmission probabilities of the conduction channels are increased continuously and, for adequate geometries [14], one channel at a time. Consequently, the QPC's conductance $G_{\mathrm{QPC}} = (n + \tau_{n+1})G_Q$ corresponds to n channels fully transmitted and one channel of transmission probability τ_{n+1}. The knowledge of the transmission probabilities combined with the ability to change them continuously make of a QPC a powerful test-bed for short coherent conductors [15]. As described later, we can change *in situ* the circuit surrounding the QPC using voltage biased metallic top gates to deplete the 2DEG underneath. It is by monitoring the QPC's resistance as a function of the circuit impedance that we can extract accurately the amplitude of DCB corrections.

The measured sample, shown in Fig. 1, was realized in a GaAs/Ga(Al)As heterojunction. The 2DEG is 94 nm deep, of density 2.5×10^{15} m^{-2}, Fermi energy 100 K and mobility 55 m^2 V^{-1} s^{-1}. The sample was patterned using *e*-beam lithography followed by chemical etching of the heterojunction and by deposition of metallic gates at the surface. The QPC is formed in the 2DEG by applying a negative voltage V_{QPC} to the metallic split gates shown in Fig. 1(b). Two stripes of width 1.4 μm and 3.8 μm [16], and of length 100 μm, much longer than the electron phase coherence length $L_\phi \sim 10$ μm, were patterned in the 2DEG by chemical etching to form an on-chip resistance in series with the QPC. Measurements were performed in a dilution refrigerator of base temperature $T = 40$ mK. All measurement lines were filtered by commercial π-filters at the top of the cryostat. At low temperature, the lines were carefully filtered and thermalized by arranging them as 1 m long resistive twisted pairs (300 Ω/m) inserted inside 260 μm inner diameter CuNi tubes tightly wrapped around a copper plate screwed to the mixing chamber. The sample was further protected from spurious high energy photons by two shields, both at base temperature. Conductance measurements were performed using standard lock-in techniques at excitation frequencies below 100 Hz. The sample was current biased by a voltage source in series with a 10 MΩ or 100 MΩ polarization resistance at room temperature. Voltages across the sample were measured using low noise room temperature amplifiers. The source (S)-drain (D) voltage was kept smaller than k_BT/e to avoid heating. We applied a small perpendicular magnetic field $B = 0.2$ T [17] to minimize nonideal behaviors of the QPC such as sharp energy dependence of the transmissions resulting from Fabry-Pérot resonances with nearby defects, and imperfect transmissions across ''open'' channels.

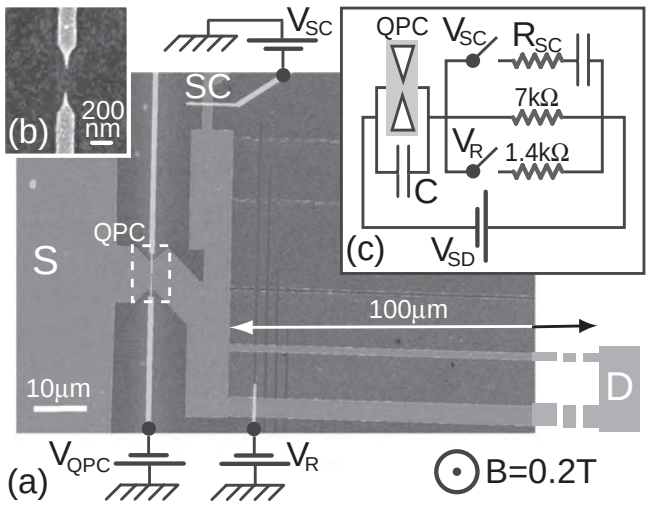

FIG. 1. (a) *E*-beam micrograph of the sample tailored in a GaAs/Ga(Al)As heterojunction. The 2DEG is patterned by chemical etching, etched areas are darker. Active top metal gates are colorized in the lighter gray. Electrode labels S, D and SC stand, respectively, for source, drain and short circuit. (b) Magnified view of the metallic split gate used to tune the QPC. (c) Schematic representation of the sample.

In our experiment the QPC is embedded in an electromagnetic environment schematically represented as a $R//C$ circuit in Fig. 1(c). The parallel capacitance (C) is the geometrical capacitance between the source electrode (S) and the vertical near rectangular conductor on the right side of the QPC. If the short circuit electrode (SC) is disconnected ($V_{\mathrm{SC}} < -0.3$ V), the on-chip series resistance can take two values $R_S = 1.2$ kΩ and 7 kΩ depending on whether the wider 2DEG stripe is, respectively, connected ($V_R = 0$) or disconnected ($V_R = -0.35$ V), using the metal gate voltage V_R as a switch. If the SC electrode is connected ($V_{\mathrm{SC}} \simeq 0$), it acts as a low impedance (R_{SC}) high frequency path to ground in parallel with R_S. Note that DCB reduces the dc conductance of a coherent conductor but that these DCB corrections depend on the impedance of the electromagnetic environment at high frequencies, typically $\nu \sim k_BT/h \in [0.8, 4]$ GHz for $T \in [40, 200]$ mK. Consequently, while the SC electrode is connected at room temperature to a high input impedance voltage amplifier, at high frequencies its impedance is expected to be reduced to the on-chip resistance of the SC electrode plus, approximately, the vacuum impedance 377 Ω due to antenna effects on length scales larger than a fourth of the electromagnetic wavelength. This is symbolized in Fig. 1(c) by a high frequency impedance R_{SC} in series with a capacitor that acts as a high frequency short circuit.

The experiment was performed as follows: (i) We first selected a series resistance $R_S = 1.2$ kΩ or 7 kΩ with V_R. (ii) With the short circuit electrode (SC) connected ($V_{\mathrm{SC}} \simeq 0$), we tuned the QPC with V_{QPC}. In this configuration the DCB corrections are minimum because the series resistance R_S is shorted at high frequency by R_{SC}. Since the SC electrode is disconnected from ground at the near DC frequencies applied to measure the sample, it could be

used to measure separately the QPC and the series resistances. (iii) We then disconnected the SC electrode by applying a negative voltage V_{SC}, therefore increasing the high frequency circuit impedance and consequently the DCB corrections. By simultaneously measuring the variations of the source (S)-drain (D) resistance, which is the sum of the QPC and the series resistance, we can extract the amplitude of DCB corrections.

Figure 2 shows δR, the resistance variation of the QPC plus the series resistance from their values at $V_{SC} = -0.8$ V, plotted versus V_{SC} at $G_{QPC}(V_{SC} = 0) = 0.5G_Q$, $T = 40$ mK and $B = 0.2$ T for $R_S = 1.2$ kΩ and 7 kΩ. The dependence of δR with V_{SC} results from two contributions: (i) At $V_{SC} < -0.3$ V the SC electrode is disconnected and δR is a linear function of V_{SC} with a negative slope that does not depend on R_S. This is a consequence of the capacitive cross talk between the metal gate controlled by V_{SC} and the QPC. We have checked (data not shown) that this slope, which is a nonmonotonic function of V_{QPC}, is proportional to the derivative of the QPC's resistance with V_{QPC}. The normalization factor $\simeq 10^{-3}$ is in rough quantitative agreement with the sample geometry. (ii) For $V_{SC} > -0.3$ V we observe, on top of the linear capacitive cross talk, a sudden drop when V_{SC} increases. We attribute this resistance drop, written hereafter δR_{DCB}, to the reduction of DCB corrections as the parallel high frequency short circuit electrode SC gets connected. As expected, δR_{DCB} is larger in the more resistive environment $R_S =$ 7 kΩ. In the following we extract δR_{DCB} by measuring the QPC in series with R_S successively at $V_{SC} = -0.1$ V (SC electrode connected) and $V_{SC} = -0.33$ V (SC electrode disconnected). We then subtract the capacitive cross talk contribution obtained from $\delta R(V_{SC} = -0.56\ \text{V}) - \delta R(V_{SC} = -0.33\ \text{V})$.

Figure 3 shows as symbols the measured temperature dependence of the DCB signal at $G_{QPC}(V_{SC} = -0.1\ \text{V}) = 0.33G_Q$ for $R_S = 1.2$ kΩ and 7 kΩ. The continuous lines are predictions of the DCB theory for tunnel junctions [3], normalized by the one-channel Fano factor $F = 1 - G_{QPC}/G_Q \simeq 0.67$. The schematic $R//C$ circuit modeling the QPC's electromagnetic environment is shown in Fig. 1(c). The real part of its impedance plugged into the theory reads $\text{Re}[Z_{env}(\nu)] = R/[1 + (2\pi RC\nu)^2]$. The calculated δR_{DCB} is the difference in the amplitude of DCB corrections for open and closed short circuit switch. The corresponding circuit resistance R is, respectively, $R = R_S$ and $R = 1/(1/R_S + 1/R_{SC})$. The only fit parameter in our calculation is the SC high frequency impedance that we fixed at $R_{SC} = 1$ kΩ, in agreement with the sum of the on-chip SC resistance estimated from the geometry to 600 ± 100 Ω and the vacuum impedance 377 Ω. Other parameters plugged into the DCB calculation are the measured series resistances $R_S = 1.2$ kΩ or $R_S = 7$ kΩ and the geometrical capacitance $C = 30$ fF estimated numerically with an accuracy of ±5 fF [18]. The very good agreement between data and theoretical predictions provides a strong support to our interpretation and allows us to now compare the measured dependence of DCB on transmission probabilities with the predicted Fano reduction factor.

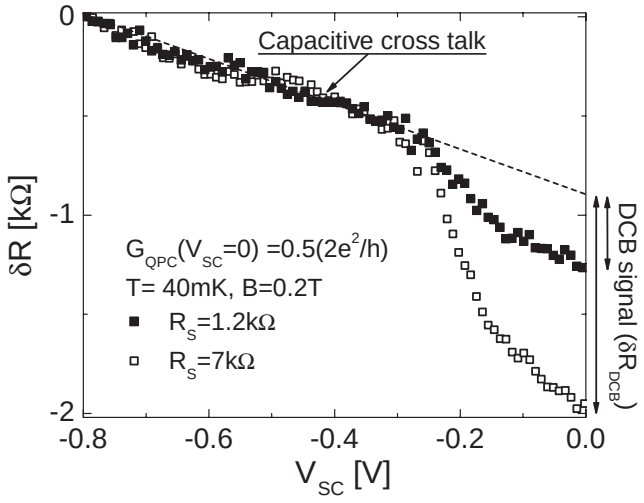

FIG. 2. Resistance variation δR of the QPC in series with the on-chip resistance $R_S = 1.2$ kΩ (■) or $R_S = 7$ kΩ (□) plotted versus the voltage V_{SC} that controls the high frequency short circuit (SC) switch [see Fig. 1(c)]. For $V_{SC} < -0.3$ V the SC switch is open and δR exhibits a linear dependence with V_{SC} due to the direct capacitive cross talk with the QPC. The DCB signal δR_{DCB} is the difference between the resistance measured at $V_{SC} \simeq 0$ (SC switch closed) and the resistance measured for an open SC switch taking into account the linear capacitive contribution (dashed line).

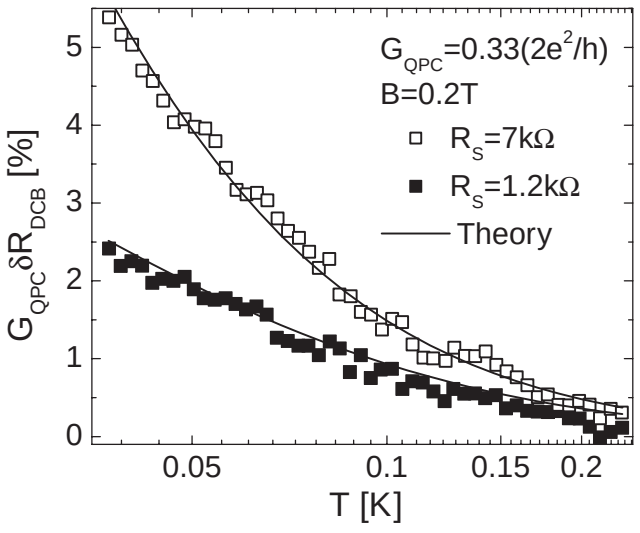

FIG. 3. Measured temperature dependence of relative DCB corrections $G_{QPC}\delta R_{DCB}$ at $G_{QPC} = 0.33G_Q$ and $B = 0.2$ T, for $R_S = 1.2$ kΩ (■) and $R_S = 7$ kΩ (□). Predictions of the DCB theory are shown as continuous lines. The only fit parameter in the calculation is the high frequency residual resistance of the short circuit path $R_{SC} = 1$ kΩ (see text).

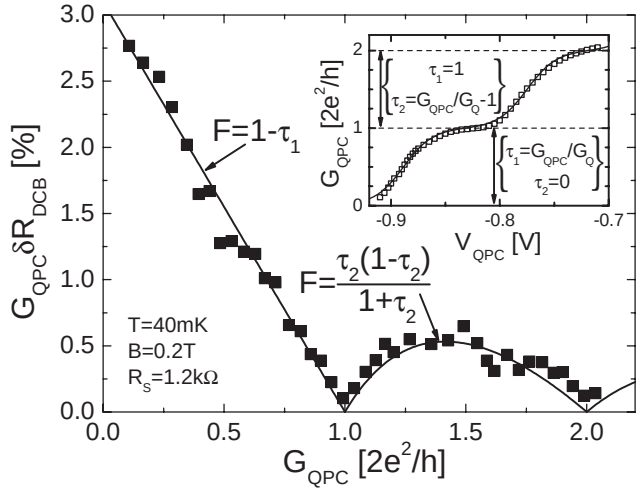

FIG. 4. Measured relative DCB corrections (■) plotted versus the QPC conductance. The continuous line is the predicted reduction by the Fano factor $F = \sum_n \tau_n(1-\tau_n)/\sum_n \tau_n$. Inset: Measured QPC conductance (□) plotted versus the split gate bias voltage V_{QPC}. The best fit using a quadratic confinement potential [14] is shown as a continuous line.

To test the generalized dynamical Coulomb blockade theory, we measured the relative amplitude of DCB corrections versus the QPC conductance at 40 mK and for $R_S = 1.2$ kΩ [19] (see Fig. 4). The predictions depend on the set $\{\tau_n\}$, it is therefore crucial to extract accurately the transmissions probabilities of the QPC. The inset in Fig. 4 shows the QPC conductance up to $2G_Q$ versus the split gate voltage V_{QPC}, measured at $T = 40$ mK and $B = 0.2$ T. We subtracted 350 Ω from the data to account for the residual DC series resistance by adjusting the first three plateaus on multiples of the conductance quantum [20]. From the maximum deviation between our data and the best fit (continuous line in inset of Fig. 4) using Büttiker's model of QPCs [14], we estimate our accuracy on the transmission probabilities $\{\tau_1 = \min[1, G_{\mathrm{QPC}}/G_Q], \tau_2 = \max[0, G_{\mathrm{QPC}}/G_Q - 1]\}$ to be better than 0.05. The continuous line in Fig. 4 shows the relative amplitude of DCB as predicted by theory [6]. We observe an excellent quantitative agreement between the data and the Fano factor $F = [\tau_1(1-\tau_1) + \tau_2(1-\tau_2)]/(\tau_1+\tau_2)$ that controls quantum shot noise [15].

To conclude, we have performed a quantitative experimental test of the generalization of dynamical Coulomb blockade theory to short coherent conductors embedded in low impedance circuits. We find dynamical Coulomb blockade corrections that are reduced in amplitude by the same Fano factor as quantum shot noise, in quantitative agreement with the predictions. This result is not only important within the fundamental field of quantum electrodynamics in mesoscopic circuits. It also provides solid grounds to engineer complex devices with coherent conductors and to use dynamical Coulomb blockade as a tool to probe the transport mechanisms. For this purpose DCB has the advantage on shot noise that the signal increases when the probed energies decrease.

The authors gratefully acknowledge inspiring discussions and suggestions by D. Estève, P. Joyez, H. Pothier and C. Urbina. We also thank M. H. Devoret, F. Portier, and B. Reulet for stimulating discussions and G. Faini, R. Giraud, and Y. Jin for permanent assistance. This work was supported by the ANR (No. ANR-05-NANO-039-03) and NanoSci-ERA (No. ANR-06-NSCI-001).

*Corresponding author.
frederic.pierre@lpn.cnrs.fr

[1] M. H. Devoret *et al.*, Phys. Rev. Lett. **64**, 1824 (1990); S. M. Girvin *et al.*, Phys. Rev. Lett. **64**, 3183 (1990).
[2] A. N. Cleland *et al.*, Phys. Rev. B **45**, 2950 (1992); T. Holst *et al.*, Phys. Rev. Lett. **73**, 3455 (1994).
[3] For a review see G.-L. Ingold and Y. V. Nazarov, in *Single Charge Tunneling*, edited by H. Grabert and M. H. Devoret (Plenum, New York, 1992), Chap. 2.
[4] P. Joyez *et al.*, Phys. Rev. Lett. **80**, 1956 (1998).
[5] F. Pierre *et al.*, Phys. Rev. Lett. **86**, 1590 (2001).
[6] D. S. Golubev and A. D. Zaikin, Phys. Rev. Lett. **86**, 4887 (2001); A. Levy Yeyati *et al.*, Phys. Rev. Lett. **87**, 046802 (2001).
[7] Th. Martin and R. Landauer, Phys. Rev. B **45**, 1742 (1992).
[8] See Y. M. Blanter and M. Büttiker, Phys. Rep. **336**, 1 (2000), and references therein.
[9] M. Büttiker and R. Landauer, IBM J. Res. Dev. **30**, 451 (1986).
[10] D. Pines and P. Nozière, *The Theory of Quantum Liquids* (W.A. Benjamin, New York, 1966); For a recent review on phase coherence of electrons in diffusive metals, see F. Pierre *et al.*, Phys. Rev. B **68**, 085413 (2003).
[11] A. V. Galaktionov *et al.*, Phys. Rev. B **68**, 085317 (2003); M. Kindermann and Y. V. Nazarov, Phys. Rev. Lett. **91**, 136802 (2003); M. Kindermann *et al.*, Phys. Rev. B **69**, 035336 (2004); I. Safi and H. Saleur, Phys. Rev. Lett. **93**, 126602 (2004).
[12] R. Cron *et al.*, in *Electronic Correlations: From Meso to Nano-Physics*, edited by , , and J. Trân Thanh Vân (EDP Sciences, Les Ulis, 2001), p. 17; R. Cron, Ph.D. thesis, Université Paris 6, 2001, http://tel.ccsd.cnrs.fr/.
[13] L. I. Glazman *et al.*, JETP Lett. **48**, 238 (1988).
[14] M. Büttiker, Phys. Rev. B **41**, 7906 (1990).
[15] M. Reznikov *et al.*, Phys. Rev. Lett. **75**, 3340 (1995); A. Kumar *et al.*, Phys. Rev. Lett. **76**, 2778 (1996).
[16] The 2DEG width is about 700 nm narrower due to lateral depletion near the edges.
[17] Shubnikov–de Haas oscillations of $R_S(B)$ are negligible up to the applied magnetic field $B = 0.2$ T.
[18] The code was provided gracefully by D. Estève.
[19] For $R_S = 7$ kΩ and $G_{\mathrm{QPC}} > 0.5G_Q$, non-negligible universal conductance fluctuations of $R_S(V_{\mathrm{SC}})$ forbade us to extract the DCB signal accurately.
[20] The corresponding impact on G_{QPC} is at most 2.5% and 5% below, respectively, the first and second plateau.

10.3.2 QPC/short-circuit gate capacitive cross-talk

In article Figure 2, we observe a linear dependence on the measured resistance with the gate voltage, V_{SC}, used to switch the short impedance path. The measured signal is the series composition of the QPC and the series resistance R_S, so that a capacitive cross-talk between the short-circuit gate and the QPC resistance gives rise to a linear dependence on the measured signal with V_{SC}.

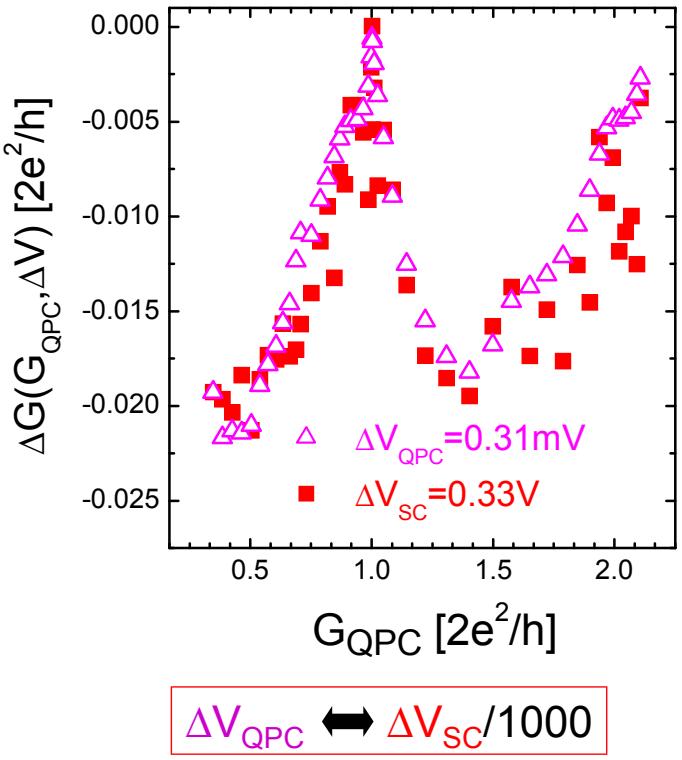

Figure 10.4: **QPC/short-circuit gate capacitive cross-talk calibration.** The finite QPC conductance change arising as a result of a small QPC gate voltage change ΔV_{QPC} =0.31 mV, as a function of the initial QPC conductance, is compared to the the one arising in response to a short-circuit gate voltage change $\sim$ 1000 higher ΔV_{SC} =0.33 V.

We have calibrated the QPC/short-circuit capacitive coupling by comparing the QPC conductance change resulting from a small increase of QPC gate voltage, ΔV_{QPC} =0.31 mV, to the one resulting from a higher decrease of the short-circuit gate voltage ΔV_{SC} =0.33 V. Figure 10.4 shows this comparison as a function of the initial QPC conductance. The agreement between both curves demonstrates the capacitive coupling between the QPC and short-circuit gate, and reveals that the cross-talk scaling factor is about 1000:

$$\frac{\partial G_{QPC}}{\partial V_{QPC}} \simeq 1000 \frac{\partial G_{QPC}}{\partial V_{SC}}.$$

This scaling factor is in rough agreement with the sample geometry since the QPC/QPC gate distance is about 0.1 μm while the QPC/short-circuit gate distance is about 33 μm.

10.3.3 Universal conductance fluctuations

The full investigation on the Fano factor dependence of the environment correction to the QPC conductance, shown in article Figure 4, was only realized for the smaller series resistance R_S =1.2 kΩ setup. Indeed strong fluctuations were found to arise for the R_S = 7 kΩ environment when sweeping the gate voltage V_{SC}, as shown in Figure 10.5. These fluctuations appear the same for different sweeps and are a consequence of the universal conductance fluctuations [54] of the thin wire used to define the series impedance. They are triggered by the capacitive coupling between the short-circuit gate and the electrostatic energy of the wire.

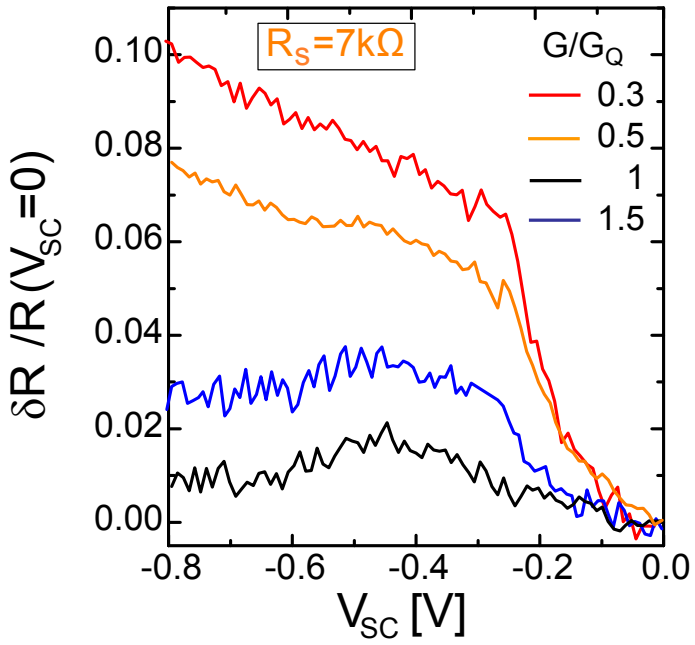

Figure 10.5: **Universal conductance fluctuations in the R_S =7 kΩ signal.** Reproducible fluctuations arise in our signal while sweeping the gate voltage V_{SC} in the R_S =7 kΩ environment. Such fluctuations are stronger as the QPC resistance becomes comparable to the series resistance.

Since our raw signal is the series composition of the QPC and the series resistance, R_S, the fluctuations in the series resistance manifest only when the QPC resistance becomes comparable to R_S. For R_S =1.2 kΩ the QPC resistance is always (much) higher and our signal is free from this contribution. However for R_S =7 kΩ the QPC resistance becomes comparable around $G_{QPC} \sim 2e^2/h$. In these conditions, universal conductance fluctuations

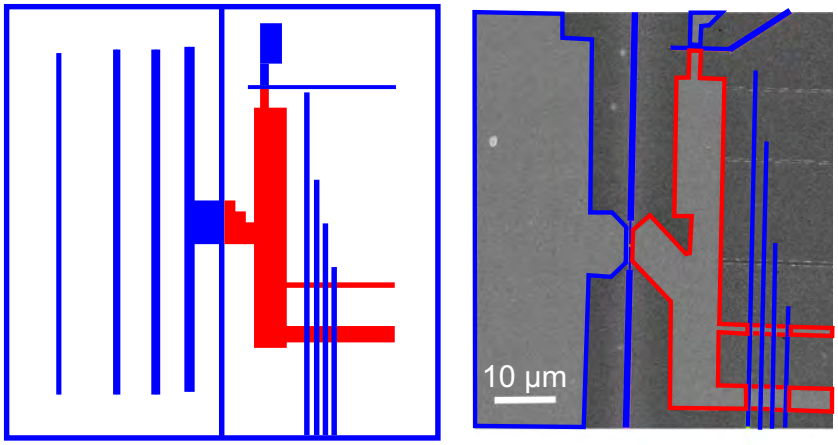

Figure 10.6: **Decomposition of the sample in electrostatic islands** The sample (shown on the right panel) is cut in different electrostatic islands (Blue and Red), taking into account the mesa and the top gates. The charge relaxation capacitance is calculated numerically as the geometric capacitance between island blue and red, on the simplified geometry shown on the left. This particular geometry yields to 25 fF.

step in our signal (see Figure 10.5) forbidding the extraction of δG_{QPC}.

10.3.4 Numerical estimation of the QPC capacitance

The geometrical capacitance of the QPC has been estimated numerically using a C code provided to us by Daniel Esteve. The code calculates the DC geometrical capacitances between different plates following an electrostatic energy relaxation algorithm [135]. We assume that the mesa and the gates are on the same plane and that the dielectric constant is simply $\epsilon = (\epsilon_0 + \epsilon_{GaAs})/2$.

We approximate the charge relaxation capacitance C as the geometrical capacitance to ground seen from the central mesa plate situated between the QPC and the resistive paths (see article Figure 1). We have to cut the sample geometry in different electrostatic islands, but we can control the stability of the resulting capacitance by using different geometries (see an example in Figure 10.6). This gives us the mean value and standard error used in the article $C = 30 \pm 5$ fF. It also informs us that C is dominated by the large mesa plates on both sides to the QPC.

10.3.5 Conclusion and perspectives

Our experiment demonstrates that, in low impedance electromagnetic environments, the dynamical Coulomb blockade corrections to the conductance of a quantum conductor are

accurately described by (10.53) as predicted by [5, 6]. This result does not only provide solid grounds to our comprehension of impedance composition laws in quantum circuits. It demonstrates an accurate novel experimental approach to measure the environment effects on a quantum conductor. It also demonstrates a strong like between the current correlations due to the quantum conductor and its coupling to its electromagnetic environment, at least in the limit of a low environment impedance.

Recent theoretical developments have generalized this link to the full counting statistics of the quantum conductor [146]. The environment corrections to the n^{th} cumulant of the current operator are found to be proportional the the $(n+1)^{th}$ uncoupled cumulant. Such predictions should be tested by measuring the environment correction to the current noise.

On the other hand, the coupling of an arbitrary quantum conductor to an arbitrarily large impedance environment is not yet fully understood, even if the particular case of a single channel coupled to an RC circuit has been exactly solved in [147]. Moreover, the composition laws between different quantum conductors, such as tow QPCs in series, are still unknown. Our experimental approach could be implemented in order to test these unexplored regimes.

Part III

Experimental methods

Chapter 11

Experimental techniques

This chapter presents the experimental techniques we have used during this thesis. All of them are quite standard, but we will present them for completeness.

First, we detail the circuit nanofabrication. We introduce how a two dimensional electron gas (2DEG) is realized at the interface of two semi-conductors and provide the different steps used to process our samples.

Second, we detail the low electric noise techniques used to bias and measure our samples at very low temperatures.

11.1 Circuit nanofabrication

During this thesis, we have worked with GaAS/Ga(Al)As based 2DEGs. They were grown by molecular beam epitaxy (MBE) in the LPN clean-room facilites. Growing good quality 2DEGs is performed, in the Phynano-Team, by Antonella Cavanna, Abdelkarim o Ouerghi, Bernard Etienne and Ulf Gennser. I will introduce here how a 2DEG can be obtained at the interface of two semi-conductors that have a different band gap. With the resulting picture, we will be able to introduce how we can tune the 2DEG geometry with voltage biased top metallic gates. Last, we will detail the fabrication process by which we define the contacts needed to bias and probe the sample, and the gates used to tune its properties.

11.1.1 GaAs/Ga(Al)As two dimensional electron gases

During this thesis we have used 2DEGs obtained at the interface of gallium arsenide (GaAs) and aluminium doped gallium arsenide (Ga(Al)As), as depicted in Figure 11.1.b.

Since GaAs and Ga(Al)As have different band gaps, their bands develop a sharp discontinuity when they are juxtaposed. In the limit of clean samples and low temperatures, their respective chemical potentials lie in the middle of their gaps (electroneutrality), and must

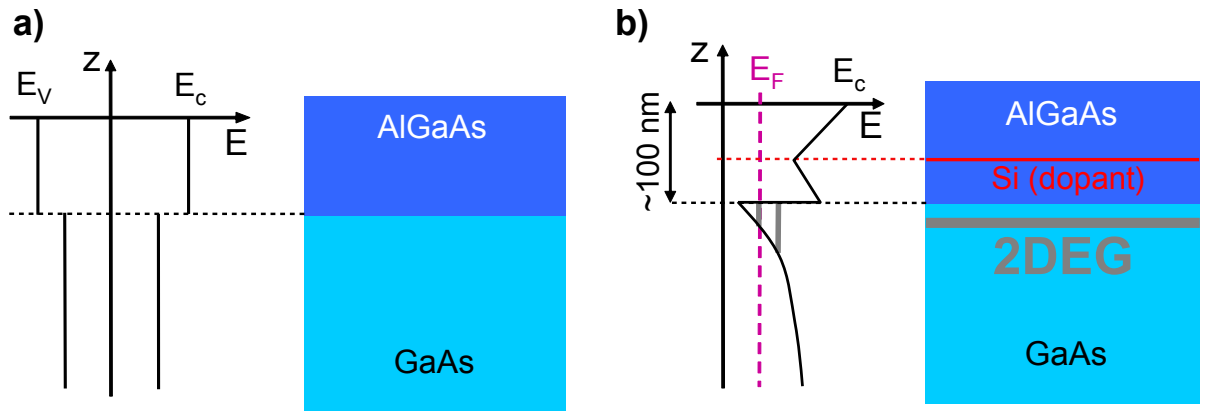

Figure 11.1: **2DEG obtained at the interface of GaAs and Ga(Al)As. a)** Non-interacting band plot (E_C: conduction band, E_V: valence band) as a function of the growing axis z. The different band gaps give rise to a band discontinuity at the heterojuntion interface. **b)** Self-consistent conduction band plot as a function of the growing axis (see text). An asymmetric quantum well develops at the interface. The quantum well traps the electrons provided by the donors (Si: silicon doping plane). The z dynamics of the trapped electrons are frozen when the Fermi energy (E_F) lies between two discrete states.

equilibrate when brought in contact (Figure 11.1.a). However, chemical potentials equilibrate as a result of a charge transfer between both materials. Therefore, the materials are not electrically balanced, and an electric field arises at the interface between them. The resulting conduction band is bent and develops an asymmetric quantum well at the interface of the heterojunction (see Figure 11.1.b). This quantum well can trap the electrons furnished by the dopant layer (here a silicium layer), even when it is spatially separated from the quantum well.

Since surface states can also trap the excess electrons, the amount of charge transfer from the doping layer to the quantum well depends on the ratio of the relative distances between surface and doping plane and between doping plane and quantum well. When the charge transferred to the quantum well fills only the lowest well level (as in Figure 11.1.b), the dynamics on the growing axis are frozen. Neglecting the zero point fluctuations in the z axis, a metallic 2DEG is formed at the heterojunction interface.

The resulting 2DEG can reach very high mobilities $\mu \gtrsim 10^6$ cm^2.V.s^{-1} as a consequence of the small disorder seen by the 2DEG. This is due to 2 main reason:

1. The string parameters of Ga(Al)As and GaAs are nearly the same. There are therefore no mechanical constrains at the interface, giving rise to a clean sharp interface.

2. The doping layer presents some disorder due to the random positioning of the dopants

in the doping plane. But, since a finite distance separates the doping plane from the electron channel, the disorder potential seen from the 2DEG is smoothed.

Of course, such arguments only apply if you can control the nature and concentration of the different chemical elements with a high precision. This is why MBE is used to grow such systems, since it permits to control them within an atomic layer accuracy. Typical parameters on the growing are: the doping plane to surface distance, the doping plane to interface distance, dopant concentration, aluminium concentration (slightly changes the gap and the string parameter). Last but not least, a cap layer of GaAs is deposited on top of the wafer to avoid the aluminium oxidation. As a result, the 2DEG properties can be long lived.

Electronic properties at cryogenic temperatures The high mobilities obtained in 2DEGs correspond to relatively large elastic scattering times $\tau = \frac{\mu}{em_{\text{eff}}} \gtrsim 40$ ps for mobilities μ in the 10^6 cm^2.V.s^{-1} range. The resulting mean free path lengths, l_{e}, for typical sheet densities $n_e \backsim 10^{15}$ m^{-2} reach tens of microns. Moreover, the reported phase coherent lengths can also reach the microns below 100 mK. This can be probed, for instance, by measuring Aharonov-Bohm oscillations in small rings [148].

Therefore, using standard nano-fabrication and cryogenic techniques, 2DEGs can be used to investigate the properties of *ballistic* electrons sensitive to *quantum phase coherence* effects.

Measured samples In all our samples, the 2DEG to surface distance is about 100 nm.

The 2DEG used to investigate the dynamical Coulomb blockade (DCB) has a moderate mobility $\mu = 0.55\ 10^6$ cm^2.V.s^{-1}, a Fermi energy of 150 K and a sheet density $n_{\text{e}} = 2.5\ 10^{15}$m^{-2}.

The 2DEG used to investigate the QHE has a high mobility $\mu = 2.5\ 10^6$ cm^2.V.s^{-1}, Fermi energy of 70 K and a sheet density $n_{\text{e}} = 2\ 10^{15}$m^{-2}. The growth parameters of this 2DEG have been optimized in order to display the smallest longitudinal resistance in the $\nu_L = 2$ plateau. It is the very same 2DEG wafer used to perform the Mach-Zehnder samples investigated by the CEA-Saclay nanoelectronics group [14, 23, 74, 128].

11.1.2 Gate depletion

As we have seen, a 2DEG is a 2D metallic conductor buried within a semi-conducting bulk and has moderate sheet densities. Therefore, its density, and even its geometry, can be modulated by field effect techniques.

A metallic gate on the surface develops a Schottky gap with the semiconductor underneath, therefore it is galvanically disconnected from the 2DEG. Since it is only capacitively

coupled with the 2DEG, a negative gate voltage will depopulate the electrons situated beneath the gate and up to a depletion length around the gate, as depicted in Figure 11.2. One can therefore tune *in situ* the geometry of the 2DEG with the help of such top metallic gates. This tunability makes a 2DEGs'circuits distinguished choices for carrying mesoscopic physics experiments.

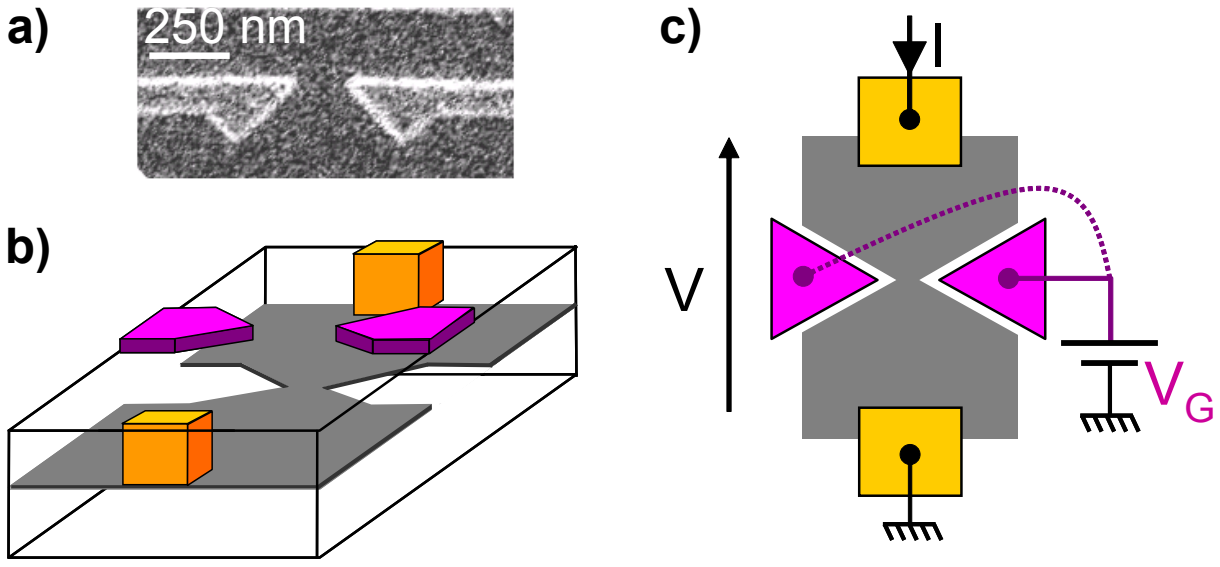

Figure 11.2: **Fine tuning the 2DEG geometry with top gates.** **a)** Electron beam micrograph a top metallic gate (appear brighter) on top of an GaAs/Ga(Al)As sample. **b)** 3D scheme of a 2DEG (grey) depleted by top metallic gates (magenta). A negative gate voltage V_G depletes the 2DEG beneath the gate and up to a transverse depletion length. The geometry of the 2DEG can be tuned *in situ*, here, to form a small constriction. Ohmic contacts (yellow) are needed to contact galvanically the 2DEG from the surface. **c)** Scheme of an electric circuit used to tune and probe a 2DEG.

11.1.3 Nano-fabrication

The circuit nanofabrication is based on electron beam lithography.

Our process follows 4 electronic insolation steps:

1. Define the ohmic contacts needed to bias and probe the sample (see Figure 11.2.b and .c).

2. Define the alignment marks, needed to obtain a good relative accuracy in the following lithographic steps (A manual alignment is here performed with step 1).

3. Define the 2DEG large geometry (mesa).

4. Define the top metallic gates.

Optical micrographs of the sample at the end of each step are presented in Figure 11.3.

The only notable difference between the DCB and QHE samples processing is that we have used titanium-gold gates in the DCB sample, while we have used aluminium gates in the QHE. Aluminium gates are preferable, since the Schottky gap to GaAs is slightly larger than for gold. Therefore, unwanted gate to 2DEG leakage should be smaller.

We now present the detailed process used to nano-structure the sample used to investigate the quantum Hall effect.

Cleaning the surface:

1. Trichlorethylene bath at 100 °C for 1 min, then 2 min with ultrasounds.

2. Aceton bath with moderate ultrasounds for 2 min.

3. Isopropanol clearing.

Ohmic contacts: see Figure 11.3.a (after annealing).

1. Resist deposition: Spin-coating with 50 g/L PMMA at 5 krpm for 60 s (Acceleration at 2 krpm/s). Deposited resist height is about 700 nm.

2. Cleaning the backside of the substrate with isopropanol in cotton sticks and sticking it to a silicium substrate with 30 g/L PMMA as glue.

3. Resist baking for about 1 h at 160 °C.

4. Electronic beam insolation to define the mask. Beam acceleration 100 kV, with typical dose 1000 $\mu C/cm^{-2}$.

5. Resist development: Bath of MIBK-isopropanol solution (respective volume ratio 1/3) for 45 s. Then clearing 10 s in an isopropanol bath.

6. Metal vapor deposition: Ohmic contacts consist in the successive deposition of Nickel: 40 Germanium: 600 Gold: 1200 Nickel: 250 Gold: 1000 in Angstroms. Contacts are mostly made from gold. Germanium dopes the semiconductor and diminishes the Schottky barrier. The Ge-Au mixtures is eutectic at eutectic temperature $T_{\text{eutectic}} = 370$ °C facilitating their penetration. Nickel substitutes to gallium, and facilitates the diffusion of gold [149]. The top gold layer on top of a thick 25 nm nickel is to facilitate the sample connection (wire bonding).

7. Lift-off (removes the metal over non-insolated regions):
   - trichlorethylene bath at 80 °C until metal removes.
   - Acetone clearing.
   - Isopropanol clearing.
8. Ohmic contact annealing (drives the vertical diffusion of the deposited metal, needed to contact the 2DEG). The contacts are pre-heated, set to eutectic temperature, then heated slightly to icrease the eutectic mixture diffusion.

risetime [*s*]	*plateau* [*s*]	T [°C]
5	40	120
10	120	370
15	50	420

9. Contacts testing: successive two wire probing of ohmic contacts, two at a time. $R_{2\text{wire}} \sim 1\ \text{k}\Omega$ at room temperature (in the dark) is dominated by the 2DEG sheet resistance. Check that I-V curves are linear.

Alignment marks: Alignement marks (Figure 11.3.b) are needed to realign the electron beam stage between the mesa definition and gate deposition.

1. Resist deposition: Spin-coating with 40 g/L PMMA at 5 krpm for 60 s (Acceleration at 2krpm/s). Deposited resist height is about 400 nm.
2. Steps 2-3-4-5 same as before.
3. Metal vapor deposition: Titanium: 200 Gold: 2000 in Angstroms.
4. Lift-off.

Mesa etching: Defines roughly the geometry of the 2DEG by chemical etching. Figure 11.3.c shows the aluminium mask used to protect the 2DEG. Figure 11.3.d shows the 2DEG sample after etching.

1. Steps 1-2-3-4-5 same as before.
2. Desoxyde the surface that is going to be covered by aluminium: 10 % HCl 5 s.
3. Aluminium metal deposition: 100 nm. Protects the 2DEG beneath.
4. Lift-off.

5. Chemical etching of the non-protected with a 1 H_2O_2−3 H_3PO_4− 80 H_2O mixture in volume. 3 successive baths for about 20 s, checking the deepness of the resulting etching between each bath. Yields to ~ 45 nm etching.

6. Check that etched regions are galvanically disconnected from mesa: measure the resistance between an ohmic contact use to contact the mesa, and a contact used to polarize a gate (etched all around). Test gives $R > 50$ MΩ (limited by measurement) even under light exposure.

Gates: Deposition of the top metallic gates, see Figure 11.3.e.

1. Test the electric beam dose needed and gate thickness to obtain good profiles: test the same pattern on a plain GaAs wafer.

2. Desoxide the surface: 10 % HCl 5 s.

3. Resist deposition: Spin-coating with PMMA A3 at 5 krpm for 60 s (Acceleration at 2 krpm/s). Deposited resist height is about 125 nm.

4. Resist baking.

5. Electronic beam insolation to define the mask. Beam acceleration 100 kV, with a dose 1400 μC/cm^{-2}.

6. Resist development.

7. Aluminium vapor deposition 50 nm.

8. Lift-off

Back-end: At the end of process, the sample is glued to a ceramic holder. The holder will be plugged in the cold finger of the dilution fridge, and permits a direct coupling with the measurement lines of the fridge. The last step in the process is the wire bonding between the ohmic and gate contacts of the chip to the ceramic contacts leading to the desired measurement lines, see Figure 11.3.f. Cold ground contacts should be bonded first to equilibrate the mesa potential to the ceramic potential. Gates should be bonded last, when the sample potential is more uniform, to avoid electrostatic shocks. All contacts and gates are shorted for transporting the sample out of the clean room.

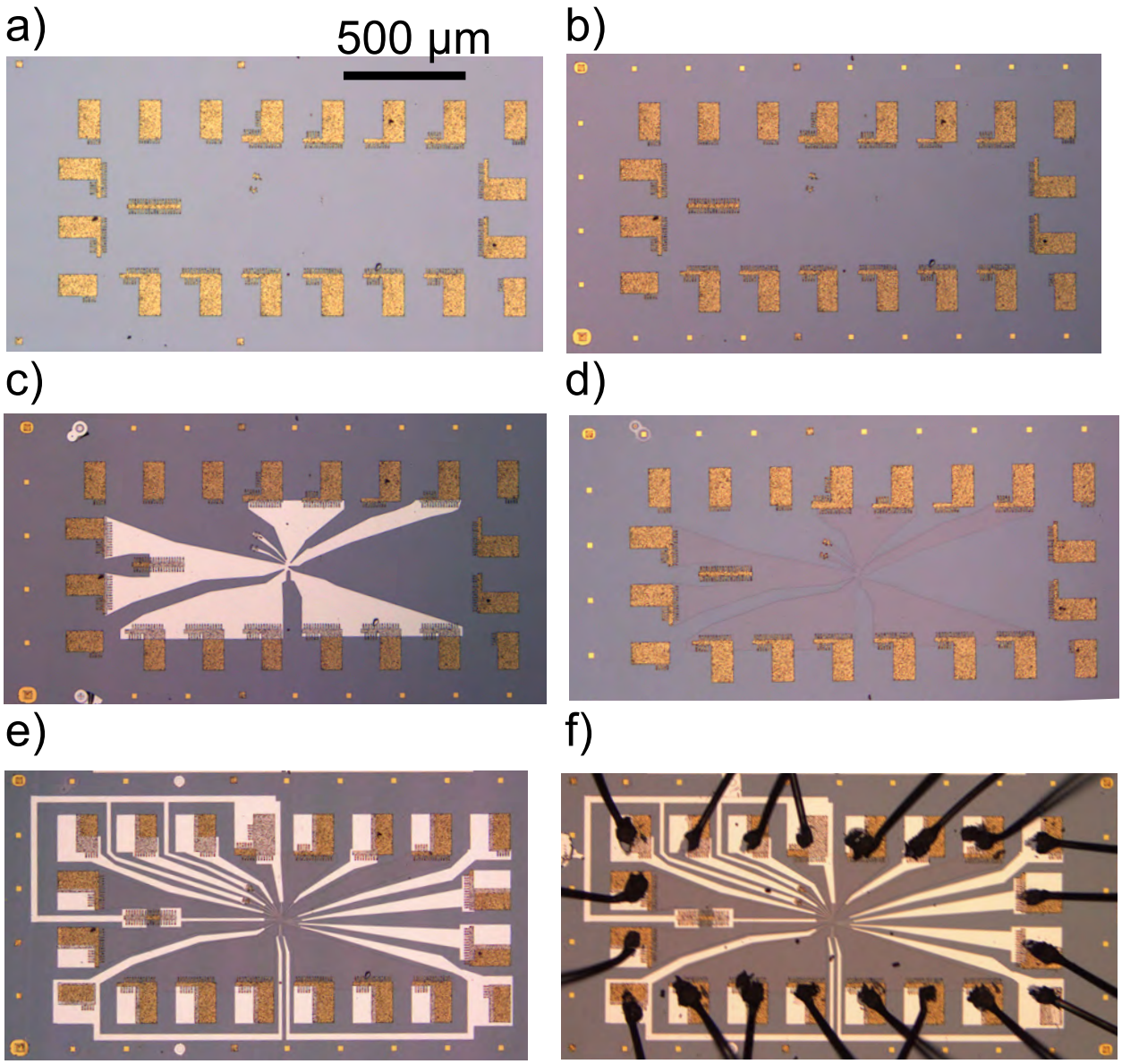

Figure 11.3: **Optical micrographs after successive process steps for the QHE sample. a)** Ohmic contacts after annealing. **b)** Alignment marks. **c)** Aluminium mask protecting the 2DEG from chemical etching. **d)** 2DEG defined by chemical etching. **e)** Top metallic gates (electron beam micrograph of the active region shown in Chapter 4). **f)** Wire bonding.

11.2 Low-noise measurement techniques

All the experiments performed in this thesis rely on near DC electronic techniques. This section presents the cryostat wiring and filtering, the room temperature electronics and polarization schemes that we have used.

11.2.1 Cryostat wiring

Cryostat wires are filtered by commercial $\pi-$filters at the top of the cryostat (room temperature). At low temperature, the lines are filtered by arranging them as 1 m long resistive twisted pairs (300 Ω/m) inserted inside 260 μm inner diameter CuNi. The tubes are tightly wrapped around a copper plate screwed to the mixing chamber assuring a good electronic thermalization. The access resistance measured at null magnetic field is dominated by the twisted pairs $R_{\text{access}} \simeq 350\ \Omega$. The sample is further protected from spurious high energy photons by two shields, both at base temperature.

11.2.2 Room-temperature electronics

DC Biasing: The samples are current biased using stabilized DC voltage sources Yokogawa 7621 in series with 10 MΩ or 100 MΩ polarization resistance. Gates are also voltage biased with the same voltage sources, or battery powered when there is no need for an accurate voltage sweep.

Conductance measurements and amplification: Conductance measurements are performed using standard lock-in techniques at excitation frequencies below 200 Hz. An AC polarization is added to the DC bias, keeping the resulting AC voltage smaller than $k_{\text{B}}T$ to avoid artificial "heating". The sample response is measured in phase at the excitation frequency. We use commercial numeric lock-ins , Standford SR810.

Small signals are pre-amplified by low noise voltage amplifiers designed and build by the Electronic Service of the Institut Neel at Grenoble (0.8 nV/$\sqrt{\text{Hz}}$ above 10 Hz).

The polarization resistances and preamplifiers are placed in a copper Faraday box connected to an earth ground piked outside the lab, which defines the ground for our measurement system. The measurement lines are shielded between the Faraday box and the top of the cryostat. Therefore, all small signals are protected from background noise.

All measurements are recorded on computer via IEEE-GPIB interfaces, optically isolated from the experiment.

Gate protection The small gates used to define the quantum point contacts (QPC) and quantum dots (QDOT) can literally explode when bruskly biased[1]. All gates are biased through home-made RC-filters of adjustable bandwidth (≥ 1 Hz), to prevent from bad cabling accidents or voltage source disfunctions. Moreover, all gates and contacts can be shorted to the ground to protect the sample during the cooling.

11.2.3 Polarization schemes in the QHE

The DCB experiment is measured performing standard four wire measurements with the precedent tools.

In the QHE experiments, we take profit of the (metrological) two wire resistance quantization due to the quantum Hall effect (see Chapter 2). All contacts[2] that are current biased see a two wire resistance to the ground. This is realized by placing as many cold grounded contacts as there are possible edge paths for the injected current. Therefore, the current polarization results directly in a voltage polarization, $V_{\rm pol} = R_{\nu_L} I_{\rm pol}$, irrespective of the 2 wire resistance of the biased QPCs or QDOT. At the opposite, if a floating contact is connected to a cold ground by the edge chirality, the voltage measured $V_{\rm meas}$ on it gives directly the current impinging on it $I_{\rm meas}$: $V_{\rm meas} = R_{\nu_L} I_{\rm meas}$.

[1] At room temperature they can even explode due to triboelectric charging. At subKelvin temperature, the electron-phonon coupling is low enough to prevent an explosion, however an electrostatic shock can translate a gate for some hundreds of nanometers.

[2] But one, it is the ohmic contact used to drive an edge channels out of equilibrium (Chapter 6), or to current bias the QPC with a 0.8 µm distance to the quantum dot (Chapter 4-5-6).

Appendix A

Sequential tunneling through multiple discrete levels

When multiple discrete levels lie in the transport window, non-intuitive dynamical effects can arise. In the sequential tunneling regime, the strong Coulomb energy impedes changes of more than one electron. Therefore, the many electron paths due to the many levels do not add in parallel. The resulting expression for the mean current can be starkly different [119] from the one found for a single level (3.8), which *limits its application range*. Moreover, dynamical effects can modify the sharp features of the stability diagrams plots at finite temperature. Both effects will *limit the experimental accuracy on the lever arm experimental calibration*, when using the simple single level model (3.8). We first define the general problem of sequential tunneling in multiple levels. We will after illustrate two of its dynamical effects: i) some expected resonances can vanish for particular ratios of the couplings, ii) the position of the resonances can be shifted for asymmetric couplings, with respect to what is expected at zero temperature (direct energy balance considerations).

A.0.4 General problem

The general problem follows from the rate equations for the occupation probabilities, P_i, of the discrete states , E_i. These probabilities can be encapsulated within the vector $\vec{P} = \{P_i\}$, whose time dependence depends on the couplings to the electrodes and their energy distributions [119]:

$$\frac{d\vec{P}}{dt} = [\Gamma]\vec{P}. \tag{A.1}$$

For example, when an electron can populate 1 of N available states, we can label P_0 the probability for no occupied states and $P_i > 0$ the probability that only state i is occupied.

With these notations, it is easy to check that the coupling matrix $[\Gamma]$ has the form:

$$[\Gamma] = \begin{pmatrix} -\sum_{i=1}^{N} \gamma_{0\to i} & \gamma_{1\to 0} & \gamma_{2\to 0} & \dots & \gamma_{N\to 0} \\ \gamma_{0\to 1} & -\gamma_{1\to 0} & 0 & \dots & 0 \\ \gamma_{0\to 2} & 0 & -\gamma_{2\to 0} & \ddots & \vdots \\ \vdots & \vdots & \ddots & \ddots & 0 \\ \gamma_{0\to N} & 0 & \dots & 0 & -\gamma_{N\to 1} \end{pmatrix} \tag{A.2}$$

where the $\gamma_{i\to j}$ take into account the couplings $\Gamma_{D/S}(E)$ and electrodes' $f_{D/S}(E)$ at the energies E_i of the coupled discrete levels:

$$\begin{aligned} \gamma_{i\to 0} &= \Gamma_D(E_i)[1 - f_D(E_i)] + \Gamma_S(E_i)[1 - f_S(E_i)] \\ \gamma_{0\to i} &= \Gamma_D(E_i) f_D(E_i) + \Gamma_S(E_i) f_S(E_i). \end{aligned} \tag{A.3}$$

In the stationary regime $d\vec{P}/dt = 0$, $\vec{P}$ is found as the eigenvector of $[\Gamma]$ of null eigenvalue, and the mean current reads [119]:

$$I = I_D = -e \sum_{1}^{N} \Gamma_D(E_i) P_i [1 - f_D(E_i)] - P_0 \sum_{1}^{N} \Gamma_D(E_i) f_D(E_i)) \tag{A.4}$$

A.0.5 Vanishing resonances and negative differential resistances

We here illustrate that the addition of a discrete level in the transport window, can not only increase the current flowing through the quantum dot, but also diminish it, or leave it the same, if the tunnel couplings are different for different levels. Indeed, when the coupling of the additional level is small, it can trap the tunneling electron for a long time, so that the mean current diminishes.

3 discrete levels:

We consider the simplest case of symmetric coupled levels, at zero temperature[1], when 1-2 electrons can populate 3 discrete levels at the energies E_i, which is depicted in Figure A.1. Left. When the drain and source couplings are symmetric, $\Gamma_D(E_i) = \Gamma_S(E_i) = \Gamma_i$, the coupling matrix $[\Gamma]$ is symmetric too and admits a uniform eigenvector for the null eigenvalue, so that the occupation numbers only depend on the number of possible states. We label $P(n_1, n_2, n_3)$ the joint probability for the occupation numbers, $n_i \in \{0, 1\}$, of the levels i. Therefore, the mean current in the regimes depicted in Figure A.1. Right can be easily found:

[1] The electrodes energy distribution functions are therefore either 0 or 1 at the discrete levels energies, which simplifies the shape of $[\Gamma]$.

- Level 2 only in the transport window (black inset and region in Figure A.1. Right) gives: $P(1,0,0) = P(1,1,0) = 1/2$, all others being null. Which yields to $|I_{black}| = e\Gamma_2/2$.

- All three levels in the transport window (red inset and region in Figure A.1. Right) give: $P(1,0,0) = P(0,1,0) = P(0,0,1) = P(1,1,0) = P(0,1,1) = P(1,0,1) = 1/6$ yielding to $|I_{red}| = e\sum_{i=1}^{3}\Gamma_i/3$.

- Two levels in the transport window (green/blue insets and regions in Figure A.1. Right) give: $P(1,0,0) = P(0,1,0) = P(1,1,0) = 1/3$ (green) and $P(0,1,0) = P(0,0,1) = P(0,1,1) = 1/3$ (blue) yielding to $|I_{green/blue}| = e(\Gamma_2 + \Gamma_{1/3})/3$.

Now, it is easy to check that $I_{red} > I_{green/blue}$ irrespective of the couplings. However, $I_{green/blue} - I_{black} = e(2\Gamma_1/3 - \Gamma_2)/6$ can be positive, negative or null. Therefore, for some special fractions of the couplings, the current can remain flat when a discrete level is in resonance with an electrode Fermi energy. Second, this can give rise to negative differential conductances for a large range of couplings defined by $2\Gamma_1/3 - \Gamma_2 < 0$.

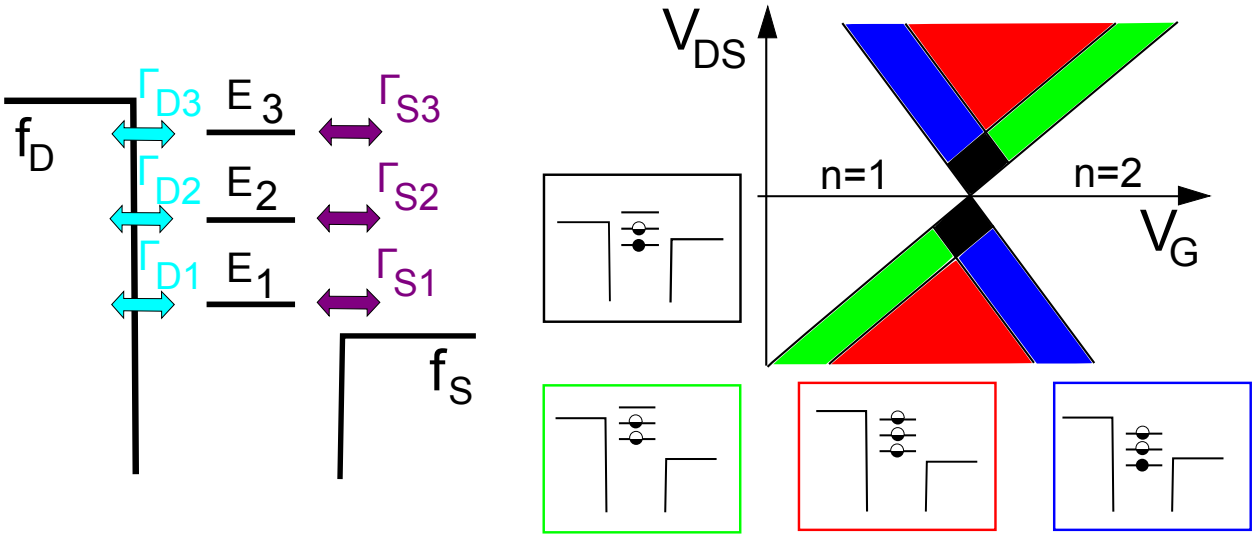

Figure A.1: **3 discrete level quantum dot.** Left: Schematic of electron tunneling through a 3 level quantum dot. Right: Stability diagram at zero temperature, colored regions correspond to color marching insets. Black: level 2 in the transport window Red: All levels in the transport window. Green: Levels 1 and 2 in the transport window. Blue: Levels 2 and 3 in the transport window.

Generalization:

As long as the couplings are symmetric and thermal occupations negligible, the same arguments can be generalized to arbitrary numbers of electrons in an arbitrary number of

discrete levels. We consider $n/n+1$ electrons that can be placed amongst N discrete levels. All possible states have a probability $P = \frac{1}{C_N^n + C_N^{n+1}}$, resulting from the number of possible states $C_N^n + C_N^{n+1}$. The mean current reads:

$$I = ePJ \sum_i^N \Gamma_i. \tag{A.5}$$

Since all states are equiprobable, the current is just a function of $\sum_i^N \Gamma_i$ multiplied by P times a factor J. J accounts for all states that are coupled to level i, namely the number of states not having an electron on it: $J = C_N^n - C_{N-1}^{n-1} = C_{N-1}^n$. Therefore the current reads:

$$I = e\frac{C_{N-1}^n}{C_N^n + C_N^{n+1}} \sum_i^N \Gamma_i. \tag{A.6}$$

Which generalizes the precedent conclusions. We have pictured in red, in Figure A.2, the ranges where the addition of a discrete level in the transport window always gives rise to a current increase.

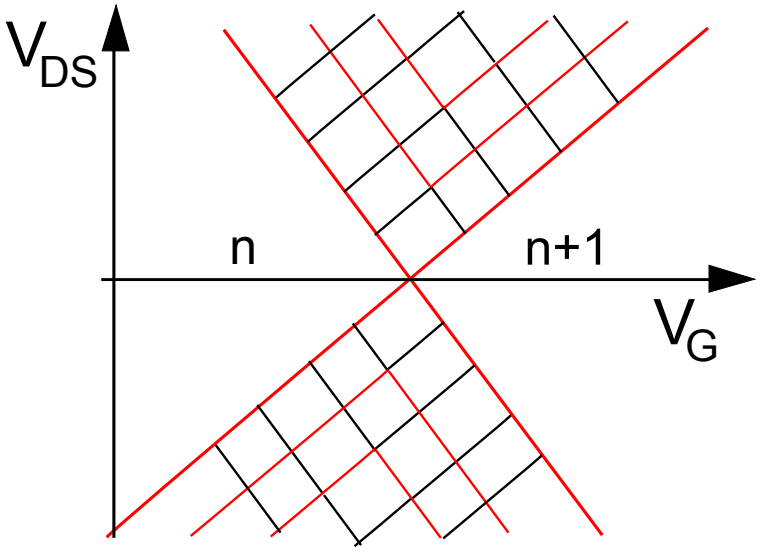

Figure A.2: **Stability diagram in a symmetric quantum dot, zero temperature.** According to (A.6): Crossing a discrete level, increasing $|V_{DS}|$, through a red line always increases the current. Crossing a discrete level through a black line can increase, diminish or maintain the current.

A.0.6 Resonance displacements

The presence of multiple levels in the transport window can translate the position of the resonances expected from energy balance considerations (3.12) at zero temperature. Therefore, the slopes of the stability diagram do not only depend on the electrostatics, but also on the

relative couplings to the multiple levels. Such effects are already discussed in [119]. We give here the simplest case where $0/1$ electrons can populate N discrete levels. We analyze the case where the lowest level, E_1, is in resonance with the source, while all the excited levels, $E_{i>1}$, face a fully occupied drain electrode (negative V_{DS}).

Under these conditions we have $f_D(E_i) = 1$, $f_S(E_1) = f$ and $f_S(E_{i>1}) = 0$. The coupling matrix Γ (A.2) is here a $N+1 \times N+1$ matrix that can be directly diagonalized. The null eigenvector gives:

$$\begin{aligned} P(0,0,\ldots) &= \frac{1}{1+\frac{\alpha_1+f}{1-f}+\sum_{i>1}\alpha_i} \\ P(1,0,\ldots) &= \frac{\alpha_1+f}{1-f}\frac{1}{1+\frac{\alpha_1+f}{1-f}+\sum_{i>1}\alpha_i} \\ P(0,\ldots,1,0,\ldots) &= \frac{\alpha_i}{1+\frac{\alpha_1+f}{1-f}+\sum_{i>1}\alpha_i} \end{aligned} \tag{A.7}$$

$$\text{where} \quad \alpha_i = \frac{\Gamma_D(E_i)}{\Gamma_S(E_i)} \tag{A.8}$$

And the corresponding stationary current reads:

$$\begin{aligned} I = I_D &= -eP_0\sum_{i=1}^{N}\Gamma_D(E_i) \\ I &= -e\frac{\sum_{i=1}^{N}\Gamma_D(E_i)}{1+\alpha_1}\frac{1-f}{1+A(1-f)} \\ \text{with} \quad A &= \frac{\sum_{i>1}\alpha_i}{1+\alpha_1} \end{aligned} \tag{A.9}$$

When f_S is a Fermi function in resonance with the lowest level, $f(E) = f_F(E-E_1) = 1/(1+\exp[(E-E_1)/k_\mathrm{B}T])$, one finds that the mean current reads:

$$\begin{aligned} I &= -e\frac{\Gamma_D(E_1)+\Gamma_D(E_2)}{(1+\alpha_1)(1+A)}\frac{1}{1+\exp[E-E_1-k_\mathrm{B}T\ln(1+A)]} \\ &= -e\frac{\Gamma_D(E_1)+\Gamma_D(E_2)}{(1+\alpha_1)(1+A)}f_F[E-E_1-k_\mathrm{B}T\ln(1+A)] \end{aligned} \tag{A.10}$$

A current step arises as for a single level (renormalized in amplitude), but the position of the current step feature occurs at an energy larger by $k_\mathrm{B}T\ln(1+A)$ than the energy of the discrete level E_1. Therefore, the presence of additional levels in the transport window translates the resonances positions on a $k_\mathrm{B}T$ scale. These shifts will limit the accuracy when extracting the lever arm from the slopes of a stability diagram.

The general problem of non symmetric multiple levels with energy dependent couplings (A.1) and (A.4) can be handled numerically [119], when the couplings to the discrete levels and their energy spacings are known. However, using this scheme to probe an unknown

$f(E)$ would need an independent calibration of the couplings which cannot be done by DC measurements alone, and complicates the analysis. In order to probe an unknown $f(E)$, it is therefore desirable use a quantum dot with a single active level within the transport window needed to probe the relevant energy scales.

Bibliography

[1] C. Altimiras, H. le Sueur, U. Gennser, A. Cavanna, D. Mailly, and F. Pierre, *Non-Equilibrium Edge Channel Spectroscopy in the Integer Quantum Hall Regime*, Nature Phys. **6**, 34 (2009).

[2] H. le Sueur, C. Altimiras, U. Gennser, A. Cavanna, D. Mailly, and F. Pierre, *Energy Relaxation in the Integer Quantum Hall Regime*, Phys. Rev. Lett. **105**, 5, 056803 (2010).

[3] C. Altimiras, H. le Sueur, U. Gennser, A. Cavanna, D. Mailly, and F. Pierre, *Tuning Energy Relaxation along Quantum Hall Channels*, Phys. Rev. Lett. **105**, 22, 226804 (2010).

[4] C. Altimiras, U. Gennser, A. Cavanna, D. Mailly, and F. Pierre, *Experimental Test of the Dynamical Coulomb Blockade Theory for Short Coherent Conductors*, Phys. Rev. Lett. **99**, 25, 256805 (2007).

[5] D. S. Golubev and A. D. Zaikin, *Coulomb Interaction and Quantum Transport through a Coherent Scatterer*, Phys. Rev. Lett. **86**, 21, 4887 (2001).

[6] A. L. Yeyati, A. Martin-Rodero, D. Esteve, and C. Urbina, *Direct Link between Coulomb Blockade and Shot Noise in a Quantum-Coherent Structure*, Phys. Rev. Lett. **87**, 4, 046802 (2001).

[7] K. v. Klitzing, G. Dorda, and M. Pepper, *New Method for High-Accuracy Determination of the Fine-Structure Constant Based on Quantized Hall Resistance*, Phys. Rev. Lett. **45**, 6, 494 (1980).

[8] Y. Ji, Y. J. Y. Chung, D. Sprinzak, M. Heiblum, D. Mahalu, and H. Strikman, *An electronic Mach-Zehnder interferometer*, Nature **422**, 415 (2003).

[9] I. Neder, N. Ofek, Y. Chung, M. Heiblum, D. Mahalu, and V. Umansky, *Interference between two indistinguishable electrons from independent sources*, Nature **448**, 333 (2007).

[10] G. Fève, A. Mahé, J.-M. Berroir, T. Kontos, B. Plaçais, D. C. Glattli, A. Cavanna, B. Etienne, and Y. Jin, *An On-Demand Coherent Single-Electron Source*, Science **316**, 1169 (2007).

[11] I. Neder, M. Heiblum, Y. Levinson, D. Mahalu, and V. Umansky, *Unexpected Behavior in a Two-Path Electron Interferometer*, Phys. Rev. Lett. **96**, 1, 016804 (2006).

[12] I. Neder, F. Marquard, M. Heiblum, D. Mahalu, and V. Umansky, *Controlled dephasing of electrons by non-gaussian shot noise*, Nature Phys. **3**, 534 (2007).

[13] L. V. Litvin, H. P. Tranitz, W. Wegscheider, and C. Strunk, *Decoherence and single electron charging in an electronic Mach-Zehnder interferometer*, Phys. Rev. B **75**, 3, 033315 (2007).

[14] P. Roulleau, F. Portier, P. Roche, A. Cavanna, G. Faini, U. Gennser, and D. Mailly, *Direct Measurement of the Coherence Length of Edge States in the Integer Quantum Hall Regime*, Phys. Rev. Lett. **100**, 12, 126802 (2008).

[15] E. Bieri, M. Weiss, O. Göktas, M. Hauser, C. Schönenberger, and S. Oberholzer, *Finite-bias visibility dependence in an electronic Mach-Zehnder interferometer*, Phys. Rev. B **79**, 24, 245324 (2009).

[16] H. A. Fertig, *A view from the edge*, Physics **2**, 15 (2009).

[17] D. B. Chklovskii, B. I. Shklovskii, and L. I. Glazman, *Electrostatics of edge channels*, Phys. Rev. B **46**, 7, 4026 (1992).

[18] A. MacDonald, S. R. E. Yang, and M. D. Johnson, *Quantum dots in strong magnetic fields: Stability criteria for the maximum density droplet*, Aust. J. Phys. **46**, 345 (1993).

[19] C. d. C. Chamon and X. G. Wen, *Sharp and smooth boundaries of quantum Hall liquids*, Phys. Rev. B **49**, 12, 8227 (1994).

[20] I. L. Aleiner and L. I. Glazman, *Novel edge excitations of two-dimensional electron liquid in a magnetic field*, Phys. Rev. Lett. **72**, 18, 2935 (1994).

[21] X. G. Wen, *Electrodynamical properties of gapless edge excitations in the fractional quantum Hall states*, Phys. Rev. Lett. **64**, 18, 2206 (1990).

[22] C. Kane and M. Fisher, *Edge state transport*, in *Perspectives in the quantum Hall effect*, edited by S. Das Sarma and A. Pinczuk, 109–159, John Wiely & Sons, Inc. (1997).

[23] P. Roulleau, F. Portier, P. Roche, A. Cavanna, G. Faini, U. Gennser, and D. Mailly, *Noise Dephasing in Edge States of the Integer Quantum Hall Regime*, Phys. Rev. Lett. **101**, 18, 186803 (2008).

[24] U. Sivan and Y. Imry, *Multichannel Landauer formula for thermoelectric transport with application to thermopower near the mobility edge*, Phys. Rev. B **33**, 1, 551 (1986).

[25] H. Pothier, S. Guéron, N. O. Birge, D. Esteve, and M. H. Devoret, *Energy Distribution Function of Quasiparticles in Mesoscopic Wires*, Phys. Rev. Lett. **79**, 18, 3490 (1997).

[26] Y.-F. Chen, T. Dirks, G. Al-Zoubi, N. O. Birge, and N. Mason, *Nonequilibrium Tunneling Spectroscopy in Carbon Nanotubes*, Phys. Rev. Lett. **102**, 3, 036804 (2009).

[27] B. J. van Wees, H. van Houten, C. W. J. Beenakker, J. G. Williamson, L. P. Kouwenhoven, D. van der Marel, and C. T. Foxon, *Quantized conductance of point contacts in a two-dimensional electron gas*, Phys. Rev. Lett. **60**, 9, 848 (1988).

[28] T. Gramespacher and M. Büttiker, *Local densities, distribution functions, and wavefunction correlations for spatially resolved shot noise at nanocontacts*, Phys. Rev. B **60**, 4, 2375 (1999).

[29] D. Pines and P. Nozières, *The Theory of Quantum Liquids*, Perseus Books (1966).

[30] A. M. Lunde, S. E. Nigg, and M. Büttiker, *Interaction-induced edge channel equilibration*, Phys. Rev. B **81**, 4, 041311(R) (2010).

[31] P. Degiovanni, C. Grenier, G. Fève, C. Altimiras, H. le Sueur, and F. Pierre, *Plasmon scattering approach to energy exchange and high-frequency noise in $\nu = 2$ quantum Hall edge channels*, Phys. Rev. B **81**, 12, 121302(R) (2010).

[32] M. Büttiker, *Role of quantum coherence in series resistors*, Phys. Rev. B **33**, 5, 3020 (1986).

[33] D. C. Tsui, H. L. Stormer, and A. C. Gossard, *Two-Dimensional Magnetotransport in the Extreme Quantum Limit*, Phys. Rev. Lett. **48**, 22, 1559 (1982).

[34] R. B. Laughlin, *Anomalous Quantum Hall Effect: An Incompressible Quantum Fluid with Fractionally Charged Excitations*, Phys. Rev. Lett. **50**, 18, 1395 (1983).

[35] R. de-Picciotto, M. Reznikov, M. Heiblum, V. Umansky, G. Bunin, and D. Mahalu, *Direct observation of a fractional charge*, Nature **389**, 6647, 162 (1997).

[36] L. Saminadayar, D. C. Glattli, Y. Jin, and B. Etienne, *Observation of the $e/3$ Fractionally Charged Laughlin Quasiparticle*, Phys. Rev. Lett. **79**, 13, 2526 (1997).

[37] D. Arovas, J. R. Schrieffer, and F. Wilczek, *Fractional Statistics and the Quantum Hall Effect*, Phys. Rev. Lett. **53**, 7, 722 (1984).

[38] X.-G. Wen, *Theory of the edges states in fractional quantum Hall effects*, Int. J. Mod. Phys B **6**, 1711 (1992).

[39] P. Fendley, A. W. W. Ludwig, and H. Saleur, *Exact Conductance through Point Contacts in the $\nu = 1/3$ Fractional Quantum Hall Effect*, Phys. Rev. Lett. **74**, 15, 3005 (1995).

[40] A. M. Chang, *Chiral Luttinger liquids at the fractional quantum Hall edge*, Rev. Mod. Phys. **75**, 4, 1449 (2003).

[41] X. G. Wen, *Gapless boundary excitations in the quantum Hall states and in the chiral spin states*, Phys. Rev. B **43**, 13, 11025 (1991).

[42] C. L. Kane, M. P. A. Fisher, and J. Polchinski, *Randomness at the edge: Theory of quantum Hall transport at filling $\nu = 2/3$*, Phys. Rev. Lett. **72**, 26, 4129 (1994).

[43] C. L. Kane and M. P. A. Fisher, *Quantized thermal transport in the fractional quantum Hall effect*, Phys. Rev. B **55**, 23, 15832 (1997).

[44] T. A. Fulton and G. J. Dolan, *Observation of single-electron charging effects in small tunnel junctions*, Phys. Rev. Lett. **59**, 1, 109 (1987).

[45] D. V. Averin, A. N. Korotkov, and K. K. Likharev, *Theory of single-electron charging of quantum wells and dots*, Phys. Rev. B **44**, 12, 6199 (1991).

[46] G.-L. Ingold and Y. V. Nazarov, *Charge Tunneling Rates in Ultrasmall Junctions*, in *Single Charge Tunneling*, edited by H. Graber and M. H. Devoret, Plenum Press (New York and London) (1992).

[47] R. Landauer, *Electrical Resistance Of Disordered One-Dimensional Lattices*, Philos. Mag. **21**, 172, 863 (1970).

[48] Y. M. Blanter and M. Büttiker, *Shot noise in mesoscopic conductors*, Physics Reports **336**, 1-2, 1 (2000).

[49] T. Martin, *Noise in mesoscopic physics*, in *Nanophysics: coherence and transport*, edited by H. Bouchiat, Y. Gefen, S. Guéron, G. Montambaux, and J. Dalibard, 283–360, Elsevier (2005).

[50] B. J. van Wees, L. P. Kouwenhoven, C. J. P. M. Harmans, J. G. Williamson, C. E. Timmering, M. E. I. Broekaart, C. T. Foxon, and J. J. Harris, *Observation of zero-dimensional states in a one-dimensional electron interferometer*, Phys. Rev. Lett. **62**, 21, 2523 (1989).

[51] R. Cron, E. Vecino, M. H. Devoret, D. Esteve, P. Joyez, A. Levy-Yeyati, A. Martin-Rodero, and C. Urbina, *Dynamical Coulomb Blockade in Quantum Point Contacts*, in *Electronic Correlations: From Meso- to Nano-Physics*, edited by T. Martin, G. Montambaux, and J. Trân Thanh Vân, EDP Sciences (New York and London) (2001).

[52] M. Reznikov, M. Heiblum, H. Shtrikman, and D. Mahalu, *Temporal Correlation of Electrons: Suppression of Shot Noise in a Ballistic Quantum Point Contact*, Phys. Rev. Lett. **75**, 18, 3340 (1995).

[53] A. Kumar, L. Saminadayar, D. C. Glattli, Y. Jin, and B. Etienne, *Experimental Test of the Quantum Shot Noise Reduction Theory*, Phys. Rev. Lett. **76**, 15, 2778 (1996).

[54] Y. Imry, *Introduction to mesoscopic physics*, Oxford University Press (USA) (1997).

[55] T. Giamarchi, *Quantum Physics in One Dimension*, Oxford University Press (USA) (2003).

[56] T. Martin and S. Feng, *Suppression of scattering in electron transport in mesoscopic quantum Hall systems*, Phys. Rev. Lett. **64**, 16, 1971 (1990).

[57] M. Büttiker, Y. Imry, R. Landauer, and S. Pinhas, *Generalized many-channel conductance formula with application to small rings*, Phys. Rev. B **31**, 10, 6207 (1985).

[58] M. Büttiker, *Scattering theory of thermal and excess noise in open conductors*, Phys. Rev. Lett. **65**, 23, 2901 (1990).

[59] T. Martin and R. Landauer, *Wave-packet approach to noise in multichannel mesoscopic systems*, Phys. Rev. B **45**, 4, 1742 (1992).

[60] D. C. Tsui, H. L. Stormer, and A. C. Gossard, *Two-Dimensional Magnetotransport in the Extreme Quantum Limit*, Phys. Rev. Lett. **48**, 22, 1559 (1982).

[61] N. W. Ashcroft and N. D. Mermin, *Solid State Physics*, Saunders College Publishing (1976).

[62] R. Prange and S. Girvin (Eds.), *The Quantum Hall effect*, Springer, New York (1987).

[63] D. Yoshioka, *The Quantum Hall Effect*, Springer (1998).

[64] B. I. Halperin, *Quantized Hall conductance, current-carrying edge states, and the existence of extended states in a two-dimensional disordered potential*, Phys. Rev. B **25**, 4, 2185 (1982).

[65] M. Büttiker, *Absence of backscattering in the quantum Hall effect in multiprobe conductors*, Phys. Rev. B **38**, 14, 9375 (1988).

[66] B. J. van Wees, E. M. M. Willems, C. J. P. M. Harmans, C. W. J. Beenakker, H. van Houten, J. G. Williamson, C. T. Foxon, and J. J. Harris, *Anomalous integer quantum Hall effect in the ballistic regime with quantum point contacts*, Phys. Rev. Lett. **62**, 10, 1181 (1989).

[67] S. Komiyama, H. Hirai, S. Sasa, and S. Hiyamizu, *Violation of the integral quantum Hall effect: Influence of backscattering and the role of voltage contacts*, Phys. Rev. B **40**, 18, 12566 (1989).

[68] U. Kla"s, W. Dietsche, K. von Klitzing, and K. Ploog, *Imaging of the dissipation in quantum-Hall-effect experiments*, Zeitschrift f"ur Physik B Condensed Matter **82**, 351 (1991). 10.1007/BF01357178.

[69] B. W. Alphenaar, P. L. McEuen, R. G. Wheeler, and R. N. Sacks, *Selective equilibration among the current-carrying states in the quantum Hall regime*, Phys. Rev. Lett. **64**, 6, 677 (1990).

[70] T. Martin and S. Feng, *Suppression of inter-edge-state equilibration due to multiple scattering with impurities*, Phys. Rev. B **44**, 16, 9084 (1991).

[71] G. Müller, D. Weiss, A. V. Khaetskii, K. von Klitzing, S. Koch, H. Nickel, W. Schlapp, and R. Lösch, *Equilibration length of electrons in spin-polarized edge channels*, Phys. Rev. B **45**, 7, 3932 (1992).

[72] M. Büttiker, *Quantized transmission of a saddle-point constriction*, Phys. Rev. B **41**, 11, 7906 (1990).

[73] B. J. van Wees, L. P. Kouwenhoven, H. van Houten, C. W. J. Beenakker, J. E. Mooij, C. T. Foxon, and J. J. Harris, *Quantized conductance of magnetoelectric subbands in ballistic point contacts*, Phys. Rev. B **38**, 5, 3625 (1988).

[74] P. Roulleau, F. Portier, D. C. Glattli, P. Roche, A. Cavanna, G. Faini, U. Gennser, and D. Mailly, *Finite bias visibility of the electronic Mach-Zehnder interferometer*, Phys. Rev. B **76**, 16, 161309 (2007).

[75] W. Kohn, *Cyclotron Resonance and de Haas-van Alphen Oscillations of an Interacting Electron Gas*, Phys. Rev. **123**, 4, 1242 (1961).

[76] P. Plochocka, J. M. Schneider, D. K. Maude, M. Potemski, M. Rappaport, V. Umansky, I. Bar-Joseph, J. G. Groshaus, Y. Gallais, and A. Pinczuk, *Optical Absorption to Probe the Quantum Hall Ferromagnet at Filling Factor $\nu = 1$*, Phys. Rev. Lett. **102**, 12, 126806 (2009).

[77] M. Kasner and A. H. MacDonald, *Thermodynamics of Quantum Hall Ferromagnets*, Phys. Rev. Lett. **76**, 17, 3204 (1996).

[78] L. Brey, H. A. Fertig, R. Côté, and A. H. MacDonald, *Skyrme Crystal in a Two-Dimensional Electron Gas*, Phys. Rev. Lett. **75**, 13, 2562 (1995).

[79] T. Martin and D. Loss, *Phase Diagram For a Luttinger Liquid Couples to Phonons in One Dimension*, Int. J. Mod. Phys. B **9**, 4-5, 495 (1995).

[80] I. P. Levkivskyi and E. V. Sukhorukov, *Dephasing in the electronic Mach-Zehnder interferometer at filling factor $\nu = 2$*, Phys. Rev. B **78**, 4, 045322 (2008).

[81] L. I. Glazman and I. A. Larkin, *Lateral position control of an electron channel in a split-gate device*, Semicond. Sci. Technol. 6, 32 (1991). **6**, 1, 32 (1991).

[82] V. A. Volkov and S. A. Mikhailov, Zh. Eksp. Teor. Fiz. **67**, 1639 (1988).

[83] D. C. Glattli, E. Y. Andrei, G. Deville, J. Poitrenaud, and F. I. B. Williams, *Dynamical Hall Effect in a Two-Dimensional Classical Plasma*, Phys. Rev. Lett. **54**, 15, 1710 (1985).

[84] J. H. Han and D. J. Thouless, *Dynamics of compressible edge and bosonization*, Phys. Rev. B **55**, 4, R1926 (1997).

[85] R. C. Ashoori, H. L. Stormer, L. N. Pfeiffer, K. W. Baldwin, and K. West, *Edge magnetoplasmons in the time domain*, Phys. Rev. B **45**, 7, 3894 (1992).

[86] N. B. Zhitenev, R. J. Haug, K. v. Klitzing, and K. Eberl, *Time-resolved measurements of transport in edge channels*, Phys. Rev. Lett. **71**, 14, 2292 (1993).

[87] G. Ernst, R. J. Haug, J. Kuhl, K. von Klitzing, and K. Eberl, *Acoustic Edge Modes of the Degenerate Two-Dimensional Electron Gas Studied by Time-Resolved Magneto-transport Measurements*, Phys. Rev. Lett. **77**, 20, 4245 (1996).

[88] G. Sukhodub, F. Hohls, and R. J. Haug, *Observation of an Interedge Magnetoplasmon Mode in a Degenerate Two-Dimensional Electron Gas*, Phys. Rev. Lett. **93**, 19, 196801 (2004).

[89] H. Kamata, T. Ota, K. Muraki, and T. Fujisawa, *Voltage-controlled Group Velocity of Edge Magnetoplasmon in the Quantum Hall Regime*, arXiv:1001.4225 (2010).

[90] V. I. Talyanski, J. E. F. Frost, M. Pepper, D. A. Ritchie, M. Grimshaw, and G. A. C. Jones, *Low-frequency edge excitations in an electrostatically confined GaAs-AlGaAs two-dimensional electron gas*, J. Phys. Condens. Matter **5**, 7643 (1993).

[91] F. Pierre, A. B. Gougam, A. Anthore, H. Pothier, D. Esteve, and N. O. Birge, *Dephasing of electrons in mesoscopic metal wires*, Phys. Rev. B **68**, 8, 085413 (2003).

[92] J. T. Chalker, Y. Gefen, and M. Y. Veillette, *Decoherence and interactions in an electronic Mach-Zehnder interferometer*, Phys. Rev. B **76**, 8, 085320 (2007).

[93] E. V. Sukhorukov and V. V. Cheianov, *Resonant Dephasing in the Electronic Mach-Zehnder Interferometer*, Phys. Rev. Lett. **99**, 15, 156801 (2007).

[94] S.-C. Youn, H.-W. Lee, and H.-S. Sim, *Nonequilibrium Dephasing in an Electronic Mach-Zehnder Interferometer*, Phys. Rev. Lett. **100**, 19, 196807 (2008).

[95] P. Degiovanni, C. Grenier, and G. Fève, *Decoherence and relaxation of single-electron excitations in quantum Hall edge channels*, Phys. Rev. B **80**, 24, 241307(R) (2009).

[96] G. Seelig and M. Büttiker, *Charge-fluctuation-induced dephasing in a gated mesoscopic interferometer*, Phys. Rev. B **64**, 24, 245313 (2001).

[97] F. D. M. Haldane, *Fractional Quantization of the Hall Effect: A Hierarchy of Incompressible Quantum Fluid States*, Phys. Rev. Lett. **51**, 7, 605 (1983).

[98] G. Fano, F. Ortolani, and E. Colombo, *Configuration-interaction calculations on the fractional quantum Hall effect*, Phys. Rev. B **34**, 4, 2670 (1986).

[99] R. L. Willett, H. L. Stormer, D. C. Tsui, A. C. Gossard, and J. H. English, *Quantitative experimental test for the theoretical gap energies in the fractional quantum Hall effect*, Phys. Rev. B **37**, 14, 8476 (1988).

[100] J. K. Jain, *Composite-fermion approach for the fractional quantum Hall effect*, Phys. Rev. Lett. **63**, 2, 199 (1989).

[101] V. J. Goldman, B. Su, and J. K. Jain, *Detection of composite fermions by magnetic focusing*, Phys. Rev. Lett. **72**, 13, 2065 (1994).

[102] R. R. Du, H. L. Stormer, D. C. Tsui, A. S. Yeh, L. N. Pfeiffer, and K. W. West, *Drastic Enhancement of Composite Fermion Mass near Landau Level Filling* $\nu = \frac{1}{2}$, Phys. Rev. Lett. **73**, 24, 3274 (1994).

[103] B. I. Halperin, P. A. Lee, and N. Read, *Theory of the half-filled Landau level*, Phys. Rev. B **47**, 12, 7312 (1993).

[104] R. R. Du, A. S. Yeh, H. L. Stormer, D. C. Tsui, L. N. Pfeiffer, and K. W. West, *Fractional Quantum Hall Effect around nu =3/2: Composite Fermions with a Spin*, Phys. Rev. Lett. **75**, 21, 3926 (1995).

[105] C. L. Kane and M. P. A. Fisher, *Nonequilibrium noise and fractional charge in the quantum Hall effect*, Phys. Rev. Lett. **72**, 5, 724 (1994).

[106] A. M. Chang, *Chiral Luttinger liquids at the fractional quantum Hall edge*, Rev. Mod. Phys. **75**, 4, 1449 (2003).

[107] A. H. MacDonald, *Edge states in the fractional-quantum-Hall-effect regime*, Phys. Rev. Lett. **64**, 2, 220 (1990).

[108] C. Kane and M. P. A. Fischer, *Contacs and edge-state equilibration in the fractional quantum Hall effect*, Phys. Rev. B **52**, 24, 17393 (1995).

[109] G. Mahan, *Many Particle Physics*, Kluwer Academic/Plenum Publishers (2000).

[110] S. Conti and G. Vignale, *Collective modes and electronic spectral function in smooth edges of quantum hall systems*, Phys. Rev. B **54**, 20, R14309 (1996).

[111] K. Yang, *Field Theoretical Description of Quantum Hall Edge Reconstruction*, Phys. Rev. Lett. **91**, 3, 036802 (2003).

[112] U. Zülicke and A. H. MacDonald, *Periphery deformations and tunneling at correlated quantum Hall edges*, Phys. Rev. B **60**, 3, 1837 (1999).

[113] F. H. L. Koppens, C. Buizert, K. J. Tielrooij, I. T. Vink, K. C. Nowack, T. Meunier, L. P. Kouwenhoven, and L. M. K. Vandersypen, *Driven coherent oscillations of a single electron spin in a quantum dot*, Nature **442**, 7104, 766 (2006).

[114] S. Gustavsson, R. Leturcq, B. Simovič, R. Schleser, T. Ihn, P. Studerus, K. Ensslin, D. C. Driscoll, and A. C. Gossard, *Counting Statistics of Single Electron Transport in a Quantum Dot*, Phys. Rev. Lett. **96**, 7, 076605 (2006).

[115] S. Sasaki, S. D. Franceschi, J. M. Elzerman, W. G. van der Wiel, M. Eto, S. Tarucha, and L. P. Kouwenhoven, *Kondo effect in an integer-spin quantum dot*, Nature **405**, 6788, 764 (2000).

[116] N. C. van der Vaart, S. F. Godijn, Y. V. Nazarov, C. J. P. M. Harmans, J. E. Mooij, L. W. Molenkamp, and C. T. Foxon, *Resonant Tunneling Through Two Discrete Energy States*, Phys. Rev. Lett. **74**, 23, 4702 (1995).

[117] F. Hohls, M. Pepper, J. P. Griffiths, G. A. C. Jones, and D. A. Ritchie, *Ballistic electron spectroscopy*, Applied Physics Letters **89**, 21, 212103 (2006).

[118] D. Esteve, *Transferring Electrons One by One*, in *Single Charge Tunneling*, edited by H. Graber and M. H. Devoret, Plenum Press (New York and London) (1992).

[119] E. Bonet, M. M. Deshmukh, and D. C. Ralph, *Solving rate equations for electron tunneling via discrete quantum states*, Phys. Rev. B **65**, 4, 045317 (2002).

[120] L. P. Kouwenhoven, C. M. Marcus, P. L. McEuen, S. Tarucha, R. M. Westervelt, and N. S. Wingreen, *Electron transport in quantum dots*, in *Mesoscopic Electron Transport Series E: Applied Sciences*, volume 345, edited by L. L. Sohn, L. P. Kouwenhoven, and G. Schön, 105–214, Kluwer Academic (1997).

[121] A. Anthore, F. Pierre, H. Pothier, and D. Esteve, *Magnetic-Field-Dependent Quasiparticle Energy Relaxation in Mesoscopic Wires*, Phys. Rev. Lett. **90**, 7, 076806 (2003).

[122] G. Granger, J. P. Eisenstein, and J. L. Reno, *Observation of Chiral Heat Transport in the Quantum Hall Regime*, Phys. Rev. Lett. **102**, 086803 (2009).

[123] G. Müller, D. Weiss, A. V. Khaetskii, K. von Klitzing, S. Koch, H. Nickel, W. Schlapp, and R. Lösch, *Equilibration length of electrons in spin-polarized edge channels*, Phys. Rev. B **45**, 7, 3932 (1992).

[124] N. B. Zhitenev, R. J. Haug, K. v. Klitzing, and K. Eberl, *Experimental determination of the dispersion of edge magnetoplasmons confined in edge channels*, Phys. Rev. B **49**, 11, 7809 (1994).

[125] G. Ernst, N. B. Zhitenev, R. J. Haug, and K. von Klitzing, *Dynamic Excitations of Fractional Quantum Hall Edge Channels*, Phys. Rev. Lett. **79**, 19, 3748 (1997).

[126] R. Ionicioiu, G. Amaratunga, and F. Udrea, *Quantum Computation with Ballistic Electrons*, Int. J. Mod. Phys. B **15**, 125 (2001).

[127] S. Oberholzer, E. Bieri, C. Schönenberger, M. Giovannini, and J. Faist, *Positive Cross Correlations in a Normal-Conducting Fermionic Beam Splitter*, Phys. Rev. Lett. **96**, 4, 046804 (2006).

[128] P. Roulleau, F. Portier, P. Roche, A. Cavanna, G. Faini, U. Gennser, and D. Mailly, *Tuning Decoherence with a Voltage Probe*, Phys. Rev. Lett. **102**, 23, 236802 (2009).

[129] S. M. Girvin, A. H. MacDonald, and P. M. Platzman, *Magneto-roton theory of collective excitations in the fractional quantum Hall effect*, Phys. Rev. B **33**, 4, 2481 (1986).

[130] M. Büttiker, A. Prêtre, and H. Thomas, *Dynamic conductance and the scattering matrix of small conductors*, Phys. Rev. Lett. **70**, 26, 4114 (1993).

[131] R. A. Webb, S. Washburn, C. P. Umbach, and R. B. Laibowitz, *Observation of $\frac{h}{e}$ Aharonov-Bohm Oscillations in Normal-Metal Rings*, Phys. Rev. Lett. **54**, 25, 2696 (1985).

[132] J. Gabelli, G. Feve, J. Berroir, B. Placais, A. Cavanna, B. Etienne, Y. Jin, and D. C. Glattli, *Violation of Kirchhoff's Laws for a Coherent RC Circuit*, Science **313**, 5786, 499 (2006).

[133] M. H. Devoret, D. Esteve, H. Grabert, G.-L. Ingold, H. Pothier, and C. Urbina, *Effect of the electromagnetic environment on the Coulomb blockade in ultrasmall tunnel junctions*, Phys. Rev. Lett. **64**, 15, 1824 (1990).

[134] S. M. Girvin, L. I. Glazman, M. Jonson, D. R. Penn, and M. D. Stiles, *Quantum fluctuations and the single-junction Coulomb blockade*, Phys. Rev. Lett. **64**, 26, 3183 (1990).

[135] J. Jackson, *Classical Electrodynamics*, Wiley (1999).

[136] L. Levitov and G. Lesovik, *Charge distribution in quantum shot noise*, JETP Lett. **58**, 3, 225 (1993).

[137] M. H. Devoret, *De l'atome aux machines quantiques*, Fayard (France) (2008).

[138] H. Nyquist, *Thermal Agitation of Electric Charge in Conductors*, Phys. Rev. **32**, 1, 110 (1928).

[139] A. O. Caldeira and A. J. Leggett, *Quantum tunnelling in a dissipative system*, Annals of Physics **149**, 2, 374 (1983).

[140] Y. V. Nazarov, *Influence of the electrodynamic environment on electron tunneling at finite traversal time*, Phys. Rev. B **43**, 7, 6220 (1991).

[141] A. N. Cleland, J. M. Schmidt, and J. Clarke, *Charge fluctuations in small-capacitance junctions*, Phys. Rev. Lett. **64**, 13, 1565 (1990).

[142] T. Holst, D. Esteve, C. Urbina, and M. H. Devoret, *Effect of a Transmission Line Resonator on a Small Capacitance Tunnel Junction*, Phys. Rev. Lett. **73**, 25, 3455 (1994).

[143] P. Joyez, D. Esteve, and M. H. Devoret, *How Is the Coulomb Blockade Suppressed in High-Conductance Tunnel Junctions?*, Phys. Rev. Lett. **80**, 9, 1956 (1998).

[144] F. Pierre, H. Pothier, P. Joyez, N. O. Birge, D. Esteve, and M. H. Devoret, *Electrodynamic Dip in the Local Density of States of a Metallic Wire*, Phys. Rev. Lett. **86**, 8, 1590 (2001).

[145] A. A. Odintsov, G. Falci, and G. Schön, *Single-electron tunneling in systems of small junctions coupled to an electromagnetic environment*, Phys. Rev. B **44**, 23, 13089 (1991).

[146] J. Tobiska and Y. V. Nazarov, *Inelastic interaction corrections and universal relations for full counting statistics in a quantum contact*, Phys. Rev. B **72**, 23, 235328 (2005).

[147] I. Safi and H. Saleur, *One-Channel Conductor in an Ohmic Environment: Mapping to a Tomonaga-Luttinger Liquid and Full Counting Statistics*, Phys. Rev. Lett. **93**, 12, 126602 (2004).

[148] M. Ferrier, L. Angers, A. C. H. Rowe, S. Guéron, H. Bouchiat, C. Texier, G. Montambaux, and D. Mailly, *Direct Measurement of the Phase-Coherence Length in a GaAs/GaAlAs Square Network*, Phys. Rev. Lett. **93**, 24, 246804 (2004).

[149] R. Bruce and G. Piercy, *An improved Au—Ge—Ni ohmic contact to n-type GaAs*, Solid-State Electronics **30**, 7, 729 (1987).